

Development and implementation of numerical models for the study of multilayered plates

Rawad Baroud

▶ **To cite this version:**

Rawad Baroud. Development and implementation of numerical models for the study of multilayered plates. Materials. Université Paris-Est; Universite Saint-Joseph (Beyrouth). Ecole superieure d'ingenieurs de Beyrouth, 2016. English. NNT : 2016PESC1084 . tel-01540362

HAL Id: tel-01540362

https://pastel.hal.science/tel-01540362

Submitted on 16 Jun 2017

HAL is a multi-disciplinary open access archive for the deposit and dissemination of scientific research documents, whether they are published or not. The documents may come from teaching and research institutions in France or abroad, or from public or private research centers.

L'archive ouverte pluridisciplinaire **HAL**, est destinée au dépôt et à la diffusion de documents scientifiques de niveau recherche, publiés ou non, émanant des établissements d'enseignement et de recherche français ou étrangers, des laboratoires publics ou privés.



UNIVERSITÉ PARIS-EST



A DISSERTATION
submitted to the departement of
Sciences, Ingénierie et Environnement (SIE)
for the degree of

DOCTOR OF PHILOSOPHY
AT THE
UNIVERSITÉ PARIS-EST

Speciality: *Structures and Materials - Civil Engineering*

presented by

Rawad BAROUD

Thesis subject :

Development and Implementation of Numerical Models for the Study of Multilayered Plates

presented at École des Ponts ParisTech on december 12, 2016
in front of the jury composed of :

President :	**Hélène DUMONTET**
Reviewers :	**Paolo VANNUCCI** **Federica DAGHIA**
Examiners :	**Karam SAB** **Fadi GEARA**
Thesis advisor :	**Jean-François CARON**
Thesis co-advisor :	**Fouad KADDAH**

Acknowledgement

The work accomplished in this thesis was conducted in Navier Laboratory at Ecole des Ponts Paritech (ENPC), with joint supervision with Université Saint Joseph (USJ). It is funded by CNRS-L formerly represented by its director Charles TABET, and Campus France-ENPC.

I first would like to express my most sincere gratitude and appreciation to the jury members for taking their time to judge this work. Thank you to Hélène DUMONTET for accepting the role of president of jury, and to Fadi GEARA for his time and presence as member of the jury. A particular thanks to both Paolo VANNUCCI and Federica DAGHIA, for having reviewed this manuscript.

I want to thank my advisor Karam SAB for his scientific support, and the efficient and dynamic monitoring of my work. I thank him equally for his moral support and his encouragement during the hard times all along these three years. I am sincerely grateful to him for his availability and the time he has devoted for me despite his numerous occupations in the supervision of Navier laboratory.

I address my warm gratitude to my advisor Jean-François CARON, head of “Materiaux et Structures Architectures (MSA)” team who directed me throughout this thesis and with whom I had many scientific exchanges and a unique opportunity to gain from his expertise, persistence in work. His patience, scientific and practical approaches as well as his generosity in behavior were a big lesson for me.

Many thanks are gratefully sent to my co-advisor in Lebanon Fouad KADDAH who took the time to examine with sympathetic attention my work and give some constructive criticism using his scientific skills that have been of a great help for me to accomplish my work. I also thank Wassim RAPHAEL for his continuous support morally and administratively.

I appreciate the hard work and support of Arthur LEBEE and Ioannis STEFANOU who helped me with the finite element tools as well as the mathematical approaches for engineers and theories formulation.

I would like to thank Robert LEROY with whom I worked on the study of a complex slab structure partially funded by Bouygues Construction Company, which is also a co-inventor with "laboratoire Navier (Ifsttar)" of the concept. I equally thank the Techniwood Company, owner of the concept PANOBLOC and who graciously provided a part of the panels used for the development of the research.

I greet Michel BALABANE who helps graduate students continuing their further educations in France and who represented the link between Lebanon (CNRS-L and USJ) and France (Campus France and ENPC).

My gratitude goes as well to Marie-Francoise KASPI the secretary of MSA team who took care of my logistical and administrative matters.

Lastly, I would like to thank my family with all my heart, who raised me with attention and has given me incessantly its support and encouragement in my life to form my personality and to pursuit my studies, consequently this dissertation.

Thank you my fellow Ph.D. students and friends in France and Lebanon for the motivation and quality time your friendship has given me.

Abstract

The use of multilayer is becoming increasingly important in the field of engineering, first in the industry, and more recently more and more in Civil Engineering. Whether complex blend of polymers, wood or concrete, significant efforts are required for accurate modeling of such materials. Indeed, phenomena induced anisotropy and heterogeneity are associated with these multi-material: edge effects, differential thermal expansion, delamination/detachment or nonlinearities viscosity type damage, plasticity in layers or interfaces. Among the models proposed in the literature, we found for example equivalent monolayer model or of "LayerWise" type (a kinematic per layer). Belonging to the second category, models have been developed in recent years in Navier allow a sufficiently detailed description to address specific issues mentioned above while maintaining a surgical nature. By introducing interface forces as generalized forces of the model, these approaches have demonstrated their effectiveness with regard to the representation of details at inter- and intra-layers. It is then easy to offer behaviors and interfaces criteria and to be effective for modeling delamination or detachment, phenomenom very present in multilayered composites assembled and glued together. Therefore, a finite element program *MPFEAP* was developed in Navier laboratory. The model was also introduced as a User Element in ABAQUS, in its simplest form (perfect interfaces).

A new layerwise model for multilayered plates is proposed in this dissertation, named Statically Compatible Layerwise Stresses with first-order membrane stress approximations per layer in thickness direction *SCLS1*. The model complies exactly with the 3D equilibrium equations and the free-edge boundary conditions. Also, a refined version of the new model is obtained by introducing several mathematical layers per physical layer. The new model has been implemented in a new version of the in-house finite element code *MPFEAP*.

In parallel, a finite element program based on the Bending-Gradient theory which was developed in Navier laboratory, is proposed here. The model is a new plate theory for out-of-plane loaded thick plates where the static unknowns are those of the Love-Kirchhoff theory, to which six components are added representing the gradient of the bending moment. The Bending-Gradient theory is obtained from the Generalized-Reissner theory: the Generalized-Reissner theory involves fifteen kinematic degrees of freedom, eight of them being related only to out-of-plane Poisson's distortion and thus, the main idea of the Bending-Gradient plate theory is to simplify the Generalized-Reissner theory by setting these eight d.o.f. to zero and to neglect the contribution of the normal stress σ_{33} in the plate model constitutive equation. A finite element program called *BGFEAP* has been developed for the implementation of the Bending-Gradient element. A User Element in Abaqus was also developed for the Bending-Gradient theory.

Keywords : Multilayered material, composites, layerwise model, Bending-Gradient model, finite element, plate theory.

Résumé

L'utilisation des multicouches prend de plus en plus d'ampleur dans le domaine des sciences de l'ingénieur, tout d'abord dans l'industrie, et plus récemment de plus en plus en Génie Civil. Qu'il s'agisse de complexes mêlant des polymères, du bois ou du béton, des efforts importants sont nécessaires pour la modélisation fine de ce type de matériaux. En effet, des phénomènes induits par l'anisotropie et l'hétérogénéité sont associés à ces multi-matériaux : effets de bords, dilatations thermiques différentielles, délaminages/décollements ou non linéarités de type viscosité, endommagement, plasticité dans les couches ou aux interfaces. Parmi les modèles proposés dans la littérature, on trouve par exemple des modèles monocouche équivalente ou de type "Layerwise" (une cinématique par couche). Appartenant à cette deuxième catégorie, des modèles ont été développés depuis quelques années dans le laboratoire Navier et permettent une description suffisamment fine pour aborder les problématiques spécifiques citées plus haut tout en conservant un caractère opératoire certain. En introduisant des efforts d'interfaces comme des efforts généralisés du modèle, ces approches ont montré leur efficacité vis-à-vis de la représentation des détails au niveau inter- et intra-couches. Il est alors aisé de proposer des comportements et des critères d'interfaces et d'être efficace pour la modélisation du délaminage ou décollement, phénomène très présent dans les composites multicouches assemblés et collés. Par conséquent, un programme éléments finis *MPFEAP* a été développé dans le laboratoire Navier. Le modèle a également été introduit sous la forme d'un User Element dans ABAQUS, dans sa forme la plus simple (interfaces parfaites).

Un nouveau model layerwise est proposé dans ce mémoire pour les plaques multicouches, appelé "Statically Compatible Layerwise Stresses with first-order membrane stress approximations per layer in thickness direction" *SCLS1*. Le modèle est conforme aux équations d'équilibre 3D ainsi qu'aux conditions aux limites de bord libre. En outre, une version raffinée du nouveau modèle est obtenu en introduisant plusieurs couches mathématiques par couche physique. Le nouveau modèle a été mis en œuvre dans une nouvelle version du code éléments finis *MPFEAP*.

En parallèle, un programme d'éléments finis basé sur la théorie Bending-Gradient développée dans le laboratoire Navier est proposé ici. Le modèle est une nouvelle théorie de plaque épaisse chargée hors-plan où les inconnues statiques sont celles de la théorie Love-Kirchhoff, à laquelle six composantes sont ajoutées représentant le gradient du moment de flexion. La théorie Bending-Gradient est obtenue à partir de la théorie Generalized-Reissner: cette dernière implique quinze degrés de liberté cinématiques, huit d'entre eux étant lié uniquement à la déformation de Poisson hors-plan, et donc l'idée principale de la théorie de plaque Bending-Gradient est de simplifier la théorie Generalized-Reissner en réglant ces huit d.d.l. à zéro et de négliger la contribution de la contrainte normale σ_{33} dans l'équation constitutive du modèle de plaque. Un programme éléments finis appelé *BGFEAP* a été développé pour la mise en œuvre de l'élément de Bending-Gradient. Un User Element dans Abaqus a été aussi développé pour la théorie Bending-Gradient.

Mots clefs : Matériaux multicouches, composites, modèle "layerwise", modèle Bending-Gradient, éléments finis, théorie de plaque.

Contents

Table of figures **10**

List of tables **14**

General introduction **17**

1 Bibliographical analysis **22**
1.1 Existing models of multilayered structures . . . 23
1.1.1 2D Plate model . . . 23
1.1.1.1 Monolayer equivalent approach . . . 23
1.1.1.1.1 The classical model of Love-Kirchhoff . . . 24
1.1.1.1.2 The classical model of Reissner-Mindlin (FSDT, First order Shear Deformation Theory) . . . 24
1.1.1.1.3 Models of higher order . . . 25
1.1.1.2 Layered approach . . . 28
1.1.1.2.1 Zig-Zag models . . . 28
1.1.1.2.2 Layer approach - discrete layers models . . . 30

2 Description of *LS1* model: formulation and finite element implementation **33**
2.1 Formulation of *LS1* model for multilayered material . . . 34
2.1.1 Approximation method of Hellinger-Reissner for a 3D problem . . . 34
2.1.2 Step 1: Stress field of the *LS1* model . . . 36
2.1.3 Step 2: Generalized displacements and strains of the *LS1* model . . . 38
2.1.3.1 Generalized displacements . . . 38
2.1.3.2 Generalized strains . . . 39
2.1.4 Step 3: Equilibrium equations and boundary conditions of *LS1* model . . . 40
2.1.4.1 Equilibrium equations . . . 40
2.1.4.2 Boundary conditions . . . 40
2.1.5 Step 4: The constitutive law of *LS1* model . . . 41
2.1.5.1 Expression of elastic energy written in stress . . . 42
2.1.5.2 The constitutive law of *LS1* model . . . 43
2.1.6 *LS1* with imperfect interface . . . 44
2.1.6.1 Interface formulation . . . 44
2.2 Presentation of the finite element of *LS1* . . . 45
2.2.1 Approximation of nodal displacement . . . 45
2.2.2 Strains and stresses . . . 47
2.2.3 Nodal approximation of strains and stresses - matrix *B* . . . 48
2.2.4 Behavior - stiffness matrix D . . . 50
2.2.5 A calculation method for a problem with initial deformation . . . 52

2.3 Contribution to *LS1* model and its finite element program *MPFEAP* 53

3 Application of *LS1* model for the study of hybrid multilayered structures 55
3.1 Introduction 56
3.2 The slab modeling 57
3.2.1 The four models 57
3.2.2 Slab rigidity 58
3.2.3 Resistance and transverse shear stresses estimation 59
3.2.4 Conclusion 60

4 A statically compatible layerwise stress model for the analysis of multilayered plates 63
4.1 Introduction 64
4.2 Theoretical formulation of the statically compatible model *SCLS1* 64
4.2.1 Problem description and notations 65
4.2.2 Governing equations of the 3D model 66
4.2.3 The static of the *SCLS1* model 67
4.2.4 The kinematics of the *SCLS1* model 69
4.2.5 The *SCLS1* model constitutive equations 70
4.2.6 The refined *SCLS1* model as a static discretization of the 3D model 72
4.3 Finite element discretization of the *SCLS1* model 74
4.3.1 Weak formulation of the *SCLS1* model 74
4.3.2 Geometry and displacement interpolations 76
4.3.3 Element stiffness matrix and nodal forces 77
4.3.4 *MPFEAP* code description 78
4.4 Examples and numerical results 78
4.4.1 Straight free-edge 79
4.4.1.1 3D FE Discretization 79
4.4.1.2 *LS1* and *SCLS1* discretization 80
4.4.1.3 Comparison between non refined *SCLS1*, non refined *LS1* and 3D FE models 81
4.4.1.4 Comparison between non refined *SCLS1* and refined *SCLS1* models 82
4.4.1.5 Parametric study of the refined *SCLS1* model 82
4.4.1.6 Parametric study of the refined *LS1* model 83
4.4.1.7 Comparison between refined *SCLS1*, refined *LS1* and 3D FE models 83
4.4.1.8 Discussion 84
4.4.2 Notched laminate under uniaxial tension 84
4.5 Conclusion 87

5 Finite Element of Bending-Gradient theory 90
5.1 Introduction 91
5.2 Notations 92
5.3 The 3D Problem 92
5.4 The Bending-Gradient theory 94
5.4.1 The Bending-Gradient equations 94
5.4.2 Localization 96
5.4.3 The case of homogeneous plates 96
5.4.4 Variational formulation 97
5.4.5 Kelvin Notations 98
5.5 Finite element discretization of the Bending-Gradient model 98

5.5.1 Methods for calculating shear stiffness matrix . . . 99
5.5.2 Geometry and displacement interpolations . . . 99
5.5.3 Weak formulation of the Bending-Gradient model . . . 100
5.5.4 Element stiffness matrix and nodal forces . . . 102
5.5.5 Bending-Gradient finite element with selective integration technique . . . 103
5.5.6 *BGFEAP* code description . . . 104
5.6 Examples and numerical results . . . 104
5.6.1 Patch tests . . . 104
5.6.1.1 Bending patch test . . . 105
5.6.1.2 Twisting patch test . . . 105
5.6.1.3 Shear patch test . . . 105
5.6.1.4 Discussion . . . 106
5.6.2 Comparison between analytical solution and Bending-Gradient finite element 106
5.6.2.1 Problem description . . . 106
5.6.2.2 Results and interpretation . . . 107
5.6.3 Comparison between Bending-Gradient FE and exact solution for multilayered plates . . . 109
5.6.3.1 Problem description . . . 109
5.6.3.2 3 Layers plate . . . 110
5.6.3.3 9 layers plate . . . 110
5.6.3.4 Discussion . . . 110
5.6.4 Mesh control: Comparison between Bending-Gradient FE, *LS1* and Abaqus 2D FE . . . 111
5.6.4.1 Problem description . . . 111
5.6.4.2 Results and discussion . . . 111
5.6.5 Comparison between Bending-Gradient FE, *LS1* and Abaqus 2D FE . . . 112
5.6.5.1 First case . . . 113
5.6.5.2 Second case . . . 116
5.6.5.3 Third case . . . 118
5.6.5.4 Fourth case . . . 120
5.6.5.5 Discussion . . . 121
5.7 Conclusion . . . 122

General conclusion and perspectives **125**

A Appendix for the statically compatible layerwise stress model *SCLS1* **128**
A.1 The closed-form expression of the stress energy w^*_{3D} . . . 129
A.2 The *SCLS1* finite element equations and matrices . . . 130
A.2.1 Stress-strain relation . . . 132
A.2.2 Behavior matrices . . . 137
A.2.2.1 Membrane behavior . . . 138
A.2.2.2 Transverse shear behavior . . . 138
A.2.2.3 Snatching efforts behavior . . . 139
A.2.2.4 Coupling behavior between membrane and snatching forces . . . 139

B Appendix for the Bending-Gradient model **141**
B.1 Other boundary conditions . . . 142
B.2 Computation of the generalized shear compliance matrix . . . 143

List of Figures

1.1 Kinematics of Love-Kirchhoff. 24
1.2 Kinematics of Reissner-Mindlin. 25
1.3 Kinematics of higher-order. 26
1.4 Geometry of the zig–zag function of Murakami. 29
1.5 Field of displacements of the zig-zag models of first-order. 29
1.6 Introduction of the function zig-zag of Murakami in the non-linear distribution. . . 30

2.1 Multilayered studied. 36
2.2 The eight-node element and its four second-order Gaussian stations. 46

3.1 An openwork (hollow) plywood cross-ply (Panobloc) connected to a concrete slab. 56
3.2 Equivalent 2D meshing (right) of the 3D structure (left). 56
3.3 Experimental and simulated mid-pan deflections (mm). 58
3.4 Mid-plane deflection depending on G_{12} and G_{13} (mm). 59
3.5 Mid-pan deflection depending on G_{23} (mm). 59
3.6 Transverse shear cracking (blue circle) between layers 2 and 3 in a transverse wooden strip. 60

4.1 Description of the multilayered plate. 65
4.2 The same multilayered plate refined through the thickness (irregular layerwise mesh through the thickness). 73
4.3 The eight-node element and its four second-order Gaussian stations. 76
4.4 Description of fiber orientation axes and angle. 79
4.5 Laminate geometry, imposed displacements and coordinate system. 79
4.6 Finite Element model of the laminate - 3D model (top); mesh in the yz plane (bottom). 80
4.7 Distribution of the interlaminar shear stress σ_{23} predicted by the non refined *SCLS1* model for two finite element meshes. 81
4.8 Zoom near the free edge on the distribution of the interlaminar shear stress σ_{23} predicted by the non refined *SCLS1* model for two finite element meshes. 81
4.9 Zoom near the free edge on the distribution of the interlaminar shear stress σ_{23} predicted by the non refined *LS1* model with $Y = 40\mu m$, the non refined *SCLS1* model with $Y = 40\mu m$ and the 3D finite element model with ($Y = 0.71\mu m, Z = 7.5\mu m$). 82
4.10 Zoom near the free edge on the distribution of the interlaminar shear stress σ_{23} predicted by the refined *SCLS1* model with $Y = 0.71\mu m$, for $e_2/h_{min} = 10$ and different values of p, the number of mathematical layers per physical layer. 82
4.11 Zoom near the free edge on the distribution of the interlaminar shear stress σ_{23} predicted by the refined *LS1* and *SCLS1* models with $Y = 0.71\mu m$, $h_{min} = 8\mu m$ in layer 2 and $p = 6$, and by the 3D FE model with ($Y = 0.71\mu m, Z = 7.5\mu m$). 84
4.12 Notched laminate plate geometry and loading. 85

4.13 Shear stress σ_{13} at the interface between layers 1 and 2 for y=0 predicted by the non refined *SCLS1* and the refined *SCLS1* model with ($X = Y = 2.5\mu m$, $h_{min} = 100\mu m$ and $p = 3$), and by the 3D FE model with ($X = Y = 2.5\mu m, Z = 100\mu m$). 85
4.14 Shear stress σ_{23} at the interface between layers 1 and 2 for $x = 0$ predicted by the non refined *SCLS1* and the refined *SCLS1* model with ($X = Y = 2.5\mu m$, $h_{min} = 100\mu m$ and $p = 3$), and by the 3D FE model with ($X = Y = 2.5\mu m, Z = 100\mu m$).. 86
4.15 Zoom on the shear stress σ_{23} at the interface between layers 1 and 2 for $x = 0$ predicted by the non refined *SCLS1* and the refined *SCLS1* model with ($X = Y = 2.5\mu m$, $h_{min} = 100\mu m$ and $p = 3$), and by the 3D FE model with ($X = Y = 2.5\mu m, Z = 100\mu m$). 86
4.16 Zoom on the shear stress σ_{23} at the interface between layers 1 and 2 for $x = 0$ predicted by the non refined *SCLS1* and the refined *SCLS1* model with ($X = Y = 2.5\mu m$, $h_{min} = 100\mu m$ and $p = 3$), and by the 3D FE model with ($X = Y = 2.5\mu m, Z = 50\mu m$). 87

5.1 Plate Configuration. 93
5.2 The eight-node element a) with four second-order Gaussian stations b) with nine second-order Gaussian stations. 99
5.3 Patch test: a patch of elements is considered in the load cases. 104
5.4 Shearing case. 106
5.5 Description of fiber orientation axes and angle. 107
5.6 Description of laminated plate configuration for cylindrical bending. 107
5.7 Displacement: $\overline{U}_3$, ϕ_{111}, ϕ_{221} and ϕ_{122}, predicted by the Bending-Gradient finite element and the analytical solution. 108
5.8 Distribution of $\overline{M}_{11}$, $\overline{M}_{22}$, $\overline{R}_{111}$ and $\overline{R}_{221}$ predicted by the Bending-Gradient finite element and the analytical solution. 108
5.9 Multilayered square plate configuration: a) stack of 3 layers 0°/90°/0°, b) stack of 9 layers 0°/90°/0°/90°/0°/90°/0°/90°/0°. 109
5.10 Convergence of deflection calculated between: A) BG FE and 2D FE Abaqus, B) *LS1* and 2D FE Abaqus. 112
5.11 Distribution of moments $\overline{M}_{11}$ and $\overline{M}_{11}$ and shear forces $\overline{Q}_1$ and $\overline{Q}_2$ at $Y = L/2$ for L/h=10, predicted by Bending-Gradient FE, *LS1* and Abaqus 2D FE for 30°/ − 30°/ − 30°/30°. 113
5.12 Deflection $\overline{U}_3$ at $Y = L/2$ for L/h=10, predicted by Bending-Gradient FE, *LS1* and Abaqus 2D FE for 30°/ − 30°/ − 30°/30°. 114
5.13 Distribution of moment of torsion $\overline{M}_{12}$ at A) diagonal between X=0, Y=0 and $X = L$, $Y = L$ and B) diagonal between X=0, $Y = L$ and $X = L$, Y=0, for L/h=10, predicted by Bending-Gradient FE, *LS1* and Abaqus 2D FE for 30°/ − 30°/ − 30°/30°. 114
5.14 Distribution of moments $\overline{M}_{11}$ and $\overline{M}_{22}$ and shear forces $\overline{Q}_1$ and $\overline{Q}_2$ at $Y = L/2$ for L/h=4, predicted by Bending-Gradient FE, *LS1* and Abaqus 2D FE for 30°/ − 30°/ − 30°/30°. 115
5.15 Deflection $\overline{U}_3$ at $Y = L/2$ for L/h=4, predicted by Bending-Gradient FE, *LS1* and Abaqus 2D FE for 30°/ − 30°/ − 30°/30°. 115
5.16 Distribution of moment of torsion $\overline{M}_{12}$ at A) diagonal between X=0, Y=0 and $X = L$, $Y = L$ and B) diagonal between X=0, $Y = L$ and $X = L$, Y=0, for L/h=4, predicted by Bending-Gradient FE, *LS1* and Abaqus 2D FE for 30°/ − 30°/ − 30°/30°. 116

5.17 Distribution of moments $\overline{M}_{11}$ and $\overline{M}_{22}$ and shear forces $\overline{Q}_1$ and $\overline{Q}_2$ at $Y = L/2$ for L/h=4, predicted by Bending-Gradient FE, *LS1* and Abaqus 2D FE for $30°/-30°/-30°/30°$. 117
5.18 Deflection $\overline{U}_3$ at $Y = L/2$ for L/h=4, predicted by Bending-Gradient FE, *LS1* and Abaqus 2D FE for $30°/-30°/-30°/30°$. 117
5.19 Distribution of moment of torsion $\overline{M}_{12}$ at A) diagonal between X=0, Y=0 and $X = L$, $Y = L$ and B) diagonal between X=0, $Y = L$ and $X = L$, Y=0, for L/h=4, predicted by Bending-Gradient FE, *LS1* and Abaqus 2D FE for $30°/-30°/-30°/30°$. 118
5.20 Distribution of moment of torsion $\overline{M}_{12}$ at $Y = b/2$, predicted by Bending-Gradient FE, *LS1* and Abaqus 2D FE for $0°/90°/90°/0°$. 119
5.21 Deflection $\overline{U}_3$ at $X = L$, predicted by Bending-Gradient FE, *LS1* and Abaqus 2D FE for $0°/90°/90°/0°$. 119
5.22 Distribution of moment of torsion $\overline{M}_{12}$ at $Y = b/2$, predicted by Bending-Gradient FE, *LS1* and Abaqus 2D FE for $60°/-60°/-60°/60°$. 120
5.23 Deflection $\overline{U}_3$ at $X = L$, predicted by Bending-Gradient FE, *LS1* and Abaqus 2D FE for $60°/-60°/-60°/60°$. 120

A.1 Description of fiber orientation axes and angle. 138

List of Tables

2.1 Type of interfacial behaviors and *LS1* corresponding references 45

3.1 Maximum transverse shear stresses σ_{13} (MPa), for each interface and for the different models a), c) and d) 60

4.1 3D Finite Element results for $Y = 0.71\mu m$ and various values of Z 80
4.2 $\sigma_{23}^{max}(MPa)$ predicted by the refined *SCLS1* model with $Y = 0.71\mu m$ for various values of h_{min} in layer 2 and p. 83
4.3 $\sigma_{23}^{ed}(MPa)$ predicted by the refined *SCLS1* model with $Y = 0.71\mu m$ for various values of h_{min} in layer 2 and p. 83
4.4 $\sigma_{23}^{max} = \sigma_{23}^{ed}(MPa)$ predicted by the refined *LS1* model with $Y = 0.71\mu m$ for various values of h_{min} in layer 2 and p. 83

5.1 The average value of moment M_{11} intensity calculated throughout the plate. 105
5.2 The average value of moment M_{12} intensity calculated throughout the plate. 105
5.3 The average value of shear Q_1 intensity calculated throughout the plate. 106
5.4 Validation of the Bending-Gradient finite element on a square plate with 3 layers. . 110
5.5 Validation of the Bending-Gradient finite element on a square plate with 9 layers. . 110
5.6 Relative difference between *LS1* (reference solution) and Bending-Gradient FE and Abaqus 2D FE for plate's overall configuration and bending direction. 121

General introduction

Thanks to the recent research, composite materials are rapidly developing in the world, in several sectors including industrial aerospace, automotive, sports and leisure, civil engineering and navy. Given that this material is both lighter and more resilient to mechanical and chemical constraints than other materials, in addition to costing less and needs much less maintenance, composite materials have proven to be the best choice for engineers.

On the other hand, composite materials bring specific internal problems due to their structures. Therefore, it is necessary to study their behavior, damage and mode of failure (delamination in matrices or fibers, ...) (Giunta et al., 2012; Abisset et al., 2016; Sun et al., 2016). Numerical methods, especially finite elements calculations are essential for the design of such complex structures in order to cope with their peculiar heterogeneous structure and anisotropy.

However, the modeling of these composites using three-dimensional models of finite elements (FE) is very expensive in terms of computational time and memory. Consequently, this method of calculation is limited to specific regions and to provide reference results for some specific configurations. They also present the disadvantage of non-converging results in the vicinity of the edges at the interfaces between layers due to the presence of singularities (Leguillon and Sanchez-Palencia, 1987; Ting and Chou, 1981; Wang and Choi, 1982; Leguillon, 1999; Chue and Liu, 2002; Mittelstedta and Becker, 2005). It has been demonstrated that differences in elastic properties of adjacent layers generally result in a highly concentrated interlaminar stresses near free edges. This phenomenon can lead to interlaminar failures (delaminations) which may cause global failure of the multilayered structure. In addition, to take well into account the effect of the interface, such as the gradients of stresses in the thickness, delamination, slip or other damages, the mesh in thickness direction should be very refined. For these reasons, and by taking into account the relatively small thickness of multilayered structures, the existence of specific models for composite materials has proven to be essential.

The purpose of this dissertation is to provide simple finite element and operational tools for global and local analysis of multilayered structures.

It is well known that the theories of conventional plates based on the assumptions of Kirchhoff, neglecting the transverse shear (Yang et al., 1966; Reissner and Stavsky, 1961) are only adequate for the analysis of thin composite plates. These theories predict badly the responses of thick modern multilayered structures with a high degree of anisotropy; the transverse shear has a more important role in anisotropic plates than in isotropic plates.

Several 2D plate models have been proposed to take into account the effect of transverse shear. We can regroup these theories of 2D plate into two general categories: equivalent monolayer models (global approximation) and discrete layer models (local approximation).

The first category contains the theory of Reissner-Mindlin type (R.D., 1951) extended to multilayers by replacing the multilayer by an equivalent homogeneous anisotropic plate. First order theories postulate a kinematics of the first degree in z (Whitney and Pagano, 1970; REISSNER, 1972); and several developments have been made based on the so called First-order Shear Deformation Theory Daghia et al. (2008). Higher-order theories are based on non-linear approximation in z of 3D displacement, 3D constraints or mixed (Tarun et al., 1982; Reissner, 1984; Reddy, 1984). An extension to multilayered plates of the Reissner-Mindlin theory has been developed in the Navier Laboratory and named Bending-Gradient. The Bending-Gradient theory (Lebée and Sab, 2011a,b) is obtained from the Generalized-Reissner theory and several projections as a Reissner-Mindlin theory are introduced.

In the second category, the models ; based on the approach by layer ; are characterized by

linearity, quadratic ... of the fields in the thickness of each layer (Di Sciuva, 1984; Pagano and Soni, 1983; Carrera, 2000, 2002, 1998, 1999a,b). These are sophisticated models that allow to study local responses, especially at the interface between layers. Of course the number of variables depends on the number of layers, which significantly increases the amount of computation. Di Sciuva proposed the model "zig-zag", source of numerous additional work, which is based on a layered approach but with a number of variables independent from the number of layers (di Sciuva, 1986; Marco and Ugo, 1993; Di Sciuva, 1984). By taking a direct inspiration from Pagano's model (Pagano, 1978), a layerwise stress model was proposed in (Naciri et al., 1998; Carreira et al., 2002; Diaz Diaz et al., 2002; Caron et al., 2006; Nguyen and Caron, 2006; Dallot and Sab, 2008; Saeedi et al., 2012a,b, 2013a,b; Lerpiniere et al., 2014). In this model, the multilayered material is considered as a superposition of Reissner-Mindlin plates linked together by interfacial stresses which are considered as additional generalized stresses. In order to make reference to Carrera's nomenclature proposed in (Carrera, 2004), this model, previously called *Multi-particle Model of Multilayered Materials (M4)*, was renamed as *LS1* which means Layerwise Stress approach with first-order membrane stress approximations per layer in the thickness direction.

The main difference between the *LS1* model and other existing layerwise models is that, most often, the other layerwise models are either displacement approaches or mixed displacement-stress approaches while the *LS1* model, derived by means of the Hellinger-Reissner mixed principle, is a pure layerwise stress approach where there are no assumptions on the displacement fields. Diaz Diaz et al. (2002) used the *LS1* model to evaluate interfacial stresses in symmetrical laminates under tensile loading with free edges. Caron et al. (2006) applied this model to the prediction of mode III delamination in multilayered materials. In (Dallot and Sab, 2008), the authors employed the *LS1* model for analyzing a sandwich plate under cylindrical bending and demonstrated the capacity of this model to capture the plastic collapse modes. In (Saeedi et al., 2012b), the authors proposed the refined *LS1* model by introducing several *mathematical layers* per physical layer in order to capture the stress concentrations occurring in delaminated multilayered plates under uniaxial tension. It was proven that the proposed layerwise mesh strategy improves considerably stress and energy release rate estimations given by the non refined *LS1* model considered in (Saeedi et al., 2012a). Nevertheless, the non refined *LS1* model reveals itself to be very effective in the simulation of mode I (Double Cantilever) and mode II (End Notched Flexure) delamination tests on multilayered plates (Saeedi et al., 2013a), and in the simulation of delamination propagation in multilayered materials at $0°/\theta°$ interfaces (Lerpiniere et al., 2014).

Thanks to its universal character, the method of finite elements is the essential engineering tool for the analysis of composite structures by the models described above. Most refined FE models based on higher order theories or discrete layers present a number of nodal variables which increase with the number of layers or the unconventional degrees of freedom. They are efficiently used for dimensioning of multilayered structures at a local level. In Navier laboratory, a refined FE called *MPFEAP* based on the *LS1* model was developed (Nguyen and Caron, 2006; Nguyen, 2004). *LS1* model uses a 2D description and a 2D meshing, for 3D structures. In this 2D plate model, each node has 5 kinematic fields per layer. Its formulation is based on the variational formulation of Hellinger-Reissner of 3D elasticity problems (Reissner, 1950), which has the advantage of giving at the same time, the generalized stresses, generalized displacement associated, equilibrium equations, boundary conditions and the behavior of the approached model. This approach has been validated by 3D FE and by comparisons with analytical solutions (Carreira et al., 2002; Nguyen and Caron, 2006).

This dissertation consists of five chapters:

First, a bibliographical synthesis citing the different approaches of existing multilayered plates along with their advantages and disadvantages.

In the second chapter, a formulation of the *LS1* model is recalled. The model considers the multilayered materials as the superposition of Reissner plates linked together with interface forces. The construction of the model is based on the approximation method of Hellinger-Reissner (Reissner, 1950). The introduction of approached stresses from generalized forces in a functional adaptation of Hellinger-Reissner helped in identifying the displacements and generalized strains. The application of Reissner theorem and with some energetic assumptions, result in the constitutive law, the equilibrium equations and the boundary conditions. The imperfect interface for the *LS1* model is summarized, and the last part of this chapter consists of presenting the finite element *MPFEAP* of *LS1* model and the contributions made to the model and its finite element program.

In the third chapter, an application for the predimensioning of a complex structure made of wood-concrete is presented. We present the 3D FE calculation of a complex structure, due to the hollow geometry of the object but also to the structural and material anisotropy. In particular, the wood has a very weak transverse rolling shear modulus. The effects of these transverse shears are important and cannot be fully accounted for an equivalent homogeneous layer that can be found in composite codes. *LS1* model based on a layerwise approach, improves the shear behavior predictions, and analyzes local responses, especially at the interface between the layers. Its finite element code *MPFEAP* allows estimating the intensity of 3D singularities using a 2D plane mesh, even for this complex 3D structure. The performance of this approach is compared with Abaqus, 2D composite shell element, and with a beam analytical model. Also comparisons are made with experimental results.

In the fourth chapter, a new layerwise model for multilayered plates is introduced. The model, called *SCLS1* for Statically Compatible Layerwise Stresses with first-order membrane stress approximations per layer in thickness direction, complies exactly with the 3D equilibrium equations and with the free-edge boundary conditions. As in the *LS1* model initially proposed in (Naciri et al., 1998), the laminated plate is considered as a superposition of Reissner plates coupled by interfacial stresses which are considered as generalized stresses. However, the divergences of the interlaminar transverse shears are introduced as additional generalized stresses in the *SCLS1* model. Also, a refined version of the new model is obtained by introducing several *mathematical layers* per physical layer. Unlike the *LS1* model which is derived by means of the Hellinger-Reissner principle, the new model is derived by means of the minimum of the complementary energy principle. This ensures the convergence of the refined *SCLS1* solution to the exact 3D solution as the number of mathematical layers per physical layer increases. The new model has been implemented in a new version of the in-house finite element code *MPFEAP*. Several comparisons are made between *LS1*, *SCLS1* and full 3D FE models in order to assess the performances of the new model which reveals to be very effective.

The last chapter is intended for the presentation of a finite-element modeling of a recent plate theory for out-of-plane loaded thick plates, named the Bending-Gradient theory (Lebée and Sab, 2011a,b; Sab and Lebée, 2015; Lebée and Sab, 2017). This theory, which has seven degrees of freedom (one transverse displacement and six generalized rotations), is a simplification of the Generalized-Reissner theory (Lebée and Sab, 2016a,b) which extends to arbitrary multilayered plates the Reissner theory (Reissner, 1944) initially introduced for homogeneous plates. A finite-element program called *BGFEAP* has been developed here for the implementation of a new eight-node element dedicated to Bending-Gradient theory. The proposed finite element model is capable of computing transverse shear stress distribution in the plate thickness. Several comparisons are made between the new Bending-Gradient finite-element, *LS1* layerwise finite-element model (Naciri et al., 1998; Caron et al., 2006; Nguyen and Caron, 2006), exact solutions and Abaqus plate finite-element model in order to assess the performances of the new model which reveals to be very effective for complex structures.

Finally, this dissertation proposes some conclusions and perspectives for this work.

CHAPTER 1

Bibliographical analysis

1.1 Existing models of multilayered structures

A multilayer composite structure can be considered as a heterogeneous body consisting of a finite number of anisotropic homogeneous layers bonded together. The geometric characteristic of a plate is a weak thickness compared to the other dimensions. Modeling of modern multilayered structures with a strong anisotropy (for example, low ratio of the transverse shear modulus of the web with respect to the longitudinal modulus of elasticity of the skin in the case of sandwich structures) requires refined theories that take into account a good description of the transverse shears. We can find in (Kant and Swaminathan, 2000; Carrera, 2000, 2002) complete reviews on the various existing models of 3D or 2D models.

In general, two types of approaches are proposed for multilayered structures:

- Three-dimensional approaches (3D)
- Plate models (2D)

The interest of a three-dimensional approach resides in obtaining accurate three-dimensional results, useful as reference. Adopting a three-dimensional approach is useful in case the differential equations finally obtained can be resolved. The three-dimensional (3D) approach is therefore limited to certain cases of geometry, stacking and simple loading (Pagano, 1969, 1970; Srinivas and Rao, 1970, 1973).

Similarly, taking into account specific laminates damage (delamination, transverse crack, ...) requires a good description of the fields in the vicinity of interfaces, privileged sites of these damages. Here again a 3D approach may provide information in some cases (free edge, plate hole...) but it is preferable to consider two-dimensional (2D) approaches of plate type. In the following, these are the 2D approaches that will be mentioned.

1.1.1 2D Plate model

During the past years, several two-dimensional models have been developed for modeling of multilayered structures taking into account the transverse shears or damages. They are grouped according to the type of the adopted approach:

- Monolayer equivalent approach
- Layered approach

1.1.1.1 Monolayer equivalent approach

In the monolayer equivalent approach, the number of degrees of freedom, which equals the number of equations, does not depend on the number of layers. The multilayered plate is homogenized and is considered as a single layer. The transverse shear can be taken into account through the inclination of the transverse section.

Among the family of the equivalent monolayers, we cite:

- The classical model of Love-Kirchhoff
- The model of Reissner-Mindlin
- The models of higher order

1.1.1.1.1 The classical model of Love-Kirchhoff

The classical model of Love-Kirchhoff is based on the assumption that the transverse section remains flat and perpendicular to the middle section after being deformed (Fig. 1.1). This means that the transverse shear is neglected and the effects due to shear are also neglected.

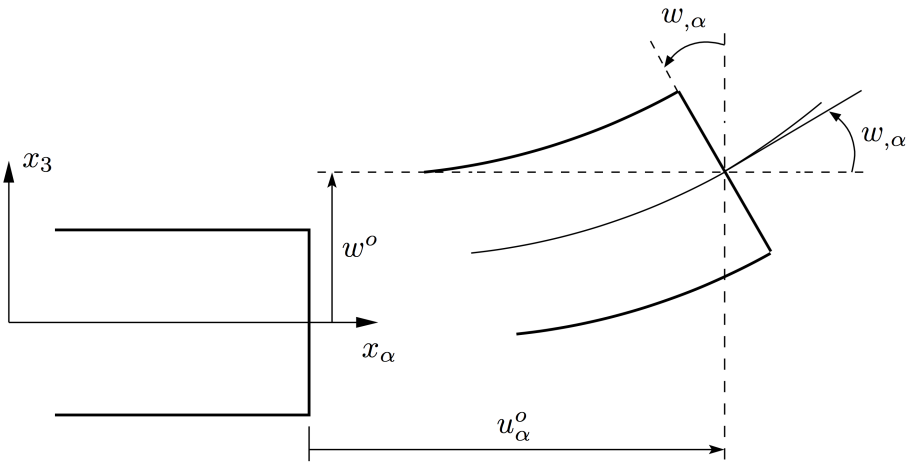


Fig. 1.1. Kinematics of Love-Kirchhoff.

The displacement field of a Love-Kirchhoff's plate is written:

$$\begin{aligned} u_\alpha(x_1, x_2, z) &= u^0_\alpha(x_1, x_2) - z\omega_{,\alpha}(x_1, x_2) \qquad \alpha = 1, 2 \\ u_3(x_1, x_2, z) &= \omega(x_1, x_2) \end{aligned} \tag{1}$$

with
1, 2: the directions in the plane of the plate
3: the normal to the plate (Fig. 1.1)
u^0_α: the membranar displacement in direction α
ω: the deflection of the plate
$\omega_{,\alpha}$: the rotation due to bending (without shear)

1.1.1.1.2 The classical model of Reissner-Mindlin (FSDT, First order Shear Deformation Theory)

To introduce the transverse shear, the kinematic assumption is made (R.D., 1951) that the section remains flat but it is no more normal to the middle section in the deformed configuration (Fig. 1.2).

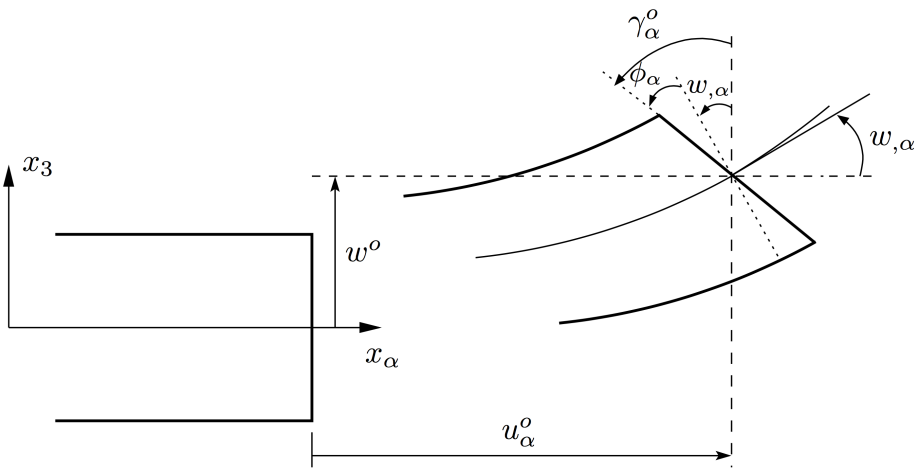


Fig. 1.2. Kinematics of Reissner-Mindlin.

The displacement field of Reissner-Mindlin's plate is written:

$$\begin{aligned} u_\alpha(x_1, x_2, z) &= u_\alpha^0(x_1, x_2) + z\phi_\alpha(x_1, x_2) \qquad \alpha = 1, 2 \\ u_3(x_1, x_2, z) &= \omega(x_1, x_2) \end{aligned} \tag{2}$$

with
u_α^0: the membranar displacement of direction α
ω: the deflection of the plate
ϕ_α: the rotation of the section around axis x_α

Therefore, the transverse shear strain is not null. u_3 is constant in z and so ϵ_{13} and ϵ_{23} are constant in z and ϵ_{33}=0. Thus, σ_{13} and σ_{23} are constant by layer, which is a bad approximation. In fact if $\sigma_{\alpha\beta}$ is refined by layer as $\epsilon_{\alpha\beta}$ then $\sigma_{\alpha 3}$ should be of second degree according to the equilibrium equations.

In addition, ϵ_{33}=0 is incompatible with the classical hypothesis of plate made in the model, i.e. σ_{33}=0. All this means that the model poorly predicts the transverse shear behavior, as soon as the slenderness ratio L/h decreases or important gradients of material properties exist in the multilayer (sandwiches).

Thus the notion of corrector coefficient is introduced to better take into account these effects of transverse shear (Whitney, 1973). The obtained results depend mainly on the empirical choice in complex situations of corrector coefficients and the study of thick composites remains random by this type of kinematic approach.

1.1.1.1.3 Models of higher order

To consider the drawbacks of first order theories, many authors (Whitney and Sun, 1973; Reddy, 1984; Cho and Parmerter, 1993; Swaminathan and Ragounadin, 2004; Cecchi and Sab, 2007; Nguyen et al., 2008) suggest theories of higher order where the fields distribution across the thickness is non-linear (Fig. 1.3).

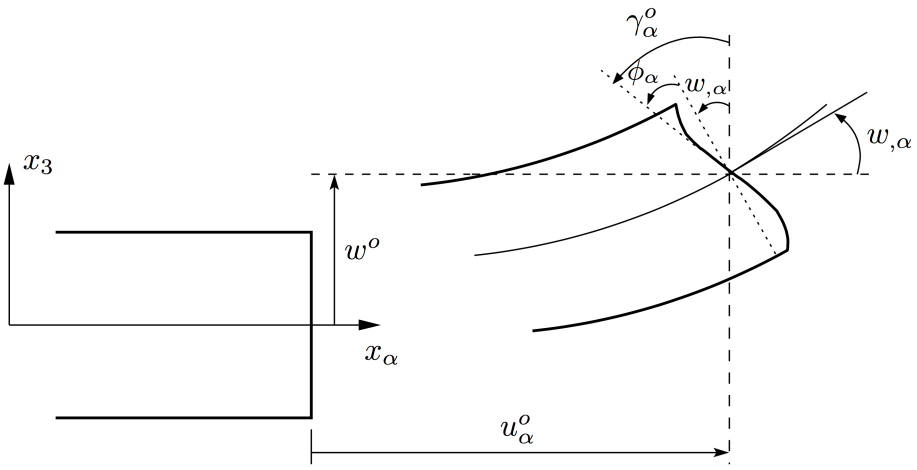


Fig. 1.3. Kinematics of higher-order.

Most of the higher-order models use a development in Taylor series of the displacement fields in order to approach the three-dimensional theory. The displacement is assumed to be of the form:

$$u_i(x_1, x_2, z) = u_i(x_1, x_2) + z\phi_i^{(1)}(x_1, x_2) + z^2\phi_i^{(2)}(x_1, x_2) + z^3\phi_i^{(3)}(x_1, x_2) + \dots \tag{3}$$

with $i = 1 \dots 3$.

The theory of the first order of Reissner-Mindlin corresponds to the Taylor series up to order j=1 and $\phi_3^{(1)}$=0.

(Hildebrand et al., 1938) are the first to have introduced this sophistication in the classical theory of plates. (Nelson and Lorch, 1974; Librescu, 1975) have applied this theory of higher-order to analyze the multilayered plates. (Lo et al., 1977a,b) have considered the effect of the transverse normal strain: $\phi_i^{0(4)}$=0 and $\phi_3^{0(3)}$=0. (Kant et al., 1982) are the first to propose a finite element of higher order. This theory considers the three-dimensional Hooke's law, it incorporates the effect of transverse normal strain and transverse shear strain. (Noor and Burton, 1989) presented a complete list of studies on theories of first-order and higher-order for the static analysis and free vibration of composite plates. (Kant and Swaminathan, 2002) gave analytical solution of different models of higher order.

In principle, these higher order models are more accurate than the first order models. However, to increase the accuracy of the theory, the number of degrees of freedom must be higher. To reduce the number of displacement parameters, several simplifications are proposed. One of the simplifications shortens the last terms of the Taylor series by introducing a "shear function". The form of the displacement through the thickness is:

$$\begin{aligned} u_\alpha(x_1, x_2, z) &= u_\alpha(x_1, x_2) - zw_{,\alpha}(x_1, x_2) + f(z)\gamma_\alpha(x_1, x_2) \qquad \alpha = 1, 2 \\ u_3(x_1, x_2, z) &= w(x_1, x_2) \end{aligned} \tag{4}$$

Some important shear functions $f(z)$ are considered:

- Ambartsumyan (1969)

$$f(z) = \frac{z}{2}\left(\frac{h^2}{4} - \frac{z^2}{3}\right) \tag{5}$$

- Reissner (1945); Panc (1975)

$$f(z) = \frac{5}{4} z \left(1 - \frac{4z^2}{3h^2}\right) \tag{6}$$

- Kassapoglou and Lagace (1987); Levinson (1980); Murthy (1981)

$$f(z) = z \left(1 - \frac{4z^2}{3h^2}\right) \tag{7}$$

with h: the thickness of the plate.

A comparison of reference models of higher order is made by (Kant and Swaminathan, 2002). The model of (Reddy, 1984) whose membranar displacement field is cubic and normal displacement w is constant through the thickness, gives a good approximation for transverse shear stresses with respect to the three-dimensional elastic solution for the homogeneous case. However, it is noted that with such a choice for $w(x, y)$ independent of z, ϵ_{33}=0 (σ_{33}=0 taken in general by the plates).

The distribution of transverse shear stresses is parabolic through the thickness (it is actually parabolic by layer). On the free surfaces, boundary conditions are matched.

Reddy model's results are also very close to the two models of higher order proposed by (Kant and Swaminathan, 2002) where the Taylor series applied to displacements extends to order 3 for the three directions of model 1 and both directions x, y for model 2. The normal displacement of model 2 remains constant through the thickness.

Using the theory of Reddy, (Senthilnathan et al., 1987) presented a simplified theory of higher-order. It consists in introducing a further reduction of the number of the degrees of freedom by taking into account the contributions of shear and bending.

The vertical displacement u_3 is considered to be the sum of the vertical displacement due to the transverse shear w^f and the deflection due to bending w^c. The description of displacements is written:

$$\begin{array}{ll} u_\alpha(x_1, x_2, z) & = u_\alpha(x_1, x_2) - z w^f_{,\alpha}(x_1, x_2) - \frac{4z^3}{3h^2} w^c_{,\alpha}(x_1, x_2) \qquad \alpha = 1, 2 \\ u_3(x_1, x_2, z) & = w^f(x_1, x_2) + w^c(x_1, x_2) \end{array} \tag{8}$$

where f and c notations mean the contributions of bending and transverse shear to normal displacement.

Polit and Touratier (1997, 2002); Touratier (1991); Idlbi et al. (1997) give the form "sinus" to the shear function $f(z)$. This function is expressed in trigonometric sinusoidal form. The function of transverse shear is written:

$$\begin{array}{ll} f(z) & = \frac{h}{\pi} sin\left(\frac{\pi z}{h}\right) = \frac{h}{\pi} \sum_{n=0}^{\infty} \frac{(-1)^n}{(2n+1)!} \left(\frac{\pi z}{h}\right)^{2n+1} \\ & = z\left(1 - \frac{\pi^2}{3!}\frac{z^2}{h^2} + \frac{\pi^4}{5!}\frac{z^4}{h^4} - \frac{\pi^6}{7!}\frac{z^6}{h^6} + \ldots\right) \end{array} \tag{9}$$

This model is very similar to the models of higher order of Taylor series type. The transverse shear stresses determined by this model take a cosinusoidal form across the thickness.

Compared to the exact solution, the model "sinus" gives better results than the model of Reddy. Based on the work of Touratier, a triangular finite element with six nodes, is built for nonlinear multilayered structures (Polit and Touratier, 1997).

Despite the fact that the models of higher order ensure a continuity of displacement and strain at the interface, the stresses $\sigma_{\alpha 3}$ and σ_{33} of the interface remain discontinuous. This has a disadvantage in the local analysis of the interface of multilayered structures that the properties of the layers are very different (edge effects on the stresses, delamination, ...).

1.1.1.2 Layered approach

1.1.1.2.1 Zig-Zag models

For the models equivalent monolayer, the number of unknowns is independent of the number of layers. Another track of development is the use of models in which we introduce a function that takes into account the distributions of the displacement field on the interfaces. This allows to refine ESL models by keeping the number of unknowns independent of the number of layers. These models are known as zig-zag (Carrera, 2002).

History of the zig-zag model is the dominating topic of Carrera's review (Carrera, 2003). In zig-zag model, the displacement of a structure is continuous along the thickness, however, the slope of the displacement function of each layer is different. This change in two adjacent perfectly glued layers is considered to be a zig-zag due to the difference of deformation of layers. The conditions of continuity of the transverse stresses on the interfaces are respected in some works. The development of the type zig-zag is performed for monolayer equivalent approaches and also for discreet layer approaches.

In the family of the zig-zag theories applied in monolayer equivalent approaches, three independent main approaches are known: Lekhnitskii multilayered theory (LMT), Ambartsumian multilayered theory (AMT) and Reissner multilayered theory (RMT). The LMT and AMT describe the effect zig-zag through the introduction of conditions of continuity of transverse stresses through the constitutive equations of each layer and the relation between strain and displacement. On the other hand, the RMT uses independent equations in the theory. Based on the RMT, Murakami (Murakami, 1986) introduced a zig-zag function of variable z to describe the effect of zig-zag displacement. The zig-zag function of Murakami (Fig. 1.4) is written:

$$M(z_i) = (-1)^i \frac{z_i}{2h_i} \tag{10}$$

where

z_i: coordinate of the considered point in the local axes of the layer i of which the abscissa is located in the middle of the layer. h_i: thickness of layer i

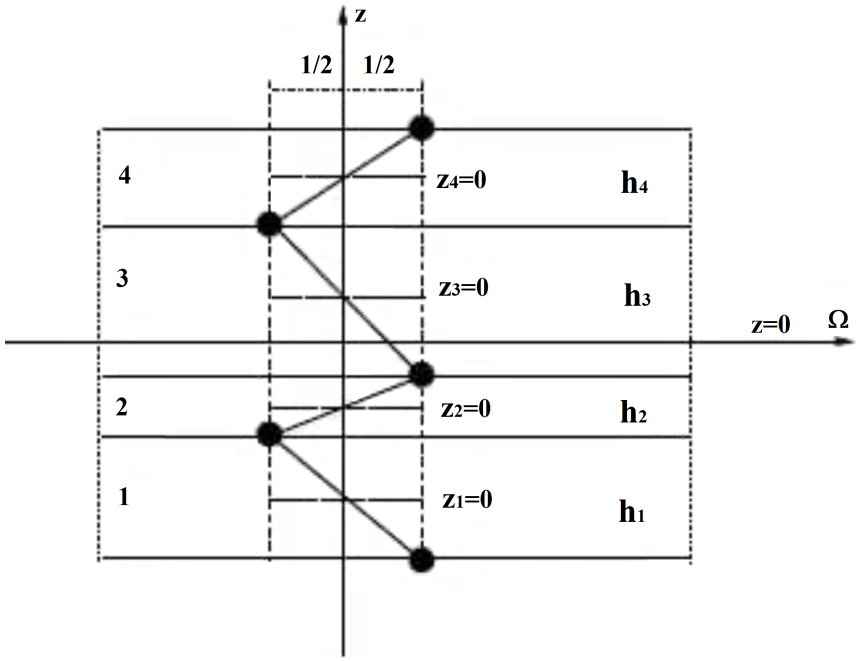


Fig. 1.4. Geometry of the zig–zag function of Murakami.

By adding the zig-zag of Murakami (MZZF) function, the shape of the displacement of the first order theory is shown on Fig. 1.5. In the same way, the function of the displacement form of the theory of higher-order becomes (Fig. 1.6):

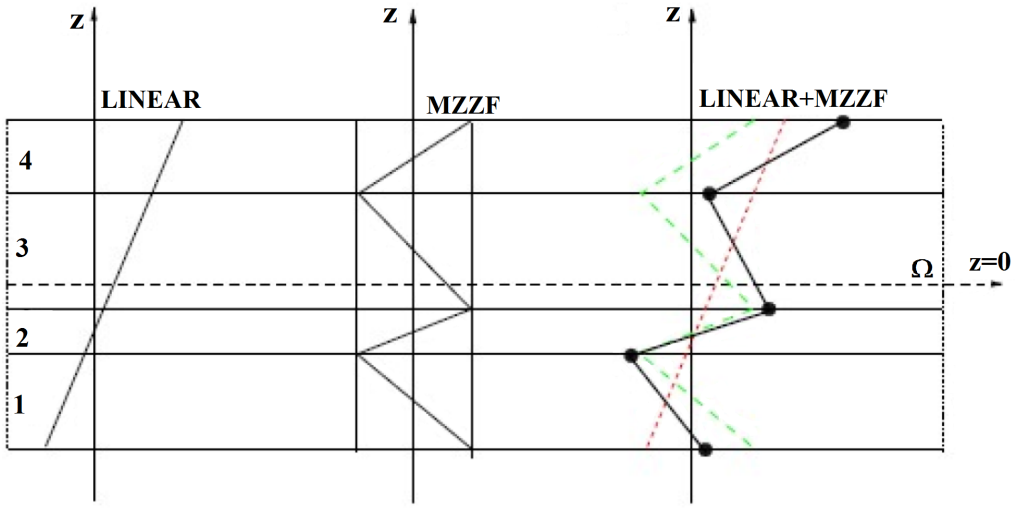


Fig. 1.5. Field of displacements of the zig-zag models of first-order.

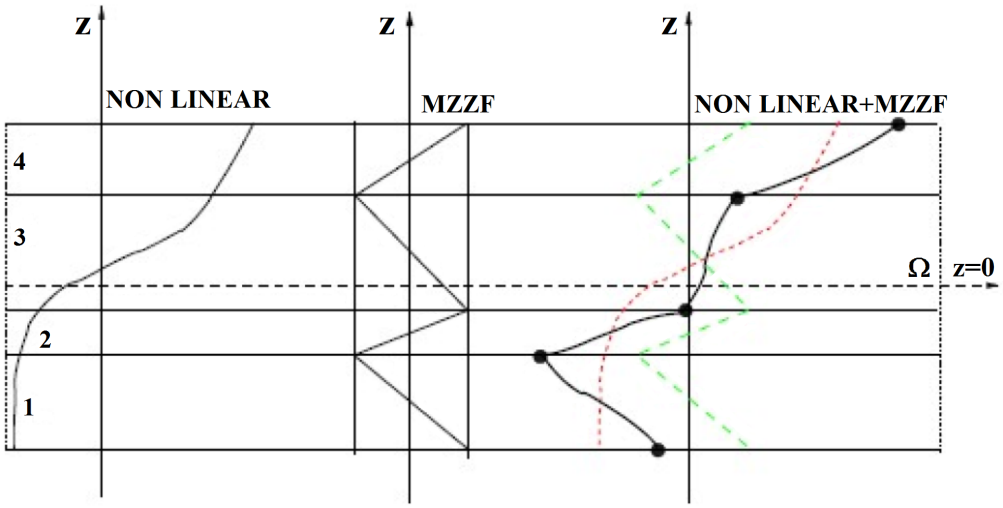


Fig. 1.6. Introduction of the function zig-zag of Murakami in the non-linear distribution.

$$u_i(x_1, x_2, z) = u_i(x_1, x_2) + z\phi_i^{(1)}(x_1, x_2) + z^2\phi_i^{(2)}(x_1, x_2) + z^3\phi_i^{(3)}(x_1, x_2) + \cdots + C^M M(z) \qquad (11)$$

where C^M is constant.

The main advantage of the displacement field of zig-zag models lies in the verification of the conditions of continuity without increasing the number of order of the fundamental equations of the theory of equivalent layer. The correction factor of the transverse shear is avoided. Based on this concept, a large number of authors improve the zig-zag model (Averill, 1994; Carrera, 2004; Cho and Parmerter, 1993; He, 1994; Icardi, 2001).

In the works of Ossadzow and Touratier (2001) and Karama et al. (1998), the zig-zag function is added to the function "sinus" of displacement to refine the effects of shear.

Zig-zag model provides a good compromise between the accuracy of solutions and the computational cost.

However, the zig-zag models are rarely used in the analysis of delamination. When the slenderness ratio L/h decreases, the calculation of the transverse shear stresses becomes less accurate (Icardi, 2001). The continuity of type C^0 of the zig-zag theory complicates their numerical implementation.

1.1.1.2.2 Layer approach - discrete layers models

This approach increases the number of unknowns as well as the complexity of the analysis, and consequently the number of degrees of freedom depends on the number of layers of composite plate. To overcome the limitations of stresses $\sigma_{\alpha 3}$ and σ_{33} discontinuity at the interface of multilayered structures of higher order models, the new proposed approaches impose conditions of continuity on stresses at the interface between two adjacent layers. Layer approaches allow to introduce them. In fact, with the models discrete layers, the multilayer is represented by a set of plates coupled by interfacial efforts.

In general, the models issued from the layered approach can be classified into two groups: the zig-zag models developed for layer approaches and the models discrete layers in which each layer is considered as a first-order or higher-order plate by imposing conditions of continuity on displacements and stresses on the interfaces. Here, we're interested only in discrete layers models. Discrete layers models adopt a finer approximation of the fields, through the thickness of the

multilayer, than the models of higher-order plate and zig-zag. Indeed they offer a kinematic by layer rather than a global kinematic. In the discrete layer model, the multilayer is represented by a set of 2D plates coupled by interfacial efforts. Conditions of continuity of stresses at interfaces are satisfied. Displacement or stress approaches also exist.

The kinematics of the first order and higher-order on the displacement field are postulated by Srinivas (1973); Seide (1980); Reddy (1987); Naciri et al. (1998); Tahani and Nosier (2003). Using stresses approaches by layer, the work of Ren (1986); Kassapoglou (1986); Kassapoglou and Lagace (1987); Yin (1994) have proposed various forms of stresses by layer. Ren has assumed a stress field in which the component of transverse shear is quadratic by layer and the displacements are considered cubic by layer and continuous at the interfaces. Yin used stresses functions of Lekhnitskii (1981) by layer in order to determine the interlaminar stresses. They are approximated in polynomial ways through the thickness. These approaches are more accurate than those on displacement but are underdeveloped because of the difficulty to generate statically admissible stresses.

A family of models of discrete layers, *LS1* was developed in Navier laboratory. The various works of Caron and Ehrlacher (1997); Chabot (1997); Naciri et al. (1998); Hadj-Ahmed et al. (2001); Diaz Diaz (2001); Carreira et al. (2002); Baroud et al. (2016) are so inspired from Pagano (1978) which offers the local model, built from the variational formulation of Hellinger-Reissner and a polynomial approximation of the stresses fields by layer. The polynomials are of the first degree for the membrane stresses, quadratic for the shear stresses and cubic for the normal stresses. The family consists of three models: $M4-7n$, $M4-5n$ (*LS1*), $M4-2n+1$, which respectively include a kinematic of the multilayer with $7n$, $5n$ and $2n+1$ fields in $(x;y)$, n is the number of layer of the plate. The $M4-5n$ model, recently called *LS1*, approach each layer by a Reissner plate; on the other hand, the model $M4-2n+1$ approach each layer by a membrane. The $7n$ is too rich to be used simply. Comparisons of the prediction of these models compared to the three-dimensional finite elements and experimental testing of delamination (Diaz Diaz, 2001) are very satisfactory.

CHAPTER 2

Description of *LS1* model: formulation and finite element implementation

2.1 Formulation of *LS1* model for multilayered material

In this section, the formulation of *LS1* model for multilayered material is recalled.

The static elastic approach with perfect interfaces (infinitely rigid and without thickness) is presented in this model (Naciri et al., 1998; Carreira et al., 2002; Diaz Diaz et al., 2002; Caron et al., 2006; Nguyen and Caron, 2006; Dallot and Sab, 2008; Saeedi et al., 2012a,b, 2013a,b; Lerpiniere et al., 2014; Baroud et al., 2016). The construction method of this model is to offer a family of stress fields approaches. By introducing this form of stress fields in the functional of Hellinger-Reissner, we deduce the generalized strains dual of the generalized interior forces. The stationarity of the Hellinger-Reissner's functional compared to a variation of generalized displacements fields gives the equilibrium equations and boundary conditions, as well as when compared to the generalized forces gives the constitutive laws.

2.1.1 Approximation method of Hellinger-Reissner for a 3D problem

We consider a volume of material Ω of boundary $\partial\Omega$. The material is assumed elastic and is denoted by

- $\underline{x}$: the space variable
- $\underline{\underline{\underline{\underline{S}}}}$: the fourth order compliance tensor in $\underline{x}$
- $\underline{\underline{\sigma}}$: the solution tensor of 3D stresses in $\underline{x}$
- $\underline{\underline{\sigma}}^*$: a tensor field of second order symmetrical of class C^1 by piece on ω
- $\underline{U}$: the 3D displacement vector in $\underline{x}$
- $\underline{U}^*$: a 3D vector field continuous over Ω of class C^1 by piece on ω
- $\underline{\underline{\varepsilon}}$: the tensor of 3D deformations in $\underline{x}$
- $\underline{U}^d$: the displacements imposed on the part $\partial\Omega_T$ of the boundary $\partial\Omega$
- $\underline{f}$: the volume forces in $\underline{x}$
- ρ: the density

The 3D elasticity problem to be solved consists in determining the displacement field $\underline{U}$ and stress field $\underline{\underline{\sigma}}$ in the three-dimensional domain Ω of boundary $\partial\Omega$ satisfying the following equations:

- compatibility equation:

$$\underline{\underline{\varepsilon}}(\underline{x}) = \frac{1}{2}\left(\overline{\overline{grad}}\,\underline{U} + {}^{T}\,\overline{\overline{grad}}\,\underline{U}\right) \tag{12}$$

- equilibrium equation:

$$\underline{div}\,\underline{\underline{\sigma}}(\underline{x}) + \underline{f}(\underline{x}) = \rho\underline{\ddot{U}}(\underline{x}) \tag{13}$$

- constitutive equation of the linear elastic behavior:

$$\bar{\bar{\varepsilon}}(\underline{x}) = \bar{\bar{\bar{\bar{S}}}}(\underline{x}) : \bar{\bar{\sigma}}(\underline{x}) \tag{14}$$

- boundary conditions:

$$\underline{U}(\underline{x}) = \underline{U}^d(\underline{x}) \quad on \quad \partial\Omega_U \tag{15}$$

$$(\bar{\bar{\sigma}}.\underline{n})(\underline{x}) = \underline{T}^d(\underline{x}) \quad on \quad \partial\Omega_T \tag{16}$$

with $\partial\Omega_U \cap \partial\Omega_T = \emptyset$ and $\partial\Omega_U \cup \partial\Omega_T = \partial\Omega$.$\underline{U}^d(\underline{x})$ the imposed displacement on the part $\partial\Omega_U$ of the boundary $\partial\Omega$ and $\underline{T}^d(\underline{x})$ the stress vector imposed on the part $\partial\Omega_T$ of the boundary $\partial\Omega$.

The functional Hellinger-Reissner on the couple $(\underline{U}^*, \bar{\bar{\sigma}}^*)$ is:

$$\begin{aligned} H.R.(\underline{U}^*, \bar{\bar{\sigma}}^*) &= \int_\Omega \left[\bar{\bar{\sigma}}^*(\underline{x}) : \bar{\bar{\varepsilon}}(\underline{U}^*)(\underline{x}) - \underline{f}(\underline{x}).\underline{U}^*(\underline{x}) - \frac{1}{2}\bar{\bar{\sigma}}^*(\underline{x}) : \bar{\bar{\bar{\bar{S}}}}(\underline{x}) : \bar{\bar{\sigma}}^*(\underline{x}) \right] d\Omega \\ &\quad - \int_{\partial\Omega_U} (\bar{\bar{\sigma}}^*.\underline{n})(\underline{x}).\left(\underline{U}^* - \underline{U}^d\right)(\underline{x}) dS - \int_{\partial\Omega_T} \underline{T}^d(\underline{x}).\underline{U}^*(\underline{x}) dS \\ &= -\int_\Omega \left[\underline{div}\bar{\bar{\sigma}}^*(\underline{x}).\underline{U}^*(\underline{x}) + \underline{f}(\underline{x}).\underline{U}^*(\underline{x}) + \frac{1}{2}\bar{\bar{\sigma}}^*(\underline{x}) : \bar{\bar{\bar{\bar{S}}}}(\underline{x}) : \bar{\bar{\sigma}}^*(\underline{x}) \right] d\Omega \\ &\quad + \int_{\partial\Omega_U} (\bar{\bar{\sigma}}^*.\underline{n})(\underline{x}).\underline{U}^d(\underline{x}) dS + \int_{\partial\Omega_T} \left((\bar{\bar{\sigma}}^*.\underline{n}) \right) - \underline{T}^d \Big)(\underline{x}).\underline{U}^*(\underline{x}) dS \end{aligned} \tag{17}$$

The Reissner theorem (Reissner, 1950) is as follows:

The solution of the elastic problem is the couple $\left(\underline{U}, \bar{\bar{\sigma}}\right)$ *that makes stationary the functional H.R.*

The stationarity relative to any variation of the three-dimensional displacement field $\underline{U}^*$ gives the equilibrium equations and boundary conditions expressed in stresses on $\partial\Omega_T$:

$$\forall \partial\underline{U}^*$$

$$-\int_\Omega \left[\underline{div}\bar{\bar{\sigma}}(\underline{x}).\partial\underline{U}^*(\underline{x}) + \underline{f}(\underline{x}).\partial\underline{U}^*(\underline{x}) \right] d\Omega + \int_{\partial\Omega_T} \left((\bar{\bar{\sigma}}.\underline{n}) \right) - \underline{T}^d \Big)(\underline{x}).\partial\underline{U}^*(\underline{x}) dS = 0$$

$$\Longleftrightarrow \begin{cases} \underline{div}\bar{\bar{\sigma}}(\underline{x}) + \underline{f}(\underline{x}) = 0 \\ (\bar{\bar{\sigma}}.\underline{n})(\underline{x}) = \underline{T}^d(\underline{x}) \qquad on \quad \partial\Omega_T \end{cases} \tag{18}$$

The stationarity relative to any variation of the three-dimensional stress field $\bar{\bar{\sigma}}$ gives the constitutive equation of the linear elastic behavior and the boundary conditions expressed in displacement on $\partial\Omega_U$:

$$\forall \partial\bar{\bar{\sigma}}^*$$

$$
\begin{aligned}
&- \int_{\Omega} \left[\underline{div} \partial\bar{\bar{\sigma}}^{*}(\underline{x}) : \underline{U}(\underline{x}) + \partial\bar{\bar{\sigma}}^{*}(\underline{x}) : \bar{\bar{\bar{\bar{S}}}}(\underline{x}) : \bar{\bar{\sigma}}(\underline{x}) \right] d\Omega \\
&+ \int_{\partial\Omega_U} (\partial\bar{\bar{\sigma}}^{*}.\underline{n})(\underline{x}).\underline{U}^{d}(\underline{x}) dS + \int_{\partial\Omega_T} \left(\partial\bar{\bar{\sigma}}^{*}.\underline{n} \right)(\underline{x}).\underline{U}(\underline{x}) dS \\
&\Longleftrightarrow \begin{cases} \bar{\bar{\varepsilon}}\left(\underline{U}(\underline{x})\right) = \bar{\bar{\bar{\bar{S}}}}(\underline{x}) : \bar{\bar{\sigma}}(\underline{x}) \\ \underline{U}(\underline{x}) = \underline{U}^{d}(\underline{x}) \qquad \text{on} \quad \partial\Omega_U \end{cases}
\end{aligned} \tag{19}
$$

2.1.2 Step 1: Stress field of the *LS1* model

Consider the multilayer composed of n layers of thickness e^i whose interfaces are denoted $\Gamma_{i,i+1}$. The volume of the multilayer is denoted $\Omega = \omega \times [h_1^-; h_n^+]$. Each layer of the *LS1* model is considered a Reissner-Mindlin's plates.

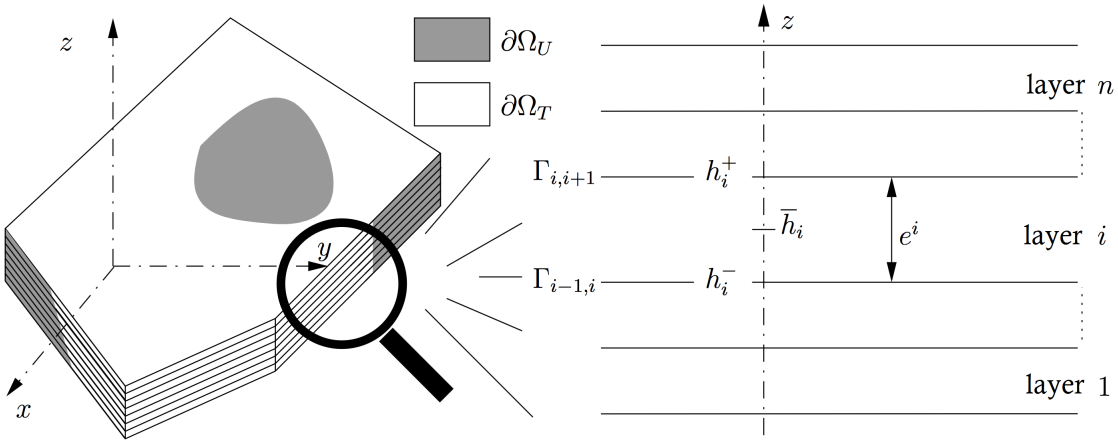


Fig. 2.1. Multilayered studied.

In this chapter, the following notations are adopted:

- i denotes the layer i and ranges from 1 to n
- $j, j+1$ denotes the interface between layers j and $j+1$ and ranges from 1 to n
- the Greek indices α and β ranges from 1 to 2 and serve to express the components of the in-plane field (x, y)

The generalized forces are chosen as follows:

- The second order tensor $\tilde{\tilde{N}}^i$ for the membrane forces of layer i

$$
N_{\alpha\beta}(x, y) = \int_{h_i^-}^{h_i^+} \sigma_{\alpha\beta}(x, y, z) dz \tag{20}
$$

- The second order tensor $\tilde{\tilde{M}}^i$ for the bending moments of the layer i relative to the mid-plane of the layer

$$M^i_{\alpha\beta}(x,y) = \int_{h_i^-}^{h_i^+} (z - \bar{h}_i)\sigma_{\alpha\beta}(x,y,z)dz \tag{21}$$

- The vector $\tilde{Q}^i$ for shear forces of layer i

$$Q^i_{\alpha}(x,y) = \int_{h_i^-}^{h_i^+} \sigma_{\alpha 3}(x,y,z)dz \tag{22}$$

- The vector $\tilde{\tau}^{i,i+1}$ for interior interface shear forces at the interface between layers $i, i+1$

$$\tau^{i,i+1}_{\alpha}(x,y) = \sigma_{\alpha 3}(x,y,h_i^+) \tag{23}$$

- The scalar $\nu^{i,i+1}$ for normal forces at the interface between layers $i, i+1$

$$\nu^{i,i+1}(x,y) = \sigma_{33}(x,y,h_i^+) \tag{24}$$

An orthogonal polynomial basis (P^i_j) is defined:

$$\begin{cases} P^i_0 = 1 \\ P^i_1 = \dfrac{z - \bar{h}_i}{e^i} \\ P^i_2 = 6(\dfrac{z - \bar{h}_i}{e^i})^2 + \dfrac{1}{2} \\ P^i_3 = -2(\dfrac{z - \bar{h}_i}{e^i}^3) + \dfrac{3}{10}(\dfrac{z - \bar{h}_i}{e^i})^2 \end{cases} \tag{25}$$

The stresses in layer i are written:

$$\sigma_{\alpha\beta}(x,y,z) = N^i_{\alpha\beta}(x,y)\frac{P^i_0(z)}{e^i} + \frac{12}{e^{i2}}M^i_{\alpha\beta}(x,y)P^i_1(z) \tag{26}$$

$$\begin{aligned}\sigma_{\alpha 3}(x,y,z) = {} & Q^i_{\alpha}(x,y)\frac{P^i_0(z)}{e^i} + \left(\tau^{i,i+1}_{\alpha}(x,y) - \tau^{i-1,i}_{\alpha}(x,y)\right)P^i_1(z) \\ & + \left(Q^i_{\alpha}(x,y) - \frac{e^i}{2}\left(\tau^{i,i+1}_{\alpha}(x,y) + \tau^{i-1,i}_{\alpha}(x,y)\right)\right)\frac{P^i_2(z)}{e^i}\end{aligned} \tag{27}$$

$$\begin{aligned}\sigma_{33}(x,y,z) = {} & \left(\frac{\nu^{i,i+1}(x,y) + \nu^{i-1,i}(x,y)}{2} + \frac{e^i}{12}div\left(\tilde{\tau}^{i,i+1}(x,y) - \tilde{\tau}^{i-1,i}(x,y)\right)\right)P^i_0(z) \\ & + \left(\frac{e^i}{12}div\left(\tilde{\tau}^{i,i+1}(x,y) + \tilde{\tau}^{i-1,i}(x,y)\right) - \frac{div\tilde{Q}^i(x,y)}{5} + \nu^{i,i+1}(x,y) - \nu^{i-1,i}(x,y)\right)P^i_1(z) \\ & + \frac{e^i}{12}div\left(\tilde{\tau}^{i,i+1}(x,y) - \tilde{\tau}^{i-1,i}(x,y)\right)P^i_2(z) \\ & + \left(\frac{e^i}{2}div\left(\tilde{\tau}^{i,i+1}(x,y) + \tilde{\tau}^{i-1,i}(x,y)\right) - div\tilde{Q}^i(x,y)\right)P^i_3(z)\end{aligned} \tag{28}$$

NOTE: $i = 1..n$

$\tilde{\tau}^{0,1}$ and $\tilde{\tau}^{n,n+1}$: the interface shear stresses on the lower side of layer 1 and the upper side of layer n

$\tilde{\nu}^{0,1}$ and $\tilde{\nu}^{n,n+1}$: the normal interface stresses on the lower side of layer 1 and the upper side of layer n

T_k^- and T_k^+ with $k = 1..3$ the components according to k for the stress vector imposed on the external lower and upper sides. We have the following relations:

$$\begin{cases} \tau_1^{0,1}(x,y) = -T_1^-(x,y) \\ \tau_2^{0,1}(x,y) = -T_2^-(x,y) \\ \nu^{0,1}(x,y) = -T_3^-(x,y) \end{cases} \quad and \quad \begin{cases} \tau_1^{n,n+1}(x,y) = T_1^+(x,y) \\ \tau_2^{n,n+1}(x,y) = T_2^+(x,y) \\ \nu^{n,n+1}(x,y) = T_3^+(x,y) \end{cases}$$

2.1.3 Step 2: Generalized displacements and strains of the *LS1* model

2.1.3.1 Generalized displacements

By replacing the generalized stresses in the Hellinger-Reissner's functional (eqn. 17) and by only taking into account the terms which reveal the displacement field $\underline{U}^*$, a functional T is obtained on $(\underline{U}^*, \bar{\bar{\sigma}}^*)$, and the generalized displacements appear. At this level, the terms involving sliding $\Gamma_i, i+1$ of the interface $\underline{\Omega}^{j,j+1*}$ are injected in order to exploit the stationarity of the Hellinger-Reissner's functional.

$$T(\underline{U}^*, \bar{\bar{\sigma}}^*) = -\int_\Omega \underline{div}\bar{\bar{\sigma}}^*.\underline{U}^* d\Omega + \int_{\partial\Omega_T} \left(\left(\bar{\bar{\sigma}}^*.\underline{n}\right) - \underline{T}^d\right).\underline{U}^* dS \tag{29}$$

The functional T on $(\underline{U}^*, \bar{\bar{\sigma}}^*)$ is calculated:

$$T(\underline{U}^*, \bar{\bar{\sigma}}^*) = -\sum_{i=1}^{n} \int_\omega \left[\begin{array}{c} \left(\tilde{div}\tilde{\tilde{N}}^{i*}(x,y) + \tilde{\tau}^{i,i+1*}(x,y) - \tilde{\tau}^{i-1,i*}(x,y)\right).\tilde{U}^{i*}(x,y) \\ +\left(\tilde{div}\tilde{\tilde{M}}^{i*}(x,y) - \tilde{Q}^{i*}(x,y) + \frac{e^i}{2}\left(\tilde{\tau}^{i,i+1*}(x,y) + \tilde{\tau}^{i-1,i*}(x,y)\right)\right).\tilde{\Phi}^{i*}(x,y) \\ +\left(div\tilde{Q}^{i*} + \nu^{i,i+1*}(x,y) - \nu^{i-1,i*}(x,y)\right).U_3^{i*}(x,y) \end{array} \right]$$

$$+\sum_{i=1}^{n} \int_{\partial\omega} \left[\begin{array}{c} \left(\tilde{\tilde{N}}^{i*}.\underline{n}\right).\tilde{U}^{i*} + \left(\tilde{M}^{i*}.\underline{n}\right).\tilde{\Phi}^{i*} + \left(\tilde{Q}^{i*}(x,y) - \frac{e^i}{2}\left(\tilde{\tau}^{i,i+1*}(x,y) + \tilde{\tau}^{i-1,i*}(x,y)\right)\right).\underline{n}\widehat{U}_3^{i*} \\ +\tilde{Q}^{i*}(x,y).\underline{n}U_3^{i*} + e^i\left(\tilde{\tau}^{i,i+1*}(x,y) - \tilde{\tau}^{i-1,i*}(x,y)\right).\underline{n}\bar{U}_3^{i*} - \int_{h_i^-}^{h_i^+} \underline{T}^d.\underline{U}^* dz \end{array} \right] \tag{30}$$

Where:

- $\tilde{U}^{i*}$: the membranar displacement field of layer i of components U_α^{i*}, $\alpha = 1, 2$ with:

$$U_\alpha^{i*}(x,y) = \int_{h_i^-}^{h_i^+} \frac{P_0^i(z)}{e^i} U_\alpha^*(x,y,z) dz \tag{31}$$

$\underline{U}^*$: the 3D displacement.

- $\tilde{\Phi}^{i*}$: the rotation field of layer i of components Φ_{α}^{i*}, $\alpha = 1, 2$ with:

$$\Phi_{\alpha}^{i*}(x, y) = \int_{h_i^-}^{h_i^+} \frac{12}{e^{i^2}} P_1^i(z) U_{\alpha}^*(x, y, z) dz \tag{32}$$

- U_3^{i*}: the normal average displacement field of layer i:

$$U_3^{i*}(x, y) = \int_{h_i^-}^{h_i^+} \frac{P_0^i(z)}{e^i} U_3^*(x, y, z) dz \tag{33}$$

- $\overline{U}_3^{i*}$: the field named the first moment of average and normal displacement of layer i :

$$\overline{U}_3^{i*}(x, y) = \frac{1}{e^i} \int_{h_i^-}^{h_i^+} P_1^i(z) U_3^*(x, y, z) dz \tag{34}$$

- $\hat{U}_3^{i*}$: the field named the second moment of average and normal displacement of layer i :

$$\hat{U}_3^{i*}(x, y) = \int_{h_i^-}^{h_i^+} \frac{P_2^i(z)}{e^i} U_3^*(x, y, z) dz \tag{35}$$

It is about the $5n$ fields in (x, y): $\tilde{U}^{i*}$, $\tilde{\Phi}^{i*}$ and U_3^{i*}

2.1.3.2 Generalized strains

Integration by parts on the divergences of the equation 2.1.3.1, gives:

$$\begin{aligned} T(\underline{U}^*, \bar{\bar{\sigma}}^*) = & \sum_{i=1}^{n} \int_{\omega} \left[\tilde{\tilde{N}}^{i*} : \tilde{\tilde{\varepsilon}}^{i*} + \tilde{\tilde{M}}^{i*} : \tilde{\tilde{\chi}}^{i*} + \tilde{Q}^{i*} . \left(\tilde{\Phi}^{i*} + g\tilde{r}adU_3^{i*} \right) \right] d\omega \\ & + \sum_{i=0}^{n} \int_{\omega} \tilde{\tau}^{i,i+1*} . \left(\tilde{U}^{i+1*} - \tilde{U}^{i*} - \frac{e^i}{2} \tilde{\Phi}^{i*} - \frac{e^{i+1}}{2} \tilde{\Phi}^{i+1*} \right) d\omega \\ & + \sum_{i=0}^{n} \int_{\omega} \nu^{i,i+1*} \left(U_3^{i+1*} - U_3^{i*} \right) d\omega \\ & - \sum_{i=1}^{n} \int_{\partial\omega} \left(\int_{h_i^-}^{h_i^+} \underline{T}^d . \underline{U}^* dz \right) ds \end{aligned} \tag{36}$$

Where:

- $\tilde{\tilde{\varepsilon}}^{i*}$: the second order tensor field of membrane strain of layer i of components:

$$\varepsilon^{i*}_{\alpha\beta}(x,y) = \frac{1}{2}\left(\frac{\partial U^{i*}_{\alpha}}{\partial x_{\beta}} + \frac{\partial U^{i*}_{\beta}}{\partial x_{\alpha}}\right) \tag{37}$$

$$\alpha,\beta = 1,2$$

- $\tilde{\tilde{\chi}}^{i*}$: the second order tensor field of curvature of layer i of components:

$$\chi^{i*}_{\alpha\beta}(x,y) = \frac{1}{2}\left(\frac{\partial \chi^{i*}_{\alpha}}{\partial x_{\beta}} + \frac{\partial \chi^{i*}_{\beta}}{\partial x_{\alpha}}\right) \tag{38}$$

$$\alpha,\beta = 1,2$$

We deduce the energy duality between generalized forces and generalized strains for $i = 1..n$ and $j = 1..n-1$:

$$\begin{array}{rcl}
\tilde{\tilde{N}}^{i} & \longleftrightarrow & \tilde{\tilde{\varepsilon}}^{i} = \dfrac{1}{2}\left(G\tilde{\tilde{r}}ad\tilde{U}^{i} +^{T} G\tilde{\tilde{r}}ad\tilde{U}^{i}\right) \\
\tilde{\tilde{M}}^{i} & \longleftrightarrow & \tilde{\tilde{\chi}}^{i} = \dfrac{1}{2}\left(G\tilde{\tilde{r}}ad\tilde{\Phi}^{i} +^{T} G\tilde{\tilde{r}}ad\tilde{\Phi}^{i}\right) \\
\tilde{Q}^{i*} & \longleftrightarrow & \tilde{\gamma}^{i} = \tilde{\Phi}^{i} + G\tilde{r}adU^{i}_{3} \\
\tilde{\tau}^{j,j+1} & \longleftrightarrow & \tilde{D}^{j,j+1} = \tilde{U}^{j+1} - \tilde{U}^{j} - \dfrac{e^{j}}{2}\tilde{\Phi}^{j} - \dfrac{e^{j+1}}{2}\tilde{\Phi}^{j+1} \\
\nu^{j,j+1} & \longleftrightarrow & D^{j,j+1}_{\nu} = U^{j+1}_{3} - U^{j}_{3}
\end{array} \tag{39}$$

2.1.4 Step 3: Equilibrium equations and boundary conditions of *LS1* model

By varying H.R. (eqn. 2.1.3.1) with respect to the interior generalized displacements, we obtain the generalized equilibrium equations and the generalized boundary conditions.

2.1.4.1 Equilibrium equations

$$\begin{array}{lll}
\tilde{div}\tilde{\tilde{N}}^{i}(x,y) + \tilde{\tau}^{i,i+1}(x,y) - \tilde{\tau}^{i-1,i}(x,y) = 0 & on & \omega \\
div\tilde{Q}^{i} + \nu^{(}i,i+1)(x,y) - \nu^{i-1,i}(x,y) = 0 & on & \omega \\
\tilde{div}\tilde{\tilde{M}}^{i}(x,y) - \tilde{Q}^{i}(x,y) + \dfrac{e^{i}}{2}\left(\tau^{(}i,i+1)(x,y) + \tilde{\tau}^{i-1,i}(x,y)\right) = 0 & on & \omega
\end{array} \tag{40}$$

2.1.4.2 Boundary conditions

The relation between the 3D displacements $\underline{U}^{*}(x,y,z)$ for $z \in [h^{-}_{i}, h^{+}_{i}]$ and the generalized displacements is written:

$$\underline{U}^{*}(x,y,z) = \left| \begin{array}{rcl}
U^{*}_{\alpha}(x,y,z) & = & P^{i}_{0}(z)U^{i*}_{\alpha}(x,y) + e^{i}P^{i}_{1}(z)\Phi^{i*}_{\alpha}(x,y) + \Delta U^{i*}_{\alpha}(x,y,z) \\
U^{*}_{3}(x,y,z) & = & P^{i}_{0}(z)U^{i*}_{3}(x,y) + \Delta U^{i*}_{3}(x,y,z)
\end{array} \right. \tag{41}$$

with $\Delta U^{i*}_{\alpha}(x,y,z)$ orthogonal to $P^{i}_{0}(z)$ and $P^{i}_{1}(z)$ and $\Delta U^{i*}_{3}(x,y,z)$ orthogonal to $P^{i}_{0}(z)$.

Hypothesis 1 *The contribution of disturbance terms $\Delta U_\alpha^{i*}(x,y,z)$ and $\Delta U_3^{i*}(x,y,z)$ in the boundary terms is supposed negligible compared with generalized displacements.*

The boundary term $-\int_{h_i^-}^{h_i^+} \underline{T}^d.\underline{U}^* dz$ is written:

$$-\tilde{N}_d^i \tilde{U}^{i*} - \tilde{M}_d^i \tilde{\Phi}^{i*} - Q_d^i U_3^{i*}$$

Where

$$\left| \begin{array}{lcl} N_{d\alpha}^i & = & \displaystyle\int_{h_i^-}^{h_i^+} T_\alpha^d.P_0^i(z)dz \\ M_{d\alpha}^i & = & \displaystyle\int_{h_i^-}^{h_i^+} e^i T_\alpha^d.P_1^i(z)dz \\ Q_d^i & = & \displaystyle\int_{h_i^-}^{h_i^+} T_3^d.P_0^i(z)dz \end{array} \right. \tag{42}$$

Thanks to the stationarity of the functional Hellinger-Reissner (eqn. 2.1.3.1) and by neglecting the boundary terms involving components $\bar{U}_3^{i*}$ and $\widehat{U}_3^{i**}$ and being part of the disturbance terms of the displacement field, the boundary conditions are obtained on the boundary $\partial\Omega$:

$$\left| \begin{array}{lcl} \tilde{\tilde{N}}^i.\underline{n} & = & \tilde{N}_d^i \\ \tilde{\tilde{M}}^i.\underline{n} & = & \tilde{M}_d^i \\ \tilde{Q}^i.\underline{n} & = & Q_d^i \end{array} \right. \tag{43}$$

These expressions by layer have the same shape as the boundary conditions of classical Reissner-Mindlin plates.

2.1.5 Step 4: The constitutive law of *LS1* model

The generalized behavior linking the interior generalized forces to the generalized strains is obtained by writing the stationarity Hellinger-Reissner's functional relative to a variation of approximate stresses and thus generalized internal forces. Therefore the functional T' is deduced from the functional HR by only taking into account the terms involving the stress field $\bar{\bar{\sigma}}$:

$$\begin{array}{rcl} T'(\underline{U}^*, \bar{\bar{\sigma}}^*) & = & -\displaystyle\int_\Omega \left[\underline{div}\bar{\bar{\sigma}}^*(\underline{x}).\underline{U}^*(\underline{x}) + \frac{1}{2}\bar{\bar{\sigma}}^*(\underline{x}) : \bar{\bar{\bar{\bar{S}}}}(\underline{x}) : \bar{\bar{\sigma}}^*(\underline{x}) \right] d\Omega \\ & & + \displaystyle\int_{\partial\Omega_T} (\bar{\bar{\sigma}}^*.\underline{n})(\underline{x}).\underline{U}^*(\underline{x}) dS \end{array} \tag{44}$$

The term $\frac{1}{2}\bar{\bar{\sigma}}^*(\underline{x}) : \bar{\bar{\bar{\bar{S}}}}(\underline{x}) : \bar{\bar{\sigma}}^*(\underline{x}) d\Omega$ is the elastic energy W_{3D}^{a*} written in stress. The fourth order compliance tensor $\bar{\bar{\bar{\bar{S}}}}(z)$ is constant in each layer and equal to the tensor $\bar{\bar{\bar{\bar{S}}}}^i$ of components S^i_{mnop} with $m,n,o,p = 1..3$. We consider orthotropic layers admitting the axis $\underline{e}_3$ as axis of orthotropy. Then, the components of the compliance matrix containing an odd number of index 3 are null.

We note $\tilde{\tilde{\tilde{\tilde{S}}}}_c^i$ the in-plane fourth order compliance tensor, S_ν^i the compliance scalar of the three-dimensional normal forces, $\tilde{\tilde{S}}_Q^i$ the second order tensor, compliance matrix of the three-dimensional interface shear and $\tilde{\tilde{S}}_3^i$ the second order tensor, compliance matrix characteristic of coupling between the membrane three-dimensional forces and normal force. These tensors have as components:

$$\left(\tilde{\tilde{\tilde{S}}}^{i}\right)_{\alpha\beta\gamma\delta} = S^{i}_{\alpha\beta\gamma\delta}; S^{i}_{\nu} = S^{i}_{3333}; \left(\tilde{\tilde{S}}^{i}_{Q}\right)_{\alpha\beta} = 4S^{i}_{\alpha 3\gamma 3}; \left(\tilde{\tilde{S}}^{i}_{3}\right)_{\alpha\beta} = 2S^{i}_{\alpha\beta 33}; (\alpha\beta\gamma\delta) = 1, 2$$

It is shown that the energy of the three-dimensional stress field is expressed on each layer based on four terms:

$$W^{a*}_{3D} = \sum_{i=1}^{n} \int_{\omega} \left[w^{ai*}_{c} + w^{ai*}_{\nu} + w^{ai*}_{Q} + w^{ai*}_{3} \right] ds \tag{45}$$

Where:

- w^{ai*}_{c} is the elastic energy of the membrane stresses $\sigma_{\alpha\beta}$ of layer i:

$$w^{ai*}_{c} = \frac{1}{2} \int_{h_i^-}^{h_i^+} \tilde{\tilde{\sigma}}^{a*} : \tilde{\tilde{S}}^{i} : \tilde{\tilde{\sigma}}^{a*} dz \tag{46}$$

- w^{ai*}_{ν} is the elastic energy of normal stress σ_{33} of layer i:

$$w^{ai*}_{\nu} = \frac{1}{2} \int_{h_i^-}^{h_i^+} \sigma^{a*}_{33} S^{i}_{\nu} \sigma^{a*}_{33} dz \tag{47}$$

- w^{ai*}_{3} is the elastic energy of coupling between membrane stresses $\sigma_{\alpha\beta}$ and normal stress σ_{33} of layer i:

$$w^{ai*}_{3} = \frac{1}{2} \int_{h_i^-}^{h_i^+} \left(\tilde{\tilde{\sigma}}^{a*} : \tilde{\tilde{S}}^{i}_{3} \right) \sigma^{a*}_{33} dz \tag{48}$$

- w^{ai*}_{Q} is the elastic energy of the interface shear perpendicular to the plane of layer i:

$$w^{ai*}_{Q} = \frac{1}{2} \int_{h_i^-}^{h_i^+} \sigma^{a*}_{\alpha 3} . \left(\tilde{\tilde{S}}^{i}_{Q} \right)_{\alpha\beta} . \sigma^{a*}_{\beta 3} dz \tag{49}$$

In order to obtain the constitutive equations in compliance (Chabot, 1997), it is sufficient to derive the elastic energies, associated with stress fields W^{a*}_{3D}, relative to each generalized interior forces.

2.1.5.1 Expression of elastic energy written in stress

By injecting the expression of stresses from eqn. 26 to eqn. 28 in the elastic energies expressions (from eqn. 46 to eqn. 49), we obtain:

$$w^{5n^{i*}}_{c} = \frac{1}{2} \left(\tilde{\tilde{N}}^{i*} : \frac{\tilde{\tilde{\tilde{S}}}^{i}}{e^{i}} : \tilde{\tilde{N}}^{i*} + \tilde{\tilde{M}}^{i*} : \frac{12}{e^{i^3}} \tilde{\tilde{\tilde{S}}}^{i} : \tilde{\tilde{M}}^{i*} \right) \tag{50}$$

$$w_{\nu}^{5n^{i*}} = \frac{1}{2} D_{\nu}^{i} \left[\begin{array}{l} e^i \left(\dfrac{\nu^{i,i+1*} + \nu^{i-1,i*}}{2} + \dfrac{e^i}{12} div(\tilde{\tau}^{i,i+1*} - \tilde{\tau}^{i-1,i*}) \right)^2 \\ + \dfrac{e^i}{12} \left(\dfrac{e^i}{10} div(\tilde{\tau}^{i,i+1*} + \tilde{\tau}^{i-1,i*}) + \dfrac{6}{5} (\tilde{\nu}^{i,i+1*} - \tilde{\nu}^{i-1,i*}) \right)^2 \\ + \dfrac{e^i}{5} \left(\dfrac{e^i}{12} div(\tilde{\tau}^{i,i+1*} - \tilde{\tau}^{i-1,i*}) \right)^2 \\ + \dfrac{e^i}{700} \left((\tilde{\nu}^{i,i+1*} - \tilde{\nu}^{i-1,i*}) + \dfrac{e^i}{2} div(\tilde{\tau}^{i,i+1*} + \tilde{\tau}^{i-1,i*}) \right)^2 \end{array} \right] \tag{51}$$

$$w_{3}^{5n^{i*}} = \frac{1}{2} \left[\begin{array}{l} \tilde{\tilde{N}}^{i*} : \tilde{\tilde{S}}_{3}^{i} \left(\left(\dfrac{\nu^{i,i+1*} + \nu^{i-1,i*}}{2} \right) + \dfrac{e^i}{12} div(\tilde{\tau}^{i,i+1*} - \tilde{\tau}^{i-1,i*}) \right) \\ + \dfrac{\tilde{\tilde{M}}^{i*}}{e^i} : \tilde{\tilde{S}}_{3}^{i} \left(\dfrac{6}{5} (\tilde{\nu}^{i,i+1*} - \tilde{\nu}^{i-1,i*}) + \dfrac{e^i}{10} div(\tilde{\tau}^{i,i+1*} + \tilde{\tau}^{i-1,i*}) \right) \end{array} \right] \tag{52}$$

$$w_{Q}^{5n^{i*}} = \frac{1}{2} \left[\begin{array}{l} \tilde{Q}^{i*} . \left(\dfrac{\tilde{\tilde{S}}_{Q}^{i}}{e^i} \right) . \tilde{Q}^{i*} + (\tilde{\tau}^{i,i+1*} + \tilde{\tau}^{i-1,i*}) . \dfrac{e^i}{12} \tilde{\tilde{S}}_{Q}^{i} . (\tilde{\tau}^{i,i+1*} + \tilde{\tau}^{i-1,i*}) \\ + \left(\tilde{Q}^{i*} - \dfrac{e^i}{12} (\tilde{\tau}^{i,i+1*} + \tilde{\tau}^{i-1,i*}) \right) . \dfrac{\tilde{\tilde{S}}_{Q}^{i}}{5e^i} . \left(\tilde{Q}^{i*} - \dfrac{e^i}{12} (\tilde{\tau}^{i,i+1*} + \tilde{\tau}^{i-1,i*}) \right) \end{array} \right] \tag{53}$$

The generalized behavior deduced from the above expressions gives too heavy calculations. We simplify the expression of elastic energy by disregarding certain contributions.

Hypothesis 1 *We neglect the energies $w_3^{5n^{i*}}$ coupling membrane stresses and stresses perpendicular to layers. This means neglecting somewhat the Poisson effect due to "pinch" of the layers. This assumption is usually done in most of plate theories and has been verified and approved where same results were obtained when comparing LS1 without these terms and full LS1 which takes into account the Poisson effect by coupling membrane stresses and stresses perpendicular to layers*

In addition, the terms $div(\tilde{\tau}^{i,i+1*} \pm \tilde{\tau}^{i-1,i*})$ and $div(\tilde{\tau}^{i,i+1*} \pm \tilde{\tau}^{i-1,i*})^2$ in the expression w_{ν}^{ai*} make the calculations very difficult while multiplied by $(e^i)^2$ or $(e^i)^3$, their contribution to energy is probably small thereby:

Hypothesis 2 *We neglect the terms in $(e^i)^2 div(\tilde{\tau}^{i,i+1*} \pm \tilde{\tau}^{i-1,i*})$ and $(e^i)^3 div(\tilde{\tau}^{i,i+1*} \pm \tilde{\tau}^{i-1,i*})^2$ in the expression of W_{3D}^{5n*}*

2.1.5.2 The constitutive law of *LS1* model

By introducing the expression of W_{3D}^{5n*} into the functional of Hellinger-Reissner, and by deriving with respect to the generalized interior forces, we deduce:

- constitutive law of normal membrane forces of layer i for $i = 1..n$:

$$\tilde{\tilde{\varepsilon}}^{i}(x,y) = \frac{\tilde{\tilde{\tilde{S}}}^{i}}{e^i} : \tilde{\tilde{N}}^{i}(x,y) \tag{54}$$

- constitutive law of bending moments and torsion in the plane of layer i for $i = 1..n$:

$$\tilde{\tilde{\chi}}^i(x,y) = \frac{12}{e^{i^3}}\tilde{\tilde{\tilde{S}}}^i : \tilde{\tilde{M}}^i(x,y) \tag{55}$$

- constitutive law of transverse shear forces of layer i for $i = 1..n$:

$$\tilde{\gamma}^i(x,y) = \frac{6}{5e^i}\tilde{\tilde{S}}^i_Q.\tilde{Q}^i - \frac{1}{10}\tilde{\tilde{S}}^i_Q.(\tilde{\tau}^{i,i+1} + \tilde{\tau}^{i-1,i}) \tag{56}$$

- constitutive law of interface shear forces at the interface $i, i+1$ for $i = 1..n-1$:

$$\begin{aligned}\tilde{D}^{i,i+1}(x,y) &= -\frac{1}{10}\tilde{\tilde{S}}^i_Q.\tilde{Q}^i - \frac{1}{10}\tilde{\tilde{S}}^{i+1}_Q.\tilde{Q}^{i+1} - \frac{e^i}{30}\tilde{\tilde{S}}^i_Q.\tilde{\tau}^{i-1,i} \\ &\quad + \frac{2}{15}\left(e^i\tilde{\tilde{S}}^i_Q + e^{i+1}\tilde{\tilde{S}}^{i+1}_Q\right).\tilde{\tau}^{i,i+1} - \frac{e^{i+1}}{30}\tilde{\tilde{S}}^{i+1}_Q.\tilde{\tau}^{i+1,i+2}\end{aligned} \tag{57}$$

- constitutive law of normal stresses at the interface $i, i+1$ for $i = 1..n-1$:

$$\begin{aligned}D_\nu^{i,i+1}(x,y) &= \frac{9}{70}e^i S^i_\nu \nu^{i-1,i} + \frac{13}{35}(e^i S^i_\nu + e^{i+1}S^{i+1}_\nu)\nu^{i,i+1} \\ &\quad + \frac{9}{70}e^{i+1}S^{i+1}_\nu \nu^{i+1,i+2}\end{aligned} \tag{58}$$

2.1.6 *LS1* with imperfect interface

In the previous developments of the *LS1* model, the interfaces were considered as perfect and interface displacements were only due to the elastic generalized displacements in the neighboring layers. Now, if the role of physical interfaces has to be specifically taken into account (elastic or plastic sliding (Diaz Diaz et al., 2002), thick elastic or plastic interface (Duong et al., 2011)), the interface behavior equations (57, 58) and (39) may highlight this new complexity.

2.1.6.1 Interface formulation

Thus, in equations 57 and 58, generalized elastic interface displacements can legitimately be expressed for $i = 1, 2, 3$, as interface generalized displacements $D_\alpha^{k,k+1}(x,y)$ and $D_z^{k,k+1}(x,y)$ (as defined in (39)), minus $\gamma_i^{k,k+1}$ which represents local interface displacements (or slips) due to an own interface behavior:

- Interlaminar shear stress:

$$\begin{aligned}D_\alpha^{k,k+1} - \gamma_\alpha^{k,k+1} = &-\frac{1}{10}\left(S^k_{Q\alpha\beta}Q^k_\beta + S^{k+1}_{Q\alpha\beta}Q^{k+1}_\beta\right) - \frac{1}{30}\left(e^k S^k_{Q\alpha\beta}\tau^{k-1,k}_\beta + e^{k+1}S^{k+1}_{Q\alpha\beta}\tau^{k+1,k+2}_\beta\right) \\ &+ \frac{2}{15}\left(e^k S^k_{Q\alpha\beta} + e^{k+1}S^{k+1}_{Q\alpha\beta}\right)\tau^{k,k+1}_\beta\end{aligned} \tag{59}$$

- Interlaminar normal stress:

$$D_z^{k,k+1} - \gamma_z^{k,k+1} = \frac{9}{70}\left(e^k\, S^k_\nu\, \nu^{k-1,k} + e^{k+1}\, S^{k+1}_\nu\, \nu^{k+1,k+2}\right) + \frac{13}{35}\left(e^k\, S^k_\nu + e^{k+1}\, S^{k+1}_\nu\right)\nu^{k,k+1} \tag{60}$$

The three localized interface displacements or slips $\gamma_x^{k,k+1}$, $\gamma_y^{k,k+1}$ and $\gamma_z^{k,k+1}$ can be, for instance, considered as elastic or plastic.

Then, in this approach, two factors may influence the interfacial rigidity between two layers: the rigidity of adjacent layers ($S_{Q\alpha\beta}^{k}$, S_{ν}^{k}, $S_{Q\alpha\beta}^{k+1}$ and S_{ν}^{k+1}) and the own behavior of the interface. The role of a thick or/and inelastic adhesive could be then represented by $\gamma_x^{k,k+1}$, $\gamma_y^{k,k+1}$ and $\gamma_z^{k,k+1}$. Poor interfacial stiffness or sliding may cause a remarkable decrease of the structure rigidity when a perfect interface (infinite stiffness) provides the expected theoretical and ideal stiffness of the structure. The different interface representations can be summarized as follows in (Table 2.1) with the main governing equations and the application cases.

Type	Denomination	Details and references
A	Elastic composite (*LS1*)	Perfect interface (39) (Carreira et al., 2002)
B	Elastic composite with elastic interface	Interface with zero thickness and isotropic stiffness (Duong et al., 2011)
C	Elastic composite with plastic slips	Interface with zero thickness and a perfectly plastic law for interfacial slips (Diaz Diaz and Caron, 2006)
D	Elastic composite with elastoplastic interface	Interface with non-zero thickness and elastoplastic behavior (Duong et al., 2011)

Tab. 2.1. Type of interfacial behaviors and *LS1* corresponding references

2.2 Presentation of the finite element of *LS1*

Viet Tung NGUYEN, in his thesis and in Nguyen and Caron (2006), proposed a finite element program called *MPFEAP* for the *LS1* model. The validation and the numerical tests in statics show that this model calculates well the interfacial stresses at free edges for multilayered material.

2.2.1 Approximation of nodal displacement

The numerical implementation of the *LS1* model will be performed by using an two-dimensional parametric element with 8 nodes (fig. 2.2).

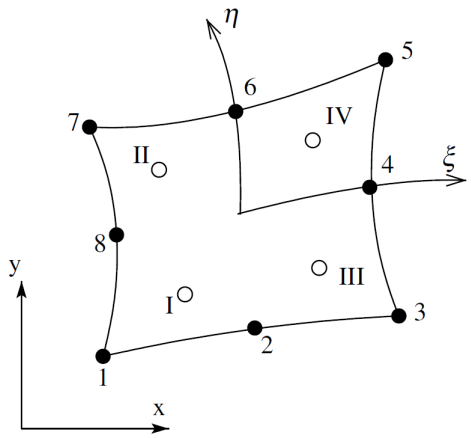


Fig. 2.2. The eight-node element and its four second-order Gaussian stations.

The parametric coordinate are denoted ξ et η. Each element's node has $5n$ d.o.f. per layer (n is the number of layers of the plate). The $x(\xi,\eta)$ and $y(\xi,\eta)$ coordinate of any point (ξ,η) is defined by:

$$\begin{aligned} x(\xi,\eta) &= \sum_{i=1}^{8} N_i(\xi,\eta).x_i \\ y(\xi,\eta) &= \sum_{i=1}^{8} N_i(\xi,\eta).y_i \end{aligned} \tag{61}$$

Where (x_i, y_i) are the coordinates of the node i, and quadratic shape functions are written :

$$\begin{aligned} N_1(\xi,\eta) &= \frac{1}{4}(1-\xi)(1-\eta)(-1-\xi-\eta) \\ N_2(\xi,\eta) &= \frac{1}{2}(1-\xi^2)(1-\eta) \\ N_3(\xi,\eta) &= \frac{1}{4}(1+\xi)(1-\eta)(-1+\xi-\eta) \\ N_4(\xi,\eta) &= \frac{1}{2}(1+\xi)(1-\eta^2) \\ N_5(\xi,\eta) &= \frac{1}{4}(1+\xi)(1+\eta)(-1+\xi+\eta) \\ N_6(\xi,\eta) &= \frac{1}{2}(1-\xi^2)(1+\eta) \\ N_7(\xi,\eta) &= \frac{1}{4}(1-\xi)(1+\eta)(-1-\xi+\eta) \\ N_8(\xi,\eta) &= \frac{1}{2}(1-\xi)(1-\eta^2) \end{aligned} \tag{62}$$

Nodal approximation for the displacement field is written using the same shape functions as geometric approximation (continuity $\mathbb{C}^o$)

$$\delta = \sum_{i=1}^{8} \mathbb{N}_i \delta_i \tag{63}$$

where the shape function matrix associated with node i is

$$\mathbb{N}_i = N_i I_{5n}$$

I_{5n} is the unit matrix of dimension $5n \times 5n$. The displacement vector at node i is written:

$$\delta_i^T = < \underbrace{U_i^1\, V_i^1\, W_i^1\, \phi_{xi}^1\, \phi_{yi}^1,\, U_i^2\, V_i^2\, W_i^2 \phi_{xi}^2 \phi_{yi}^2, \ldots, U_i^n V_i^n W_i^n \phi_{xi}^n \phi_{yi}^n}_{5n} > \tag{64}$$

The derived interpolation functions are calculated using the formula:

$$\begin{aligned} \frac{\partial N_i}{\partial x} &= \frac{\partial N_i}{\partial \xi}.\frac{\partial \xi}{\partial x} + \frac{\partial N_i}{\partial \eta}.\frac{\partial \eta}{\partial x} \\ \frac{\partial N_i}{\partial y} &= \frac{\partial N_i}{\partial \xi}.\frac{\partial \xi}{\partial y} + \frac{\partial N_i}{\partial \eta}.\frac{\partial \eta}{\partial y} \end{aligned} \tag{65}$$

2.2.2 Strains and stresses

The strains vector ϵ of dimension $11n - 3$ is defined by separating the components for membrane behavior ϵ^c, normal behavior ϵ^ν and interface shear behavior ϵ^Q:

$$\epsilon^T = \left\langle \epsilon^c, \epsilon^\nu, \epsilon^Q \right\rangle \tag{66}$$

The generalized membrane strains are written:

$$\epsilon^c = < \underbrace{\varepsilon_{xx}^1\, \varepsilon_{yy}^1\, 2\varepsilon_{xy}^1 \chi_{xx}^1 \chi_{yy}^1\, 2\chi_{xy}^1, \ldots, \varepsilon_{xx}^n\, \varepsilon_{yy}^n\, 2\varepsilon_{xy}^n \chi_{xx}^n \chi_{yy}^n 2\chi_{xy}^n}_{6n} >^T \tag{67}$$

The generalized normal strains are written:

$$\epsilon^\nu = < \underbrace{D_\nu^{1,2}\, D_\nu^{2,3}\, \ldots D_\nu^{n-1,n}}_{n-1} >^T \tag{68}$$

The generalized shear strains are written:

$$\epsilon^Q = < \underbrace{\gamma_x^1 \gamma_y^1\, D_x^{1,2}\, D_y^{1,2}\, \gamma_x^2 \gamma_y^2, \ldots, \gamma_x^{n-1} \gamma_y^{n-1}\, D_x^{n-1,n}\, D_y^{n-1,n}\, \gamma_x^n \gamma_y^n}_{4n-2} >^T \tag{69}$$

The expression of these generalized strains defined by Equation 39 can be written explicitly as shown below, for $i = 1..n$:

$$\begin{array}{lllllll} \varepsilon_{xx}^i &=& \dfrac{\partial U^i}{\partial x} & \varepsilon_{xy}^i &=& \dfrac{1}{2}\left(\dfrac{\partial U^k}{\partial y} + \dfrac{\partial V^k}{\partial x}\right) & \varepsilon_{yy}^i = \dfrac{\partial V^i}{\partial y} \\ \chi_{xx}^i &=& \dfrac{\partial \phi_x^i}{\partial x} & \chi_{xy}^i &=& \dfrac{1}{2}\left(\dfrac{\partial \phi_x^k}{\partial y} + \dfrac{\partial \phi_y^k}{\partial x}\right) & \chi_{yy}^i = \dfrac{\partial \phi_y^i}{\partial y} \\ \gamma_x^i &=& \dfrac{\partial W^i}{\partial x} + \phi_x^i & \gamma_y^i &=& \dfrac{\partial W^i}{\partial y} + \phi_y^i & \end{array} \tag{70}$$

and for $j = 1..n-1$:

$$\begin{aligned} D_x^{j,j+1} &= U^{j+1} - U^j - \frac{e^j}{2}\phi_x^j - \frac{e^{j+1}}{2}\phi_x^{j+1} \\ D_y^{j,j+1} &= V^{j+1} - V^j - \frac{e^j}{2}\phi_y^j - \frac{e^{j+1}}{2}\phi_y^{j+1} \\ D_\nu^{j,j+1} &= W^{j+1} - W^j \end{aligned} \tag{71}$$

The vector of stresses associated with ϵ is defined as

$$\sigma^T =< \sigma^c, \sigma^\nu, \sigma^Q > \tag{72}$$

where

$$\sigma^c =< N^1_{xx}\, N^1_{yy}\, N^1_{xy}\, M^1_{xx}\, M^1_{yy}\, M^1_{xy}, \ldots, N^n_{xx}\, N^n_{yy}\, N^n_{xy}\, M^n_{xx}\, M^n_{yy}\, M^n_{xy} >^T \tag{73}$$

$$\sigma^\nu =< \nu^{1,2}\, \nu^{2,3}, \ldots, \nu^{n-1,n} >^T \tag{74}$$

$$\sigma^Q =< Q^1_x\, Q^1_y\, \tau^{1,2}_x\, \tau^{1,2}_y\, Q^2_x\, Q^2_y, \ldots, Q^{n-1}_x\, Q^{n-1}_y\, \tau^{n-1,n}_x\, \tau^{n-1,n}_y\, Q^n_x\, Q^n_y >^T \tag{75}$$

2.2.3 Nodal approximation of strains and stresses - matrix B

The nodal approximation of the strains field of the element is written as:

$$\epsilon = \sum_{i=1}^{8} B_i \delta_i = [B_1, \ldots, B_8]\delta \tag{76}$$

With:

$$\epsilon^c = \sum_{i=1}^{8} B^c_i \delta_i = [B^c_1, \ldots, B^c_8]\delta \tag{77}$$

$$\epsilon^\nu = \sum_{i=1}^{8} B^\nu_i \delta_i = [B^\nu_1, \ldots, B^\nu_8]\delta \tag{78}$$

$$\epsilon^Q = \sum_{i=1}^{8} B^Q_i \delta_i = [B^Q_1, \ldots, B^Q_8]\delta \tag{79}$$

The matrices B_i consist of n unit matrices B_{ik} ($k = 1 \ldots n$) for each layer:

- The matrix B^c_{ik} is written:

$$B^c_{ik} = \begin{bmatrix} N_{i,x} & 0 & 0 & 0 & 0 \\ 0 & N_{i,y} & 0 & 0 & 0 \\ N_{i,y} & N_{i,x} & 0 & 0 & 0 \\ 0 & 0 & 0 & N_{i,x} & 0 \\ 0 & 0 & 0 & 0 & N_{i,y} \\ 0 & 0 & 0 & N_{i,y} & N_{i,x} \end{bmatrix} \tag{80}$$

- The matrix B^ν_{ik} is written:

$$\begin{aligned} B^\nu_{ik} &= \begin{bmatrix} 0 & 0 & -N_i & 0 & 0 & 0 & 0 & N_i & 0 & 0 \end{bmatrix} \\ &= \begin{bmatrix} B^{\nu 1}_{ik} & B^{\nu 2}_{ik} \end{bmatrix} \end{aligned} \tag{81}$$

  where the matrices $B^{\nu 1}_{ik}$ and $B^{\nu 2}_{ik}$ are of dimension 1×5. They serve to better explain the matrix B_i building in the equation below.

- The matrix B_{ik}^{Q} is written:

$$
\begin{aligned}
B_{ik}^{Q} &= \begin{bmatrix}
0 & 0 & N_{i,x} & N_i & 0 & 0 & 0 & 0 & 0 & 0 \\
0 & 0 & N_{i,y} & 0 & N_i & 0 & 0 & 0 & 0 & 0 \\
-N_i & 0 & 0 & -\frac{e_k}{2}N_i & 0 & N_i & 0 & 0 & -\frac{e_{k+1}}{2}N_i & 0 \\
0 & -N_i & 0 & 0 & -\frac{e_k}{2}N_i & 0 & N_i & 0 & 0 & -\frac{e_{k+1}}{2}N_i
\end{bmatrix} \\
&= \begin{bmatrix} B_{ik}^{Q1} & B_{ik}^{Q2} \end{bmatrix}
\end{aligned}
\tag{82}
$$

  where B_{ik}^{Q1} and B_{ik}^{Q2} are the matrices of dimension 4×5 and are used for the same reason as $B_{ik}^{\nu 1}$ and $B_{ik}^{\nu 2}$.

In fact, the matrix B_i^c of dimension $6n \times 5n$ is defined by

$$
\begin{aligned}
B_i^c &= \begin{bmatrix}
B_{i1}^c & 0 & . & 0 \\
0 & B_{i2}^c & . & 0 \\
. & . & . & . \\
0 & 0 & . & B_{in}^c
\end{bmatrix} \\
&= \begin{bmatrix}
N_{i,x} & 0 & 0 & 0 & 0 & . & 0 & 0 & 0 & 0 & 0 \\
0 & N_{i,y} & 0 & 0 & 0 & . & 0 & 0 & 0 & 0 & 0 \\
N_{i,y} & N_{i,x} & 0 & 0 & 0 & . & 0 & 0 & 0 & 0 & 0 \\
0 & 0 & 0 & N_{i,x} & 0 & . & 0 & 0 & 0 & 0 & 0 \\
0 & 0 & 0 & 0 & N_{i,y} & . & 0 & 0 & 0 & 0 & 0 \\
0 & 0 & 0 & N_{i,y} & N_{i,x} & . & 0 & 0 & 0 & 0 & 0 \\
. & . & . & . & . & . & . & . & . & . & . \\
. & . & . & . & . & . & . & . & . & . & . \\
0 & 0 & 0 & 0 & 0 & . & N_{i,x} & 0 & 0 & 0 & 0 \\
0 & 0 & 0 & 0 & 0 & . & 0 & N_{i,y} & 0 & 0 & 0 \\
0 & 0 & 0 & 0 & 0 & . & N_{i,y} & N_{i,x} & 0 & 0 & 0 \\
0 & 0 & 0 & 0 & 0 & . & 0 & 0 & 0 & N_{i,x} & 0 \\
0 & 0 & 0 & 0 & 0 & . & 0 & 0 & 0 & 0 & N_{i,y} \\
0 & 0 & 0 & 0 & 0 & . & 0 & 0 & 0 & N_{i,y} & N_{i,x}
\end{bmatrix}
\end{aligned}
\tag{83}
$$

and the matrix B_i^{ν} of dimension $(n-1) \times 5n$ is defined by

$$
\begin{aligned}
B_i^{\nu} &= \begin{bmatrix}
B_{i1}^{\nu 1} & B_{i1}^{\nu 2} & 0 & . & 0 & 0 \\
0 & B_{i2}^{\nu 1} & B_{i2}^{\nu 2} & . & 0 & 0 \\
. & . & . & . & . & . \\
0 & 0 & 0 & . & B_{i\,n-1}^{\nu 1} & B_{i\,n-1}^{\nu 2}
\end{bmatrix} \\
&= \begin{bmatrix}
0 & 0 & -N_i & 0 & 0 & 0 & 0 & N_i & 0 & 0 & . & . & . & . & . & . \\
. & . & . & . & . & 0 & 0 & -N_i & 0 & 0 & . & . & . & . & . & . \\
. & . & . & . & . & . & . & . & . & . & . & . & . & . & . & . \\
. & . & . & . & . & . & . & . & . & . & . & . & . & . & . & . \\
. & . & . & . & . & . & . & . & . & . & . & 0 & 0 & N_i & 0 & 0
\end{bmatrix}
\end{aligned}
\tag{84}
$$

Finally, the matrix B_i^{Q} of dimension $(4n-2) \times 5n$ is defined by

$$B_i^Q = \begin{bmatrix} B_{i1}^{Q1} & B_{i1}^{Q2} & 0 & . & 0 & 0 \\ 0 & B_{i2}^{Q1} & B_{i2}^{Q2} & . & 0 & 0 \\ . & . & . & . & . & . \\ 0 & 0 & 0 & . & B_{i\,n-1}^{Q1} & B_{i\,n-1}^{Q2} \\ 0 & 0 & 0 & . & 0 & \text{First 2 lines of } B_{i\,n}^{Q1} \end{bmatrix}$$

$$= \begin{bmatrix} 0 & 0 & N_{i,x} & N_i & 0 & 0 & 0 & 0 & 0 & 0 & . & . & . \\ 0 & 0 & N_{i,y} & 0 & N_i & 0 & 0 & 0 & 0 & 0 & . & . & . \\ -N_i & 0 & 0 & -\frac{e^1}{2}N_i & 0 & N_i & 0 & 0 & -\frac{e^2}{2}N_i & 0 & . & . & . \\ 0 & -N_i & 0 & 0 & -\frac{e^1}{2}N_i & 0 & N_i & 0 & 0 & -\frac{e^2}{2}N_i & . & . & . \\ . & . & . & . & . & . & . & . & . & . & . & . & . \\ . & . & . & . & . & . & . & . & 0 & 0 & N_{i,x} & N_i & 0 \\ . & . & . & . & . & . & . & . & 0 & 0 & N_{i,y} & 0 & N_i \end{bmatrix} \tag{85}$$

2.2.4 Behavior - stiffness matrix D

Behavior in compliance

The behavior of *LS1* model in compliance can be written in matrix form

$$\epsilon = S\sigma + \epsilon^o \tag{86}$$

The vector ϵ^o contains the terms related to surface tractions $\underline{T}^-$ and $\underline{T}^+$. In this case, we are dealing with a problem with initial deformation. Its resolution is the subject of the next section. In eqn. 86, S is the compliance matrix of dimension $(11n-3)\times(11n-3)$

$$S = \begin{bmatrix} S^c & 0 & 0 \\ 0 & S^\nu & 0 \\ 0 & 0 & S^Q \end{bmatrix} \tag{87}$$

The compliance matrices S^c, S^ν and S^Q correspond to the compliance matrices of each layer S_k^c, S_k^ν and S_k^Q $(k = 1 \dots n)$. These matrices are formulated from the constitutive equations of the model (eqns. 54-58):

$$S_k^c = \begin{bmatrix} \frac{S_{11}^k}{e^k} & \frac{S_{12}^k}{e^k} & \frac{S_{16}^k}{e^k} & 0 & 0 & 0 \\ \frac{S_{21}^k}{e^k} & \frac{S_{22}^k}{e^k} & \frac{S_{26}^k}{e^k} & 0 & 0 & 0 \\ \frac{S_{16}^k}{e^k} & \frac{S_{26}^k}{e^k} & \frac{S_{66}^k}{e^k} & 0 & 0 & 0 \\ 0 & 0 & 0 & \frac{12S_{11}^k}{(e^k)^3} & \frac{12S_{12}^k}{(e^k)^3} & \frac{12S_{16}^k}{(e^k)^3} \\ 0 & 0 & 0 & \frac{12S_{21}^k}{(e^k)^3} & \frac{12S_{22}^k}{(e^k)^3} & \frac{12S_{26}^k}{(e^k)^3} \\ 0 & 0 & 0 & \frac{12S_{16}^k}{(e^k)^3} & \frac{12S_{26}^k}{(e^k)^3} & \frac{12S_{66}^k}{(e^k)^3} \end{bmatrix} \tag{88}$$

$$S_k^\nu = \begin{bmatrix} \frac{9e^kS_{33}^k}{70} & \frac{13(e^kS_{33}^k+e^{k+1}S_{33}^{k+1})}{35} & \frac{9e^{k+1}S_{33}^{k+1}}{70} \end{bmatrix} \tag{89}$$

$$S_k^Q = \begin{bmatrix} 0 & \frac{-S_Q^k}{10} & \frac{6S_Q^k}{5e^k} & \frac{-S_Q^k}{10} & 0 & 0 \\ 0 & \frac{-e^kS_Q^k}{30} & \frac{-S_Q^k}{10} & \frac{2(e^kS_Q^k+e^{k+1}S_Q^{k+1})}{15} & \frac{-S_Q^{k+1}}{10} & \frac{-e^{k+1}S_Q^{k+1}}{30} \end{bmatrix} \tag{90}$$

By combining the matrices of each layer, we obtain the elementary compliance matrices below: S^c matrix of dimension $6n \times 6n$ defined by

$$S^c = \begin{pmatrix}
\frac{S^1_{11}}{e^1} & \frac{S^1_{12}}{e^1} & \frac{S^1_{16}}{e^1} & 0 & 0 & 0 & \cdot & \cdot & \cdot & \cdot & \cdot & \cdot & \cdot & \cdot \\
\frac{S^1_{21}}{e^1} & \frac{S^1_{22}}{e^1} & \frac{S^1_{26}}{e^1} & 0 & 0 & 0 & \cdot & \cdot & \cdot & \cdot & \cdot & \cdot & \cdot & \cdot \\
\frac{S^1_{16}}{e^1} & \frac{S^1_{26}}{e^1} & \frac{S^1_{66}}{e^1} & 0 & 0 & 0 & \cdot & \cdot & \cdot & \cdot & \cdot & \cdot & \cdot & \cdot \\
0 & 0 & 0 & \frac{12S^1_{11}}{(e^1)^3} & \frac{12S^1_{12}}{(e^1)^3} & \frac{12S^1_{16}}{(e^1)^3} & \cdot & \cdot & \cdot & \cdot & \cdot & \cdot & \cdot & \cdot \\
0 & 0 & 0 & \frac{12S^1_{21}}{(e^1)^3} & \frac{12S^1_{22}}{(e^1)^3} & \frac{12S^1_{26}}{(e^1)^3} & \cdot & \cdot & \cdot & \cdot & \cdot & \cdot & \cdot & \cdot \\
0 & 0 & 0 & \frac{12S^1_{16}}{(e^1)^3} & \frac{12S^1_{26}}{(e^1)^3} & \frac{12S^1_{66}}{(e^1)^3} & \cdot & \cdot & \cdot & \cdot & \cdot & \cdot & \cdot & \cdot \\
\cdot & \cdot & \cdot & \cdot & \cdot & \cdot & \cdot & \cdot & \cdot & \cdot & \cdot & \cdot & \cdot & \cdot \\
\cdot & \cdot & \cdot & \cdot & \cdot & \cdot & \cdot & \cdot & \cdot & \cdot & \cdot & \cdot & \cdot & \cdot \\
\cdot & \cdot & \cdot & \cdot & \cdot & \cdot & \cdot & \frac{S^1_{11}}{e^n} & \frac{S^1_{12}}{e^n} & \frac{S^1_{16}}{e^n} & 0 & 0 & 0 \\
\cdot & \cdot & \cdot & \cdot & \cdot & \cdot & \cdot & \frac{S^1_{21}}{e^n} & \frac{S^1_{22}}{e^n} & \frac{S^1_{26}}{e^n} & 0 & 0 & 0 \\
\cdot & \cdot & \cdot & \cdot & \cdot & \cdot & \cdot & \frac{S^1_{16}}{e^n} & \frac{S^1_{26}}{e^n} & \frac{S^1_{66}}{e^n} & 0 & 0 & 0 \\
\cdot & \cdot & \cdot & \cdot & \cdot & \cdot & \cdot & 0 & 0 & 0 & \frac{12S^1_{11}}{(e^n)^3} & \frac{12S^1_{12}}{(e^n)^3} & \frac{12S^1_{16}}{(e^n)^3} \\
\cdot & \cdot & \cdot & \cdot & \cdot & \cdot & \cdot & 0 & 0 & 0 & \frac{12S^1_{12}}{(e^n)^3} & \frac{12S^1_{22}}{(e^n)^3} & \frac{12S^1_{26}}{(e^n)^3} \\
\cdot & \cdot & \cdot & \cdot & \cdot & \cdot & \cdot & 0 & 0 & 0 & \frac{12S^1_{16}}{(e^n)^3} & \frac{12S^1_{26}}{(e^n)^3} & \frac{12S^1_{66}}{(e^n)^3}
\end{pmatrix} \tag{91}$$

S^ν matrix of dimension $(n-1)\times(n-1)$ defined by

$$S^\nu = \begin{pmatrix}
\frac{13(e^1S^1_{33}+e^2S^2_{33})}{35} & \frac{9e^2S^2_{33}}{70} & \cdot & \cdot & \cdot \\
\frac{9e^2S^2_{33}}{70} & \frac{13(e^2S^2_{33}+e^3S^3_{33})}{35} & \frac{9e^3S^3_{33}}{70} & \cdot & \cdot \\
\cdot & \cdot & \cdot & \cdot & \cdot \\
\cdot & \cdot & \frac{9e^{n-2}S^{n-2}_{33}}{70} & \frac{13(e^{n-2}S^{n-2}_{33}+e^{n-1}S^{n-1}_{33})}{35} & \frac{9e^{n-1}S^{n-1}_{33}}{70} \\
\cdot & \cdot & \cdot & \frac{9e^{n-1}S^{n-1}_{33}}{70} & \frac{13(e^{n-1}S^{n-1}_{33}+e^nS^n_{33})}{35}
\end{pmatrix} \tag{92}$$

S^Q matrix of dimension $(4n-2)\times(4n-2)$ defined by

$S^Q =$

$$\begin{pmatrix}
\frac{6S^1_Q}{5e^1} & \frac{-S^1_Q}{10} & 0 & 0 & \cdot & \cdot & \cdot & \cdot & \cdot & \cdot & \cdot \\
\frac{-S^1_Q}{10} & \frac{2(e^1S^1_Q+e^2S^2_Q)}{15} & \frac{-S^2_Q}{10} & \frac{-e^2S^2_Q}{30} & \cdot & \cdot & \cdot & \cdot & \cdot & \cdot & \cdot \\
0 & \frac{-S^2_Q}{10} & \frac{6S^2_Q}{5e^2} & \frac{-S^2_Q}{10} & 0 & 0 & \cdot & \cdot & \cdot & \cdot & \cdot \\
0 & \frac{-e^2S^2_Q}{30} & \frac{-S^2_Q}{10} & \frac{2(e^2S^2_Q+e^3S^3_Q)}{15} & \frac{-S^3_Q}{10} & \frac{-e^3S^3_Q}{30} & \cdot & \cdot & \cdot & \cdot & \cdot \\
\cdot & \cdot & 0 & \frac{-S^3_Q}{10} & \frac{6S^3_Q}{5e^3} & \frac{-S^3_Q}{10} & 0 & 0 & \cdot & \cdot & \cdot \\
\cdot & \cdot & 0 & \frac{-e^3S^3_Q}{30} & \frac{-S^3_Q}{10} & \frac{2(e^3S^3_Q+e^4S^4_Q)}{15} & \frac{-S^4_Q}{10} & \frac{-e^4S^4_Q}{30} & \cdot & \cdot & \cdot \\
\cdot & \cdot & \cdot & \cdot & \cdot & \cdot & \cdot & \cdot & \cdot & \frac{-S^n_Q}{10} & \frac{6S^n_Q}{5e^n}
\end{pmatrix} \tag{93}$$

where S^j_Q is the interface shear compliance of layer j.

The vector of initial deformations due to imposed surface stresses ϵ^o, of dimension $11n-3$ with $n>2$ is defined by

$$\epsilon^o = \left\{ \begin{array}{c} 0 \\ . \\ . \\ 0 \\ \frac{9}{70}e^1 S^1_{33}\nu^{0,1} \\ 0 \\ . \\ . \\ 0 \\ \frac{9}{70}e^n S^n_{33}\nu^{n,n+1} \\ -\frac{1}{10}(S^1_{55}\tau_x^{0,1} + S^1_{54}\tau_y^{0,1}) \\ -\frac{1}{10}(S^1_{45}\tau_x^{0,1} + S^1_{44}\tau_y^{0,1}) \\ -\frac{e^1}{30}(S^1_{55}\tau_x^{0,1} + S^1_{54}\tau_y^{0,1}) \\ -\frac{e^1}{30}(S^1_{45}\tau_x^{0,1} + S^1_{44}\tau_y^{0,1}) \\ 0 \\ . \\ . \\ 0 \\ -\frac{e^n}{30}(S^n_{55}\tau_x^{n,n+1} + S^n_{54}\tau_y^{n,n+1}) \\ -\frac{e^n}{30}(S^n_{45}\tau_x^{n,n+1} + S^n_{44}\tau_y^{n,n+1}) \\ -\frac{1}{10}(S^n_{55}\tau_x^{n,n+1} + S^n_{54}\tau_y^{n,n+1}) \\ -\frac{1}{10}(S^n_{45}\tau_x^{n,n+1} + S^n_{44}\tau_y^{n,n+1}) \end{array} \right\} = \left\{ \begin{array}{c} 0 \\ . \\ . \\ 0 \\ \frac{9}{70}e^1 S^1_{33}T_3^- \\ 0 \\ . \\ . \\ 0 \\ \frac{9}{70}e^n S^n_{33}T_3^+ \\ -\frac{1}{10}(S^1_{55}T_1^- + S^1_{54}T_2^-) \\ -\frac{1}{10}(S^1_{45}T_1^- + S^1_{44}T_2^-) \\ -\frac{e^1}{30}(S^1_{55}T_1^- + S^1_{54}T_2^-) \\ -\frac{e^1}{30}(S^1_{45}T_1^- + S^1_{44}T_2^-) \\ 0 \\ . \\ . \\ 0 \\ -\frac{e^n}{30}(S^n_{55}T_1^+ + S^n_{54}T_2^+) \\ -\frac{e^n}{30}(S^n_{45}T_1^+ + S^n_{44}T_2^+) \\ -\frac{1}{10}(S^n_{55}T_1^+ + S^n_{54}T_2^+) \\ -\frac{1}{10}(S^n_{45}T_1^+ + S^n_{44}T_2^+) \end{array} \right\} \begin{array}{c} | \\ | \\ | \\ \downarrow \\ 6n+1 \\ | \\ | \\ | \\ \downarrow \\ 7n-1 \\ | \\ | \\ | \\ | \\ | \\ | \\ | \\ | \\ | \\ | \\ \downarrow \\ 11n-3 \end{array} \tag{94}$$

Behavior in stiffness

The behavior in stiffness of the model is written

$$\sigma = S^{-1}(\epsilon - \epsilon^o) = D(\epsilon - \epsilon^o) \tag{95}$$

where D is the compliance matrix of dimension $(11n-3)\times(11n-3)$

$$D = S^{-1} = \begin{pmatrix} D^c & 0 & 0 \\ 0 & D^\nu & 0 \\ 0 & 0 & D^Q \end{pmatrix} = \begin{pmatrix} S^{c-1} & 0 & 0 \\ 0 & S^{\nu-1} & 0 \\ 0 & 0 & S^{Q-1} \end{pmatrix} \tag{96}$$

2.2.5 A calculation method for a problem with initial deformation

Consider an element submitted to nodal solicitations F^e and volume solicitations p. The element is in equilibrium and is subjected to a stress field σ. It is assumed that the element is subjected to a virtual field of arbitrary nodal displacements δ^e_*. The displacement field and the internal deformation field compatibles are δ_* and ϵ_*. At the element level, the principle of virtual work is written:

$$\delta^{eT}_* F^e + \int_{\Omega^e} \delta^T_* p d\Omega = \int_{\Omega^e} \epsilon^T_* \sigma d\Omega \tag{97}$$

In the displacement formulation of the finite element method, the displacement field is obtained by a nodal interpolation

$$\delta = \mathbb{N}\delta^e \tag{98}$$

where $\mathbb{N}$ is the set of interpolation functions called shape functions and δ^e is the vector of nodal elementary displacements. The deformations in the element can be expressed in terms of nodal displacements as shown below

$$\epsilon = \mathbb{B}\delta^e \tag{99}$$

By using eqns. 99 and 98, we obtain:

$$\delta_*^{eT}\left(F^e + \int_{\Omega^e} \mathbb{N}^T p d\Omega\right) = \delta_*^{eT} \int_{\Omega^e} \mathbb{B}^T \sigma d\Omega \tag{100}$$

As the virtual nodal displacements field is arbitrary, the above expression must be true for all values δ_*^e. Then

$$F^e + \int_{\Omega^e} \mathbb{N}^T p d\Omega = \int_{\Omega^e} \mathbb{B}^T \sigma d\Omega. \tag{101}$$

By replacing σ by $D(\epsilon - \epsilon^0)$, with ϵ^0 the initial deformation field

$$F^e + \int_{\Omega^e} \mathbb{N}^T p d\Omega = \left(\int_{\Omega^e} \mathbb{B}^T D\mathbb{B} d\Omega\right)\delta^e - \int_{\Omega^e} \mathbb{B}^T D\epsilon^0 d\Omega, \tag{102}$$

or

$$F^e + F_p^e + F_{\epsilon^0}^e = K^e\delta^e, \tag{103}$$

where

$$K^e = \int_{\Omega^e} \mathbb{B}^T D\mathbb{B} d\Omega, \tag{104}$$

$$F_p^e = \int_{\Omega^e} \mathbb{N}^T p d\Omega, \tag{105}$$

$$F_{\epsilon^0}^e = \int_{\Omega^e} \mathbb{B}^T D\epsilon^0 d\Omega. \tag{106}$$

2.3 Contribution to *LS1* model and its finite element program *MPFEAP*

In this thesis work, several contributions and improvements were made regarding *LS1* model and its finite element program *MPFEAP* :

- Implementation of a full *LS1* version which takes into account the coupling between membrane stresses and perpendicular stresses (Poisson effect). By comparing full *LS1* and *LS1*, the same results were obtained.
- Increase the number of stored variables and the way they are stored which reduces significantly the computation time (more than 5 times). Regarding the dimension or size of the problem (refinement of the mesh and number of layers) that can be processed by *MPFEAP*, with these improvements, a bigger multilayered structure, with more layers and a more refined mesh, can be studied.
- Program debugging, with correction of some minor bugs.

CHAPTER 3

Application of *LS1* model for the study of hybrid multilayered structures

3.1 Introduction

The modeling of a hybrid, innovative and complex structure for civil engineering is proposed here. A concrete slab is connected to an openwork (hollow) crossed plywood panel PANOBLOC (Techniwood) (Fig. 3.1). The 3D finite element of this kind of structure is extremely complex due to the non-continuous aspects and also to the strong anisotropy of the pieces of wood, especially in term of transverse shear behavior (a very weak rolling shear). The effects of these transverse shears are extremely important for the panel stiffness and have to be correctly taken into account. From a resistance point of view, the stress singularities along the holes of the hollow structure are difficult to be estimated with 3D finite element, even with very refined mesh, since non convergent. Real scale tests, on 6-meter-long panels, have shown that the rupture initiates precisely at these locations, the free edges of wood parts. The estimation of these stress intensities remains consequently an important goal for the design of these structures.

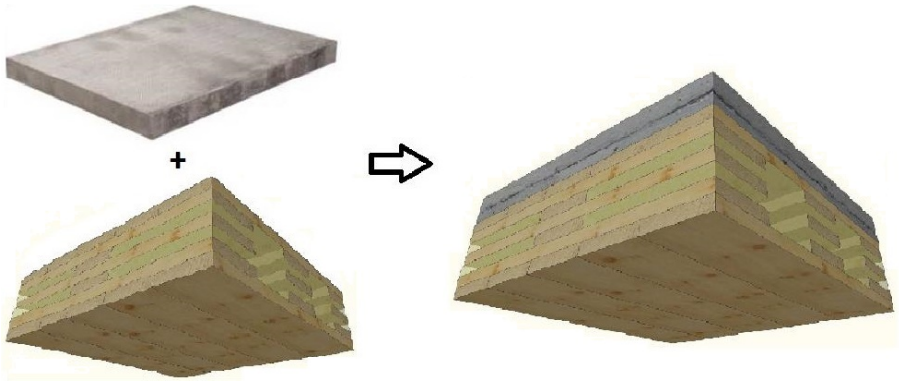


Fig. 3.1. An openwork (hollow) plywood cross-ply (Panobloc) connected to a concrete slab.

Several approaches and models are compared, in terms of both stiffness and resistance, a shell composite element of Abaqus, an analytical beam method, and *MPFEAP* (Multi particular Finite Element Approach Program) from Navier laboratory. Based on the layerwise approach *LS1*, it permits a 2D description and a 2D meshing of 3D structures, as shown in Fig. 3.2. For the *MPFEAP* approach, two variants are tested: one with an equivalent homogeneous and continuous description of the hollow multilayer, and another one, complete, more precise, where the hollow parts are integrated in the thickness of the local 2D description. Experimental results are also used for comparisons.

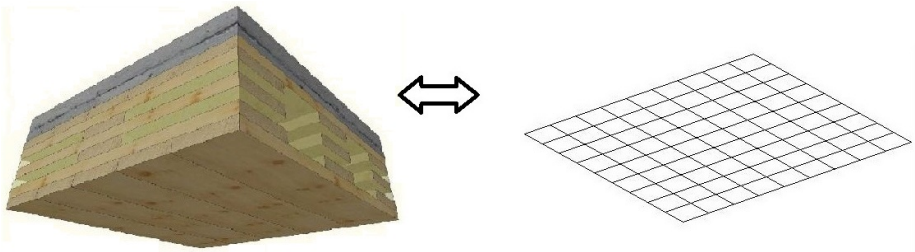


Fig. 3.2. Equivalent 2D meshing (right) of the 3D structure (left).

The objective is to promote this 2D approach versus 3D calculations, since the cost of 3D calculations is too high for a pre-design phase. In addition, 3D FE are not always fully relevant in

the presence of singularities, for example at the interfaces and in the vicinity of the free edges, since not convergent and mesh dependent.

3.2 The slab modeling

The slab considered in this study is 6 meters length and 1 meter width. The 6 layers stacking sequence is relatively complex. The first layer, on the top of the slab, is made by a high performance concrete plate of a thickness of 5 cm. The 5 next layers are constituted by wooden strips, non-contiguous, and alternatively in the axial and transverse directions. The loading case is a 3 points bending test and the materials properties experimentally identified and used in the simulations, are for concrete:
E = 37 GPa,
G = 15.417 GPa,
ν = 0.2.

and for wood:
E_1 = 11 GPa, $E_2 = E_3$ = 0.5 GPa,
$G_{12} = G_{13}$ = 0.7 GPa, G_{23} = 0.04 GPa,
$\nu_{12} = \nu_{13} = \nu_{23}$ = 0.35.

Note the very weak rolling transverse shear G_{23}, which plays an important role in the design, and seen in the tests, may induce the first rupture of the multilayer.

3.2.1 The four models

Several methods of calculation are used for the modeling of the plywood-concrete slab, and comparisons are made between these models. The rigidity of the slab is firstly estimated with homogeneous approaches. The resistance estimation needs more precise approaches since the transverse shear at the interfaces between the layers has to be estimated, taking into account the porosity and the actual position of the strips of wood in the longitudinal and transverse directions. The four models are described now:

(a) Analytical estimation: the Timoshenko beam model is used to calculate structural stiffness and resistance of the multilayer since the beam is quite thick, and since large differences exist between the different material constants, increasing the transverse shear effects. Regarding stiffness, and to estimate the deflection of the slab, the porosity is just integrated by an ad-hoc and proportional decrease of equivalent layer stiffnesses. For shear strength, the approach of Jourasky (1856) allows to estimate the distribution of shear in the thickness of a continuous multilayered beam. In the case of an uniform porosity along the beam, the method can give an estimation of transverse shear (not taking into account the singularities)

(b) Standard Finite Element calculation: the S8R (Abaqus) standard thick plate element for composite materials is used for the slab stiffness estimation. The porosity is again integrated by an ad-hoc and proportional decrease of equivalent layer stiffnesses. The 3D finite element has not been used since very heavy to implement for this quite complex structure, and according to the author's experience, gives very close results to *MPFEAP*'s ones, as demonstrated several times in publications (Carreira et al., 2002; Nguyen and Caron, 2006, 2009; Thai et al., 2013)

(c) *MPFEAP* analysis with equivalent homogeneous layers description: similar in spirit to the b) approach (Abaqus), this model integrates however more precisely transverse shear behaviors, introducing no correction factors for these stiffnesses. However, as previous models, it provides no information on the stress concentrations due to porosities, that it doesn't describe

(d) *MPFEAP* complete analysis: describing porosities and the wooden strips in the 2 longitudinal and transverse directions, it is a rich 2D model, but easier to manage than 3D approach, and allowing the stress concentrations estimation

3.2.2 Slab rigidity

A calculation of slab stiffness is performed with the a), b) and c) approaches and compared with the results of experimental tests. A force is applied in the middle of the slab, up to 64 KN, provoking the rupture of the slab. Fig. 3.3 shows the different mid-pan deflections obtained with the different models and measured on the intrados of the panel.

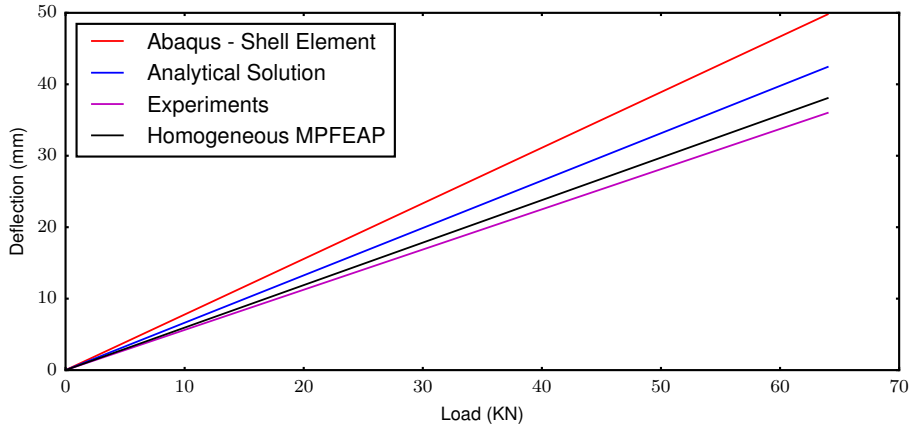


Fig. 3.3. Experimental and simulated mid-pan deflections (mm).

The best fit is realized with the c) model, the homogeneous equivalent *MPFEAP* without the precise openwork description. It takes accurately into account the high gradient of properties between the different layers, especially concerning the transverse shear phenomenon. The model d), the complete *MPFEAP*, not reported here, doesn't improve this rigidity prediction. The analytical approach provides a not so bad estimation, but this is only for very simple cases, 1D beams with simple loadings, elastic behavior, and uniform distribution of strips and porosities. The more interesting aspect is perhaps the difficulty for the 2D plate elements from ABAQUS to simulate this situation. It's mainly due to the hazardous estimation of correction factors for transverse shear stiffnesses, depending, moreover, on the case loading.

To confirm the important role of transverse shear G_{23} in such structures, and that it should be well considered, we present in Fig. 3.4, simulations for different values of shear plane G_{12} and G_{13} and in Fig. 3.5 for different values of transverse shear G_{23}. If G_{12} and G_{13} hardly influence the deflection, weak G_{23} decreases strongly and quickly the stiffness.

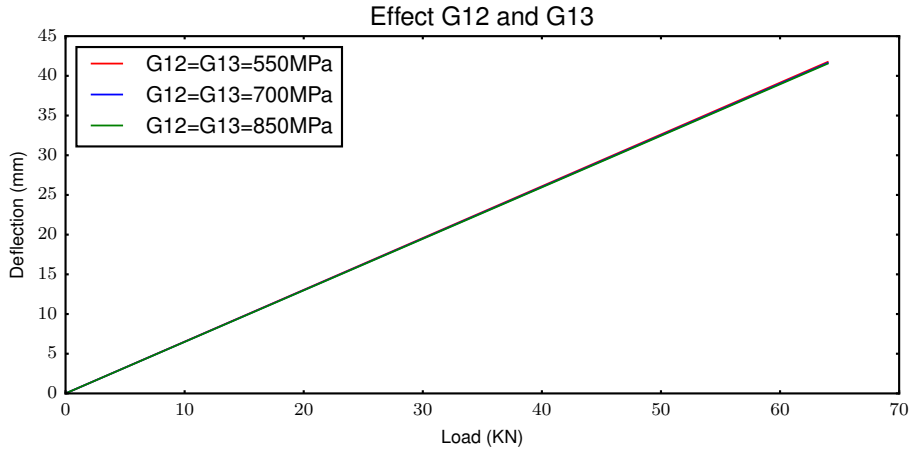


Fig. 3.4. Mid-plane deflection depending on G_{12} and G_{13} (mm).

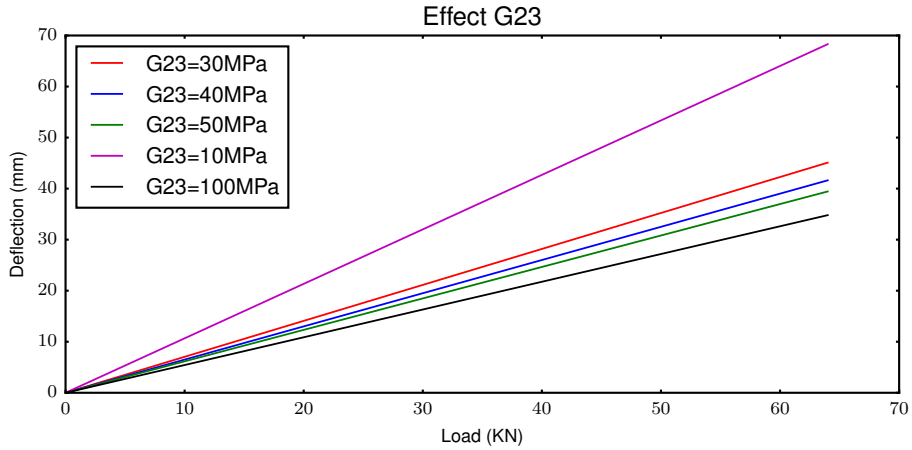


Fig. 3.5. Mid-pan deflection depending on G_{23} (mm).

3.2.3 Resistance and transverse shear stresses estimation

Here we compare the numerical results a), c) and d), with the experimental rupture of the slab. Fig. 3.6 shows the slab after rupture. The rupture appears between layers 2 and 3 (layer 5 is the intrados one). The ultimate load is 64 KN. The maximum transverse shear stresses σ_{13} calculated for this loading, with the different models a), c) and d) and for each interface, are reported in table 3.1. Some tests were also made on the wood strips alone, to estimate the transverse shear strengths of the wood, and especially in the Transverse Normal direction (rolling shear). An average value of 1.73 MPa has been found.

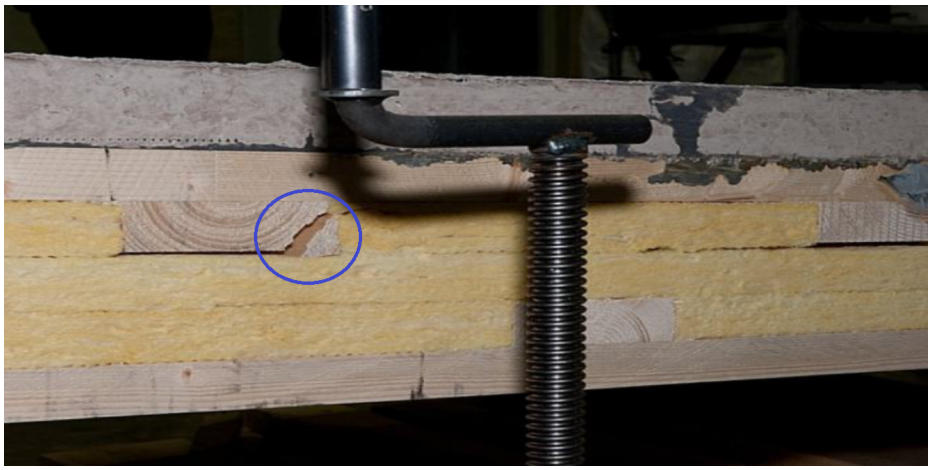


Fig. 3.6. Transverse shear cracking (blue circle) between layers 2 and 3 in a transverse wooden strip.

Interface	Analytical model a)	Equivalent *MPFEAP* c)	Complete *MPFEAP* d)
0-1	0.46	0.48	0.52
1-2	0.68	0.63	0.81
2-3	2.01	1.86	1.77
3-4	1.71	1.55	1.48
4-5	0.55	0.52	0.7

Tab. 3.1. Maximum transverse shear stresses σ_{13} (MPa), for each interface and for the different models a), c) and d)

The three approaches are consistent and locate correctly the rupture. The analytical approach is however reserved to very simple cases, 1D beams with simple loading, elastic behavior, and uniform distribution of strips and porosities. For more complex cases, local densification of strips, 2D slabs, complex loading or boundary conditions, the homogeneous *MPFEAP* model c) permits a good first estimation of the ultimate limit state of the slab. Soon, it will be also possible to take into account inelastic phenomenon, as the compression damage of concrete for instance.

Finally the complete model d), which describes the exact geometrical positions of the strips of wood in the 2 longitudinal and transverse directions as well as porosity, locates correctly too the stress concentration and the weak area of the slab, but allows also a better estimation of the transverse shear stress in these quite difficult conditions. The experimental strength is very close to the numerical estimation, 1.77 MPa. We highlight once again that this model remains a 2 FE approach, involving only plane elements.

3.2.4 Conclusion

In this chapter, the relevance of an original 2D plate approach is demonstrated through the calculation of a highly complex structure combining several materials, wood, high performance concrete and an openwork design (Techniwood). The model is Layerwise, named *LS1* (Thai et al., 2013) since it involves first-order membrane stresses. The 2D associated finite element code *MPFEAP* easily allows the description of the 3D complex structure and the estimation of the transverse shear effects and the intensity of the singularities along the free edges. The performance of this approach is

compared with classical homogeneous solutions, obtained analytically or numerically (Abaqus). For the estimation of the structure rigidity, the homogeneous equivalent *MPFEAP* without the precise openwork description (c) takes accurately into account the high gradient of properties between the different layers, especially concerning the transverse shear phenomenon. The analytical approach can only be applied to very simple cases, 1D beams with simple loading, elastic behavior, and uniform distribution of strips and porosities, and the 2D plate elements from ABAQUS doesn't estimate correctly the transverse shear behavior. Concerning the ultimate behavior, all the models locate correctly the rupture, but once again, the analytical approach can treat only very simple cases. For real and complex cases, local densification of strips, 2D slabs, complex loading or boundary conditions, the homogeneous *MPFEAP* model permits a good first estimation of the ultimate limit state of the slab. If a more precise estimation is needed the model d), which describes the exact geometrical positions of the wooden strips as well as porosity, allows a better estimation of the transverse shear stress in these quite difficult conditions. The experimental strength is very close to the numerical estimation. Note that this fine description remains a 2D plane description, a quite interesting alternative to the heavy 3D descriptions, and relevant for real and complex material and geometries.

CHAPTER 4

A statically compatible layerwise stress model for the analysis of multilayered plates

4.1 Introduction

For the analysis of multilayered structures, although ESL models can provide acceptable results for global response of multilayers, they may lead to very inaccurate estimations of local response especially near free-edges. Layerwise models have been proposed to overcome the drawbacks of ESL models (Barbero and Reddy, 1991; Robbins and Reddy, 1993; Gaudenzi et al., 1995; Dakshina Moorthya and Reddy, 1998; Carrera, 1998; Botello et al., 1999). In these approaches, each layer of the multilayered structure is considered as an independent plate. Therefore, the number of governing equations depends on the number of the layers. This increases significantly the computational cost in layerwise approaches. However, thanks to their accuracy with respect to ESL models and their efficiency with respect to full 3D models, layerwise models have been proven to be very good alternatives to 3D models. In Navier laboratory, a layerwise stress model was proposed and is named *LS1* which means a Layerwise Stress approach with first-order membrane stress approximations per layer in the thickness direction.

Even if the *LS1* model and its refined version are very effective models, they can be still improved. Indeed, firstly, the 3D stress free boundary conditions cannot be exactly met by these models, and secondly, as these models are derived by means of the Hellinger-Reissner mixed variational principle, there is no theoretical guarantee of the convergence of the refined *LS1* model to the 3D model, as the number of mathematical layers per physical layer increases.

The objective of this chapter is to improve the *LS1* model by removing these drawbacks. For this purpose, a new layerwise model, called *Statically Compatible LS1 (*SCLS1*)*, is introduced. As in *LS1*, the laminated plate is still considered as a superposition of Reissner plates coupled by interfacial stresses. However, the divergences of the interlaminar transverse shears are introduced as new generalized efforts. Moreover, the new model is derived by means of the minimum of the complementary potential energy ensuring the convergence of its refined version to the exact 3D model, as the number of mathematical layers per physical layer increases.

Furthermore, the new model has been implemented in a new version of the in-house finite element code called *MPFEAP* (for MultiParticle Finite Element Analysis Program). The new 2D finite element has eight nodes with $6n-1$ degrees of freedom per node, n being the number of layers constituting the laminate. Finally, several comparisons are made between *LS1*, *SCLS1*, refined *LS1*, refined *SCLS1* and full 3D FE models for straight free edge plate and notched laminate under uniaxial tension.

This chapter is organized as follows: the next section is dedicated to the theoretical formulation of the *SCLS1* model referring also to the original *LS1* model, highlighting the differences. Section 3 discusses the FE discretization of the new model and its implementation. Section 4 presents the numerical comparisons between the different models. The chapter ends with a conclusion which synthesizes the main results and discusses prospects for future developments.

4.2 Theoretical formulation of the statically compatible model *SCLS1*

In this section, the new model for linear elastic multilayered plates called *SCLS1* is described. It is derived from the 3D exact model by considering Statically Compatible Layerwise Stresses with first-order membrane stress approximations per layer in the thickness direction. The generalized stresses of the proposed model are actually those of a Reissner-Mindlin plate per layer in addition to inter-laminar shear and normal stresses at the interfaces between layers and the divergences of these inter-laminar shear stresses. The exact 3D equilibrium equations lead to $6n-1$ equilibrium

equations on the generalized stresses, where n is the number of layers. Therefore, the kinematics of the *SCLS1* model, obtained by dualization of the equilibrium equations, has $6n - 1$ degrees of freedom at each point of the middle surface of the plate. Finally, the generalized constitutive equations of the *SCLS1* model linking the generalized stresses to the generalized strains are derived by using the stress energy formulation.

4.2.1 Problem description and notations

The multilayered plate under consideration is composed of n perfectly bonded orthotropic elastic layers (fig. 4.1). The plate occupies the 3D domain $\Omega = \omega \times]h_1^-, h_n^+[$ where ω is the middle surface of the plate. In the following, x and y are the in-plane coordinates and z is the out-of-plane coordinate. The following notations are introduced:

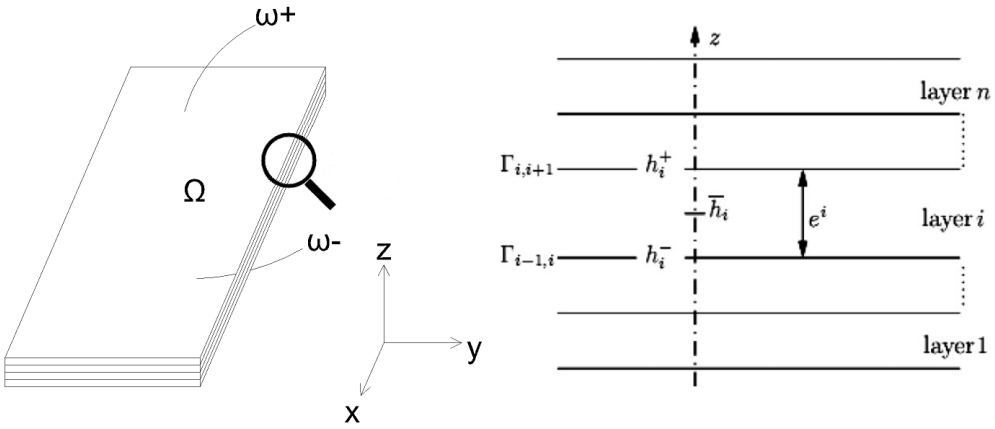


Fig. 4.1. Description of the multilayered plate.

- The superscripts i and j, $j+1$ indicate layer i and the interface between layer j and j+1 with $1 \leqslant i \leqslant n$ and $1 \leqslant j \leqslant n-1$, respectively. By extension, the superscript 0, 1 refers to the lower face $\omega^- = \omega \times h_1^-$ and the superscript $n, n+1$ refers to the upper face $\omega^+ = \omega \times h_n^+$.
- In each layer i, h_i^-, h_i^+ and $\bar{h}_i$ are , respectively, the bottom, the top and the mid-plane z coordinates of the layer, and $e_i = h_i^+ - h_i^-$ is its thickness. Hence, we have $h_{i+1}^- = h_i^+$ for all $1 \leqslant i \leqslant n-1$. By convention, we set $h_0^+ = h_1^-$ and $h_{n+1}^- = h_n^+$.
- Greek subscripts $\alpha, \beta, \gamma, \delta$,... indicate the in-plane components (x,y) and go through 1, 2.
- Latin subscripts k, l, m, n,... indicate the components (x,y,z) and go through 1, 2, 3.
- $\mathbf{S}^i = (S^i_{klmn})$ is the fourth-order compliance tensor of layer i with the minor and major symmetries: $S^i_{klmn} = S^i_{lkmn} = S^i_{klnm} = S^i_{mnkl}$. $\mathbf{S}^i$ is monoclinic in direction z: $S^i_{\alpha\beta\gamma 3} = S^i_{\alpha 333} = 0$.
- $\sigma_{\alpha\beta}(x, y, z)$ are the in-plane stress components, $\sigma_{\alpha 3}(x, y, z)$ are the transverse shear stresses and $\sigma_{33}(x, y, z)$ is the normal stress.
- $\epsilon_{\alpha\beta}(x, y, z)$ are the in-plane strain components, $\epsilon_{\alpha 3}(x, y, z)$ are the transverse strain stresses and $\epsilon_{33}(x, y, z)$ is the normal strain.
- $u_\alpha(x, y, z)$ are the in-plane 3D displacement components, $u_3(x, y, z)$ is the out-of-plane 3D displacement component.

- The Einstein's convention of summation over repeated indexes is adopted.

The plate is loaded on its upper face ω^+ and lower face ω^- with the distributed surface forces $\mathbf{T}^+ = (T_k^+)$ and $\mathbf{T}^- = (T_k^-)$, respectively. The lateral boundary is decomposed into two complementary parts: a free part $\partial\Omega_T = \partial\omega_T \times]h_1^-, h_n^+[$ where $\mathbf{T} = (T_k) = (\sigma_{kl} n_l)$ is set to zero, and a restrained part $\partial\Omega_u = \partial\omega_u \times]h_1^-, h_n^+[$ where the displacement $\mathbf{u} = (u_k)$ is set to zero . Here, the subsets $\partial\omega_T$ and $\partial\omega_u$ are a partition of $\partial\omega$, $\partial\omega = \partial\omega_T \cup \partial\omega_u$ with $\partial\omega_T \cap \partial\omega_u = \emptyset$, and $\mathbf{n} = (n_k)$ is the outer normal to $\partial\Omega_T$.

4.2.2 Governing equations of the 3D model

The 3D problem is to find a statically compatible stress field $\boldsymbol{\sigma} = (\sigma_{kl})$ and a kinematically strain field $\boldsymbol{\epsilon} = (\epsilon_{kl})$ which comply with the constitutive equation:

$$\epsilon_{kl}(x, y, z) = S_{klmn}(z)\sigma_{mn}(x, y, z) \quad \text{on } \Omega. \tag{107}$$

A stress field $\boldsymbol{\sigma}$ is statically compatible if it complies with the equilibrium equations:

$$\sigma_{kl,l} = 0 \quad \text{on } \Omega, \tag{108}$$

and the stress conditions on the lower and upper faces:

$$\sigma_{k3} = -T_k^- \quad \text{on } \omega^-, \quad \sigma_{k3} = T_k^+ \quad \text{on } \omega^+, \tag{109}$$

and on the lateral boundary:

$$\sigma_{kl} n_l = 0 \quad \text{on } \partial\Omega_T. \tag{110}$$

A strain field $\boldsymbol{\epsilon}$ is kinematically compatible if there exists a displacement field $\mathbf{u} = (u_k)$ complying with the displacement conditions on the lateral boundary:

$$u_k = 0 \quad \text{on } \partial\Omega_u, \tag{111}$$

and such that:

$$\epsilon_{kl} = \frac{1}{2}(u_{k,l} + u_{l,k}) \quad \text{on } \Omega. \tag{112}$$

It is well-known that, according to the theorem of the minimum of the complementary energy, the solution stress field minimizes the following stress energy among all possible statically compatible stress fields:

$$W^* = \frac{1}{2}\int_\Omega S_{klmn}(z)\sigma_{mn}\sigma_{kl}\, dxdydz \tag{113}$$

The main idea of the proposed model is to restrict the above minimization problem to those statically compatible stress fields whose in-plane components, $\sigma_{\alpha\beta}$, are layerwise linear functions of z. Those fields define the *SCLS1* subset of statically compatible stress fields.

4.2.3 The static of the *SCLS1* model

Since in the *SCLS1* model $\sigma_{\alpha\beta}$ are layerwise linear functions of z, then, by virtue of the 3D equilibrium equations, the transverse shear stresses $\sigma_{\alpha 3}$ are necessarily layerwise quadratic functions of z and the normal stress σ_{33} is necessarily a layerwise third-order polynomial function of z. Taking into account the continuity of the stresses $\sigma_{\alpha 3}$ and σ_{33} at the interfaces between the layers, it can be easily established that such stress fields have the following expressions in layer i: for $1 \leqslant i \leqslant n$,

$$\sigma^{3D}_{\alpha\beta}(x,y,z) = N^i_{\alpha\beta}(x,y)\frac{P^i_0(z)}{e^i} + \frac{12}{e^{i2}}M^i_{\alpha\beta}(x,y)P^i_1(z) \tag{114}$$

$$\begin{aligned}\sigma^{3D}_{\alpha 3}(x,y,z) =& Q^i_\alpha(x,y)\frac{P^i_0(z)}{e^i} + \left(\tau^{i,i+1}_\alpha(x,y) - \tau^{i-1,i}_\alpha(x,y)\right)P^i_1(z) + \\ & \left(Q^i_\alpha(x,y) - \frac{e^i}{2}\left(\tau^{i,i+1}_\alpha(x,y) + \tau^{i-1,i}_\alpha(x,y)\right)\right)\frac{P^i_2(z)}{e^i}\end{aligned} \tag{115}$$

$$\begin{aligned}\sigma^{3D}_{33}(x,y,z) =& \left(\frac{1}{2}\left(\nu^{i,i+1}(x,y) + \nu^{i-1,i}(x,y)\right) + \frac{e^i}{12}\left(\pi^{i,i+1}(x,y) - \pi^{i-1,i}(x,y)\right)\right)P^i_0(z) + \\ & \left(\frac{e^i}{10}\left(\pi^{i,i+1}(x,y) + \pi^{i-1,i}(x,y)\right) + \frac{6}{5}\left(\nu^{i,i+1}(x,y) - \nu^{i-1,i}(x,y)\right)\right)P^i_1(z) + \\ & \frac{e^i}{12}\left(\pi^{i,i+1}(x,y) - \pi^{i-1,i}(x,y)\right)P^i_2(z) + \\ & \left(\frac{e^i}{2}\left(\pi^{i,i+1}(x,y) + \pi^{i-1,i}(x,y)\right) + \left(\nu^{i,i+1}(x,y) - \nu^{i-1,i}(x,y)\right)\right)P^i_3(z)\end{aligned} \tag{116}$$

where $N^i_{\alpha\beta}$, $M^i_{\alpha\beta}$ and Q^i_α are generalized stresses associated to layer i, $\tau^{i,i+1}_\alpha$, $\nu^{i,i+1}$ and $\pi^{i,i+1}$ are generalized stresses associated to the interface between layer i and layer $i+1$, and P^i_k, $k = 0,1,2,3$, are the orthogonal Legendre-like polynomials basis defined on layer i by: for $h^-_i \leq z \leq h^+_i$,

$$\begin{cases} P^i_0(z) = 1 \\ P^i_1(z) = \dfrac{z - \bar{h}_i}{e^i} \\ P^i_2(z) = -6\left(\dfrac{z-\bar{h}_i}{e^i}\right)^2 + \dfrac{1}{2} \\ P^i_3(z) = -2\left(\dfrac{z-\bar{h}_i}{e^i}\right)^3 + \dfrac{3}{10}\left(\dfrac{z-\bar{h}_i}{e^i}\right) \end{cases} \tag{117}$$

The interpretation of the generalized stresses defined on layer i is as follows: $\mathbf{N}^i = (N^i_{\alpha\beta})$ is the in-plane stress resultant tensor, $\mathbf{M}^i = (M^i_{\alpha\beta})$ is the moment resultant tensor and $\mathbf{Q}^i = (Q^i_\alpha)$ is the out-of-plane shear stress resultant vector. They can be expressed in terms of the 3D stress field $\boldsymbol{\sigma}^{3D}$ in layer i as follows:

$$\begin{aligned} N^i_{\alpha\beta}(x,y) &= \int_{h^-_i}^{h^+_i} \sigma^{3D}_{\alpha\beta}(x,y,z)dz \\ M^i_{\alpha\beta}(x,y) &= \int_{h^-_i}^{h^+_i} (z-\bar{h}_i)\sigma^{3D}_{\alpha\beta}(x,y,z)dz \\ Q^i_\alpha(x,y) &= \int_{h^-_i}^{h^+_i} \sigma^{3D}_{\alpha 3}(x,y,z)dz \end{aligned} \tag{118}$$

The interlaminar shear and normal stresses at the interface between layer j and layer $j+1$, for $0 \leqslant j \leqslant n$, are given by:

$$\begin{array}{l} \tau_\alpha^{j,j+1}(x,y) = \sigma_{\alpha 3}^{3D}(x,y,h_j^+) = \sigma_{\alpha 3}^{3D}(x,y,h_{j+1}^-) \\ \nu^{j,j+1}(x,y) = \sigma_{33}^{3D}(x,y,h_j^+) = \sigma_{33}^{3D}(x,y,h_{j+1}^-) \end{array} \tag{119}$$

Note that, unlike all the other introduced generalized stresses, $\pi^{j,j+1}$ defined on the interface between layer j and layer $j+1$ is a new generalized stress which was not considered in the *LS1* model. Its interpretation will be given in the sequel.

Now, we seek for conditions on the generalized stresses which enforce statical compatibility of $\boldsymbol{\sigma}^{3D}$. Let us compute the 3D equilibrium equations $\sigma_{kl,l}^{3D}$ in layer i, we obtain:

$$\begin{aligned} \sigma_{\alpha l,l}^{3D} &= \left(N_{\alpha\beta,\beta}^i + \tau_\alpha^{i,i+1} - \tau_\alpha^{i-1,i}\right)\frac{P_0^i(z)}{e^i} + \\ &\quad \left(M_{\alpha\beta,\beta}^i - Q_\alpha^i + \frac{e^i}{2}\left(\tau_\alpha^{i,i+1} + \tau_\alpha^{i-1,i}\right)\right)\frac{12P_1^i(z)}{e^{i2}} \\ \sigma_{3l,l}^{3D} &= \left(Q_{\beta,\beta}^i + \nu^{i,i+1} - \nu^{i-1,i}\right)\frac{P_0^i(z)}{e^i} + \\ &\quad \left(\tau_{\beta,\beta}^{i,i+1} - \tau_{\beta,\beta}^{i-1,i} - \pi^{i,i+1} + \pi^{i-1,i}\right)P_1^i(z) + \\ &\quad \left(\left(Q_{\beta,\beta}^i + \nu^{i,i+1} - \nu^{i-1,i}\right)\frac{2}{e^i} - \tau_{\beta,\beta}^{i,i+1} - \tau_{\beta,\beta}^{i-1,i} + \pi^{i,i+1} + \pi^{i-1,i}\right)\frac{P_2^i(z)}{2} \end{aligned} \tag{120}$$

Hence, the $\boldsymbol{\sigma}^{3D}$ stress field will comply with the 3D equilibrium equations (108), if, and only if, the following equations hold true for all (x,y) in ω and for all $i = 1,...,n$ and $j = 0,...,n$:

$$\begin{array}{l} N_{\alpha\beta,\beta}^i + \tau_\alpha^{i,i+1} - \tau_\alpha^{i-1,i} = 0 \\ Q_{\alpha,\alpha}^i + \nu^{i,i+1} - \nu^{i-1,i} = 0 \\ M_{\alpha\beta,\beta}^i - Q_\alpha^i + \dfrac{e^i}{2}\left(\tau_\alpha^{i,i+1} + \tau_\alpha^{i-1,i}\right) = 0 \\ \tau_{\alpha,\alpha}^{j,j+1} - \pi^{j,j+1} = 0 \end{array} \tag{121}$$

The last equation gives the interpretation of $\pi^{i,i+1}$ which is equal to the divergence of the interlaminar shear stress vector $\boldsymbol{\tau}^{i,i+1} = (\tau_\alpha^{i,i+1})$. Now, if we seek for the statically compatibility of σ_{ij}^{3D}, we have to enforce the stress boundary conditions in addition to equations (121). The lateral boundary conditions $\sigma_{ij}^{3D} n_j = 0$ on $\partial\Omega_T$ are equivalent to the following equations for $i = 1,...,n$ and $j = 0,...,n$:

$$N_{\alpha\beta}^i n_\beta = 0, \quad M_{\alpha\beta}^i n_\beta = 0, \quad Q_\alpha^i n_\alpha = 0, \quad \tau_\alpha^{j,j+1} n_\alpha = 0, \quad \text{on } \partial\omega_T. \tag{122}$$

The boundary conditions (109) on the lower and upper faces are, respectively,

$$\left\{\begin{array}{l} \tau_1^{0,1}(x,y) = -T_1^-(x,y) \\ \tau_2^{0,1}(x,y) = -T_2^-(x,y) \\ \nu^{0,1}(x,y) = -T_3^-(x,y) \end{array}\right. \text{ and } \left\{\begin{array}{l} \tau_1^{n,n+1}(x,y) = T_1^+(x,y) \\ \tau_2^{n,n+1}(x,y) = T_2^+(x,y) \\ \nu^{n,n+1}(x,y) = T_3^+(x,y) \end{array}\right. \tag{123}$$

It should be noticed that the boundary conditions (122) and (123) cannot be simultaneously verified unless $T_\alpha^\pm n_\alpha = 0$ on $\partial\omega_T$, which will be assumed in the sequel. Moreover, from the last equation of (121) for $j = 0$ and $j = n$, we see that:

$$\pi^{0,1} = -T^{-}_{\alpha,\alpha} \quad \text{and} \quad \pi^{n,n+1} = T^{+}_{\alpha,\alpha} \tag{124}$$

Finally, we have established that the stress field $\boldsymbol{\sigma}^{3D}$ is statically compatible when it complies with the generalized equilibrium equations on ω: (121) for $i = 1, ..., n$ and $j = 1, ..., n-1$, (123) and (124), and with the generalized stress free boundary conditions on $\partial\omega_T$: (122) for $i = 1, ..., n$ and $j = 1, ..., n-1$.

It should be emphasized that in the *LS1* model, the authors considered 3D stresses of the form (114-115-116) where $\tau^{j,j+1}_{\alpha,\alpha}$ is substituted for $\pi^{j,j+1}$. Hence, the last equation of (121) is absent from the *LS1* model. Moreover, the free boundary conditions $\tau^{j,j+1}_{\alpha} n_\alpha = 0$ in (122) cannot be mathematically enforced by the model so that the 3D stresses of the *LS1* model are not statically compatible in this case.

4.2.4 The kinematics of the *SCLS1* model

It is obtained by writing the weak form of the statically compatibility conditions on $\boldsymbol{\sigma}^{3D}$. First, the weak form of the 3D equilibrium equation (108):

$$\int_\Omega \sigma^{3D}_{kl,l} u_k \, dxdydz = 0 \tag{125}$$

is written for any trial displacement field $\mathbf{u} = (u_k)$. Using conditions (123) and (124) and introducing the following notations for $i = 1, ..., n$ and $j = 1, ..., n-1$:

$$U^i_\alpha(x,y) = \int_{h_i^-}^{h_i^+} \frac{P^i_0(z)}{e^i} u_\alpha(x,y,z)\, dz, \tag{126}$$

$$\Phi^i_\alpha(x,y) = \int_{h_i^-}^{h_i^+} \frac{12}{e^{i2}} P^i_1(z) u_\alpha(x,y,z)\, dz, \tag{127}$$

$$U^i_3(x,y) = \int_{h_i^-}^{h_i^+} \left(\frac{P^i_0(z)}{e^i} + \frac{P^i_2(z)}{e^i} \right) u_3(x,y,z)\, dz, \tag{128}$$

$$W^i_\pm(x,y) = \int_{h_i^-}^{h_i^+} \left(P^i_1(z) \pm \frac{P^i_2(z)}{2} \right) u_3(x,y,z)\, dz \tag{129}$$

and

$$V^{j,j+1}(x,y) = W^j_-(x,y) - W^{j+1}_+(x,y) \tag{130}$$

we obtain:

$$\begin{aligned}
\int_\Omega \sigma^{3D}_{kl,l} u_k \, dxdydz = &\sum_{i=1}^{n} \int_\omega \left(N^i_{\alpha\beta,\beta} + \tau^{i,i+1}_\alpha - \tau^{i-1,i}_\alpha \right) U^i_\alpha \, dxdy + \\
&\sum_{i=1}^{n} \int_\omega \left(Q^i_{\alpha,\alpha} + \nu^{i,i+1} - \nu^{i-1,i} \right) U^i_3 \, dxdy + \\
&\sum_{i=1}^{n} \int_\omega \left(M^i_{\alpha\beta,\beta} - Q^i_\alpha + \frac{e^i}{2} \left(\tau^{i,i+1}_\alpha + \tau^{i-1,i}_\alpha \right) \right) \Phi^i_\alpha \, dxdy + \\
&\sum_{j=1}^{n-1} \int_\omega \left(\tau^{j,j+1}_{\alpha,\alpha} - \pi^{j,j+1} \right) V^{j,j+1} \, dxdy = 0.
\end{aligned} \tag{131}$$

Actually, $U^i_\alpha(x,y)$, $U^i_3(x,y)$, $\Phi^i_\alpha(x,y)$ are the five Reissner-Mindlin generalized displacements of layer i already introduced in the *LS1* model: respectively, the two in-plane displacements, the vertical displacement and the two bending rotations. In contrast, $V^{j,j+1}(x,y)$ is a new kinematical variable, having the dimension of an area, which is dual of the static variable $\pi^{j,j+1}(x,y)$ defined on interface $j, j+1$.

Integrating by parts the second term of (131), restricting the trial fields $\mathbf{u}$ to those which are null on the lateral boundary $\partial\Omega_u$, and hence the following generalized boundary conditions are prescribed for $i = 1, ..., n$ and $j = 0, ..., n$:

$$U^i_\alpha = 0, \quad U^i_3 = 0, \quad \Phi^i_\alpha = 0, \quad V^{j,j+1} = 0, \quad \text{on } \partial\omega_u, \tag{132}$$

and taking into account the generalized stress free boundary conditions on $\partial\omega_T$, (122), then we obtain:

$$\begin{aligned}
&\sum_{i=1}^{n} \int_\omega N^i_{\alpha\beta}\varepsilon^i_{\alpha\beta} + M^i_{\alpha\beta}\chi^i_{\alpha\beta} + Q^i_\alpha\gamma^i_\alpha \, dxdy + \\
&\qquad \sum_{j=1}^{n-1} \int_\omega \tau^{j,j+1}_\alpha D^{j,j+1}_\alpha + \nu^{j,j+1} D^{j,j+1}_\nu + \pi^{j,j+1}\lambda^{j,j+1} \, dxdy = \\
&\qquad \int_\omega T^+_\alpha \times \left(U^n_\alpha + \frac{e^n}{2}\Phi^n_\alpha\right) + T^-_\alpha \times \left(U^1_\alpha - \frac{e^1}{2}\Phi^1_\alpha\right) + T^+_3 U^n_3 + T^-_3 U^1_3 \, dxdy
\end{aligned} \tag{133}$$

where the generalized strains dual of the generalized stresses $N^i_{\alpha\beta}$, $M^i_{\alpha\beta}$, Q^i_α, $\tau^{j,j+1}_\alpha$, $\nu^{j,j+1}$, $\pi^{j,j+1}$ for $i = 1, ..., n$ and $j = 1, ..., n-1$ are respectively expressed in terms of the generalized displacements as:

$$\begin{aligned}
&\varepsilon^i_{\alpha\beta} = \frac{1}{2}\left(U^i_{\alpha,\beta} + U^i_{\beta,\alpha}\right), \\
&\chi^i_{\alpha\beta} = \frac{1}{2}\left(\Phi^i_{\alpha,\beta} + \Phi^i_{\beta,\alpha}\right), \\
&\gamma^i_\alpha = \Phi^i_\alpha + U^i_{3,\alpha}, \\
&D^{j,j+1}_\alpha = U^{j+1}_\alpha - U^j_\alpha - \frac{e^j}{2}\Phi^j_\alpha - \frac{e^{j+1}}{2}\Phi^{j+1}_\alpha + V^{j,j+1}_{,\alpha}, \\
&D^{j,j+1}_\nu = U^{j+1}_3 - U^j_3, \\
&\lambda^{j,j+1} = V^{j,j+1}.
\end{aligned} \tag{134}$$

By comparison, if the terms $\pi^{j,j+1}\lambda^{j,j+1}$ are omitted in (133) and the terms $V^{j,j+1}_{,\alpha}$ are omitted in (134_4), then the kinematical compatibility conditions of the *LS1* model are retrieved.

4.2.5 The *SCLS1* model constitutive equations

The 3D elastic stress energy of the stress field $\boldsymbol{\sigma}^{3D}$ can be written in the following form:

$$\begin{aligned}
W^*_{3D} &= \int_\Omega \frac{1}{2} S_{klmn}(z)\sigma^{3D}_{mn}\sigma^{3D}_{kl} \, dxdydz \\
&= \int_\omega w^*_{3D} \, dxdy
\end{aligned} \tag{135}$$

where w^*_{3D} is the generalized stress energy density per unit area of the plate defined by:

$$w^*_{3D} = \int_{h_1^-}^{h_n^+} \frac{1}{2} S_{klmn}(z)\sigma^{3D}_{mn}\sigma^{3D}_{kl}\, dz \tag{136}$$

Inserting equations (114-115-116) into the above definition, an explicit expression of w^*_{3D} in terms of the generalized stresses is derived. See Appendix A.1.

Using the weak formulation (133) and standard variational calculus reasoning, it can be established that the generalized stresses which realize the minimum of W^*_{3D} over all statically compatible stress fields of the form (114-115-116) are such that the partial derivatives of w^*_{3D}, with respect to these generalized stresses, are the generalized strains (134) generated by some generalized displacement fields U^i_α, U^i_3, ϕ^i_α, $V^{j,j+1}$, $i = 1, ..., n$, $j = 1, ..., n-1$, which are null on $\partial\omega_u$. Hence, the constitutive equations write:

- Membrane constitutive equation of layer i:

$$\begin{aligned}\varepsilon^i_{\alpha\beta} =& \frac{\partial w^*_{3D}}{\partial N^i_{\alpha\beta}} \\ =& \frac{1}{e^i} S^{\,i}_{\alpha\beta\gamma\delta} N^i_{\gamma\delta} + S^{\,i}_{\alpha\beta 33}\left(\frac{1}{2}\left(v^{i,i+1} + v^{i-1,i}\right) + \frac{e^i}{12}\left(\pi^{i,i+1} - \pi^{i-1,i}\right)\right)\end{aligned} \tag{137}$$

- Bending constitutive equation of layer i:

$$\begin{aligned}\chi^i_{\alpha\beta} =& \frac{\partial w^*_{3D}}{\partial M^i_{\alpha\beta}} \\ =& \frac{12}{e^{i^3}} S^{\,i}_{\alpha\beta\gamma\delta} M^i_{\gamma\delta} + \frac{1}{e^i} S^{\,i}_{\alpha\beta 33}\left(\frac{6}{5}\left(v^{i,i+1} - v^{i-1,i}\right) + \frac{e^i}{10}(\pi^{i,i+1} + \pi^{i-1,i})\right)\end{aligned} \tag{138}$$

- Transverse shear constitutive equation of layer i:

$$\gamma^i_\alpha = \frac{\partial w^*_{3D}}{\partial Q^i_\alpha} = \frac{24}{5e^i} S^{\,i}_{\alpha 3\beta 3} Q^i_\beta - \frac{2}{5} S^{\,i}_{\alpha 3\beta 3}\left(\tau^{i,i+1}_\beta + \tau^{i-1,i}_\beta\right) \tag{139}$$

- Shear constitutive equation of interface $j, j+1$:

$$\begin{aligned}D^{j,j+1}_\alpha =& \frac{\partial w^*_{3D}}{\partial \tau^{j,j+1}_\alpha} \\ =& -\frac{2}{5} S^{\,j}_{\alpha 3\beta 3} Q^j_\beta - \frac{2}{5} S^{\,j+1}_{\alpha 3\beta 3} Q^{j+1}_\beta - \frac{2}{15} e^j S^{\,j}_{\alpha 3\beta 3} \tau^{j-1,j}_\beta \\ &+ \frac{8}{15}\left(e^j S^{\,j}_{\alpha 3\beta 3} + e^{j+1} S^{\,j+1}_{\alpha 3\beta 3}\right)\tau^{j,j+1}_\beta - \frac{2}{15} e^{j+1} S^{\,j+1}_{\alpha 3\beta 3} \tau^{j+1,j+2}_\beta\end{aligned} \tag{140}$$

- Normal constitutive equation of interface $j, j+1$:

$$\begin{aligned}D^{j,j+1}_\nu =& \frac{\partial w^*_{3D}}{\partial v^{j,j+1}} \\ =& \frac{9}{70} e^j S^{\,j}_{3333} v^{j-1,j} + \frac{13}{35}\left(e^j S^{\,j}_{3333} + e^{j+1} S^{\,j+1}_{3333}\right) v^{j,j+1} + \frac{9}{70} e^{j+1} S^{\,j+1}_{3333} v^{j+1,j+2} \\ &- \frac{13}{420}(e^j)^2 S^{\,j}_{3333} \pi^{j-1,j} + \frac{11}{210}\left((e^j)^2 S^{\,j}_{3333} - (e^{j+1})^2 S^{\,j+1}_{3333}\right)\pi^{j,j+1} \\ &+ \frac{13}{420}(e^{j+1})^2 S^{\,j+1}_{3333} \pi^{j+1,j+2} \\ &+ \frac{1}{2} S^{\,j}_{\alpha\beta 33} N^j_{\alpha\beta} + \frac{1}{2} S^{\,j+1}_{\alpha\beta 33} N^{j+1}_{\alpha\beta} + \frac{6}{5e^j} S^{\,j}_{\alpha\beta 33} M^j_{\alpha\beta} - \frac{6}{5e^{j+1}} S^{\,j+1}_{\alpha\beta 33} M^{j+1}_{\alpha\beta}\end{aligned} \tag{141}$$

- Constitutive equation for the π generalized stress at interface j, $j+1$:

$$\begin{aligned}\lambda^{j,j+1} =& \frac{\partial w^*_{3D}}{\partial \pi^{j,j+1}} \\ =& -\frac{1}{140}(e^j)^3 S^{j}_{3333}\pi^{j-1,j} + \frac{1}{105}\left((e^j)^3 S^{j}_{3333} + (e^{j+1})^3 S^{j+1}_{3333}\right)\pi^{j,j+1} \\ & -\frac{1}{140}(e^{j+1})^3 S^{j+1}_{3333}\pi^{j+1,j+2} \\ & +\frac{13}{420}(e^j)^2 S^{j}_{3333}\nu^{j-1,j} + \frac{11}{210}\left((e^j)^2 S^{j}_{3333} - (e^{j+1})^2 S^{j+1}_{3333}\right)\nu^{j,j+1} \\ & -\frac{13}{420}(e^{j+1})^2 S^{j+1}_{3333}\nu^{j+1,j+2} \\ & +\frac{1}{12}e^j S^{j}_{\alpha\beta 33} N^{j}_{\alpha\beta} - \frac{1}{12}e^{j+1} S^{j+1}_{\alpha\beta 33} N^{j+1}_{\alpha\beta} + \frac{1}{10} S^{j}_{\alpha\beta 33} M^{j}_{\alpha\beta} + \frac{1}{10} S^{j+1}_{\alpha\beta 33} M^{j+1}_{\alpha\beta}\end{aligned} \tag{142}$$

By comparison, the constitutive equations of the *LS1* model are retrieved if the last equation (142) is omitted and if the coupling terms ν and π are neglected in (137) and (138), and the coupling terms $N_{\alpha\beta}$, $M_{\alpha\beta}$ and π are neglected in (141).

In summary, the *SCLS1* problem is to find the $6n-1$ generalized displacement fields $U^i_\alpha(x,y)$, $U^i_3(x,y)$, $\phi^i_\alpha(x,y)$ and $V^{j,j+1}(x,y)$ and the $12n-4$ generalized stress fields $N^i_{\alpha\beta}$, $M^i_{\alpha\beta}$, Q^i_α, $\nu^{j,j+1}$, $\tau^{j,j+1}_\alpha$ and $\pi^{j,j+1}$ defined on ω for $i = 1, ..., n$ and $j = 1, ..., n-1$ complying with the equilibrium equations (121), the compatibility equations (134), the constitutive equations (137-142) and the boundary conditions (122) and (132). To be complete, the description of the *LS1* problem is given in the previous Chapter 1.

4.2.6 The refined *SCLS1* model as a static discretization of the 3D model

As it has been explained above, the *SCLS1* model is obtained by restricting the minimization of the total stress energy over the set of statically compatible 3D stress fields having in-plane components $\sigma_{\alpha\beta}$ which are piece-wise linear in the thickness of each physical layer. Now, if we discretize each physical layer in p mathematical layers as shown in Fig. 4.2, resulting in a total of np mathematical layers, then the new statically compatible 3D stress field obtained by this refined model, called refined *SCLS1*, will be a better approximation of the real 3D stress field than the non refined *SCLS1*. Moreover, it will asymptotically coincide with the exact 3D stress field as the number p of mathematical layers per physical layer increases to infinity. Indeed, for sufficiently large p, the in-plane components $\sigma_{\alpha\beta}$ of the real 3D stress field can be accurately represented by piece-wise linear functions in the thickness of each mathematical layer. Hence, the refined *SCLS1* model appears as a consistent static discretization of the 3D model in the z co-ordinate. A rigorous mathematical proof of the convergence of the refined *SCLS1* model to the 3D model, as p increases, is beyond the scope of this chapter.

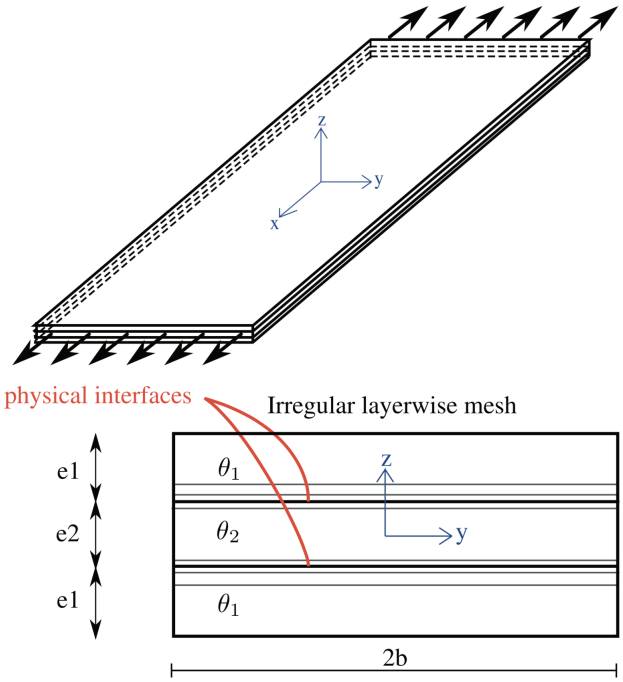


Fig. 4.2. The same multilayered plate refined through the thickness (irregular layerwise mesh through the thickness).

Actually, as pointed out in (Saeedi et al., 2012b) for the *LS1* model, an irregular discretization of the physical layers is more suitable than a regular one because of the stress concentration at the interfaces between the physical layers. Thus, one must refine the mesh near the interfaces. That is why the geometric discretization proposed by Saeedi et al. (2012b) will be adopted. According to this layerwise mesh strategy, the thicknesses of the mathematical layers are in the form of a geometric progression. In other words, if the thickness of the mathematical layers at the vicinity of the physical interface are set equal to h_{min}, then the thicknesses of the next layers will be equal to $r \times h_{min}, r^2 \times h_{min}, ...$ where r is the common ratio of the geometric progression in the considered layer. The determination of r in terms of h_{min}, e, the thickness of the physical layer, and p, the number of mathematical layers per physical layer, is obtained by solving the following equation which depends on the considered case:

- Physical layer with one physical interface (top or bottom layer) and $p > 1$

$$h_1 = h_{min};\ h_2 = r \times h_{min} \quad ... \quad h_p = r^{p-1} \times h_{min}$$

$$\sum_{i=1}^{p} h_i = e \Rightarrow 1 + r + r^2 + ... + r^{p-1} = \frac{e}{h_{min}}$$

- Physical layer with two physical interfaces (inside layer) and $p > 2$

  p is an even number

$$h_1 = h_p = h_{min};\ h_2 = h_{p-1} = r \times h_{min} \quad ... \quad h_{\frac{p}{2}} = h_{\frac{p}{2}+1} = r^{\frac{p}{2}-1} \times h_{min}$$

$$\sum_{i=1}^{p} h_i = e \Rightarrow 2 \times (1 + r + r^2 + ... + r^{\frac{p}{2}-1}) = \frac{e}{h_{min}}$$

p is an odd number

$$h_1 = h_p = h_{min};\ h_2 = h_{p-1} = r \times h_{min} \quad ... \quad h_{\frac{p+1}{2}} = r^{\frac{p-1}{2}} \times h_{min}$$

$$\sum_{i=1}^{p} h_i = e \Rightarrow 2 \times (1 + r + r^2 + ... + r^{\frac{p-3}{2}}) + r^{\frac{p-1}{2}} = \frac{e}{h_{min}}$$

So, the discretization of a physical layer is completely determined once the two non dimensional parameters p and $R = \frac{e}{h_{min}}$ are given. A possible strategy is to adopt the same values of $(p, \frac{e}{h_{min}})$ for all the physical layers.

4.3 Finite element discretization of the *SCLS1* model

This section deals with the displacement finite element formulation of the *SCLS1* presented in the previous section. An eight-node isoparametric quadrilateral element with $6n - 1$ d.o.f. at each nodal point will be formulated as follows. This element has the same interpolation functions as the *LS1*'s element which is integrated in the *MPFEAP* in-house software described in (Nguyen and Caron, 2006).

4.3.1 Weak formulation of the *SCLS1* model

The following notations are introduced:

- The $6n - 1$ generalized displacement vector $[\delta_i]$ is defined as:

$$[\delta_i]^T = \Big(\underbrace{U_1^1,\ U_2^1,\ U_3^1,\ \Phi_1^1,\ \Phi_2^1, \ldots, U_1^n,\ U_2^n,\ U_3^n,\ \Phi_1^n,\ \Phi_2^n,\ V^{1,2}, \ldots, V^{n-1,n}}_{6n-1}\Big),$$

  where $[X]^T$ is the transpose of $[X]$

- The $12n$-4 generalized strain vector $[E]$ is defined as:

$$[E]^T = \left(\left[E^K\right]^T, [E^\nu]^T, \left[E^Q\right]^T, \left[E^\lambda\right]^T\right)$$

  where the generalized Kirchhoff strain vector is:

$$\left[E^K\right]^T = \Big(\underbrace{\varepsilon_{11}^1,\ \varepsilon_{22}^1,\ 2\varepsilon_{12}^1,\ \chi_{11}^1,\ \chi_{22}^1,\ 2\chi_{12}^1, \ldots, \varepsilon_{11}^n,\ \varepsilon_{22}^n,\ 2\varepsilon_{12}^n,\ \chi_{11}^n,\ \chi_{22}^n,\ 2\chi_{12}^n}_{6n}\Big),$$

  the generalized normal strain vector is:

$$[E^\nu]^T = \Big(\underbrace{D_\nu^{1,2},\ D_\nu^{2,3}, \ldots, D_\nu^{n-1,n}}_{n-1}\Big),$$

  the generalized shear strain vector is:

$$\left[E^{Q}\right]^{T} = \left(\underbrace{\gamma_1^1,\, \gamma_2^1,\, D_1^{1,2},\, D_2^{1,2},\, \gamma_1^2,\, \gamma_2^2, \ldots, \gamma_1^{n-1},\, \gamma_2^{n-1},\, D_1^{n-1,n},\, D_2^{n-1,n},\, \gamma_1^n,\, \gamma_2^n}_{4n-2}\right),$$

and the strain related to the λ variables is:

$$\left[E^{\lambda}\right]^{T} = \left(\underbrace{\lambda^{1,2},\, \lambda^{2,3}, \ldots, \lambda^{n-1,n}}_{n-1}\right)$$

- Finally, the $12n$-4 generalized strain vector $[\Sigma]$ is defined as:

$$[\Sigma]^{T} = \left(\left[\Sigma^{K}\right]^{T}, [\Sigma^{\nu}]^{T}, \left[\Sigma^{Q}\right]^{T}, [\Sigma^{\pi}]^{T}\right)$$

where

$$\left[\Sigma^{K}\right]^{T} = \left(N_{11}^1,\, N_{22}^1,\, N_{12}^1,\, M_{11}^1,\, M_{22}^1,\, M_{12}^1, \ldots, N_{11}^n,\, N_{22}^n,\, N_{12}^n,\, M_{11}^n,\, M_{22}^n,\, M_{12}^n\right),$$

$$[\Sigma^{\nu}]^{T} = \left(\nu^{1,2},\, \nu^{2,3}, \ldots, \nu^{n-1,n}\right),$$

$$\left[\Sigma^{Q}\right]^{T} = \left(Q_1^1,\, Q_2^1,\, \tau_1^{1,2},\, \tau_2^{1,2},\, Q_1^2,\, Q_2^2, \ldots, Q_1^{n-1},\, Q_2^{n-1},\, \tau_1^{n-1,n},\, \tau_2^{n-1,n},\, Q_1^n,\, Q_2^n\right),$$

and

$$[\Sigma^{\pi}]^{T} = \left(\pi^{1,2},\, \pi^{2,3}, \ldots, \pi^{n-1,n}\right).$$

With these notations, the *SCLS1* constitutive equations (137-142) can be rewritten as:

$$[E] = [S]\,[\Sigma] + \left[E^{P}\right] \tag{143}$$

where the generalized compliance matrix $[S]$ of dimension $(12n-4)\times(12n-4)$ has the following block form:

$$[S] = \begin{bmatrix} \left[S^{K}\right] & \left[S^{K\nu}\right] & 0 & \left[S^{K\pi}\right] \\ \left[S^{\nu K}\right] & [S^{\nu}] & 0 & [S^{\nu\pi}] \\ 0 & 0 & \left[S^{Q}\right] & 0 \\ \left[S^{\pi K}\right] & [S^{\pi\nu}] & 0 & [S^{\pi}] \end{bmatrix}, \tag{144}$$

and the generalized prestrain vector $\left[E^{P}\right]$ contains the contributions to the generalized strain vector of the applied surface forces $\underline{T}^{-}$ and $\underline{T}^{+}$. More precisely, explicit expression of $\left[E^{P}\right]$ can be obtained by using equations (123-124) in (137-142) while setting all the components of $[\Sigma]$ to zero.

The constitutive equation (143) can be inverted leading to:

$$[\Sigma] = [S]^{-1}\left([E] - \left[E^{P}\right]\right) = [D]\left([E] - \left[E^{P}\right]\right) \tag{145}$$

where $[D] = [S]^{-1}$ is the generalized stiffness matrix of dimensions $(12n-4)\times(12n-4)$ having the same block form as $[S]$.

Using the above constitutive equation into the weak form of the equilibrium equations (133), the weak formulation of the *SCLS1* problem is obtained: Find a generalized displacement vector $[\delta]$ complying with the boundary conditions (123) such that:

$$\int_{\omega} [E']^T [D] [E] \; dxdy = \int_{\omega} [\delta']^T [F] + [E']^T [D] \left[E^P\right] \; dxdy \tag{146}$$

for any generalized displacement field vector $[\delta']$ complying with the boundary conditions (132). Here, $[E]$ and $[E']$ are, respectively, the generalized strain fields associated to $[\delta]$ and $[\delta']$ via the compatibility equations (134), and $[F]$ is the generalized force vector of dimension $6n-1$ given by:

$$[F]^T = \left(T_1^-,\, T_2^-,\, T_3^-,\, -\frac{e^1}{2}T_1^-,\, -\frac{e^1}{2}T_2^-, 0, \ldots, 0, T_1^+,\, T_2^+,\, T_3^+,\, \frac{e^n}{2}T_1^+,\, \frac{e^n}{2}T_2^+,\, 0, \ldots, 0\right)$$

4.3.2 Geometry and displacement interpolations

The representation of the geometry of the finite element mesh is based on a quadrilateral master element defined in the (ξ,η) space as shown in Fig. 4.3.

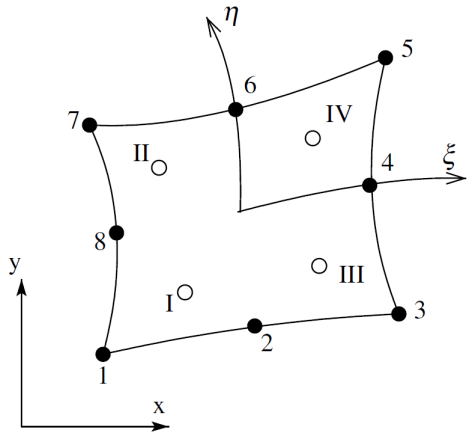


Fig. 4.3. The eight-node element and its four second-order Gaussian stations.

The geometry interpolation can be written as

$$\begin{aligned} x(\xi,\eta) &= \sum_{i=1}^{8} N_i(\xi,\eta) x_i \\ y(\xi,\eta) &= \sum_{i=1}^{8} N_i(\xi,\eta) y_i \end{aligned} \tag{147}$$

where (x_i, y_i) are the co-ordinates of node i, $i = 1, \ldots, 8$, and $N_i(\xi,\eta)$ its shape function given by: for $-1 \leq \xi \leq 1$, $-1 \leq \eta \leq 1$,

$$\begin{aligned}
N_1(\xi,\eta) &= \frac{1}{4}(1-\xi)(1-\eta)(-1-\xi-\eta)\\
N_2(\xi,\eta) &= \frac{1}{2}(1-\xi^2)(1-\eta)\\
N_3(\xi,\eta) &= \frac{1}{4}(1+\xi)(1-\eta)(-1+\xi-\eta)\\
N_4(\xi,\eta) &= \frac{1}{2}(1+\xi)(1-\eta^2)\\
N_5(\xi,\eta) &= \frac{1}{4}(1+\xi)(1+\eta)(-1+\xi+\eta)\\
N_6(\xi,\eta) &= \frac{1}{2}(1-\xi^2)(1+\eta)\\
N_7(\xi,\eta) &= \frac{1}{4}(1-\xi)(1+\eta)(-1-\xi+\eta)\\
N_8(\xi,\eta) &= \frac{1}{2}(1-\xi)(1-\eta^2)
\end{aligned} \tag{148}$$

In order to achieve the general applicability, an isoparametric finite element formulation is adopted, which interpolates the co-ordinates and element displacements using the same shape functions. The displacement field interpolation is hence expressed as:

$$[\delta](x,y) = \sum_{i=1}^{8} N_i(\xi,\eta)\,[\delta_i] \tag{149}$$

where $[\delta_i]$ is the value of the $6n-1$ generalized displacement vector at node i.

Using the compatibility conditions (134) and the following derivation rules for the interpolation functions:

$$\begin{aligned}
\frac{\partial N_i}{\partial x} &= \frac{\partial N_i}{\partial \xi}\frac{\partial \xi}{\partial x} + \frac{\partial N_i}{\partial \eta}\frac{\partial \eta}{\partial x},\\
\frac{\partial N_i}{\partial y} &= \frac{\partial N_i}{\partial \xi}\frac{\partial \xi}{\partial y} + \frac{\partial N_i}{\partial \eta}\frac{\partial \eta}{\partial y},
\end{aligned} \tag{150}$$

one can explicitly express the generalized strain vector as:

$$[E](x,y) = \sum_{i=1}^{8} [B_i](\xi,\eta)\,[\delta_i] \tag{151}$$

where $[B_i]$ is of dimension $(12n-4)\times(6n-1)$.

4.3.3 Element stiffness matrix and nodal forces

Inserting (149) and (151) into the weak formulation of the problem (146), and restricting the integration over the considered element ω^e, it is found that the strain energy stored in the element is:

$$W^e = \sum_{i=1}^{8}\sum_{j=1}^{8}\frac{1}{2}\int_{\omega^e}[\delta_i]^T[B_i]^T[D]\left[B_j\right]\left[\delta_j\right]\,dxdy = \sum_{i=1}^{8}\sum_{j=1}^{8}\frac{1}{2}[\delta_i]^T\left[K_{ij}^e\right]\left[\delta_j\right]$$

where the element stiffness matrix $\left[K_{ij}^e\right]$ is given by:

$$\left[K_{ij}^e\right] = \int_{\omega^e}[B_i]^T[D]\left[B_j\right]\,dxdy,$$

and that the work of the external forces in the element ω^e is:

$$\sum_{i=1}^{8} [\delta_i]^T [F_i^e]$$

where the element nodal force $\left[F_i^e\right]$ is given by:

$$[F_i^e] = \int_{\omega^e} N_i [F] + [B_i]^T [D] \left[E^P\right] dxdy$$

By assembling all the element stiffness matrices and all the element nodal forces, and by taking into account the kinematic boundary conditions, a system of linear equations is obtained the solution of which is the vector of the nodal d.o.f. From the latter, the corresponding strain and stresses can be deduced from, respectively, equations (151) and (145).

In appendix A.2, matrices and equations of *SCLS1* model are detailed.

4.3.4 *MPFEAP* code description

MPFEAP (MultiParticle Finite Element Analysis Program) is an in-house code of the Laboratoire Navier which has been developed during the last years. It was initially dedicated to find a Finite Element solution of the *LS1* model. The code is written using standard Fortran 77 and is a development of the program MEF presented in (Dhatt and Touzot, 1984). The program *MPFEAP* uses text files for data input and results output can be visualized using GID program described in (CIMNE and GID). A new version of *MPFEAP* has been written. It calculates the Finite Element solution of the new *SCLS1* model described above.

4.4 Examples and numerical results

In this part, comparisons are made between *LS1*, enhanced *LS1*, *SCLS1*, enhanced *SCLS1* and full 3D FE models in order to assess the performances of the new model. The 3D FE calculations are performed with the commercial *ABAQUS* software. The new verison of the *MPFEAP* code is used for *SCLS1* and enhanced *SCLS1* models, while the old version of *MPFEAP* described in (Nguyen and Caron, 2006) is used for *LS1* and enhanced *LS1* models. Two different case studies on a $(90°, 0°, 90°)$ laminate under uniaxial tension are considered: the interlaminar shear stress is first studied at a straight free-edge and then, the stress distribution is studied in the vicinity of a circular hole situated at the plate's center. The material properties are as in (Wang and Crossman, 1977b) and (Pagano and Pipes, 1970).

For the first and third layer, the thickness is $e_1 = e_3$ =1mm, the fiber orientation is 90° and the elastic constants are:
E_1 = 140 GPa, $E_2 = E_3$ = 15 GPa,
$G_{12} = G_{13} = G_{23}$ = 5.85 GPa,
$\nu_{12} = \nu_{13} = \nu_{23}$ = 0.21.
where 1, 2 and 3 refer , respectively, to the fiber, transverse, and thickness direction as shown in Fig. 4.4.

For the layer 2, the thickness is e_2 =0.8mm, the fiber orientation is 0° and the elastic constants are:
E_1 = 160 GPa, $E_2 = E_3$ = 8.5 GPa,
$G_{12} = G_{13}$ = 4.1 GPa, G_{23} = 2.8 GPa,
$\nu_{12} = \nu_{13}$ = 0.33 , ν_{23} = 0.5.

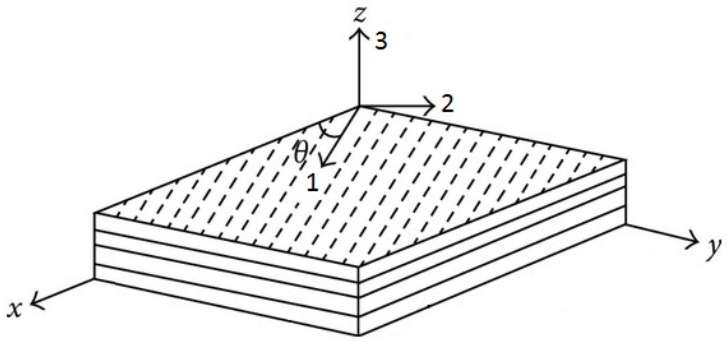


Fig. 4.4. Description of fiber orientation axes and angle.

4.4.1 Straight free-edge

The laminate under consideration is a plate with a length of $2l$ and a width of $2b$ respectively in the x and y directions (Fig. 4.5). The thickness of the laminate following z direction is equal to $2h = 2e_1 + e_2$ and the middle plane of the plate is located at z=0. Uniform displacements $\pm\Delta$ in the x direction are imposed at the edges $x = \pm l$ while the other edges remain free. The applied strain in the x axis direction is $\Delta/l = 0.05$. The dimension of $2b$ is set to 56mm, hence the slenderness ratio b/h is 20, whereas the plate is assumed to be so long in the x direction ($l >> b$) that the stress, strain components are independent of the x-coordinate far from the ends $x = \pm l$. As a consequence, instead of modeling the whole plate, it is sufficient to use only one 3D finite element in the x direction, the size of this element in the x axis direction being irrelevant.

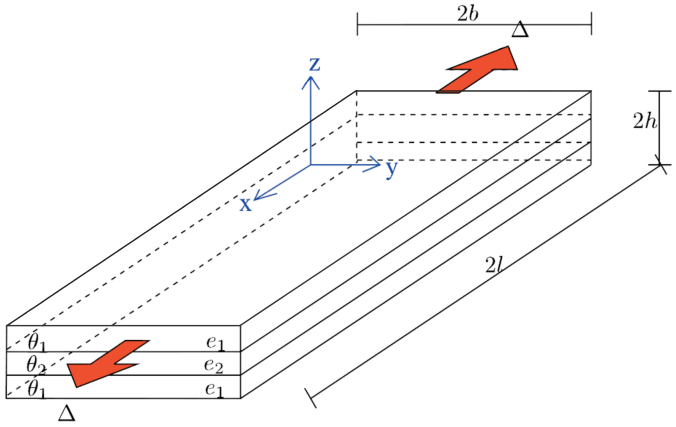


Fig. 4.5. Laminate geometry, imposed displacements and coordinate system.

It is well-known that, in this configuration, the normal stress σ_{33} is singular at the 90°/0° interface near the free edges, while the shear stress σ_{23} is null at the free edges and highly concentrated in the vicinity of these edges. Hence, it is a real challenge for numerical methods to capture the shear stress distribution near the free edges.

4.4.1.1 3D FE Discretization

The commercial ABAQUS software has been used with C3D8R element (3D, 8-node, linear, isoparametric element with reduced integration). In order to obtain accurate results, a very strong mesh refinement is applied near the free edges and at the interfaces between layers (see Fig. 4.6).

Element sizes in y and z axis follow geometric progressions and the smallest elements are located at the intersection of the free edges with the interfaces between layers. The smallest element size in the y axis direction is set to $Y = 0.71\mu m$. Let Z be the smallest element size in the z axis direction. The following table 4.1 shows, for different values of Z, the maximum value σ_{23}^{max-} (resp. σ_{23}^{max+}) of the shear stress σ_{23} taken at the interface $90°/0°$ in the $90°$ layer (resp. in the $0°$ layer) and its value σ_{23}^{ed-} (resp. σ_{23}^{ed+}) taken at the intersection of the free edge with the $90°/0°$ interface in the $90°$ layer (resp. in the $0°$ layer).

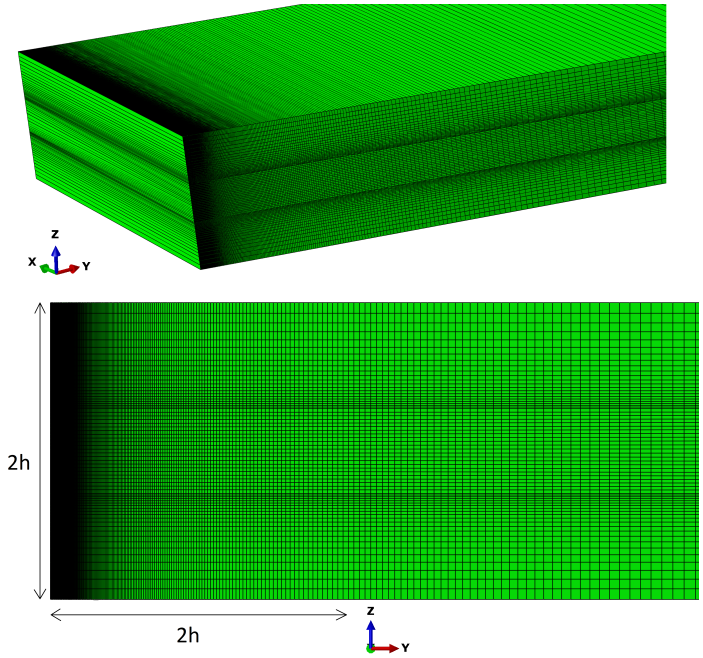


Fig. 4.6. Finite Element model of the laminate - 3D model (top); mesh in the yz plane (bottom).

Z(μm)	150	80	10	7.5	4	1	0.71
$\sigma_{23}^{max-}(MPa)$	63.15	69.74	80.81	81.77	83.61	86.76	87.63
$\sigma_{23}^{max+}(MPa)$	49.37	58.47	75.66	77.13	79.81	84.13	84.95
$\sigma_{23}^{ed-}(MPa)$	1.036	0.966	9.536	15.035	23.222	48.327	54.997
$\sigma_{23}^{ed+}(MPa)$	-0.104	1.577	3.084	6.206	10.934	29.68	35.896

Tab. 4.1. 3D Finite Element results for $Y = 0.71\mu m$ and various values of Z

It is seen that as Z decreases, σ_{23}^{max-} and σ_{23}^{max+} increase, and σ_{23}^{ed-} and σ_{23}^{ed+} depart from the theoretical value (zero). We consider that the values of σ_{23}^{ed-} and σ_{23}^{ed+} are both acceptable for $Z = 7.5\mu m$.

4.4.1.2 *LS1* and *SCLS1* discretization

For *LS1* and *SCLS1* models, element size in the y axis direction follows geometric progression with the smallest element size located near free edges. In Fig. 4.7 and 4.8, we plot the distribution of the interlaminar shear stresses σ_{23} at the $90°/0°$ interface for the non refined *SCLS1* model with two different mesh refinements: $Y = 250\mu m$ for a total of 100×1 mesh and $Y = 40\mu m$ for a total

of 350×1 mesh. We have found that the results are actually completely coincident for the mesh size varying from $Y = 40\mu m$ for a total of 350×1 mesh to $Y = 0.71\mu m$ for a total of 13050×1 mesh. Hence, only the stress distributions of the 100×1 mesh and the 350×1 mesh are represented in Fig. 4.7 and 4.8.

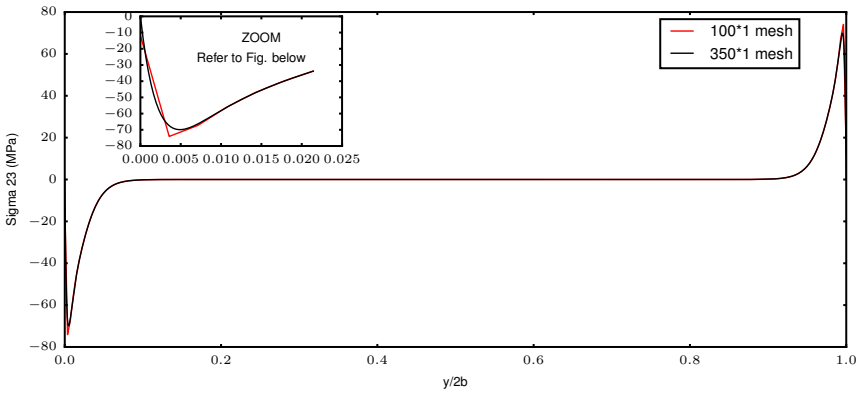


Fig. 4.7. Distribution of the interlaminar shear stress σ_{23} predicted by the non refined *SCLS1* model for two finite element meshes.

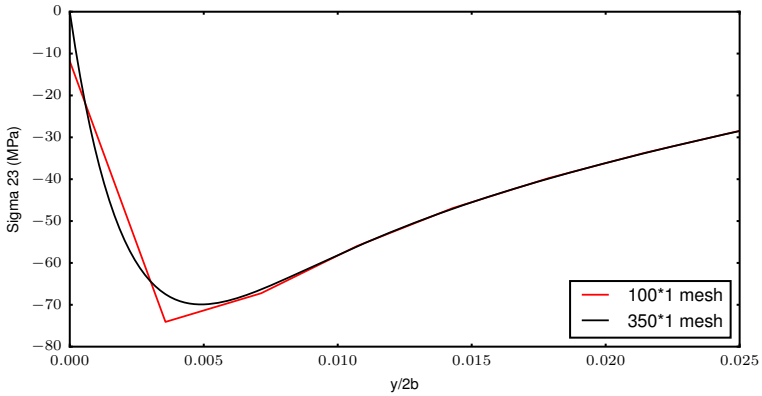


Fig. 4.8. Zoom near the free edge on the distribution of the interlaminar shear stress σ_{23} predicted by the non refined *SCLS1* model for two finite element meshes.

4.4.1.3 Comparison between non refined *SCLS1*, non refined *LS1* and 3D FE models

The non refined *LS1* and *SCLS1* models with $Y = 40\mu m$ discretization are compared to the 3D FE with ($Y = 0.71\mu m, Z = 7.5\mu m$) discretization. These three models give identical stress distributions except near the free edges. In Fig. 4.9, we plot a zoom of the distribution of the interlaminar shear stresses σ_{23} near the free edge. Here, EF^- (resp. EF^+) is the shear stress σ_{23} taken at the interface 90°/0° in the 90° layer (resp. in the 0° layer). Note that the *SCLS1* and 3D FE models reproduce correctly the free-edge boundary condition $\sigma_{23} = 0$, whereas the *LS1* model does not. On the other side, *SCLS1* and 3D FE models do not predict the same maximum value of the interlaminar shear stress. This is due to the lack of sufficient discretization in the thickness (z axis) of the non refined *SCLS1* model.

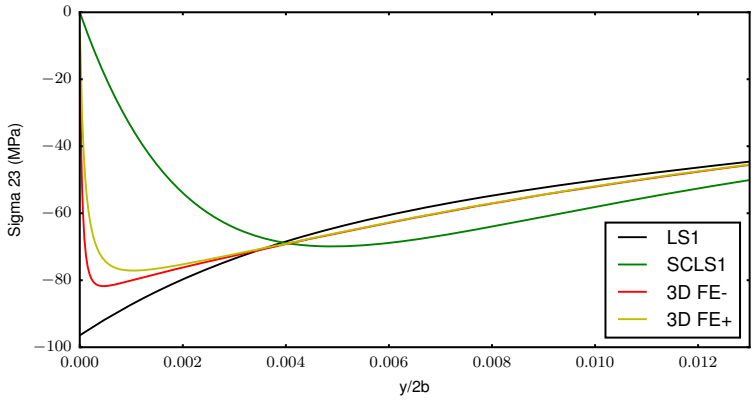


Fig. 4.9. Zoom near the free edge on the distribution of the interlaminar shear stress σ_{23} predicted by the non refined *LS1* model with $Y = 40\mu m$, the non refined *SCLS1* model with $Y = 40\mu m$ and the 3D finite element model with $(Y = 0.71\mu m, Z = 7.5\mu m)$.

4.4.1.4 Comparison between non refined *SCLS1* and refined *SCLS1* models

Now, the refined *SCLS1* model with $Y = 0.71\mu m$ discretization is considered. Recall that there are two additional parameters in this model: p, the number of mathematical layers per physical layer, and the ratio R of the physical layer thickness to the smallest mathematical layer thickness in this physical layer, this ratio being the same for all the physical layers. Choosing $R = 10$, so $h_{min} = 80\mu m$ in layer 2, a parametric study on p has been performed. It can be seen in Fig. 4.10 that the convergence is quickly reached for $p \geq 3$.

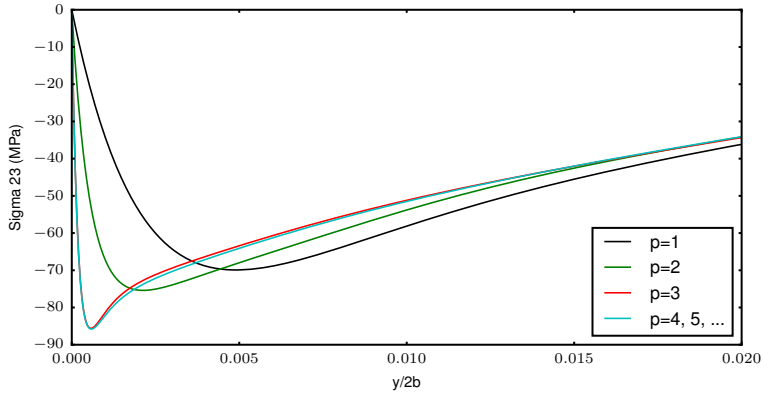


Fig. 4.10. Zoom near the free edge on the distribution of the interlaminar shear stress σ_{23} predicted by the refined *SCLS1* model with $Y = 0.71\mu m$, for $e_2/h_{min} = 10$ and different values of p, the number of mathematical layers per physical layer.

4.4.1.5 Parametric study of the refined *SCLS1* model

In this section, the influence of both parameters R and p is studied. The considered values for R are 10, 20, 30, 50 and 100 corresponding to the following values in μm for h_{min} in layer 2: 80, 40, 26.67, 16 and 8, respectively. Table 4.2 gives the values of the maximum interlaminar shear stress σ_{23}^{max} predicted by the refined *SCLS1* model with $Y = 0.71\mu m$, and table 4.3 gives σ_{23}^{ed}, the predicted

value at the free edge. It can be seen that for fixed R, the convergence of σ_{23}^{max} always occurs as p is increased, and that the limit value is independent of R with an error less than 4%. Moreover, σ_{23}^{ed} is clearly negligible when compared to σ_{23}^{max}.

	$p=3$	$p=4$	$p=5$	$p=6$
$h_{min}=80\mu m$	85.6	85.8	-	-
$h_{min}=40\mu m$	85.71	87.07	87.26	-
$h_{min}=26.67\mu m$	84.91	87.24	87.89	-
$h_{min}=16\mu m$	83.29	86.81	88.49	88.56
$h_{min}=8\mu m$	80.47	85.31	89.03	89.26

Tab. 4.2. $\sigma_{23}^{max}(MPa)$ predicted by the refined *SCLS1* model with $Y=0.71\mu m$ for various values of h_{min} in layer 2 and p.

	$p=3$	$p=4$	$p=5$	$p=6$
$h_{min}=80\mu m$	0.051	0.053	-	-
$h_{min}=40\mu m$	0.146	0.152	0.158	-
$h_{min}=26.67\mu m$	0.284	0.292	0.303	-
$h_{min}=16\mu m$	0.655	0.683	0.713	0.729
$h_{min}=8\mu m$	2.087	2.184	2.276	2.322

Tab. 4.3. $\sigma_{23}^{ed}(MPa)$ predicted by the refined *SCLS1* model with $Y=0.71\mu m$ for various values of h_{min} in layer 2 and p.

4.4.1.6 Parametric study of the refined *LS1* model

For the seek of completeness, the same parametric study is conducted for the refined *LS1* model with $Y=0.71\mu m$. In this case, σ_{23}^{ed} and σ_{23}^{max} are coincident. It can be seen in Table 4.4 that, for fixed R, the convergence of σ_{23}^{max} always occurs as p is increased, and that the limit value is independent of R. However, this value is 7% higher than the limit value of σ_{23}^{max} predicted by the refined *SCLS1* model.

	$p=3$	$p=4$	$p=5$	$p=6$	$p=7$	$p=8$
$h_{min}=80\mu m$	94.67	97.13	98.13	98.35	-	-
$h_{min}=40\mu m$	91.77	95.39	97.55	97.95	-	-
$h_{min}=26.67\mu m$	89.94	94.14	97.09	97.62	98.02	-
$h_{min}=16\mu m$	87.81	92.37	96.38	97.04	97.67	97.88
$h_{min}=8\mu m$	84.85	89.88	95.2	96.07	97.03	97.34

Tab. 4.4. $\sigma_{23}^{max}=\sigma_{23}^{ed}(MPa)$ predicted by the refined *LS1* model with $Y=0.71\mu m$ for various values of h_{min} in layer 2 and p.

4.4.1.7 Comparison between refined *SCLS1*, refined *LS1* and 3D FE models

In Fig. 4.11, we plot the distribution of the interlaminar shear stresses σ_{23} at the $90°/0°$ interface between layer 1 and 2 as predicted by 3D FE with $Y=0.71\mu m$ and $Z=7.5\mu m$ and by the refined

LS1 and *SCLS1* models with $h_{min} = 8\mu m$ in layer 2 and $p = 6$. It is seen that the refined *SCLS1* model is the only model which can efficiently predict both stress concentration and free boundary conditions. It must be highlighted that even if the refined *LS1* model doesn't comply with the exact 3D boundary conditions at free edges, nevertheless, it predicts the stress concentration with good accuracy (8%).

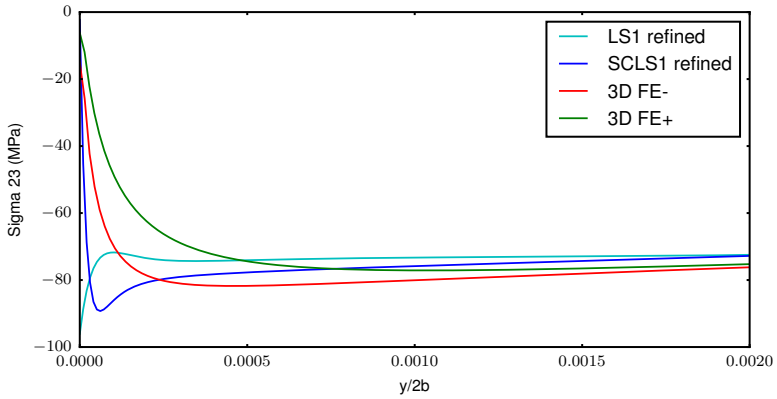


Fig. 4.11. Zoom near the free edge on the distribution of the interlaminar shear stress σ_{23} predicted by the refined *LS1* and *SCLS1* models with $Y = 0.71\mu m$, $h_{min} = 8\mu m$ in layer 2 and $p = 6$, and by the 3D FE model with $(Y = 0.71\mu m, Z = 7.5\mu m)$.

4.4.1.8 Discussion

According to the results obtained, we can conclude that the refined *SCLS1* model converges to the exact value for both σ_{23}^{ed} and σ_{23}^{max}. It predicts 89Mpa for σ_{23}^{max}. On the other hand, the 3D FE model cannot predict correctly both values of σ_{23}^{ed} and σ_{23}^{max} for the same refinement, see Table 1. By construction, the refined *LS1* model cannot predict the exact value of σ_{23}^{ed}. It predicts 97MPa for σ_{23}^{max} which is 8% higher than the value computed using the refined *SCLS1* model. Hence, the *LS1* model can be considered as an acceptable approximation of the *SCLS1* model, and thus of the 3D model, for the prediction of stress concentration near free edge boundaries.
When considering the n umber of degrees of freedom (d.o.f.), the refined *SCLS1* model has $6np - 1$ degrees of freedom in the thickness direction to be compared to $3N$ where N is the number of FE nodes in the thickness direction. In the present study, N was up to 200. So, for p=3 (n=3 in our case), the d.o.f. for the refined *SCLS1* model are more than 10 times less than for Abaqus 3D FE.
In the light of the foregoing, it can be concluded that the best mesh strategy for the refined models is as follows:

- For the refined *SCLS1* model, we recommend using $p = 3$ and $R = e/hmin = 10$.
- For the refined *LS1* model, we recommend using $p = 4$ and $R = e/hmin = 10$.

4.4.2 Notched laminate under uniaxial tension

A $(90°, 0°, 90°)$ laminate with a circular hole is subjected to a tensile load. The mechanical properties of the plies are the same as in the previous section, whereas the thicknesses are all equal: $e_1 = e_2 = e_3 = e$ =1mm. In Fig. 4.12 this three-ply laminate with a thickness of $3e$, a length of $2l = 160e$ and a width of $2b = 80e$ is shown. The central circular hole has a radius $R = 10e$. The

ends of the laminate are subjected to a uniform displacement in the x direction so that an overall uniaxial longitudinal strain ϵ_{xx}=0.0375 is applied in the x direction. The reference $Oxyz$ is located at the center of the hole.

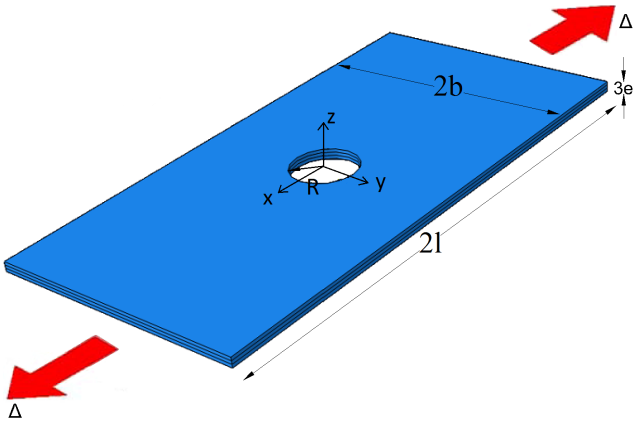


Fig. 4.12. Notched laminate plate geometry and loading.

Because of the symmetries of the problem, only one quarter of the laminate was analyzed using the non refined *SCLS1* model with ($X = Y = 2.5\mu m$) discretization, the refined *SCLS1* model with ($X = Y = 2.5\mu m, h_{min} = 100\mu m, p = 3$) discretization and compared to the 3D FE calculations with ($X = Y = 2.5\mu m, Z = 100\mu m$) and ($X = Y = 2.5\mu m, Z = 50\mu m$) discretization. Fig. 4.13 shows the interlaminar shear stress σ_{13} for $y = 0$ at the interface $90°/0°$ between the first and second layers as predicted by 3D FE with $Z = 100\mu m$ and by the *SCLS1* models. Here, FE^- (resp. FE^+) corresponds to the shear stress σ_{13} taken at the interface $90°/0°$ in the $90°$ layer (resp. in the $0°$ layer); Fig. 4.14 and 4.15 show the interlaminar shear stress σ_{23} for $x = 0$ at the interface $90°/0°$ between the first and second layers, with the same convention for FE^- and FE^+, as predicted by 3D FE with $Z = 100\mu m$ and by the *SCLS1* models. Fig. 4.16 shows the σ_{23} predicted near the free boundary by the *SCLS1* models and the 3D FE with $Z = 50\mu m$.

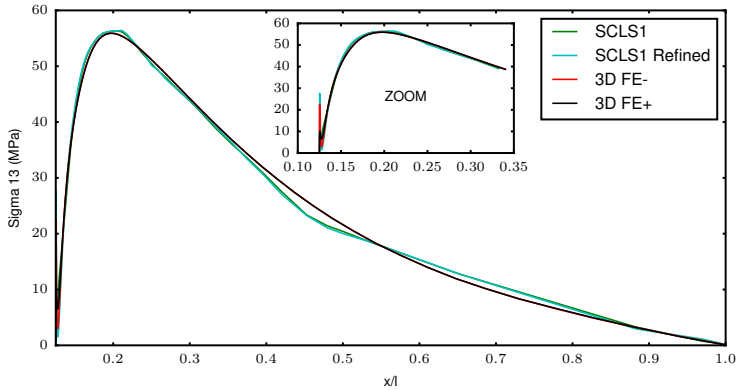


Fig. 4.13. Shear stress σ_{13} at the interface between layers 1 and 2 for y=0 predicted by the non refined *SCLS1* and the refined *SCLS1* model with ($X = Y = 2.5\mu m$, $h_{min} = 100\mu m$ and $p = 3$), and by the 3D FE model with ($X = Y = 2.5\mu m, Z = 100\mu m$).

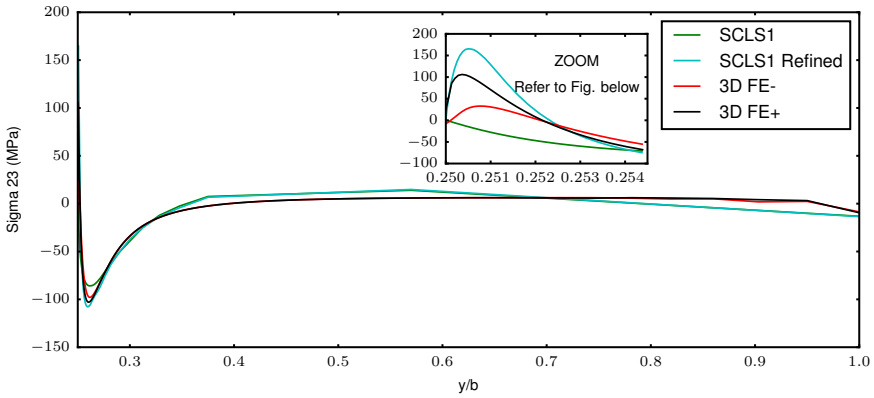


Fig. 4.14. Shear stress σ_{23} at the interface between layers 1 and 2 for $x = 0$ predicted by the non refined *SCLS1* and the refined *SCLS1* model with ($X = Y = 2.5\mu m$, $h_{min} = 100\mu m$ and $p = 3$), and by the 3D FE model with ($X = Y = 2.5\mu m, Z = 100\mu m$)..

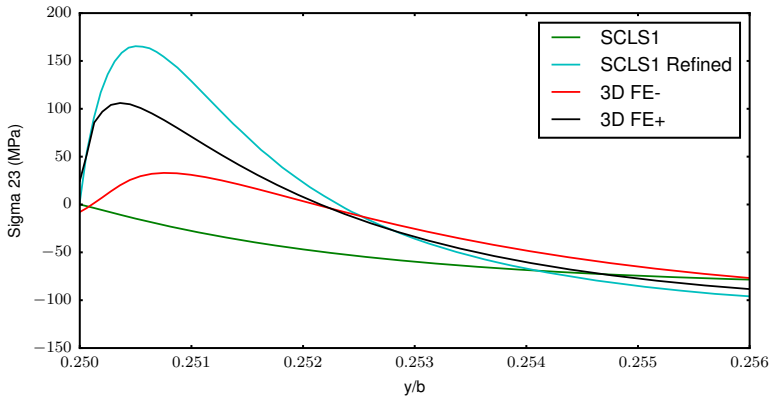


Fig. 4.15. Zoom on the shear stress σ_{23} at the interface between layers 1 and 2 for $x = 0$ predicted by the non refined *SCLS1* and the refined *SCLS1* model with ($X = Y = 2.5\mu m$, $h_{min} = 100\mu m$ and $p = 3$), and by the 3D FE model with ($X = Y = 2.5\mu m, Z = 100\mu m$).

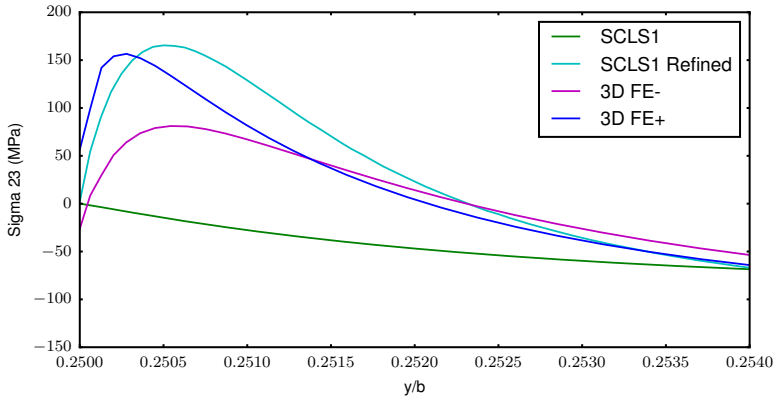


Fig. 4.16. Zoom on the shear stress σ_{23} at the interface between layers 1 and 2 for $x = 0$ predicted by the non refined *SCLS1* and the refined *SCLS1* model with ($X = Y = 2.5\mu m$, $h_{min} = 100\mu m$ and $p = 3$), and by the 3D FE model with ($X = Y = 2.5\mu m, Z = 50\mu m$).

Here again, as for the case of the un-notched plate, it is seen that the 3D FE model is unable to capture accurately and effectively both the boundary condition and the stress concentration at a free edge. On the other hand, this example shows the robustness of the refined *SCLS1* model on a complex example such as the considered notched plate. When comparing the number of d.o.f, a ratio of 9 is found between Abaqus 3D FE and the refined *SCLS1* model leading to a drastic reduction in the computational time.

4.5 Conclusion

In this chapter, a new statically compatible layerwise stress model for laminated plates, called *SCLS1*, has been presented. To the authors' knowledge, this is the first fully static model dedicated to multilayered plates which can exactly comply with the 3D equilibrium equations and the 3D free edge boundary conditions. As in the *LS1* model initially proposed by Naciri et al. (1998), the laminated plate is considered as a superposition of Reissner plates coupled by interlaminar stresses which are considered as generalized stresses. However, the divergences of the interlaminar transverse shears are introduced as additional generalized stresses in the proposed *SCLS1* model. Also, a *refined* version of the new model is obtained by introducing several mathematical layers per physical layer. The refined version is specially designed to effectively capture both stress concentration and boundary conditions at the free edges.

In addition to that, an eight-node isoparametric quadrilateral finite element with $6np - 1$ d.o.f. at each nodal point has been formulated. Here, n is the number of physical layers and p is the number of mathematical layers per physical layer. In this finite element formulation, the interlaminar stresses are given in a straightforward manner using the constitutive equations, and without any post-processing work. The existing finite element program called *MPFEAP* initially dedicated to the *LS1* model has been updated in order to take into account the new model. The proposed new finite element program presents a 2D type data structure that provides several advantages over a conventional 3D finite element model: simplified input data, ease of results' interpretation and big reduction of calculation time.

The performances of this new element have been compared with those of a standard 3D FE for free edge problems including geometric effects (presence of a hole). It has been demonstrated that the proposed *SCLS1* model has better performances because it is able to reproduce both stress

concentration and free edge boundary conditions at a reduced cost. Another important point is that, although the refined *LS1* model cannot comply with the exact free edge boundary conditions, it can still be considered as an acceptable approximation of the *SCLS1* model, and thus of the 3D model, for the prediction of stress concentration near free edge boundaries.

Following the ideas of Chataigner et al. (2011), Duong et al. (2011) and Alvarez-Lima et al. (2012) it would be interesting to extend the *SCLS1* model to the case where the interfaces between the layers are not perfectly bonded showing an elastic or inelastic behavior.

CHAPTER 5

Finite Element of the Bending-Gradient theory for laminated plates

5.1 Introduction

The Kirchhoff-Love plate model (classical plate theory), is easy to implement and gives good estimates when the plate slenderness ratio L/h (h: plate thickness and L: plate span) is large enough (thin plate). In this theory, the contribution of out-of-plane stress components to the stress energy is neglected. However, for thick plates, transverse shear stresses have an increasing influence on the plate deflection.

Two main approaches can be found in the literature to handle the effects of transverse shear stresses: asymptotic approaches and axiomatic approaches. The first class of approaches is mainly based on asymptotic expansions in the small parameter h/L (Caillerie and Nedelec, 1984; Lewinski, 1991a,b,c). However, higher-order terms yield only intricate Kirchhoff-Love plate equations and no distinction between relevant fields and unknowns is made. Such asymptotic approaches lead to models which are not simple to implement.

The second main class of approaches is based on assuming *ad hoc* displacement or stress 3D fields and it seems easier to implement in finite element codes. These models can be Equivalent Single Layer (ESL) or Layerwise. Equivalent Single Layer models treat the whole laminate as an equivalent homogeneous plate. However, when dealing with laminated plates, these models lead systematically to discontinuous transverse shear stress distributions through the thickness as indicated by Reddy (1989). The most refined Equivalent Single Layers models, which finally led to continuous shear stress are zigzag models (Ambartsumian, 1960; Whitney, 1969; Carrera, 2003). However, these models are restricted to some specific configurations (symmetry of the plate and material constitutive equation) and involve higher-order partial derivative equations than the simple Reissner-Mindlin plate model. The difficulties encountered with transverse stress fields instigated the consideration of layerwise models. In layerwise models, all plate degrees of freedom are introduced in each layer of the laminate and continuity conditions are enforced between layers. Layerwise models lead to correct estimates of local 3D fields. However, their main drawback is that they involve a number of degrees of freedom proportional to the number of layers than Equivalent Single Layer models. The limitation is immediately pointed out with functionally graded materials, where the plate constituent's properties vary continuously through the thickness Nguyen et al. (2008).

On the other hand, the extension of the original approach from Reissner (Reissner, 1944) based on the principle of minimum complementary energy led to an Equivalent Single Layer plate theory called the Generalized-Reissner theory (Lebée and Sab, 2016a,b). This theory takes accurately into account shear effects and does not require any specific constitutive material symmetry. When suitably simplified, this theory becomes the Bending-Gradient theory already introduced in (Lebée and Sab, 2011a,b, 2012; Sab and Lebée, 2015; Lebée and Sab, 2017). Here, shear forces are replaced by the gradient of the bending moment $\underset{\sim}{\boldsymbol{R}} = \underset{\sim}{\boldsymbol{M}} \otimes \underset{\sim}{\boldsymbol{\nabla}}$. Hence, the Bending-Gradient theory belongs to the family of higher-order gradient models. The mechanical meaning of the $\underset{\sim}{\boldsymbol{R}}$ was identified as self-equilibrated static unknowns associated to warping functions in addition to conventional shear forces. The kinematic degrees of freedom (d.o.f.) are the deflection, and the generalized rotation which may have between two and six d.o.f.. Indeed, it was also established that, when the plate is homogeneous, then the original theory from Reissner (Reissner, 1944) with three d.o.f. (one deflection, two rotations) is fully recovered.

Since the Bending-Gradient model is not yet implemented in a finite element program and its usage is limited to analytical solutions (Lebée and Sab, 2011b) used to calculate 1D models with some restrictions; for this, the purpose of this chapter is to present the finite element implementation of the Bending-Gradient model and to show its accuracy when compared to Bending-Gradient analytical model, ABAQUS composite layup plate finite element model, and *LS1* finite element

layerwise model (Naciri et al., 1998; Carreira et al., 2002; Diaz Diaz et al., 2002; Caron et al., 2006; Nguyen and Caron, 2006; Dallot and Sab, 2008; Saeedi et al., 2012a,b, 2013a,b; Lerpiniere et al., 2014; Baroud et al., 2016)
This chapter is organized as follows. The notations of (Sab and Lebée, 2015)) and the definition of the 3D problem for the laminated plate are introduced in Sections 5.2 and 5.3, respectively. Then, the Bending-Gradient theory is recalled in Section 5.4, and Section 5.5 discusses the finite element discretization of the Bending-Gradient model and its implementation. Finally, Section 5.6 presents numerical comparisons between the different models. The chapter ends with a conclusion which synthesizes the main results.

5.2 Notations

First, second, third, fourth and sixth order tensors are respectively noted: $\underline{\boldsymbol{X}}$, $\underline{\underline{\boldsymbol{X}}}$, $\underline{\underline{\underline{\boldsymbol{X}}}}$, $\underline{\underline{\underline{\underline{\boldsymbol{X}}}}}$ and $\underline{\underline{\underline{\underline{\underline{\boldsymbol{X}}}}}}$. When dealing with plates, both 2D and 3D tensors are utilized. Thus, $\underline{\boldsymbol{X}}$ will denote a 3D vector or a 2D vector depending on its nature. The same convention is used for higher-order tensors. When using tensor components, the indices typeface specify the dimension: (X_{ij}) denotes the 3D tensor $\underline{\boldsymbol{X}}$ with Latin indices $i, j, k.. = 1, 2, 3$ while $(X_{\alpha\beta})$ denotes the 2D tensor $\underline{\boldsymbol{X}}$ with Greek indices $\alpha, \beta, \gamma.. = 1, 2$.

The transpose operation ${}^T\bullet$ is applied to any order tensors as follows: $({}^TX)_{\alpha\beta\ldots\psi\omega} = X_{\omega\psi\ldots\beta\alpha}$. Five symbols are defined: $(\cdot)$, $(:)$, $(\vdots)$, $(\vdots\!\vdots)$, and $(\vdots\!\vdots\!\vdots)$ for contraction on, respectively, one, two, three, four and six indices. By convention, the closest indices are successively summed together in contraction products. Thus, $\underline{\underline{\underline{\underline{\boldsymbol{X}}}}} \vdots \underline{\underline{\underline{\boldsymbol{Y}}}} = (X_{\alpha\beta\gamma\delta\lambda\mu}Y_{\mu\lambda\delta})$ and $\underline{\underline{\underline{\boldsymbol{X}}}} \cdot \underline{\boldsymbol{Y}} = (X_{\alpha\beta\gamma}Y_{\gamma})$ is different from $\underline{\boldsymbol{Y}} \cdot \underline{\underline{\underline{\boldsymbol{X}}}} = (Y_{\alpha}X_{\alpha\beta\gamma})$.

The identity for 2D vectors is $\underline{\boldsymbol{\delta}} = (\delta_{\alpha\beta})$ where $\delta_{\alpha\beta}$ is Kronecker symbol ($\delta_{\alpha\beta} = 1$ if $\alpha = \beta$, $\delta_{\alpha\beta} = 0$ otherwise). The identity for 2D symmetric fourth order tensors is $\underline{\underline{\underline{\underline{\boldsymbol{i}}}}}$ where

$$i_{\alpha\beta\gamma\delta} = \frac{1}{2}\left(\delta_{\alpha\gamma}\delta_{\beta\delta} + \delta_{\alpha\delta}\delta_{\beta\gamma}\right).$$

The reader may check this:

$$\underline{\underline{\underline{\underline{\boldsymbol{i}}}}} : \underline{\underline{\underline{\underline{\boldsymbol{i}}}}} = \underline{\underline{\underline{\underline{\boldsymbol{i}}}}}, \quad \underline{\underline{\underline{\underline{\boldsymbol{i}}}}} \vdots \underline{\underline{\underline{\underline{\boldsymbol{i}}}}} = \frac{3}{2}\underline{\boldsymbol{\delta}}, \quad \underline{\underline{\underline{\underline{\boldsymbol{i}}}}} \vdots\!\vdots \underline{\underline{\underline{\underline{\boldsymbol{i}}}}} = 3,$$

and that

$$\underline{\underline{\underline{\underline{\boldsymbol{i}}}}} \cdot \underline{\underline{\underline{\underline{\boldsymbol{i}}}}} = (i_{\alpha\beta\gamma\delta}i_{\delta\epsilon\zeta\eta})$$

is a sixth-order tensor.

The gradient of a scalar field X writes $X\underline{\boldsymbol{\nabla}} = (X_{,\beta})$ and the gradient of vectors or higher order tensor fields writes $\underline{\boldsymbol{X}} \otimes \underline{\boldsymbol{\nabla}} = (X_{\alpha\beta,\gamma})$, where $\otimes$ is the dyadic product. The divergence of a vector field, a second-order tensor field, a third-order tensor field is noted $\underline{\boldsymbol{X}} \cdot \underline{\boldsymbol{\nabla}} = (X_{\alpha,\alpha})$, $\underline{\underline{\boldsymbol{X}}} \cdot \underline{\boldsymbol{\nabla}} = (X_{\alpha\beta,\beta})$ and $\underline{\underline{\underline{\boldsymbol{X}}}} \cdot \underline{\boldsymbol{\nabla}} = (X_{\alpha\beta\gamma,\gamma})$, respectively.

5.3 The 3D Problem

The plate occupies the volume $\Omega = \omega \times \mathcal{T}$ where ω denotes the mid-plane surface of the plate and $\mathcal{T} = \left]-\frac{t}{2}, \frac{t}{2}\right[$ is the transverse coordinate range. The boundary, $\partial\Omega$, is decomposed into three parts (Figure 5.1):

$$\begin{gathered} \partial\Omega = \partial\Omega_{\text{lat}} \cup \partial\Omega_3^+ \cup \partial\Omega_3^-, \\ \text{with} \quad \partial\Omega_{\text{lat}} = \partial\omega \times \mathcal{T} \quad \text{and} \quad \partial\Omega_3^{\pm} = \omega \times \left\{\pm\frac{t}{2}\right\}. \end{gathered} \tag{152}$$

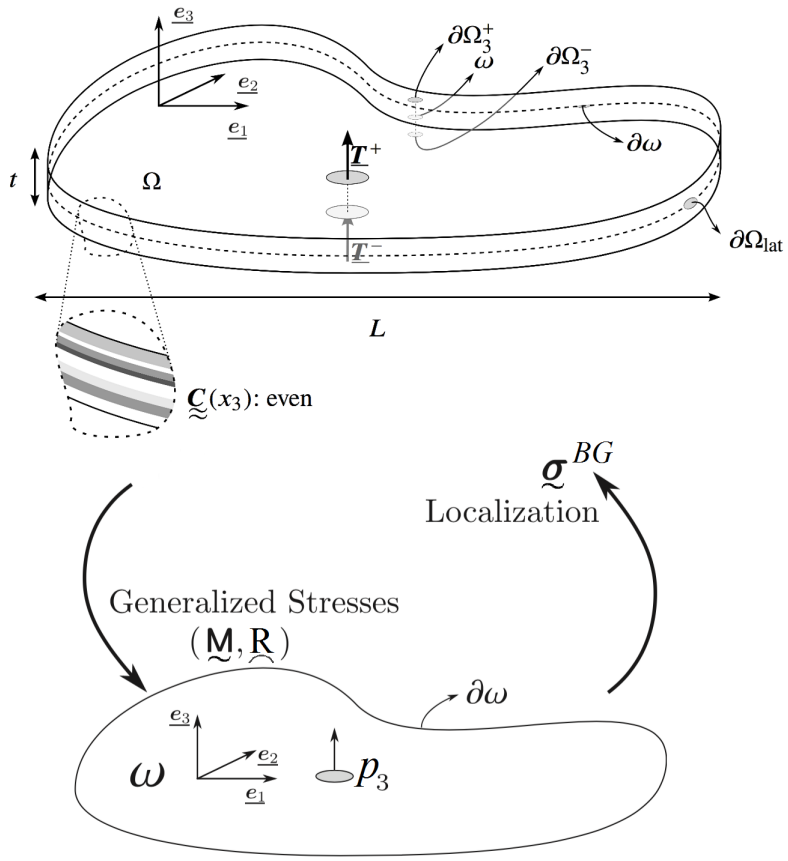


Fig. 5.1. Plate Configuration.

It is assumed that the local stiffness tensor $\underset{\approx}{\boldsymbol{C}} = \left(C_{ijkl}\right)$ at every point $\underline{\boldsymbol{x}} = (x_1, x_2, x_3)$ of Ω is invariant with respect to translations in the (x_1, x_2) plane and is an even function of x_3: $\underset{\approx}{\boldsymbol{C}}(x_3) = \underset{\approx}{\boldsymbol{C}}(-x_3)$. The plate is clamped on its lateral boundary $\partial\Omega_{\text{lat}}$ (other conditions can be also considered) and is loaded with the out-of-plane distributed surface force along x_3 direction on both faces $\partial\Omega_3^{\pm}$:

$$\underline{\boldsymbol{T}}^{\pm}(x_1, x_2) = \frac{1}{2} p_3(x_1, x_2)\, \underline{\boldsymbol{e}}_3$$

The compliance tensor $\underset{\approx}{\boldsymbol{S}} = \underset{\approx}{\boldsymbol{C}}^{-1}$ follows the classical symmetries of linear elasticity and it is positive definite. In addition, monoclinic symmetry is assumed:

$$S_{3\alpha\beta\gamma} = S_{\alpha 333} = 0. \tag{153}$$

Thus, the constitutive equation writes as:

$$\begin{aligned} \varepsilon_{\alpha\beta} &= S_{\alpha\beta\gamma\delta}\sigma_{\delta\gamma} + S_{\alpha\beta 33}\sigma_{33}, \\ \varepsilon_{\alpha 3} &= 2S_{\alpha 3\beta 3}\sigma_{3\beta}, \\ \varepsilon_{33} &= S_{33\alpha\beta}\sigma_{\beta\alpha} + S_{3333}\sigma_{33}, \end{aligned} \tag{154}$$

where $\underset{\sim}{\boldsymbol{\sigma}} = \left(\sigma_{ij}\right)$ is the stress tensor and $\underset{\sim}{\boldsymbol{\varepsilon}} = \left(\varepsilon_{ij}\right)$ is the strain tensor. The following notations are needed for the partial compliance tensors:

$$\underset{\approx}{\boldsymbol{S}}^{\sigma} = \left(S_{\alpha\beta\gamma\delta}\right), \quad \underset{\approx}{\boldsymbol{C}}^{\sigma} = \left(\underset{\approx}{\boldsymbol{S}}^{\sigma}\right)^{-1}, \quad \underset{\sim}{\boldsymbol{S}}^{\gamma} = \left(4S_{\alpha 3\beta 3}\right), \quad \underset{\sim}{\boldsymbol{S}}^{\nu} = \left(S_{\alpha\beta 33}\right), \tag{155}$$

where $\underset{\approx}{\boldsymbol{S}}^{\sigma}$ corresponds to plane stress compliance, $\underset{\approx}{\boldsymbol{C}}^{\sigma}$ to plane stress stiffness, $\underset{\sim}{\boldsymbol{S}}^{\gamma}$ to transverse shear compliance and $\underset{\sim}{\boldsymbol{S}}^{\nu}$ is the out-of-plane Poisson coupling.

From the symmetries of the problem it can be established that the 3D solution components $\sigma^{3D}_{\alpha\beta}$, σ^{3D}_{33}, $\varepsilon^{3D}_{\alpha\beta}$, ε^{3D}_{33} and u^{3D}_{α} are odd in x_3 while $\sigma^{3D}_{\alpha 3}$, $\varepsilon^{3D}_{\alpha 3}$ and u^{3D}_{3} are even in x_3. Here, $\underline{\boldsymbol{u}}^{3D}$ is the 3D displacement.

5.4 The Bending-Gradient theory

The Generalized-Reissner theory of Lebée and Sab (2016a,b) is the extension to laminates of Reissner theory for homogeneous and isotropic plates (Reissner, 1944). However, it involves fifteen kinematic degrees of freedom (d.o.f.), eight of them being related only to out-of-plane Poisson's distortion, not really interesting for engineering applications. Thus, the main idea of the Bending-Gradient plate theory, initially introduced in (Lebée and Sab, 2011a,b), is to simplify the Generalized-Reissner theory by setting these eight d.o.f. to zero and to neglect the contribution of the normal stress σ_{33} in the plate model constitutive equation.

5.4.1 The Bending-Gradient equations

Hence, the Bending-Gradient theory has only seven d.o.f.: $\left(U_3, \underset{\approx}{\boldsymbol{\Phi}}\right)$ where the scalar U_3 is the out-of-plane displacement of the plate (or deflection) and $\underset{\approx}{\boldsymbol{\Phi}} = \left(\Phi_{\alpha\beta\gamma}\right)$ with $\Phi_{\alpha\beta\gamma} = \Phi_{\beta\alpha\gamma}$ is the generalized third-order rotation tensor.

The generalized stresses in the Bending-Gradient theory are the bending moment tensor $\underset{\sim}{\boldsymbol{M}} = \left(M_{\alpha\beta}\right)$, with $M_{\alpha\beta} = M_{\beta\alpha}$, and the generalized shear force $\underset{\sim}{\boldsymbol{R}} = \left(R_{\alpha\beta\gamma}\right)$ with $R_{\alpha\beta\gamma} = R_{\beta\alpha\gamma}$. In this theory, the 3D stress is approximated by:

$$\underset{\sim}{\boldsymbol{\sigma}}^{\mathrm{BG}} = \begin{cases} \sigma^{\mathrm{BG}}_{\alpha\beta} = s^{M}_{\alpha\beta\gamma\delta}(x_3)\, M_{\delta\gamma}(x_1, x_2), \\ \sigma^{\mathrm{BG}}_{\alpha 3} = s^{R}_{\alpha\beta\gamma\delta}(x_3)\, R_{\delta\gamma\beta}(x_1, x_2), \\ \sigma^{\mathrm{BG}}_{33} = 0. \end{cases} \tag{156}$$

Here, the in-plane stress localization fourth-order tensor $\underset{\approx}{\boldsymbol{s}}^{M}$ related to bending moment $\underset{\sim}{\boldsymbol{M}}$ writes as:

$$\underset{\approx}{\boldsymbol{s}}^{M}(x_3) = x_3 \underset{\approx}{\boldsymbol{C}}^{\sigma}(x_3) : \underset{\approx}{\boldsymbol{D}}^{-1}, \tag{157}$$

where $\underset{\approx}{\boldsymbol{D}} = \left(\left\langle x_3^2 C^{\sigma}_{\alpha\beta\gamma\delta}(x_3)\right\rangle\right)$ is the bending stiffness tensor and the integration through the thickness of the plate is noted:

$$\langle f(x_3)\rangle = \int_{-\frac{t}{2}}^{\frac{t}{2}} f(x_3)\, dx_3.$$

Note that, by definition of $\underset{\approx}{\boldsymbol{s}}^{M}$, we have $M_{\alpha\beta} = \left\langle x_3 \sigma^{\mathrm{BG}}_{\alpha\beta}\right\rangle$.

The transverse shear stress localization fourth-order tensor $\underset{\approx}{\boldsymbol{s}}^{R}$ related to the generalized shear force $\underset{\sim}{\boldsymbol{R}}$ writes as:

$$\underset{\approx}{\boldsymbol{s}}^{R}(x_3) = \int_{-\frac{t}{2}}^{x_3} -\underset{\approx}{\boldsymbol{s}}^{M}(y_3)\, dy_3. \tag{158}$$

Because some components of $\underset{\sim}{\underset{\frown}{\boldsymbol{R}}}$ might not contribute to $\sigma^{\mathrm{BG}}_{\alpha 3}$, it will be assumed that $\underset{\sim}{\underset{\frown}{\boldsymbol{R}}}$ belongs to subspace $\underset{\sim}{\underset{\frown}{\boldsymbol{\mathcal{S}}}}$ defined as:

$$\underset{\sim}{\underset{\frown}{\boldsymbol{\mathcal{S}}}} = \mathrm{Span}\left\{\underset{\sim}{\underset{\frown}{\boldsymbol{s}}}^{M_1}(x_3), \underset{\sim}{\underset{\frown}{\boldsymbol{s}}}^{M_2}(x_3), \quad \forall x_3 \in \mathcal{T}\right\}, \tag{159}$$

where

$$s^{M_1}_{\alpha\beta\gamma}(x_3) = s^{M}_{1\gamma\beta\alpha}(x_3) \quad \text{and} \quad s^{M_2}_{\alpha\beta\gamma}(x_3) = s^{M}_{2\gamma\beta\alpha}(x_3). \tag{160}$$

Indeed, it can be shown that if $\underset{\sim}{\underset{\frown}{\underset{\approx}{\boldsymbol{s}}}}^{R}(x_3) : \underset{\sim}{\underset{\frown}{\boldsymbol{R}}} = 0$ for all x_3, then $\underset{\sim}{\underset{\frown}{\boldsymbol{R}}}$ belongs necessarily to the orthogonal of $\underset{\sim}{\underset{\frown}{\boldsymbol{\mathcal{S}}}}$. Hence, restricting $\underset{\sim}{\underset{\frown}{\boldsymbol{R}}}$ to $\underset{\sim}{\underset{\frown}{\boldsymbol{\mathcal{S}}}}$ ensures that $\sigma^{\mathrm{BG}}_{\alpha 3} = 0$ for all x_3 is equivalent to $\underset{\sim}{\underset{\frown}{\boldsymbol{R}}} = 0$.

Note that the conventional shear force $Q_\alpha = \left\langle \sigma^{\mathrm{BG}}_{\alpha 3} \right\rangle$ is derived from the generalized shear force through:

$$\underset{\sim}{\boldsymbol{Q}} = \underset{\sim}{\underset{\frown}{\underset{\approx}{\boldsymbol{i}}}} \vdots \underset{\sim}{\underset{\frown}{\boldsymbol{R}}} \quad \text{or} \quad Q_\alpha = R_{\alpha\beta\beta}. \tag{161}$$

Another important property is that the dimension of subspace $\underset{\sim}{\underset{\frown}{\boldsymbol{\mathcal{S}}}}$ is at least two. Indeed, let us introduce the following two-dimensional subspace:

$$\underset{\sim}{\underset{\frown}{\boldsymbol{\mathcal{S}}}}^{(i)} = \mathrm{Span}\left\{\underset{\sim}{\underset{\frown}{\boldsymbol{i}}}^{(1)}, \underset{\sim}{\underset{\frown}{\boldsymbol{i}}}^{(2)}\right\} \tag{162}$$

where

$$\underset{\sim}{\underset{\frown}{\boldsymbol{i}}}^{(1)} = \left(i^{(1)}_{\alpha\beta\gamma}\right) = \left(i_{1\gamma\beta\alpha}\right) \text{ and } \underset{\sim}{\underset{\frown}{\boldsymbol{i}}}^{(2)} = \left(i^{(2)}_{\alpha\beta\gamma}\right) = \left(i_{2\gamma\beta\alpha}\right) \tag{163}$$

Then, we have $\underset{\sim}{\underset{\frown}{\boldsymbol{\mathcal{S}}}}^{(i)} \subset \underset{\sim}{\underset{\frown}{\boldsymbol{\mathcal{S}}}}$. This means that the two independent tensors $\underset{\sim}{\underset{\frown}{\boldsymbol{i}}}^{(1)}$ and $\underset{\sim}{\underset{\frown}{\boldsymbol{i}}}^{(2)}$ are in $\underset{\sim}{\underset{\frown}{\boldsymbol{\mathcal{S}}}}$.

The equilibrium equations of the Bending-Gradient theory write:

$$\begin{cases} \underset{\sim}{\underset{\frown}{\boldsymbol{R}}} - \underset{\sim}{\underset{\frown}{\underset{\approx}{\boldsymbol{P}}}}^{S} \vdots \left(\underset{\sim}{\boldsymbol{M}} \otimes \underset{\sim}{\boldsymbol{\nabla}}\right) = \underset{\sim}{\boldsymbol{0}}, & \text{(164a)} \\ \left(\underset{\sim}{\underset{\frown}{\underset{\approx}{\boldsymbol{i}}}} \vdots \underset{\sim}{\underset{\frown}{\boldsymbol{R}}}\right) \cdot \underset{\sim}{\boldsymbol{\nabla}} + p_3 = 0. & \text{(164b)} \end{cases}$$

where the sixth-order tensor $\underset{\sim}{\underset{\frown}{\underset{\approx}{\boldsymbol{P}}}}^{S}$ is the projection operator on $\underset{\sim}{\underset{\frown}{\boldsymbol{\mathcal{S}}}}$.

The Bending-Gradient generalized strains, dual of $\left(\underset{\sim}{\boldsymbol{M}}, \underset{\sim}{\underset{\frown}{\boldsymbol{R}}}\right)$, are $\left(\underset{\sim}{\boldsymbol{\chi}}, \underset{\sim}{\underset{\frown}{\boldsymbol{\Gamma}}}\right)$ where $\underset{\sim}{\boldsymbol{\chi}}$ is the curvature second order tensor and $\underset{\sim}{\underset{\frown}{\boldsymbol{\Gamma}}} \in \underset{\sim}{\underset{\frown}{\boldsymbol{\mathcal{S}}}}$ is the generalized shear strain third order tensor. These generalized strains derive from the generalized displacements $\left(U_3, \underset{\sim}{\underset{\frown}{\boldsymbol{\Phi}}}\right)$ using the following compatibility conditions on ω:

$$\begin{cases} \underset{\sim}{\boldsymbol{\chi}} = \underset{\sim}{\underset{\frown}{\boldsymbol{\Phi}}} \cdot \underset{\sim}{\boldsymbol{\nabla}}, \\ \underset{\sim}{\underset{\frown}{\boldsymbol{\Gamma}}} = \underset{\sim}{\underset{\frown}{\boldsymbol{\Phi}}} + \underset{\sim}{\underset{\frown}{\underset{\approx}{\boldsymbol{i}}}} \cdot \underset{\sim}{\boldsymbol{\nabla}} U_3, \end{cases} \tag{165}$$

and the clamped boundary conditions on $\partial\omega$:

$$\underset{\sim}{\underset{\frown}{\boldsymbol{\Phi}}} \cdot \underset{\sim}{\boldsymbol{n}} = \underset{\sim}{\boldsymbol{0}} \quad \text{and} \quad U_3 = 0 \quad \text{on} \quad \partial\omega. \tag{166}$$

Note that other boundary conditions can be considered. Refer to Appendix B.1.

The condition $\underset{\sim}{\underset{\frown}{\boldsymbol{\Gamma}}} \in \underset{\sim}{\underset{\frown}{\boldsymbol{\mathcal{S}}}}$ is actually equivalent to $\underset{\sim}{\underset{\frown}{\boldsymbol{\Phi}}} \in \underset{\sim}{\underset{\frown}{\boldsymbol{\mathcal{S}}}}$ since $\underset{\sim}{\underset{\frown}{\underset{\approx}{\boldsymbol{i}}}} \cdot \underset{\sim}{\boldsymbol{\nabla}} U_3$ is in $\underset{\sim}{\underset{\frown}{\boldsymbol{\mathcal{S}}}}^{(i)}$, and $\underset{\sim}{\underset{\frown}{\boldsymbol{\mathcal{S}}}}^{(i)}$ is a subset of $\underset{\sim}{\underset{\frown}{\boldsymbol{\mathcal{S}}}}$. This means that the kinematic degrees of freedom of the Bending-Gradient model are the deflection U_3 and n generalized rotations, n being the dimension of $\underset{\sim}{\underset{\frown}{\boldsymbol{\mathcal{S}}}}$ with $2 \leq n \leq 6$ depending on the 3D elastic properties of the laminated plate.

The Bending-Gradient constitutive equations write as:

$$\begin{cases} \underset{\sim}{\chi} = \underset{\approx}{\boldsymbol{d}} : \underset{\sim}{\boldsymbol{M}}, \\ \underset{\sim}{\boldsymbol{\Gamma}} = \underset{\approx}{\boldsymbol{h}} \vdots \underset{\sim}{\boldsymbol{R}}. \end{cases} \tag{167}$$

where $\underset{\approx}{\boldsymbol{d}} = \underset{\approx}{\boldsymbol{D}}^{-1}$ is the bending compliance tensor and $\underset{\approx}{\boldsymbol{h}}$ is the shear compliance tensor given by:

$$\underset{\approx}{\boldsymbol{h}} = \left\langle {}^{T}\underset{\approx}{\boldsymbol{s}}^{R} . \underset{\sim}{\boldsymbol{S}}^{\gamma} . \underset{\approx}{\boldsymbol{s}}^{R} \right\rangle \tag{168}$$

It should be emphasized that $\underset{\approx}{\boldsymbol{h}}$ is symmetric and positive but it is definite only on the subspace $\underset{\sim}{\boldsymbol{S}}$. In other words, $\underset{\sim}{\boldsymbol{S}}$ is the orthogonal of the kernel of $\underset{\approx}{\boldsymbol{h}}$. When the kernel of $\underset{\approx}{\boldsymbol{h}}$ is zero, then $\underset{\sim}{\boldsymbol{S}}$ coincides with the whole space of third-order tensors which are symmetric with respect to their two first subscripts.

5.4.2 Localization

Once the solution of the Bending-Gradient plate equations (164-167) is found, it is possible to derive the 3D stress and displacements fields, respectively approximated by $\underset{\sim}{\boldsymbol{\sigma}}^{BG}$ given by (156), and by $\underline{\boldsymbol{u}}^{BG}$ as follows:

$$u_3^{\mathrm{BG}} = U_3^{\mathrm{BG}} + w^M_{\alpha\beta} M_{\beta\alpha} \quad \text{and} \quad u_\alpha^{\mathrm{BG}} = -x_3 U^{\mathrm{BG}}_{3,\alpha} + u^R_{\alpha\beta\gamma\delta} R_{\delta\gamma\beta}. \tag{169}$$

Here, the transverse Poisson's effect is carried by the bending moment $\underset{\sim}{\boldsymbol{M}}$:

$$w^M_{\alpha\beta}(x_3) = \int_R -y_3 \frac{C_{33\alpha\beta}}{C_{3333}} dy_3. \tag{170}$$

where $\int_R f$ denotes the unique primitive of the function f of the x_3 coordinate such:

$$\left\langle \frac{1}{3} \underset{\approx}{\boldsymbol{s}}^{R} \vdots \underset{\approx}{\boldsymbol{i}} \int_R f \right\rangle = 0. \tag{171}$$

The in-plane warping related to transverse shear effects are carried by the generalized shear force $\underset{\sim}{\boldsymbol{R}}$:

$$u^R_{\alpha\beta\gamma\delta}(x_3) = \int_0^{x_3} \left(S^{\gamma}_{\alpha\eta} s^R_{\eta\beta\gamma\delta} - \delta_{\alpha\beta} w^M_{\gamma\delta} \right) dy_3. \tag{172}$$

5.4.3 The case of homogeneous plates

In this case, the Reissner plate equations are retrieved. Indeed, $\underset{\sim}{\boldsymbol{S}}$ is completely generated by $\underset{\sim}{\boldsymbol{i}}^{(1)}$ and $\underset{\sim}{\boldsymbol{i}}^{(2)}$. It is hence equal to $\underset{\sim}{\boldsymbol{S}}^{(i)}$ of dimension two and we have the following equations:

$$\underset{\sim}{\boldsymbol{R}} = \frac{2}{3} \underset{\approx}{\boldsymbol{i}} \cdot \underline{\boldsymbol{Q}}, \tag{173}$$

and

$$\underset{\approx}{\boldsymbol{P}}^{S} \vdots \left(\underset{\sim}{\boldsymbol{M}} \otimes \underline{\boldsymbol{\nabla}} \right) = \frac{2}{3} \underset{\approx}{\boldsymbol{i}} \vdots \left(\underset{\sim}{\boldsymbol{M}} \cdot \underline{\boldsymbol{\nabla}} \right) \tag{174}$$

Thus, the equilibrium equations (164) become:

$$\begin{cases} \underline{Q} - \underset{\sim}{M} \cdot \underline{\nabla} = 0\,, & \text{(175a)} \\ \underline{Q} \cdot \underline{\nabla} + p_3 = 0. & \text{(175b)} \end{cases}$$

Moreover, in the case of homogeneous plates, the generalized shear compliance writes:

$$\underset{\approx}{h} = \frac{6}{5t}\underset{\approx}{i} \cdot \underset{\sim}{S}^{\gamma} \cdot \underset{\approx}{i} \tag{176}$$

The tensor $\underset{\sim}{\Phi}$ being in $\underset{\sim}{S} = \underset{\sim}{S}^{(i)}$, it has necessarily the following form:

$$\underset{\sim}{\Phi} = \underset{\approx}{i} \cdot \underline{\phi}, \tag{177}$$

where $\underline{\phi} = (\phi_\alpha)$ is the rotation vector. The corresponding constitutive law becomes:

$$\underset{\sim}{\Gamma} = \underset{\sim}{\Phi} + \underset{\approx}{i} \cdot \underline{\nabla} U_3 = \underset{\approx}{i} \cdot \left(\underline{\phi} + \underline{\nabla} U_3\right) = \underset{\approx}{h} \vdots \underset{\sim}{R}, \tag{178}$$

or equivalently:

$$\underline{\phi} + \underline{\nabla} U_3 = \frac{6}{5t}\underset{\sim}{S}^{\gamma} \cdot \underline{Q}. \tag{179}$$

5.4.4 Variational formulation

Like 3D elasticity problems, the Bending-Gradient problem can be given a variational framework. For this purpose, the set KC^{BG} of kinematically compatible Bending-Gradient displacements are defined as:

$$KC^{\mathrm{BG}} = \left\{\left(U_3, \underset{\sim}{\Phi}\right)(x_1, x_2),\ \ \underset{\sim}{\Phi} \in \underset{\sim}{S},\ \ (x_1, x_2) \in \omega, \quad \text{such that (166)}\right\}, \tag{180}$$

The theorem of the minimum of the potential energy says that the solution $\left(U_3^{\mathrm{BG}}, \underset{\sim}{\Phi}^{\mathrm{BG}}\right)$ of the Bending-Gradient problem achieves the minimum of the potential energy functional P^{BG} defined on KC^{BG} as:

$$P^{\mathrm{BG}} = \int_\omega w^{\mathrm{BG}}\left(\underset{\sim}{\chi}, \underset{\sim}{\Gamma}\right) d\omega - \int_\omega p_3 U_3 d\omega, \tag{181}$$

where $\underset{\sim}{\chi}$ and $\underset{\sim}{\Gamma}$ are the generalized strains associated to the generalized displacements $\left(U_3, \underset{\sim}{\Phi}\right)$ through the compatibility equations (165) and w^{BG} is the Bending-Gradient strain energy density function given by:

$$w^{\mathrm{BG}}\left(\underset{\sim}{\chi}, \underset{\sim}{\Gamma}\right) = \frac{1}{2}\underset{\sim}{\chi} : \underset{\approx}{D} : \underset{\sim}{\chi} + \frac{1}{2}{}^{T}\underset{\sim}{\Gamma} \vdots \underset{\approx}{H} \vdots \underset{\sim}{\Gamma}. \tag{182}$$

where the generalized shear stiffness tensor $\underset{\approx}{H}$ is the Moore-Penrose pseudo inverse of $\underset{\approx}{h}$. Indeed, as mentioned before, the shear compliance tensor $\underset{\approx}{h}$ is symmetric and positive but it is definite only on subspace $\underset{\sim}{S}$. The corresponding generalized shear strain energy density is defined for all $\underset{\sim}{\Gamma}$ in $\underset{\sim}{S}$ as:

$$\frac{1}{2}{}^{T}\underset{\sim}{\Gamma} \vdots \underset{\approx}{H} \vdots \underset{\sim}{\Gamma} = \max_{\underset{\sim}{R} \in \underset{\sim}{S}} \left\{ {}^{T}\underset{\sim}{R} \vdots \underset{\sim}{\Gamma} - \frac{1}{2}{}^{T}\underset{\sim}{R} \vdots \underset{\approx}{h} \vdots \underset{\sim}{R} \right\}$$

5.4.5 Kelvin Notations

In this section, we introduce Kelvin notation in order to turn contraction products into conventional matrix products. Brackets [•] are used to denote that a tensor is considered in a matrix form. Thus, [•] is a linear operator reallocating tensor components. For instance, the bending moment and curvature second-order tensors are reallocated in a vector form:

$$\left[\underset{\sim}{\boldsymbol{M}}\right] = \begin{pmatrix} M_{11} \\ M_{22} \\ \sqrt{2}M_{12} \end{pmatrix}, \quad \left[\underset{\sim}{\boldsymbol{\chi}}\right] = \begin{pmatrix} \chi_{11} \\ \chi_{22} \\ \sqrt{2}\chi_{12} \end{pmatrix}, \tag{183}$$

as well as the fourth-order compliance tensor $\underset{\approx}{\boldsymbol{d}}$ is reallocated in a matrix form so that constitutive equation $\underset{\sim}{\boldsymbol{\chi}} = \underset{\approx}{\boldsymbol{d}} : \underset{\sim}{\boldsymbol{M}}$ becomes a vector-matrix product:

$$\left[\underset{\approx}{\boldsymbol{d}}\right] = \begin{pmatrix} d_{1111} & d_{2211} & \sqrt{2}d_{1211} \\ d_{2211} & d_{2222} & \sqrt{2}d_{1222} \\ \sqrt{2}d_{1211} & \sqrt{2}d_{1222} & 2d_{1212} \end{pmatrix} \tag{184}$$

The same Kelvin notation applied to $\underset{\approx}{\boldsymbol{C}}^{\sigma}$ can be used for the computation of $\underset{\approx}{\boldsymbol{D}}$ as:

$$\left[\underset{\approx}{\boldsymbol{D}}\right] = \left\langle x_3^2 \left[\underset{\approx}{\boldsymbol{C}}^{\sigma}(x_3)\right] \right\rangle, \tag{185}$$

Similar procedure is applied to shear variables and the corresponding constitutive equation. Shear unknowns are reallocated in the following vector form:

$$\left[\underset{\frown}{\boldsymbol{R}}\right] = \begin{pmatrix} R_{111} \\ R_{221} \\ \sqrt{2}R_{121} \\ R_{112} \\ R_{222} \\ \sqrt{2}R_{122} \end{pmatrix}, \quad \left[\underset{\frown}{\boldsymbol{\Gamma}}\right] = \begin{pmatrix} \Gamma_{111} \\ \Gamma_{221} \\ \sqrt{2}\Gamma_{121} \\ \Gamma_{112} \\ \Gamma_{222} \\ \sqrt{2}\Gamma_{122} \end{pmatrix}, \quad \left[\underset{\frown}{\boldsymbol{\Phi}}\right] = \begin{pmatrix} \Phi_{111} \\ \Phi_{221} \\ \sqrt{2}\Phi_{121} \\ \Phi_{112} \\ \Phi_{222} \\ \sqrt{2}\Phi_{122} \end{pmatrix}. \tag{186}$$

The shear constitutive sixth-order tensors $\underset{\frown}{\boldsymbol{h}}$ and $\underset{\frown}{\boldsymbol{H}}$ are turned into a 6×6 matrix of the form:

$$\left[\underset{\frown}{\boldsymbol{f}}\right] = \begin{pmatrix} f_{111111} & f_{111122} & \sqrt{2}f_{111121} & f_{111211} & f_{111222} & \sqrt{2}f_{111221} \\ f_{221111} & f_{221122} & \sqrt{2}f_{221121} & f_{221211} & f_{221222} & \sqrt{2}f_{221221} \\ \sqrt{2}f_{121111} & \sqrt{2}f_{121122} & 2f_{121121} & \sqrt{2}f_{121211} & \sqrt{2}f_{121222} & 2f_{121221} \\ f_{112111} & f_{112122} & \sqrt{2}f_{112121} & f_{112211} & f_{112222} & \sqrt{2}f_{112221} \\ f_{222111} & f_{222122} & \sqrt{2}f_{222121} & f_{222211} & f_{222222} & \sqrt{2}f_{222221} \\ \sqrt{2}f_{122111} & \sqrt{2}f_{122122} & 2f_{122121} & \sqrt{2}f_{122211} & \sqrt{2}f_{122222} & 2f_{122221} \end{pmatrix} \tag{187}$$

Finally, when using Kelvin matrices components, the same typeface is used. The number of indexes indicates unambiguously whether it is the tensor component or the matrix component: f_{222221} is the tensor component of $\underset{\frown}{\boldsymbol{f}}$ and $f_{56} = \sqrt{2}f_{222221}$ is the matrix component of $\left[\underset{\frown}{\boldsymbol{f}}\right]$. For more details about the computation of matrix $\left[\underset{\frown}{\boldsymbol{h}}\right]$, refer to Appendix B.2.

5.5 Finite element discretization of the Bending-Gradient model

This section deals with the displacement finite element formulation of the Bending-Gradient model presented in the previous section. An eight-node isoparametric quadrilateral element with 7 d.o.f. at

each nodal point will be presented. This element has the same interpolation functions as the *LS1* and *SCLS1* 's element which was integrated in the *MPFEAP* in-house software (Nguyen and Caron, 2006; Baroud et al., 2016).

5.5.1 Methods for calculating shear stiffness matrix

As noted before, the shear compliance tensor $\underset{\approx}{\underset{\approx}{\boldsymbol{h}}}$ is symmetric and positive. It is definite on the subspace $\underset{\approx}{\boldsymbol{S}}$ whose dimension is between two and six depending on the elastic properties of the laminated plate. Hence, there are two possible numerical strategies to handle this problem. The first one is to introduce the constraint $\underset{\approx}{\boldsymbol{\Phi}} \in \underset{\approx}{\boldsymbol{S}}$ when the dimension of $\underset{\approx}{\boldsymbol{S}}$ is strictly lower than six. The second one, which will be adopted in our computer code, is to regularize the problem by adding a small strictly positive compliance to the diagonal components of the exact shear compliance tensor $\underset{\approx}{\underset{\approx}{\boldsymbol{h}}}$, which becomes the inversible compliance $\underset{\approx}{\underset{\approx}{\boldsymbol{h}}}^{\xi}$:

$$\left[\underset{\approx}{\underset{\approx}{\boldsymbol{H}}}^{\xi}\right] = \left[\underset{\approx}{\underset{\approx}{\boldsymbol{h}}}^{\xi}\right]^{-1} = \left(\left[\underset{\approx}{\underset{\approx}{\boldsymbol{h}}}\right] + \frac{\sqrt{\sum h^2_{\alpha\beta\gamma\delta\zeta\eta}}}{10^{\xi}}\left[\underset{\approx}{\underset{\approx}{\boldsymbol{I}}}\right]\right)^{-1} \tag{188}$$

where $\alpha = \beta = \gamma = \delta = \zeta = \eta = 1, 2$, $\left[\underset{\approx}{\underset{\approx}{\boldsymbol{I}}}\right]$ is the identity 6×6-matrix and ξ is a positive parameter.

A parametric study was conducted in which the exponent ξ was varied between 1 and 8. We recommend to set $\xi = 3$ unless in the case of a concentrated loading force applied on a thick plate (slenderness ratio L/h between 3 and 10) for which $\xi = 5$ is recommended.

5.5.2 Geometry and displacement interpolations

The representation of the geometry of the finite element mesh is based on a quadrilateral master element defined in the (ξ, η) space as shown in Fig. 5.2.

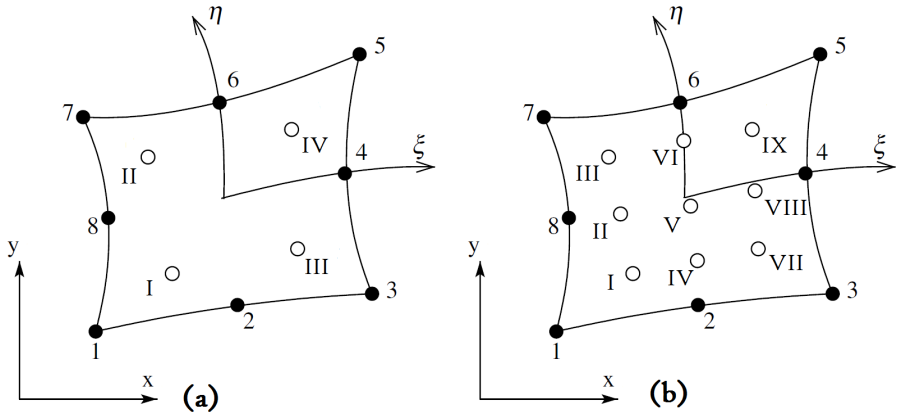


Fig. 5.2. The eight-node element a) with four second-order Gaussian stations b) with nine second-order Gaussian stations.

The geometry interpolation can be written as

$$\begin{aligned} x(\xi,\eta) &= \sum_{i=1}^{8} N_i(\xi,\eta)x_i \\ y(\xi,\eta) &= \sum_{i=1}^{8} N_i(\xi,\eta)y_i \end{aligned} \tag{189}$$

where (x_i, y_i) are the co-ordinates of node i, $i = 1, \ldots, 8$, and $N_i(\xi,\eta)$ its shape function given by: for $-1 \le \xi \le 1$, $-1 \le \eta \le 1$,

$$\begin{aligned} N_1(\xi,\eta) &= \frac{1}{4}(1-\xi)(1-\eta)(-1-\xi-\eta) \\ N_2(\xi,\eta) &= \frac{1}{2}(1-\xi^2)(1-\eta) \\ N_3(\xi,\eta) &= \frac{1}{4}(1+\xi)(1-\eta)(-1+\xi-\eta) \\ N_4(\xi,\eta) &= \frac{1}{2}(1+\xi)(1-\eta^2) \\ N_5(\xi,\eta) &= \frac{1}{4}(1+\xi)(1+\eta)(-1+\xi+\eta) \\ N_6(\xi,\eta) &= \frac{1}{2}(1-\xi^2)(1+\eta) \\ N_7(\xi,\eta) &= \frac{1}{4}(1-\xi)(1+\eta)(-1-\xi+\eta) \\ N_8(\xi,\eta) &= \frac{1}{2}(1-\xi)(1-\eta^2) \end{aligned} \tag{190}$$

In order to achieve the general applicability, an isoparametric finite element formulation is adopted, which interpolates the co-ordinates and element displacements using the same shape functions.

5.5.3 Weak formulation of the Bending-Gradient model

- The generalized displacement vector $[\delta]$ is defined as:

$$[\delta]^T = \Big(\underbrace{U_3,\ \Phi_{111},\ \Phi_{221},\ \sqrt{2}\Phi_{121},\ \Phi_{112},\ \Phi_{222},\ \sqrt{2}\Phi_{122}}_{7}\Big),$$

  where $[X]^T$ is the transpose of $[X]$. The displacement field interpolation is hence expressed as:

$$[\delta]\,(x,y) = \sum_{i=1}^{8} N_i(\xi,\eta)\,[\delta_i] \tag{191}$$

  where $[\delta_i]$ is the value of the 7 generalized displacement vector at node i.

- The generalized strain vector $[E]$ defined as:

$$[E]^T = \left(\left[\underset{\sim}{\chi}\right]^T, \left[\underset{\sim}{\Gamma}\right]^T\right)$$

  where the generalized curvature strain vector is:

$$\left[\underset{\sim}{\chi}\right]^T = \Big(\underbrace{\chi_{11},\ \chi_{22},\ \sqrt{2}\chi_{12}}_{3}\Big),$$

and the generalized shear strain vector is:

$$\left[\underset{\sim}{\mathbf{\Gamma}}\right]^T = \Big(\underbrace{\Gamma_{111},\, \Gamma_{221},\, \sqrt{2}\Gamma_{121},\, \Gamma_{112},\, \Gamma_{222},\, \sqrt{2}\Gamma_{122}}_{6}\Big).$$

The expression of these generalized strains (165) may be explicitly written as

$$\begin{cases} \chi_{11} = \dfrac{\partial \Phi_{111}}{\partial x} + \dfrac{\partial \Phi_{112}}{\partial y}, \quad \chi_{22} = \dfrac{\partial \Phi_{221}}{\partial x} + \dfrac{\partial \Phi_{222}}{\partial y}, \\ \chi_{12} = \dfrac{\partial \Phi_{121}}{\partial x} + \dfrac{\partial \Phi_{122}}{\partial y}, \\ \Gamma_{111} = \Phi_{111} + \dfrac{\partial U_3}{\partial x}, \qquad \Gamma_{221} = \Phi_{221}, \\ \Gamma_{121} = \Phi_{121} + \dfrac{\partial U_3}{\partial y}, \qquad \Gamma_{112} = \Phi_{112}, \\ \Gamma_{222} = \Phi_{222} + \dfrac{\partial U_3}{\partial y}, \qquad \Gamma_{122} = \Phi_{122} + \dfrac{\partial U_3}{\partial x}, \end{cases} \tag{192}$$

Using the following derivation rules for the interpolation functions:

$$\begin{aligned} \frac{\partial N_i}{\partial x} &= \frac{\partial N_i}{\partial \xi}\frac{\partial \xi}{\partial x} + \frac{\partial N_i}{\partial \eta}\frac{\partial \eta}{\partial x}, \\ \frac{\partial N_i}{\partial y} &= \frac{\partial N_i}{\partial \xi}\frac{\partial \xi}{\partial y} + \frac{\partial N_i}{\partial \eta}\frac{\partial \eta}{\partial y}, \end{aligned} \tag{193}$$

The strain field interpolation can be written as:

$$\left[\underset{\sim}{\chi}\right] = \sum_{i=1}^{8} \left[B_i^{\chi}\right][\delta_i] = [B_1^{\chi}, \ldots, B_8^{\chi}]\,[\delta] \tag{194}$$

where $\left[B_i^{\chi}\right]$ of dimension 3×7 is defined as:

$$\left[B_i^{\chi}\right] = \begin{bmatrix} 0 & N_{i,x} & 0 & 0 & N_{i,y} & 0 & 0 \\ 0 & 0 & N_{i,x} & 0 & 0 & N_{i,y} & 0 \\ 0 & 0 & 0 & N_{i,x} & 0 & 0 & N_{i,y} \end{bmatrix}, \tag{195}$$

and

$$\left[\underset{\sim}{\mathbf{\Gamma}}\right] = \sum_{i=1}^{8} \left[B_i^{\Gamma}\right][\delta_i] = [B_1^{\Gamma}, \ldots, B_8^{\Gamma}]\,[\delta] \tag{196}$$

where $\left[B_i^{\Gamma}\right]$ of dimension 6×7 is defined as:

$$\left[B_i^{\Gamma}\right] = \begin{bmatrix} N_{i,x} & N_i & 0 & 0 & 0 & 0 & 0 \\ 0 & 0 & N_i & 0 & 0 & 0 & 0 \\ \dfrac{N_{i,y}}{\sqrt{2}} & 0 & 0 & N_i & 0 & 0 & 0 \\ 0 & 0 & 0 & 0 & N_i & 0 & 0 \\ N_{i,y} & 0 & 0 & 0 & 0 & N_i & 0 \\ \dfrac{N_{i,x}}{\sqrt{2}} & 0 & 0 & 0 & 0 & 0 & N_i \end{bmatrix} \tag{197}$$

By assembling $\left[B_i^\chi\right]$ and $\left[B_i^\Gamma\right]$ into $[B_i]$, we obtain:

$$[E] = \sum_{i=1}^{8} [B_i]\,[\delta_i] = [B_1, \ldots, B_8]\,[\delta] \tag{198}$$

- Finally, the generalized stress vector $[\Sigma]$ is defined as:

$$[\Sigma]^T = \left(\left[\underset{\sim}{\Sigma}^\chi\right]^T, \left[\underset{\sim}{\Sigma}^\Gamma\right]^T\right) \tag{199}$$

where

$$\left[\underset{\sim}{\Sigma}^\chi\right]^T = \left(M_{11},\ M_{22},\ \sqrt{2}M_{12}\right). \tag{200}$$

and

$$\left[\underset{\sim}{\Sigma}^\Gamma\right]^T = \left(R_{111},\ R_{221},\ \sqrt{2}R_{121}, R_{112},\ R_{222},\ \sqrt{2}R_{122}\right), \tag{201}$$

With these notations, the Bending-Gradient constitutive equations (167) can be rewritten as:

$$[E] = [S]\,[\Sigma]\,, \quad [\Sigma] = [C]\,[E]\,, \tag{202}$$

where $[S]$ is the generalized compliance matrix and $[C] = [S]^{-1}$ is the generalized stiffness matrix.

5.5.4 Element stiffness matrix and nodal forces

Inserting (198) and (191) into the variational formulation of the problem (181-182), and restricting the integration over the considered element ω^e, it is found that the strain energy stored in the element is:

$$W^e = \sum_{i=1}^{8}\sum_{j=1}^{8} \frac{1}{2}\int_{\omega^e} [\delta_i]^T\,[B_i]^T\,[C]\left[B_j\right]\left[\delta_j\right]\,dxdy = \sum_{i=1}^{8}\sum_{j=1}^{8} \frac{1}{2}\,[\delta_i]^T\left[K_{ij}^e\right]\left[\delta_j\right]$$

where the element stiffness matrix $\left[K_{ij}^e\right]$ is given by:

$$\left[K_{ij}^e\right] = \int_{\omega^e} [B_i]^T\,[C]\left[B_j\right]\,dxdy = \int_{\omega^e} \left(\left[B_i^\chi\right]^T\,[D]\left[B_j^\chi\right] + \left[B_i^\Gamma\right]^T\left[H^\xi\right]\left[B_j^\Gamma\right]\right)\,dxdy,$$

and that the work of the external forces in the element ω^e is:

$$\sum_{i=1}^{8} [\delta_i]^T\,[F_i^e]$$

where the element nodal force $\left[F_i^e\right]$ is given by:

$$[F_i^e] = \int_{\omega^e} N_i\,[F]\,\,dxdy$$

By assembling all the element stiffness matrices and all the element nodal forces, and by taking into account the kinematic boundary conditions, a system of linear equations is obtained the solution of which is the vector of the nodal d.o.f. From the latter, the corresponding strain and stresses can be deduced from, respectively, equations (198) and (202).

5.5.5 Bending-Gradient finite element with selective integration technique

It is well-known that the selective integration technique can be used to avoid shear locking in Reissner-Mindlin finite elements. In order to apply this technique to our model, the idea is to decompose the elasticity shear matrix into two elasticity shear matrices:

$$\left[\underset{\approx}{\boldsymbol{H}}^{\xi}\right] = \left[\underset{\approx}{\boldsymbol{H}}^{s,\xi}\right] + \left[\underset{\approx}{\boldsymbol{H}}^{d,\xi}\right] \tag{203}$$

where the part of the shear energy $\frac{1}{2}{}^{T}\underset{\sim}{\boldsymbol{\Gamma}} : \underset{\approx}{\boldsymbol{H}}^{\xi} : \underset{\sim}{\boldsymbol{\Gamma}}$ associated to matrix $\left[\underset{\approx}{\boldsymbol{H}}^{s,\xi}\right]$ is numerically integrated with four Gauss points while the part associated to matrix $\left[\underset{\approx}{\boldsymbol{H}}^{d,\xi}\right]$ is subjected to full integration with nine Gauss points (or more, the results are the same).

The construction of $\left[\underset{\approx}{\boldsymbol{H}}^{s,\xi}\right]$ and $\left[\underset{\approx}{\boldsymbol{H}}^{d,\xi}\right]$ is as follows: The space generated by all possible $\underset{\approx}{\boldsymbol{\Phi}}$ is orthogonally decomposed, in the sense of the scalar product defined by $\underset{\approx}{\boldsymbol{H}}^{\xi}$, into the subspace $\underset{\sim}{\boldsymbol{S}}^{(i)}$ introduced in (162) which is generated by the $\underset{\approx}{\boldsymbol{\Phi}}$ of the form $\underset{\approx}{\boldsymbol{i}} \cdot \underline{\boldsymbol{\nabla}} U_3$, and its orthogonal counterpart. In order to achieve this orthogonal decomposition, the standard Schmidt orthogonalization technique is used. Using the matrix Kelvin notation, we have:

$$\left[\underset{\approx}{\boldsymbol{i}} \cdot \underline{\boldsymbol{\nabla}} U_3\right] = U_{3,1}\left[\underset{\sim}{\boldsymbol{i}}^{(1)}\right] + U_{3,2}\left[\underset{\sim}{\boldsymbol{i}}^{(2)}\right] \tag{204}$$

where

$${}^{T}\left[\underset{\sim}{\boldsymbol{i}}^{(1)}\right] = \left[1,\ 0,\ 0,\ 0,\ 0,\ \frac{1}{\sqrt{2}}\right], \quad {}^{T}\left[\underset{\sim}{\boldsymbol{i}}^{(2)}\right] = \left[0,\ 0,\ \frac{1}{\sqrt{2}},\ 0,\ 0,\ 1\right]. \tag{205}$$

We define the following two orthonormal basis vectors $\left\{\left[\underset{\sim}{\boldsymbol{\Gamma}}^{(1)}\right], \left[\underset{\sim}{\boldsymbol{\Gamma}}^{(2)}\right]\right\}$ as:

$$\begin{aligned} \left[\underset{\sim}{\boldsymbol{\Gamma}}^{(1)}\right] &= \frac{1}{\sqrt{a_{11}}}\left[\underset{\sim}{\boldsymbol{i}}^{(1)}\right], \\ \left[\underset{\sim}{\boldsymbol{\Gamma}}^{(2)}\right] &= \frac{-a_{12}}{\sqrt{a_{11}}\sqrt{a_{11}a_{22} - a_{12}^2}}\left[\underset{\sim}{\boldsymbol{i}}^{(1)}\right] + \frac{\sqrt{a_{11}}}{\sqrt{a_{11}a_{22} - a_{12}^2}}\left[\underset{\sim}{\boldsymbol{i}}^{(2)}\right] \end{aligned} \tag{206}$$

with

$$a_{\alpha\beta} = {}^{T}\left[\underset{\sim}{\boldsymbol{i}}^{(\alpha)}\right]\left[\underset{\approx}{\boldsymbol{H}}^{\xi}\right]\left[\underset{\sim}{\boldsymbol{i}}^{(\beta)}\right], \quad \alpha,\beta = 1,2. \tag{207}$$

The following properties hold true:

$$a_{11} > 0,\ a_{11}a_{22} - a_{12}^2 > 0,\ \ a_{12} = a_{21},\ \ {}^{T}\left[\underset{\sim}{\boldsymbol{\Gamma}}^{(\alpha)}\right]\left[\underset{\approx}{\boldsymbol{H}}^{\xi}\right]\left[\underset{\sim}{\boldsymbol{\Gamma}}^{(\beta)}\right] = \delta_{\alpha\beta} \tag{208}$$

Moreover, $\underset{\sim}{\boldsymbol{S}}^{(i)}$ is equal to the subspace generated by vectors $\left\{\left[\underset{\sim}{\boldsymbol{\Gamma}}^{(1)}\right], \left[\underset{\sim}{\boldsymbol{\Gamma}}^{(2)}\right]\right\}$. Hence, the orthogonal projection operator $\left[\underset{\approx}{\boldsymbol{P}}\right]$ of $\left[\underset{\approx}{\boldsymbol{\Phi}}\right]$ on $\underset{\sim}{\boldsymbol{S}}^{(i)}$ the is the 6×6 matrix whose components are given by:

$$P_{ij} = \left(\Gamma_i^{(1)}\Gamma_k^{(1)} + \Gamma_i^{(2)}\Gamma_k^{(2)}\right) H_{kj}^{\xi} \tag{209}$$

where H_{kj}^{ξ} are the components of the 6×6 matrix $\left[\underset{\approx}{\boldsymbol{H}}^{\xi}\right]$ with $i, j, k = 1, 2, ...6$.
We easily check that:

1. $\left[\underset{\approx}{\boldsymbol{P}}\right]\left[\underset{\sim}{\boldsymbol{\Gamma}}^{(\alpha)}\right] = \left[\underset{\sim}{\boldsymbol{\Gamma}}^{(\alpha)}\right], \quad \alpha$=1, 2
2. ${}^{T}\left[\underset{\approx}{\boldsymbol{P}}\right]\left[\underset{\approx}{\boldsymbol{H}}^{\xi}\right]\left[\underset{\approx}{\boldsymbol{P}}\right] = \left[\underset{\approx}{\boldsymbol{H}}^{\xi}\right]\left[\underset{\approx}{\boldsymbol{P}}\right] = {}^{T}\left[\underset{\approx}{\boldsymbol{P}}\right]\left[\underset{\approx}{\boldsymbol{H}}^{\xi}\right] \equiv \left[\underset{\approx}{\boldsymbol{H}}^{s,\xi}\right]$

Thus, each $\left[\underset{\frown}{\boldsymbol{\Phi}}\right]$ is uniquely decomposed as follows:

$$\left[\underset{\frown}{\boldsymbol{\Phi}}\right] = \left[\underset{\frown}{\boldsymbol{\Phi}}^{s}\right] + \left[\underset{\frown}{\boldsymbol{\Phi}}^{d}\right]$$

with

$$\left[\underset{\frown}{\boldsymbol{\Phi}}^{s}\right] = \left[\underset{\frown}{\boldsymbol{P}}\right]\left[\underset{\frown}{\boldsymbol{\Phi}}\right], \quad \left[\underset{\frown}{\boldsymbol{\Phi}}^{d}\right] = \left[\underset{\frown}{\boldsymbol{I}} - \underset{\frown}{\boldsymbol{P}}\right]\left[\underset{\frown}{\boldsymbol{\Phi}}\right], \quad {}^{T}\left[\underset{\frown}{\boldsymbol{\Phi}}^{s}\right]\left[\underset{\frown}{\underset{\frown}{\boldsymbol{H}}}^{\xi}\right]\left[\underset{\frown}{\boldsymbol{\Phi}}^{d}\right] = 0.$$

Finally, the matrix $[\underset{\frown}{\underset{\frown}{\boldsymbol{H}}}^{\xi}]$ is decomposed as in (203) with:

$$\left[\underset{\frown}{\underset{\frown}{\boldsymbol{H}}}^{s,\xi}\right]=\left[\underset{\frown}{\underset{\frown}{\boldsymbol{H}}}^{\xi}\right]\left[\underset{\frown}{\boldsymbol{P}}\right], \quad \left[\underset{\frown}{\underset{\frown}{\boldsymbol{H}}}^{d,\xi}\right] = \left[\underset{\frown}{\underset{\frown}{\boldsymbol{H}}}^{\xi}\right]\left[\underset{\frown}{\boldsymbol{I}} - \underset{\frown}{\boldsymbol{P}}\right]. \tag{210}$$

5.5.6 *BGFEAP* code description

BGFEAP (Bending-Gradient Finite Element Analysis Program) is a code developed in the Laboratoire Navier. The code is written using standard Fortran 77 and is a development of the program MEF presented in Dhatt and Touzot (1984). The program *BGFEAP* uses text files for data input and results output can be visualized using GID program described in CIMNE and GID. In parallel, a user element for Abaqus was developed, and it is based on *BGFEAP*.

5.6 Examples and numerical results

In this part, comparisons are made between Bending-Gradient finite element, Bending-Gradient analytical solution, exact solution for multilayered plates, *LS1* finite element and plate bending FE model in order to assess the performances of the new model. Moreover, patch tests for constant shear and moment were performed with Bending-Gradient finite element. The 2D FE calculations are performed with the commercial *ABAQUS* software.

5.6.1 Patch tests

The patch tests can prove, in addition to consistency requirements (which were initially the only item tested), the stability of the approximation by requiring that for a patch consisting of an assembly of one or more elements the stiffness matrices are non-singular whatever the boundary conditions are. Patch tests performed on plates with meshes of arbitrary quadrilaterals of the type shown in Fig. 5.3 can represent fields of constant moment or shear for both thick and thin plates.

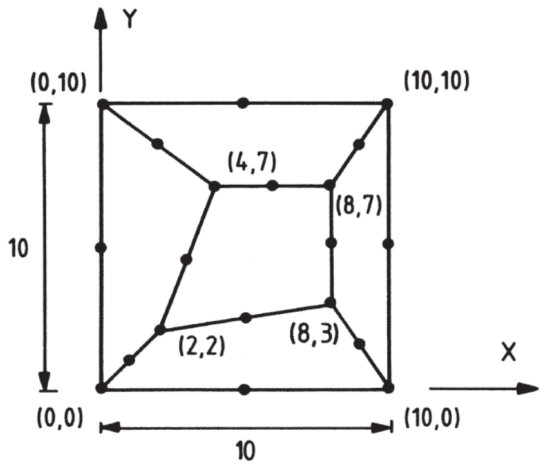


Fig. 5.3. Patch test: a patch of elements is considered in the load cases.

In this section, 3 multilayered plates were studied: the first case with one layer, the second one with 4 symmetric layers and the third case with 6 symmetric layers. The material properties and fiber orientation have no influence on the results. The total layers thickness is noted h.
For the first case with one layer, the fiber orientation is 0°.
For the second case with 4 layers, the fiber orientation is 0°/90°/90°/0°.
For the third case with 6 layers, the fiber orientation is 45°/0°/90°/90°/0°/45°.

5.6.1.1 Bending patch test

In the bending patch test, a distributed edge couple of constant intensity, equal to 1, is applied with the suitable boundary conditions:

U_3 is set equal to zero on 3 nodes on the corners. On X=0 and 10, a linear load along ϕ_{111} is applied equal to -1 and 1 respectively. On Y=0 and 10, a linear load along ϕ_{112} is applied equal to -1 and 1 respectively.

In table 5.1, results for bending patch are shown for the 3 cases cited above and for different slenderness ratio L/h.

L/h	5	10	20
6 layers	0.988	0.963	0.913
4 layers	0.997	0.989	0.971
1 layer	0.999	0.999	0.995

Tab. 5.1. The average value of moment M_{11} intensity calculated throughout the plate.

5.6.1.2 Twisting patch test

In the twisting patch test, a distributed edge couple that generate a constant twisting, with an intensity equal to 1, is applied with the suitable boundary conditions:

U_3 is set equal to zero on 3 nodes. On X=0 and 10, a linear load along ϕ_{121} is applied equal to -1 and 1 respectively. On Y=0 and 10, a linear load along ϕ_{122} is applied equal to -1 and 1 respectively.

In table 5.2, results for twisting patch test are shown for the 3 cases cited above and for different slenderness ratio L/h.

L/h	5	10	20
6 layers	0.998	0.993	0.99
4 layers	0.998	0.993	0.984
1 layer	0.996	0.984	0.941

Tab. 5.2. The average value of moment M_{12} intensity calculated throughout the plate.

5.6.1.3 Shear patch test

In the patch test for shear shown in Fig. 5.4, a lateral distributed edge load of constant intensity, equal to 1, is applied at the right-hand edge of the patch of elements which is fully clamped at the left-hand edge. It is also necessary to constrain all of the rotations to zero in order to prevent a field of bending moments developing.

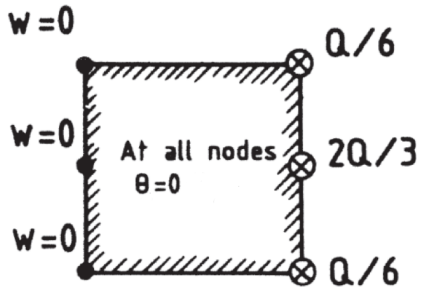


Fig. 5.4. Shearing case.

In table 5.3, results for shear patch test are shown for the 3 cases cited above and for different slenderness ratio L/h.

L/h	5	10	20
6 layers	1.001	1.001	1.001
4 layers	1.001	1.001	1.001
1 layer	1.001	1.001	1.001

Tab. 5.3. The average value of shear Q_1 intensity calculated throughout the plate.

5.6.1.4 Discussion

According to the results obtained, we can conclude that the Bending-Gradient finite element model converges to the exact constant value for bending, twisting and shear patch tests, specially for small slenderness ratio (L/h). Therefore, the best performance range for the Bending-Gradient finite element is for a slenderness ratio lower than 20.

5.6.2 Comparison between analytical solution and Bending-Gradient finite element

5.6.2.1 Problem description

The laminate used in this example is composed of 3 layers (Lebée and Sab, 2011b). Each layer is made of unidirectional fiber-reinforced material oriented at θ relative to the direction x. All plies are perfectly bounded. The constitutive behavior of a ply is assumed to be transversely isotropic along the direction of the fibers and engineering constants are chosen similar to those of Pagano (1969):

For the first and third layer, the thickness is $e_1 = e_3 = 1$, the fiber orientation is 90° and the elastic constants are:

$E_1 = 25E$, $E_2 = E_3 = 1E$,

$G_{12} = G_{13} = 0.5E$, $G_{23} = \dfrac{E_2}{2(1+\nu_{32})} = 0.4E$,

$\nu_{12} = \nu_{13} = \nu_{23} = 0.25$.

where 1, 2 and 3 refer, respectively, to the fiber, transverse, and thickness direction as shown in Fig. 5.5.

For the layer 2, the thickness is $e_2 = 2$, the fiber orientation is 0° and the elastic constants are the same as the first and third layer.

The plate slenderness ratio (L/h) is set equal to 5.

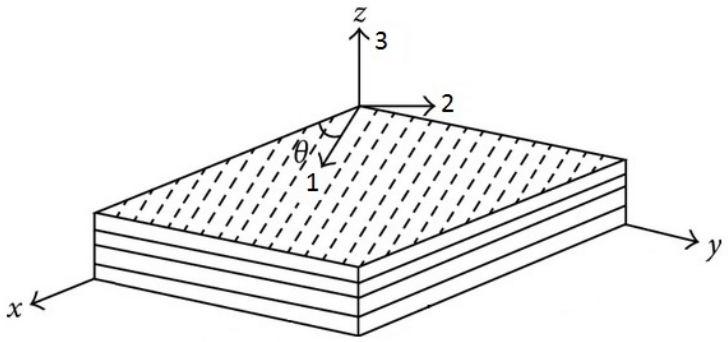


Fig. 5.5. Description of fiber orientation axes and angle.

The laminate is subjected to a cylindrical bending with a simply supported edges (Fig. 5.6) with L=20, and where the plate is invariant and infinite in Y direction and transversely loaded with a uniformly distributed load applied along z axis, equal to $0.003E$. The particular choice of 3D boundary conditions is shown on Fig. 5.6 and the invariance of the solution in Y direction enable a variable separation between Y and X, and the derivation of a closed form solution. It should be mentioned that Y=0 and Y=150 are free edges. It is important to note that this solution does not present any boundary layer in the region near the simple support.

The following notation is used:

$$\overline{U_3} = \frac{U_3}{L},$$

$$\overline{R}_{\alpha\beta\gamma} = \frac{R_{\alpha\beta\gamma}}{EL^2}, \quad \overline{M}_{\alpha\beta} = \frac{M_{\alpha\beta}}{EL}$$

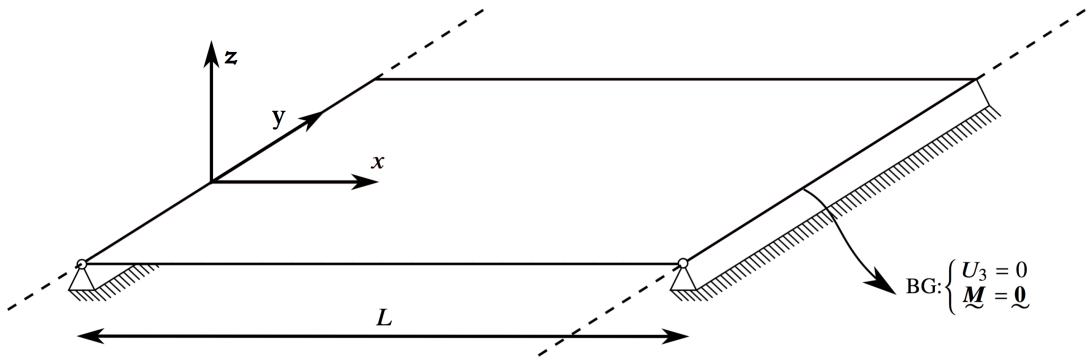


Fig. 5.6. Description of laminated plate configuration for cylindrical bending.

5.6.2.2 Results and interpretation

In the following section, comparisons are made between Bending-Gradient finite element and the analytical solution of the Bending-Gradient theory:
In Fig. 5.7, deflection $\overline{U}_3$, ϕ_{111}, ϕ_{221} and ϕ_{122} are plotted for the Bending-Gradient finite element and the analytical solution. It should be noted that ϕ_{121}, ϕ_{112} and ϕ_{222} are equal to zero in both Bending-Gradient finite element and the analytical solution of the Bending-Gradient model. In Fig. 5.8, the distribution of $\overline{M}_{11}$, $\overline{M}_{22}$, $\overline{R}_{111}$ and $\overline{R}_{221}$ are plotted for the Bending-Gradient finite element

and the analytical solution. It should be noted that $\overline{M}_{12}, \overline{R}_{221}, \overline{R}_{121}, \overline{R}_{112}$ and $\overline{R}_{222}$ are equal to zero in both Bending-Gradient finite element and the analytical solution of the Bending-Gradient model.

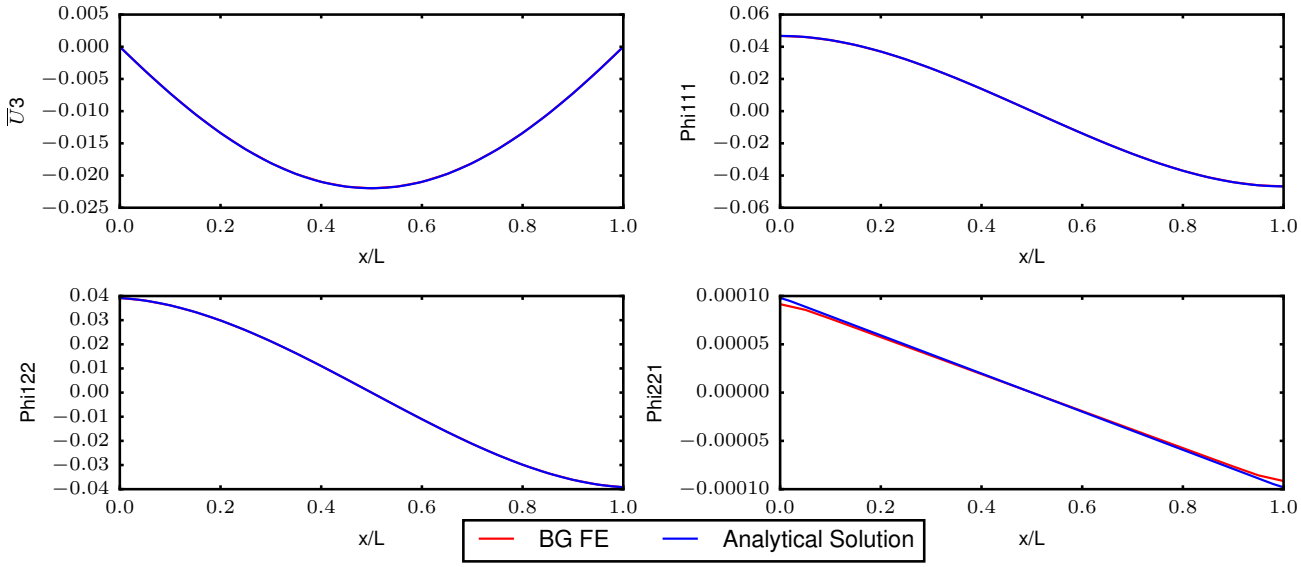


Fig. 5.7. Displacement: $\overline{U}_3$, ϕ_{111}, ϕ_{221} and ϕ_{122}, predicted by the Bending-Gradient finite element and the analytical solution.

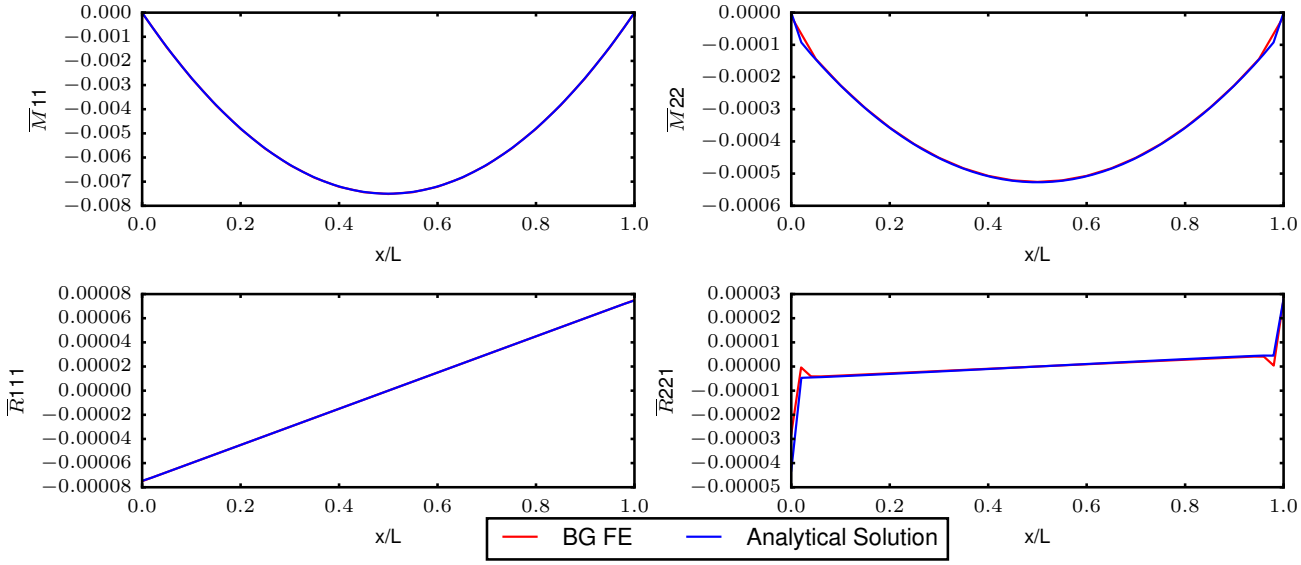


Fig. 5.8. Distribution of $\overline{M}_{11}$, $\overline{M}_{22}$, $\overline{R}_{111}$ and $\overline{R}_{221}$ predicted by the Bending-Gradient finite element and the analytical solution.

According to the results obtained, we can conclude that the Bending-Gradient finite element converge to the exact analytical solution for both displacements and stresses.

5.6.3 Comparison between Bending-Gradient FE and exact solution for multilayered plates

We present in this section tests on a multilayered plates composed of 3 and 9 layers.

5.6.3.1 Problem description

We consider a simply supported plate and subjected to a double sinusoidal load. We study two sequences of stack of layers: the first sequence of three layers of 0° / 90° / 0° and the second is nine layers of 0° / 90° / 0° / 90° / 0° / 90° / 0° / 90° / 0°. The mechanical characteristics of the layers are shown in Fig. 5.9 with $L = 10$. The constitutive behavior of a ply is assumed to be transversely isotropic along the direction of the fibers and engineering constants are chosen as follows:
$E_1 = 25E$, $E_2 = E_3 = 1E$,
$G_{12} = G_{13} = 0.5E$, $G_{23} = 0.2E$,
$\nu_{12} = \nu_{13} = \nu_{23} = 0.25$.
where 1, 2 and 3 refer, respectively, to the fiber, transverse, and thickness direction as shown in Fig. 5.5.

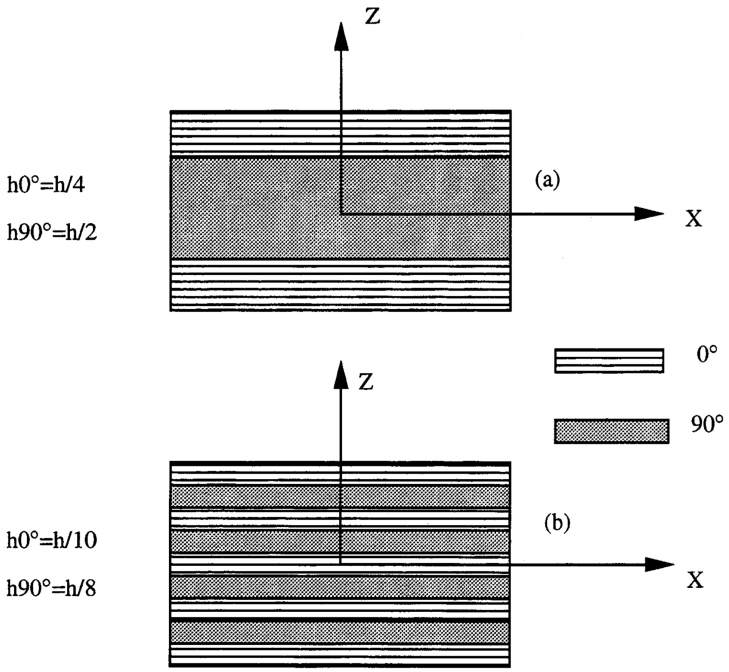


Fig. 5.9. Multilayered square plate configuration: a) stack of 3 layers 0°/90°/0°, b) stack of 9 layers 0°/90°/0°/90°/0°/90°/0°/90°/0°.

We dispose for this test a reference solution based on the 3D elasticity PAGANO and HATFIELD (1972).
The following notation is used:

$$\overline{W} = W\frac{\pi^4 Q}{12S^4 h q_0}, \quad \mathrm{S}=\frac{L}{h}, \quad \mathrm{Q}=4G_{12}+\frac{E_1+E_2(1+2\nu_{23})}{1-\nu_{12}\nu_{21}},$$

$$(\overline{\sigma}_{11}\ \ \overline{\sigma}_{22}) = \frac{1}{q_0 S^2}(\sigma_{11}\ \ \sigma_{22}), \quad (\overline{\sigma}_{13}\ \ \overline{\sigma}_{23}) = \frac{1}{q_0 S}(\sigma_{13}\ \ \sigma_{23}),$$

5.6.3.2 3 Layers plate

In this section, results of the Bending-Gradient finite element and the reference solution, for a square plate with 3 layers 0°/90°/0°, are presented in table 5.4.

L/h	Model	$\overline{\sigma}_{11}$ ($L/2$, $L/2$, $-h/2$)	$\overline{\sigma}_{22}$ ($L/2$, $L/2$, $-h/4$)	$\overline{\sigma}_{13}$ (0, $L/2$, 0)	$\overline{\sigma}_{23}$ ($L/2$, 0, 0)	$\overline{\overline{W}}$ ($L/2$, $L/2$, 0)
4	BG FE	0.374	0.67497	0.26739	0.313	4.868
4	3D Elasticity	0.72	0.663	0.219	0.292	4.491
4	2D Abaqus	0.38	0.6726	-	-	4.9
10	BG FE	0.4874	0.403	0.325	0.206	1.745
10	3D Elasticity	0.559	0.403	0.301	0.196	1.709
20	BG FE	0.525	0.308	0.343	0.18	1.2
20	3D Elasticity	0.543	0.308	0.328	0.156	1.189
50	BG FE	0.5363	0.276	0.348	0.166	1.033
50	3D Elasticity	0.539	0.276	0.337	0.141	1.031
100	BG FE	0.538	0.271	0.347	0.159	1.008
100	3D Elasticity	0.539	0.271	0.339	0.139	1.008

Tab. 5.4. Validation of the Bending-Gradient finite element on a square plate with 3 layers.

5.6.3.3 9 layers plate

In this section, results of the Bending-Gradient finite element and the reference solution, for a square plate with 9 layers 0°/90°/0°/90°/0°/90°/0°/90°/0°, are presented in table 5.5.

L/h	Model	$\overline{\sigma}_{11}$ ($L/2$, $L/2$, $-h/2$)	$\overline{\sigma}_{22}$ ($L/2$, $L/2$, $-2h/5$)	$\overline{\sigma}_{13}$ (0, $L/2$, 0)	$\overline{\sigma}_{23}$ ($L/2$, 0, 0)	$\overline{\overline{W}}$ ($L/2$, $L/2$, 0)
4	BG FE	0.493	0.4914	0.244	0.246	4.245
4	3D Elasticity	0.684	0.628	0.223	0.223	4.079
4	2D Abaqus	0.497	0.0234	-	-	4.2645
10	BG FE	0.5225	0.459	0.261	0.239	1.534
10	3D Elasticity	0.551	0.477	0.247	0.226	1.512
20	BG FE	0.5346	0.441	0.268	0.237	1.139
20	3D Elasticity	0.541	0.444	0.255	0.221	1.129
50	BG FE	0.538	0.433	0.269	0.235	1.023
50	3D Elasticity	0.539	0.433	0.258	0.219	1.021
100	BG FE	0.538	0.431	0.268	0.232	1.006
100	3D Elasticity	0.539	0.431	0.259	0.219	1.005

Tab. 5.5. Validation of the Bending-Gradient finite element on a square plate with 9 layers.

5.6.3.4 Discussion

An analysis of the results shows that the Bending-Gradient finite element works well in the case of three layers with large slenderness: the error found on the deflection and the normal stresses (σ_{11} and σ_{22}) is less than 1%. For small slenderness, there is a significant deviation from the reference

solution which is 48% on the normal stresses σ_{11}, 1.8% on σ_{22} and 8% on the deflection for both Bending-Gradient FE and Abaqus 2D FE. For the plate with nine layers, it is observed the same trend with smaller errors in the case of small slenderness: the error is 27% on the normal stresses σ_{11}, 21% on σ_{22} and 4% on the deflection for both Bending-Gradient FE and Abaqus 2D FE. Shear stresses are relatively well calculated for the two stacking sequences and for different values of slenderness. Indeed, the average error observed is of the order of 10%. It decreases with the reduction in the thickness and increasing the number of layers.

It should be noted that the exact solution for multilayered plates is more accurate for thin plates.

5.6.4 Mesh control: Comparison between Bending-Gradient FE, *LS1* and Abaqus 2D FE

5.6.4.1 Problem description

The plate under consideration is a simply supported square plate with a length of its sides equal to L=10. The plate is subjected to a concentrated load P=-0.0002EL^2 applied in the middle of the plate, it is composed of 1 layer with a thickness equal to h. The plate slenderness ratio is denoted by L/h. The material properties are isotropic:

The elastic constants are:

$E = 138\,000\ E$,

$G = \dfrac{E}{2(1+\nu)} = 57\,000\ E$,

$\nu = 0.21$.

5.6.4.2 Results and discussion

We will study in this section the convergence of the Bending-Gradient finite element in terms of displacement. The square plate is modeled with different meshes. Reference values are given by the Abaqus 2D FE composite layup module. We present in Fig. 5.10 the percentage of relative difference for deflection at the middle of the plate, calculated between Bending-Gradient finite element and Abaqus 2D finite element for different meshes, and between *LS1* and Abaqus 2D finite element for different meshes.

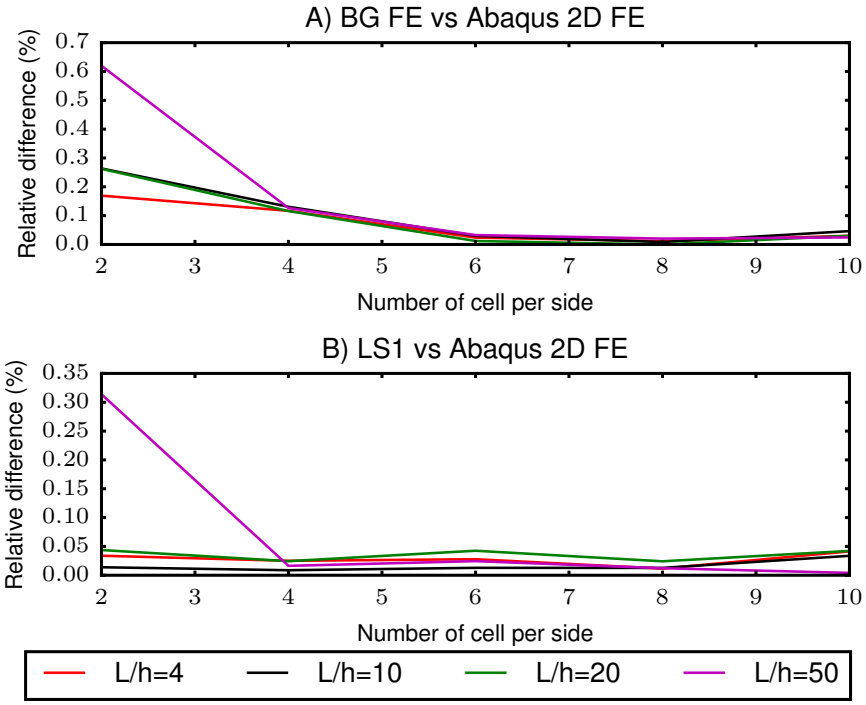


Fig. 5.10. Convergence of deflection calculated between: A) BG FE and 2D FE Abaqus, B) *LS1* and 2D FE Abaqus.

Based on the results shown above, a good behavior of the Bending-Gradient finite element is found. For Bending-Gradient at convergence, deviation error from the exact solution is 0.03% and 0.0244% in the case of thick plate ($L/h = 4$) and thin ($L/h = 50$), respectively. Same results are approximately obtained for Bending-Gradient finite element and the reference values, which leads to the conclusion that our model passes well the convergence test for thin and thick plates.
It should be noted that for *LS1* at convergence, deviation from the exact solution is 0.041% and 0.004% in the case of thick plate ($L/h = 4$) and thin ($L/h = 50$), respectively. Same results and conclusion for the *LS1* model.

5.6.5 Comparison between Bending-Gradient FE, *LS1* and Abaqus 2D FE

In this section, we present 4 different cases, the first case is a simply supported square plate with a uniformly distributed load; the second case is a simply supported square plate with a concentrated load applied in the middle of the plate as a uniformly distributed load on a very small surface, the third case is a rectangular plate fixed on one side and subjected to a linear load on the opposed side causing the twisting of the plate and the fourth case is a cylindrical bending of a simply supported plate. The commercial ABAQUS software has been used with S8R element (2D 8-node quadratic shell element with reduced integration). Comparisons are made between Bending-Gradient FE, *LS1* and Abaqus 2D FE composite layup module with the same mesh refinement.

The following notation is used:

$$\overline{U_3} = \frac{U_3}{L},$$

$$\overline{Q_\alpha} = \frac{Q_\alpha}{EL^2}, \quad \overline{M_{\alpha\beta}} = \frac{M_{\alpha\beta}}{EL}$$

5.6.5.1 First case

The laminate under consideration is a square plate with a length and width of L=10 in the x and y directions. The thickness of the laminate, following z direction, is equal to h=4e and the middle plane of the plate is located at z=0. The plate is simply supported on its 4 edges, and is subjected to a uniform load equal to $0.48E$. The slenderness ratio L/h is set equal to 4 and 10.

The material properties are as in Wang and Crossman (1977a) and Pagano and Pipes (1970). For the first and fourth layers, the fiber orientation is 30° and the elastic constants are:
$E_1 = 140\,000\ E$, $E_2 = E_3 = 15\,000\ E$,
$G_{12} = G_{13} = G_{23} = 5\,850\ E$,
$\nu_{12} = \nu_{13} = \nu_{23} = 0.21$.
where 1, 2 and 3 refer, respectively, to the fiber, transverse, and thickness direction as shown in Fig. 5.5.

For the second and third layers, the fiber orientation is −30° and the elastic constants are:
$E_1 = 160\,000\ E$, $E_2 = E_3 = 8\,500\ E$,
$G_{12} = G_{13} = 4\,100\ E$, $G_{23} = 2\,800\ E$,
$\nu_{12} = \nu_{13} = 0.33$, $\nu_{23} = 0.5$.

For L/h=10: In Fig. 5.11, we plot the distribution of moments $\overline{M}_{11}$ and $\overline{M}_{22}$ and shear forces $\overline{Q}_1$ and $\overline{Q}_2$, at $Y = L/2$ as predicted by Bending-Gradient FE, *LS1* and Abaqus 2D FE. In Fig. 5.12, we plot the deflection $\overline{U}_3$ at $Y = L/2$ as predicted by Bending-Gradient FE, *LS1* and Abaqus 2D FE. In Fig. 5.13, we plot the distribution of moment of torsion $\overline{M}_{12}$, at A) diagonal between X=0, Y=0 and $X = L$, $Y = L$ and B) diagonal between X=0, $Y = L$ and $X = L$, Y=0, as predicted by Bending-Gradient FE, *LS1* and Abaqus 2D FE.

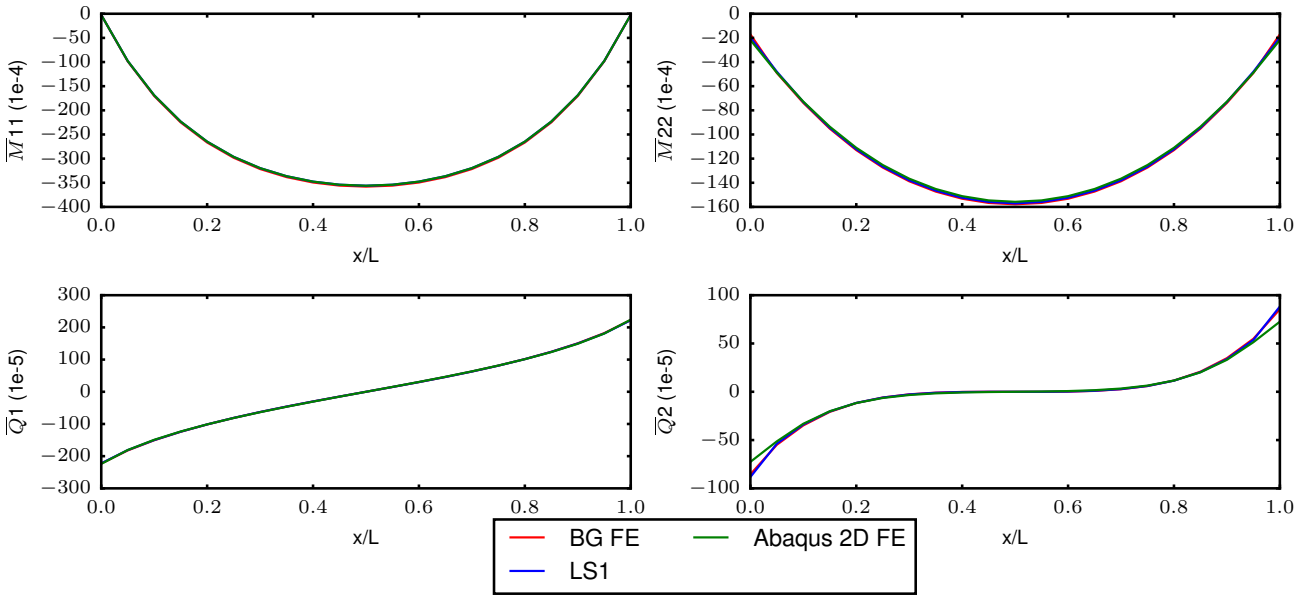


Fig. 5.11. Distribution of moments $\overline{M}_{11}$ and $\overline{M}_{11}$ and shear forces $\overline{Q}_1$ and $\overline{Q}_2$ at $Y = L/2$ for L/h=10, predicted by Bending-Gradient FE, *LS1* and Abaqus 2D FE for 30°/ − 30°/ − 30°/30°.

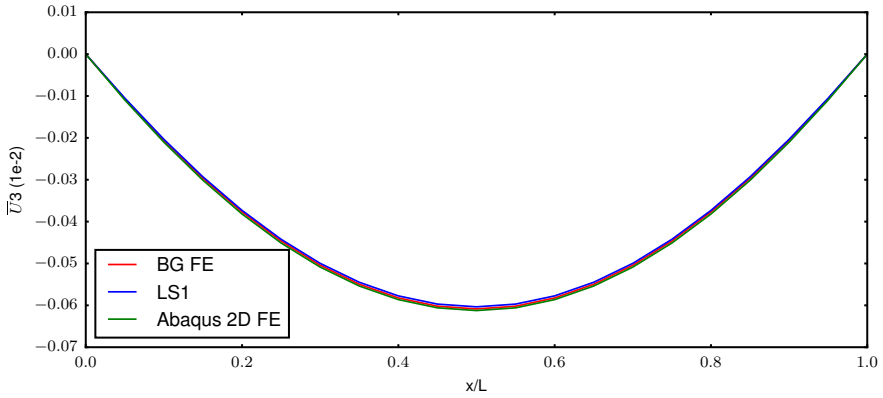


Fig. 5.12. Deflection $\overline{U}_3$ at $Y = L/2$ for L/h=10, predicted by Bending-Gradient FE, *LS1* and Abaqus 2D FE for $30°/-30°/-30°/30°$.

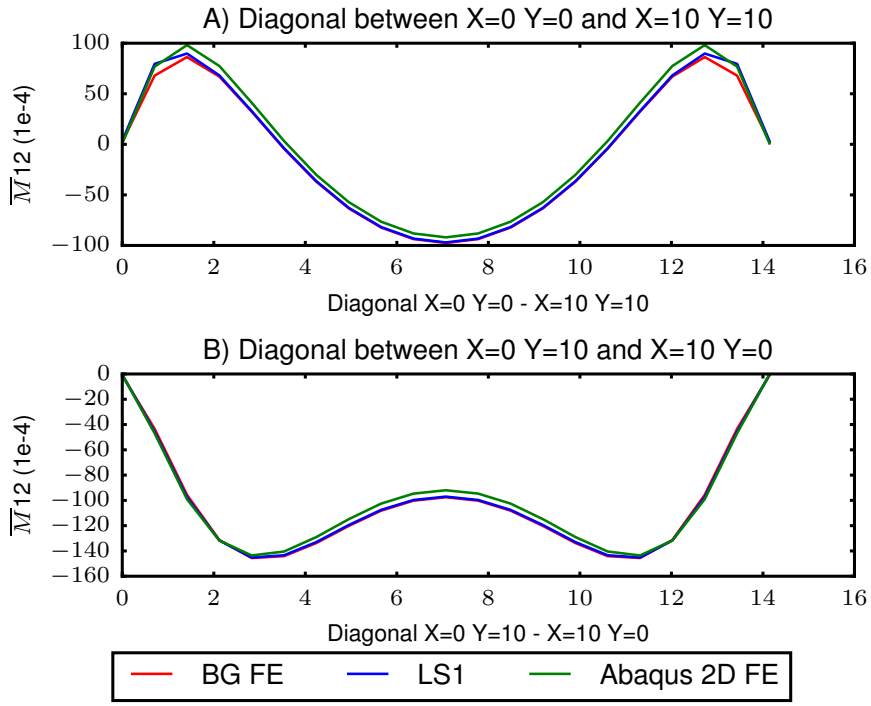


Fig. 5.13. Distribution of moment of torsion $\overline{M}_{12}$ at A) diagonal between X=0, Y=0 and $X = L$, $Y = L$ and B) diagonal between X=0, $Y = L$ and $X = L$, Y=0, for L/h=10, predicted by Bending-Gradient FE, *LS1* and Abaqus 2D FE for $30°/-30°/-30°/30°$.

For L/h=4: In Fig. 5.14, we plot the distribution of moments $\overline{M}_{11}$ and $\overline{M}_{22}$ and shear forces $\overline{Q}_1$ and $\overline{Q}_2$, at $Y = L/2$ as predicted by Bending-Gradient FE, *LS1* and Abaqus 2D FE. In Fig. 5.15, we plot the deflection $\overline{U}_3$ at $Y = L/2$ as predicted by Bending-Gradient FE, *LS1* and Abaqus 2D FE. In Fig. 5.16, we plot the distribution of moment of torsion $\overline{M}_{12}$, at A) diagonal between X=0, Y=0 and $X = L$, $Y = L$ and B) diagonal between X=0, $Y = L$ and $X = L$, Y=0, as predicted by Bending-Gradient FE, *LS1* and Abaqus 2D FE.

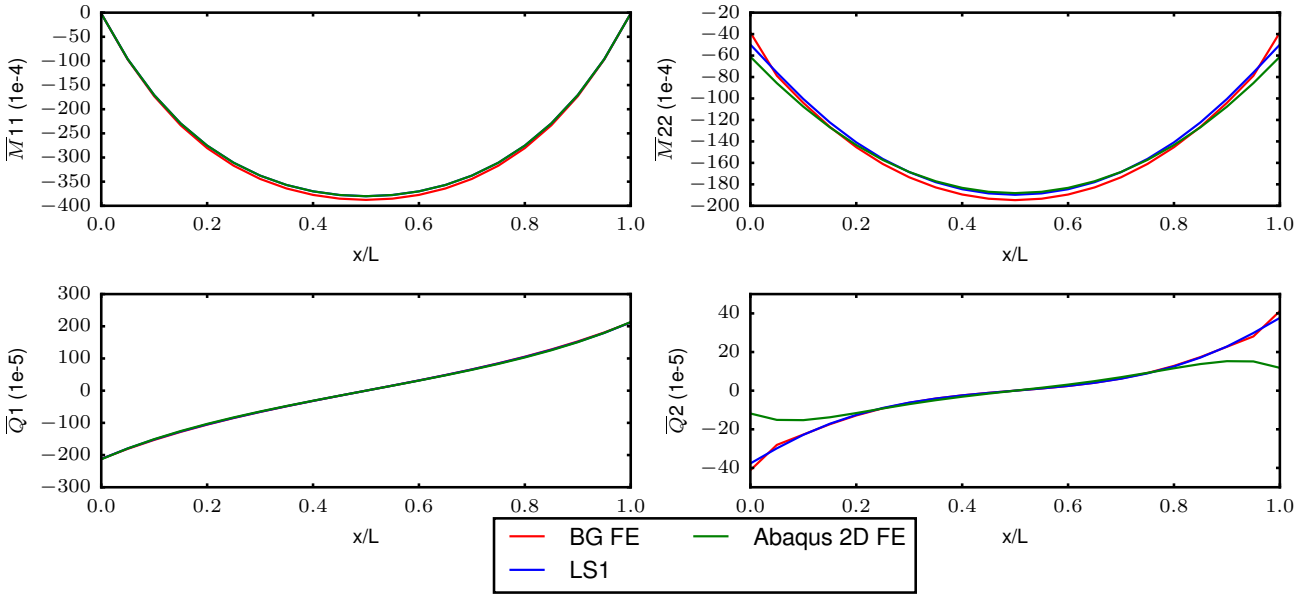


Fig. 5.14. Distribution of moments $\overline{M}_{11}$ and $\overline{M}_{22}$ and shear forces $\overline{Q}_1$ and $\overline{Q}_2$ at $Y = L/2$ for L/h=4, predicted by Bending-Gradient FE, *LS1* and Abaqus 2D FE for $30°/-30°/-30°/30°$.

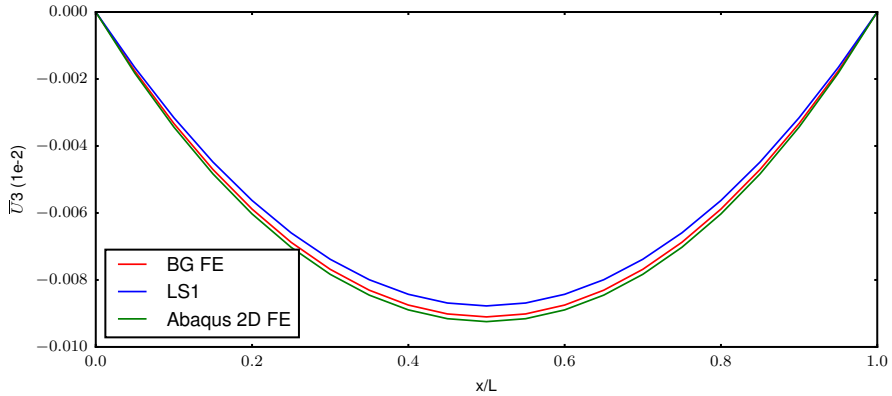


Fig. 5.15. Deflection $\overline{U}_3$ at $Y = L/2$ for L/h=4, predicted by Bending-Gradient FE, *LS1* and Abaqus 2D FE for $30°/-30°/-30°/30°$.

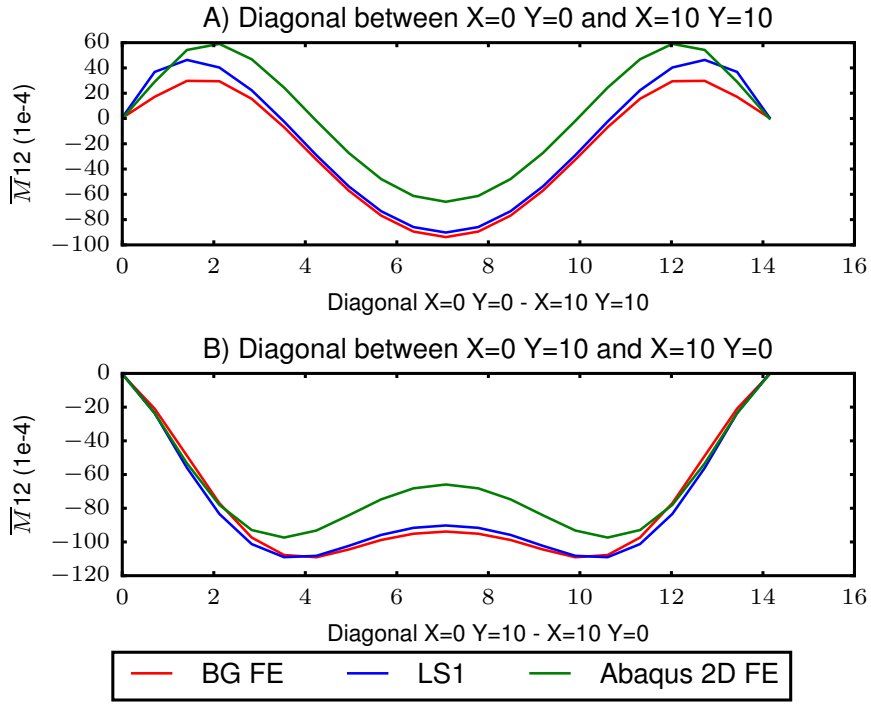


Fig. 5.16. Distribution of moment of torsion $\overline{M}_{12}$ at A) diagonal between X=0, Y=0 and $X = L$, $Y = L$ and B) diagonal between X=0, $Y = L$ and $X = L$, Y=0, for L/h=4, predicted by Bending-Gradient FE, *LS1* and Abaqus 2D FE for $30°/-30°/-30°/30°$.

5.6.5.2 Second case

The laminate under consideration is a square plate with a length and width of L=10 in the X and Y directions. The thickness of the laminate, following z direction, is equal to h=4e and the middle plane of the plate is located at z=0. The plate is simply supported on its 4 edges, and is subjected to a concentrated load equal to $5EL^2$ applied in the middle of the plate as a uniformly distributed load on a small surface (2×2). The slenderness ratio L/h is set equal to 4.

The material properties are the same as the first case.

In Fig. 5.17, we plot the distribution of moments $\overline{M}_{11}$ and $\overline{M}_{22}$ and shear forces $\overline{Q}_1$ and $\overline{Q}_2$, at $Y = L/2$ as predicted by Bending-Gradient FE, *LS1* and Abaqus 2D FE. In Fig. 5.18, we plot the deflection $\overline{U}_3$ at $Y = L/2$ as predicted by Bending-Gradient FE, *LS1* and Abaqus 2D FE. In Fig. 5.19, we plot the distribution of moment of torsion $\overline{M}_{12}$, at A) diagonal between X=0, Y=0 and $X = L$, $Y = L$ and B) diagonal between X=0, $Y = L$ and $X = L$, Y=0, as predicted by Bending-Gradient FE, *LS1* and Abaqus 2D FE.

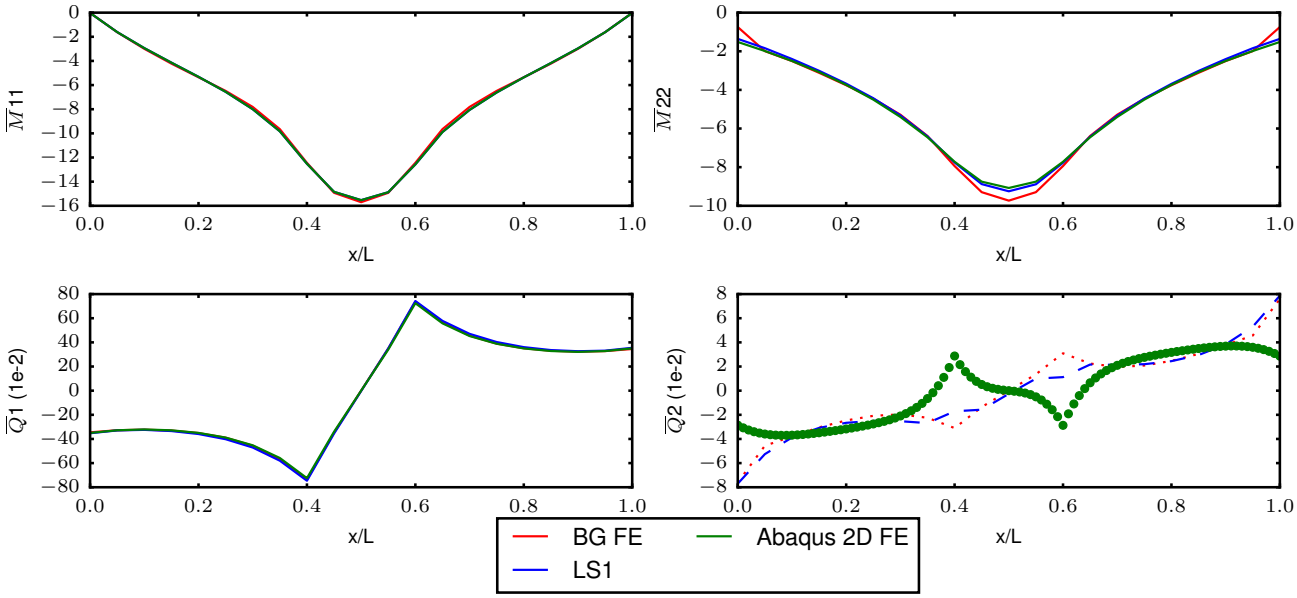


Fig. 5.17. Distribution of moments $\overline{M}_{11}$ and $\overline{M}_{22}$ and shear forces $\overline{Q}_1$ and $\overline{Q}_2$ at $Y = L/2$ for L/h=4, predicted by Bending-Gradient FE, *LS1* and Abaqus 2D FE for $30°/-30°/-30°/30°$.

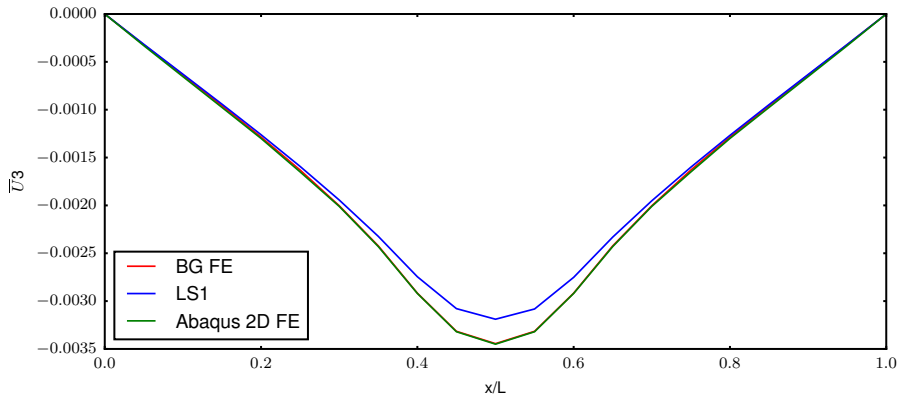


Fig. 5.18. Deflection $\overline{U}_3$ at $Y = L/2$ for L/h=4, predicted by Bending-Gradient FE, *LS1* and Abaqus 2D FE for $30°/-30°/-30°/30°$.

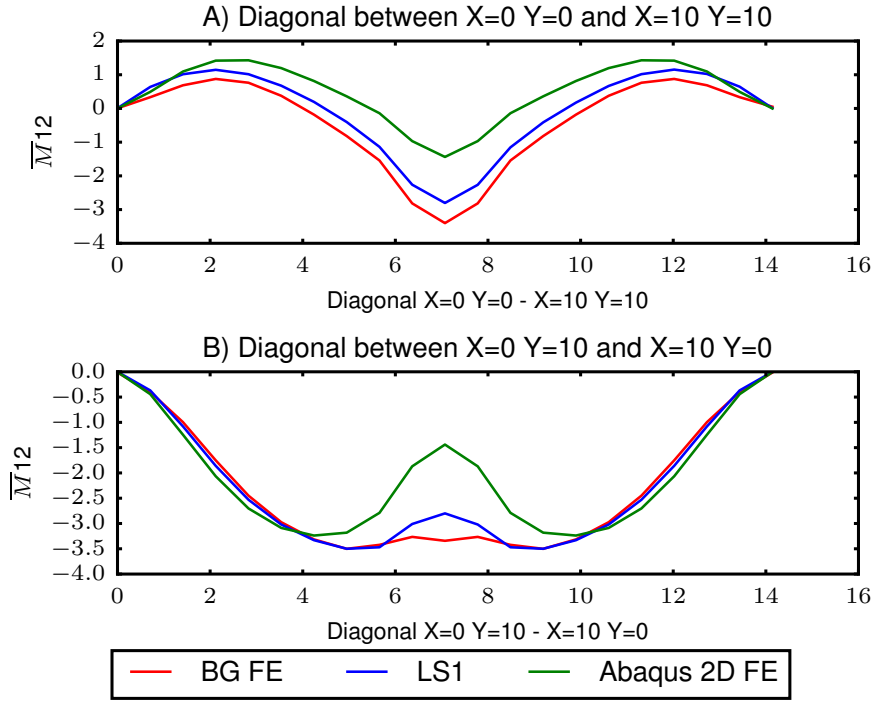


Fig. 5.19. Distribution of moment of torsion $\overline{M}_{12}$ at A) diagonal between X=0, Y=0 and $X = L$, $Y = L$ and B) diagonal between X=0, $Y = L$ and $X = L$, Y=0, for L/h=4, predicted by Bending-Gradient FE, *LS1* and Abaqus 2D FE for $30°/-30°/-30°/30°$.

5.6.5.3 Third case

The laminate under consideration is a plate with a length of L=10 and a width of b=5 respectively in the X and Y directions and made up of 4 layers. The thickness of the laminate, following z direction, is equal to $h = 4e$ and the middle plane of the plate is located at z=0. The slenderness ratio b/h is set equal to 6.25. The plate is fixed on its X=0 edge, and is subjected to a linear load on the $X = L$ edge and equal to $9EL$ between Y=0 and $Y = b/2$ and -$9EL$ between $Y = b/2$ and $Y = b$. This load type causes the plate to twist.

The material properties are as in (Wang and Crossman, 1977a) and (Pagano and Pipes, 1970). For the first and fourth layer, the fiber orientation is 0° and the elastic constants are:
$E_1 = 140\,000\,E$, $E_2 = E_3 = 15\,000\,E$,
$G_{12} = G_{13} = G_{23} = 5\,850\,E$,
$\nu_{12} = \nu_{13} = \nu_{23} = 0.21$.
where 1, 2 and 3 refer, respectively, to the fiber, transverse, and thickness direction as shown in Fig. 5.5.

For the second and third layer, the fiber orientation is 90° and the elastic constants are:
$E_1 = 160\,000\,E$, $E_2 = E_3 = 8\,500\,E$,
$G_{12} = G_{13} = 4\,100\,E$, $G_{23} = 2\,800\,E$,
$\nu_{12} = \nu_{13} = 0.33$, $\nu_{23} = 0.5$.

In Fig. 5.20, we plot the distribution of moment of torsion $\overline{M}_{12}$ at $Y = b/2$ as predicted by Bending-Gradient FE, *LS1* and Abaqus 2D FE. In Fig. 5.21, we plot the deflection $\overline{U}_3$ at $X = L$ as predicted by Bending-Gradient FE, *LS1* and Abaqus 2D FE.

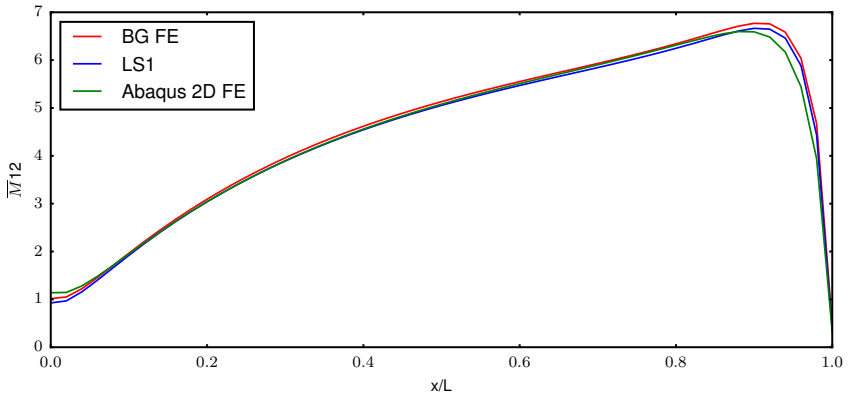


Fig. 5.20. Distribution of moment of torsion $\overline{M}_{12}$ at $Y = b/2$, predicted by Bending-Gradient FE, *LS1* and Abaqus 2D FE for $0°/90°/90°/0°$.

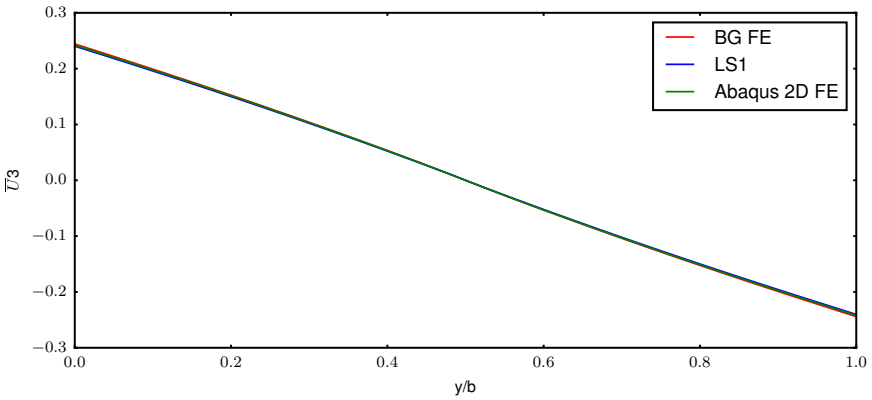


Fig. 5.21. Deflection $\overline{U}_3$ at $X = L$, predicted by Bending-Gradient FE, *LS1* and Abaqus 2D FE for $0°/90°/90°/0°$.

The same problem and plate is now studied with the same material properties of the previous example, but with the following fiber orientation: for the first and fourth layer, the fiber orientation is $60°$, and for the second and third layer, the fiber orientation is $-60°$.
In Fig. 5.22, we plot the distribution of moment of torsion $\overline{M}_{12}$ at $Y = b/2$ as predicted by Bending-Gradient FE, *LS1* and Abaqus 2D FE. In Fig. 5.23, we plot the deflection $\overline{U}_3$ at $X = L$ as predicted by Bending-Gradient FE, *LS1* and Abaqus 2D FE.

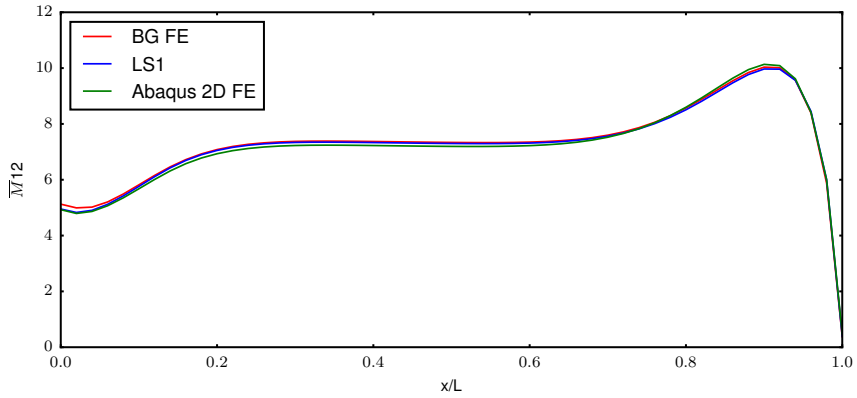


Fig. 5.22. Distribution of moment of torsion $\overline{M}_{12}$ at $Y = b/2$, predicted by Bending-Gradient FE, *LS1* and Abaqus 2D FE for $60°/-60°/-60°/60°$.

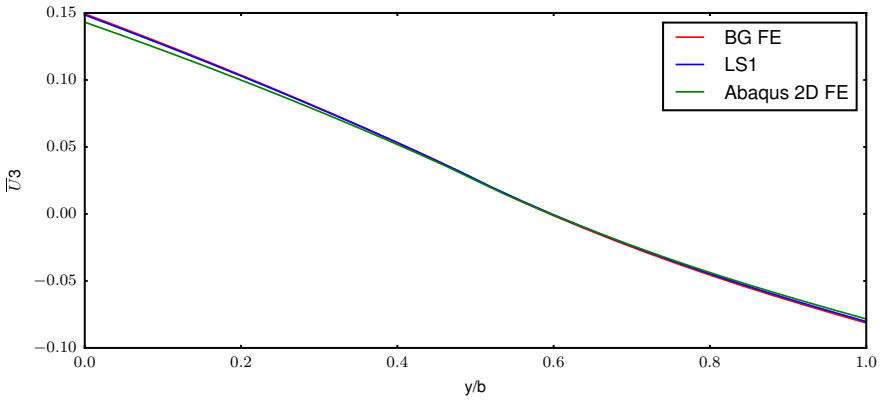


Fig. 5.23. Deflection $\overline{U}_3$ at $X = L$, predicted by Bending-Gradient FE, *LS1* and Abaqus 2D FE for $60°/-60°/-60°/60°$.

5.6.5.4 Fourth case

The laminate used in this example is composed of 8 layers. Each layer is made of unidirectional fiber-reinforced material oriented at θ relative to the direction x. All the plies are perfectly bounded. The constitutive behavior of a ply is assumed to be transversely isotropic along the direction of the fibers and engineering constants are chosen similar to those of Pagano (1969):

The thickness of each layer is set equal to 0.625, the fiber orientation is $[0°, -45°, 90°, 45°]$s and the elastic constants are:

$E_1 = 25E$, $E_2 = E_3 = 1E$,

$G_{12} = G_{13} = 0.5E$, $G_{23} = \dfrac{E_2}{2(1+\nu_{32})} = 0.4E$,

$\nu_{12} = \nu_{13} = \nu_{23} = 0.25$.

where 1, 2 and 3 refer, respectively, to the fiber, transverse, and thickness direction as shown in Fig. 5.5. The plate slenderness ratio (L/h) is set equal to 4.

The laminate is subjected to a cylindrical bending of a simply supported composite laminates (Fig. 5.6), with L=20 and where the plate is invariant and infinite in Y direction and a uniformly distributed load equal to $0.05E$ is applied. The particular choice of 3D boundary conditions on Fig.

5.6 and the invariance of the solution in Y direction enable a variable separation between z and X, and the derivation of a closed form solution. It is important to note that this solution does not present any boundary layer in the region near the simple support.

In this example, the plate is studied with respect to the bending direction which is the plate's overall configuration rotated relative to z axis. In table 5.6, the relative difference for deflection and moments M_{22} and M_{12} are presented at $X = L/2$ for *LS1* (reference solution), Bending-Gradient and Abaqus 2D FE.

It should be noted that the relative difference between *LS1* and Bending-Gradient FE is calculated as follows:

$$\Delta^{BG/LS1} = \frac{BG - LS1}{LS1}$$

$[0°, -45°, 90°, 45°]s$	Model	U_3	M_{22}	M_{12}
+0°	$\Delta^{BG/LS1}$	0.003475936	-0.00754134	-0.013216837
	$\Delta^{Abaqus\ 2D\ FE/LS1}$	0.00155615	0.087379228	0.036639273
+15°	$\Delta^{BG/LS1}$	0.004379947	-0.003530737	0.014864941
	$\Delta^{Abaqus\ 2D\ FE/LS1}$	0.009343008	0.113267216	-0.447439409
+30°	$\Delta^{BG/LS1}$	0.005373494	0.000160823	0.008319649
	$\Delta^{Abaqus\ 2D\ FE/LS1}$	0.045862651	-0.013292055	-0.392058748
+45°	$\Delta^{BG/LS1}$	0.006357895	0.002014597	0.00720255
	$\Delta^{Abaqus\ 2D\ FE/LS1}$	0.058105263	-0.125204338	-0.363731131

Tab. 5.6. Relative difference between *LS1* (reference solution) and Bending-Gradient FE and Abaqus 2D FE for plate's overall configuration and bending direction.

It should be noted that the values obtained for M_{11}, Q_1 and Q_2 are the same for the 3 different models.

According to the results obtained, we can conclude that the Bending-Gradient finite element converge to the reference *LS1* solution with a good accuracy for deflection, moments and shear forces for all plate's configuration and bending direction, unlike Abaqus 2D FE which cannot predict plate's behavior for all cases.

5.6.5.5 Discussion

It is seen that for these extreme four cases, the Bending-Gradient FE model can efficiently predict the same response solution as the *LS1* (which was validated in (Naciri et al., 1998; Carreira et al., 2002; Diaz Diaz et al., 2002; Caron et al., 2006; Nguyen and Caron, 2006; Dallot and Sab, 2008; Saeedi et al., 2012a,b, 2013a,b; Lerpiniere et al., 2014; Baroud et al., 2016)) and Abaqus 2D FE. It should be noted, for thick plate (L/h=4), that Abaqus 2D FE is not very efficient as shown by the results above. We have found that the results are actually completely coincident for the 3 models for thin plates (L/h>5). Accordingly, the new Bending-Gradient finite element has been proved as an efficient and reliable model for the study of complex multilayered structures (thick and thin plates) with minimum computational time.

5.7 Conclusion

In this chapter, the Bending-Gradient model for laminated plates, dedicated for out-of-plane load, and its finite element, are presented. An eight-node isoparametric quadrilateral finite element with 7 degrees of freedom at each nodal point has been formulated. The current finite element program called *BGFEAP* has been developed in order to take into account the Bending-Gradient theory. The new proposed finite element program presents a 2D type data structure that provides several advantages over a conventional 3D finite element model: simplified input data, ease of results' interpretation and a huge reduction of calculation time. When comparing the number of degree of freedom, regardless of the number of layers of the laminate, just 7 d.o.f. per node are sufficient which leads to a drastic reduction in the computational time when compared to a 3D FE or even to layerwise models. In view of the previous results, this new model has passed patch test for bending, twisting and shear, and similar results have been obtained when comparing Bending-Gradient FE to analytical solution of the Bending-Gradient model. Also, the Bending-Gradient FE model was compared to exact solution for multilayered plates, where the results of Bending-Gradient FE model has converged to the exact solution for difference slenderness ratio and with multilayer plates with 3 and 9 layers. In addition, the performances of this new element has been compared with those of a standard 2D FE and *LS1* layerwise model. It has been demonstrated that the proposed Bending-Gradient FE model has better performances because it is able to reproduce almost the same results as conventional FE and layerwise model, at a reduced cost. Thus, this new FE model can be used for the predimensioning of highly complex multilayered structures where very good and reliable results are obtained.

In summary, all the comparisons made between the new Bending-Gradient finite element model and different reference solutions, clearly show the usefulness, lightness and efficiency of the Bending-Gradient model as an ESL model for the analysis of complex and huge multilayered structures.

General conclusion and perspectives

An efficient design of multilayered structures requires dedicated numerical tools that cope with their peculiar heterogeneous structure and anisotropy. For the structural engineer, the multilayered plate is conveniently represented as a stack of homogeneous, anisotropic plies. One of the major issues in design and analysis of such plate is related to free-edge effects. It has been demonstrated that differences in elastic properties of adjacent layers generally result in a highly concentrated interlaminar stresses near free edges. This phenomenon can lead to interlaminar failures (delaminations) which may cause global failure of the multilayered structure.

In the light of a solid interest from industry for reliable models, numerous recommendations have been made. We present some crucial necessities for such a model: the principal objective is to simplify a computationally heavy 3D model into a 2D plate model without losing local 3D fields' accuracy. First, good estimation of macroscopic deflection, with no limitation on local material symmetries, the plate theory should be easy to implement with standard finite element program and a good relocalization of 3D fields in order to calculate local stresses.

In this dissertation, two different approaches for the study of multilayered materials have been proposed, implemented and validated: these two 2D models can be classified as layerwise theories and equivalent single layer (ESL) theories.

A layerwise stress model named *LS1*, was proposed in Navier Laboratory. In this model, the multilayered material is considered as a superposition of Reissner-Mindlin plates linked together by interfacial stresses. Even if the *LS1* model is very effective model, it can be still improved: the 3D stress free boundary conditions cannot be exactly met by this model and stresses concentration near free edges.

In order to improve the *LS1* model by removing these drawbacks, a new layerwise model, called *Statically Compatible LS1 (SCLS1)* is developed and presented in this dissertation. As in *LS1*, the laminated plate is still considered as a superposition of Reissner plates coupled by interfacial stresses. However, the divergences of the interlaminar transverse shears are introduced as new generalized efforts.

This model has been implemented in a new version of the in-house finite element program *MPFEAP*. An eight-node and 4 Gauss points isoparametric quadrilateral element with $6n$-1 d.o.f. at each nodal point is formulated (n is the number of layers of the laminate). It should be mentioned that in order to study 3D structures, *LS1* and *SCLS1* models use a 2D description and a 2D planar mesh for the design of such complex structures. In order to validate the new model, different comparisons were made between the new *SCLS1* model, *LS1*, their refined version and Abaqus 3D FE, for laminate under uniaxial tension: the interlaminar shear stresses is studied at a straight free edge, and in the vicinity of a circular hole located in the middle of the plate. Accurate estimations of local response especially near free-edges have been found with *SCLS1* model. The new *SCLS1* model, that has been validated in this dissertation, has shown efficiency with respect to full 3D FE models and has been proven to be very good alternatives to 3D FE models. Several advantages were found for this new layerwise model over a conventional 3D finite element model: simplified input data, ease of results' interpretation and a huge reduction of calculation time; in addition, *SCLS1* model has better performances because it is able to reproduce both stress concentration and free edge boundary conditions at a reduced cost.

Therefore, in this model, the number of governing equations depends on the number of the layers. This increases significantly the computational cost in layerwise approaches. Consequently, a theory belonging to the ESL family is taken into consideration in order to study the multilayer with a limited number of degree of freedom. In ESL theories, the multilayer is considered as a one-layer homogeneous plate with an equivalent global behavior. Therefore, the number of governing equations is independent of the number of plate layers. This theory, called the Bending-Gradient plate theory, dedicated for out-of-plane load, is an extension of the Reissner-Mindlin plate theory

and improves the predictions of shear stress distributions in laminated plates.

The Bending-Gradient model for laminated plates, and its finite element, are presented. The in-house finite element program for Bending-Gradient model, called *BGFEAP* and in parallel an Abaqus User element, have been developed, implemented and validated in this work. An eight-node isoparametric quadrilateral element with 7 d.o.f. at each nodal point with selective integration technique is implemented. The new proposed finite element program presents a 2D type data structure that provides several advantages over a conventional 3D finite element model: simplified input data, ease of results' interpretation and an enormous reduction of calculation time. When comparing the number of degree of freedom, regardless of the number of layers of the laminate, 7 d.o.f. per node are present which lead to a drastic reduction in the computational time when compared to a 3D FE or even to layerwise models. The Bending-Gradient finite element has shown good and reliable results when compared to analytical solution, exact solution, standard 2D FE and *LS1* model, as well as Bending-Gradient finite element has passed patch test for bending, twisting and shear: this proves the usefulness, lightness and efficiency of the Bending-Gradient model as an ESL model for the analysis of complex and huge multilayered structures.

The work presented in this thesis is conceived to study linear elastic behavior for multilayered plates. It may pave the way to extensions to nonlinear mechanical behaviors for both models *SCLS1* and Bending-Gradient.

APPENDIX A

Appendix for the statically compatible layerwise stress model *SCLS1*

A.1 The closed-form expression of the stress energy w^*_{3D}

The constitutive equations derive from the following closed-form expression of w^*_{3D} in terms of the generalized stresses:

$$w^*_{3D} = \sum_{i=1}^{n} w^{*i}_K + w^{*i}_\nu + w^{*i}_c + w^{*i}_Q \tag{211}$$

where:

- w^{*i}_K is the contribution to the elastic energy of the in-plane stresses $\sigma^{3D}_{\alpha\beta}$ of layer i (Kirchhoff):

$$\begin{aligned} w^{*i}_K =& \int_{h_i^-}^{h_i^+} \frac{1}{2} S^{\,i}_{\alpha\beta\gamma\delta} \sigma^{3D}_{\alpha\beta} \sigma^{3D}_{\gamma\delta}\, dz \\ =& \frac{1}{2e^i} S^{\,i}_{\alpha\beta\gamma\delta} N^i_{\alpha\beta} N^i_{\gamma\delta} + \frac{6}{e^{i3}} S^{\,i}_{\alpha\beta\gamma\delta} M^i_{\alpha\beta} M^i_{\gamma\delta} \end{aligned} \tag{212}$$

- w^{*i}_ν is the contribution to the elastic energy of the normal stress σ^{3D}_{33} of layer i:

$$\begin{aligned} w^{*i}_\nu =& \int_{h_i^-}^{h_i^+} \frac{1}{2} S^{\,i}_{3333} \left(\sigma^{3D}_{33}\right)^2 dz \\ =& \frac{e^i}{2} S^{\,i}_{3333} \left(\frac{1}{2} \left(\nu^{i,i+1} + \nu^{i-1,i} \right) + \frac{e^i}{12} \left(\pi^{i,i+1} - \pi^{i-1,i} \right) \right)^2 + \\ & \frac{e^i}{24} S^{\,i}_{3333} \left(\frac{e^i}{10} \left(\pi^{i,i+1} + \pi^{i-1,i} \right) + \frac{6}{5} \left(\nu^{i,i+1} - \nu^{i-1,i} \right) \right)^2 + \\ & \frac{e^i}{10} S^{\,i}_{3333} \left(\frac{e^i}{12} \left(\pi^{i,i+1} - \pi^{i-1,i} \right) \right)^2 + \\ & \frac{e^i}{1400} S^{\,i}_{3333} \left(\left(\nu^{i,i+1} - \nu^{i-1,i} \right) + \frac{e^i}{2} \left(\pi^{i,i+1} + \pi^{i-1,i} \right) \right)^2 \end{aligned} \tag{213}$$

- w^*_c is the contribution to the elastic energy of the coupling between in-plane stresses $\sigma^{3D}_{\alpha\beta}$ and the normal stress σ^{3D}_{33} of layer i:

$$\begin{aligned} w^*_c =& \int_{h_i^-}^{h_i^+} \frac{1}{2} \times 2 S^{\,i}_{\alpha\beta 33} \sigma^{3D}_{\alpha\beta} \sigma^{3D}_{33}\, dz \\ =& S^{\,i}_{\alpha\beta 33} N^i_{\alpha\beta} \left(\frac{1}{2} \left(\nu^{i,i+1} + \nu^{i-1,i} \right) + \frac{e^i}{12} \left(\pi^{i,i+1} - \pi^{i-1,i} \right) \right) + \\ & \frac{1}{e^i} S^{\,i}_{\alpha\beta 33} M^i_{\alpha\beta} \left(\frac{6}{5} \left(\nu^{i,i+1} - \nu^{i-1,i} \right) + \frac{e^i}{10} \left(\pi^{i,i+1} + \pi^{i-1,i} \right) \right) \end{aligned} \tag{214}$$

- w^*_Q is the elastic energy of transverse shear of layer i:

$$
\begin{aligned}
w_Q^* = & \int_{h_i^-}^{h_i^+} \frac{1}{2} \times 4 S^{i}_{\alpha 3 \beta 3} \sigma^{3D}_{\alpha 3} \sigma^{3D}_{\beta 3} \, dz \\
= & \frac{2}{e^i} S^{i}_{\alpha 3 \beta 3} Q^i_\alpha Q^i_\beta + \\
& \frac{e^i}{6} S^{i}_{\alpha 3 \beta 3} \left(\tau_\alpha^{i,i+1} - \tau_\alpha^{i-1,i} \right) \left(\tau_\beta^{i,i+1} - \tau_\beta^{i-1,i} \right) + \\
& \frac{2}{5e^i} S^{i}_{\alpha 3 \beta 3} \left(Q^i_\alpha - \frac{e^i}{2} \left(\tau_\alpha^{i,i+1} + \tau_\alpha^{i-1,i} \right) \right) \left(Q^i_\beta - \frac{e^i}{2} \left(\tau_\beta^{i,i+1} + \tau_\beta^{i-1,i} \right) \right)
\end{aligned}
\tag{215}
$$

A.2 The *SCLS1* finite element equations and matrices

The strain field interpolation $[E]$ a vector of dimension $12n$-4, is written as

$$
[E]^T = \left(\left[E^K \right]^T, [E^\nu]^T, \left[E^Q \right]^T, \left[E^\lambda \right]^T \right) = \left(\sum_{i=1}^{8} [B_i][\delta_i] = [B_1, \ldots, B_8][\delta] \right)^T \tag{216}
$$

Where the $6n$-1 displacement vector $[\delta_i]$ is defined as

$$
[\delta_i]^T = \left(\underbrace{U_1^1,\ U_2^1,\ U_3^1,\ \Phi_1^1,\ \Phi_2^1, \ldots, U_1^n,\ U_2^n,\ U_3^n,\ \Phi_1^n,\ \Phi_2^n,\ V^{1,2}, \ldots, V^{n-1,n}}_{6n-1} \right), \tag{217}
$$

$[\delta]$ is the total displacement vector of the element, of dimension $48n$-8, defined as follows

$$
[\delta] = [\delta_1\ \delta_2\ \delta_3\ \delta_4\ \delta_5\ \delta_6\ \delta_7\ \delta_8] \tag{218}
$$

The $12n$-4 strain vector $[E]$ is defined by separating the components concerning the membrane behavior $\left[E^K \right]$ vector of dimension $6n$, the normal behavior $[E^\nu]$ vector of dimension n-1, the shearing behavior $\left[E^Q \right]$ vector of dimension $4n$-2 and the behavior related to λ, $\left[E^\lambda \right]$ vector of dimension n-1 as follows:

$$
[E^K] = \sum_{i=1}^{8} [B_i^K][\delta_i] = [B_1^K, \ldots, B_8^K][\delta] \tag{219}
$$

$$
[E^\nu] = \sum_{i=1}^{8} [B_i^\nu][\delta_i] = [B_1^\nu, \ldots, B_8^\nu][\delta] \tag{220}
$$

$$
[E^Q] = \sum_{i=1}^{8} [B_i^Q][\delta_i] = [B_1^Q, \ldots, B_8^Q][\delta] \tag{221}
$$

$$
[E^\lambda] = \sum_{i=1}^{8} [B_i^\lambda][\delta_i] = [B_1^\lambda, \ldots, B_8^\lambda][\delta] \tag{222}
$$

The total matrix B^{total} of dimension $(12n-4) \times (48n-8)$ is defined as

$$B^{total} = \begin{bmatrix} B_1^K & B_2^K & B_3^K & B_4^K & B_5^K & B_6^K & B_7^K & B_8^K \\ B_1^\nu & B_2^\nu & B_3^\nu & B_4^\nu & B_5^\nu & B_6^\nu & B_7^\nu & B_8^\nu \\ B_1^Q & B_2^Q & B_3^Q & B_4^Q & B_5^Q & B_6^Q & B_7^Q & B_8^Q \\ B_1^\lambda & B_2^\lambda & B_3^\lambda & B_4^\lambda & B_5^\lambda & B_6^\lambda & B_7^\lambda & B_8^\lambda \end{bmatrix} \tag{223}$$

The matrix B_i^K of dimension $6n\times(6n\text{-}1)$ is defined as

$$B_i^K = \begin{bmatrix} N_{i,x} & 0 & 0 & 0 & 0 & . & . & . & . & . & . & . & 0 & . & . & 0 \\ 0 & N_{i,y} & 0 & 0 & 0 & . & . & . & . & . & . & . & 0 & . & . & 0 \\ N_{i,y} & N_{i,x} & 0 & 0 & 0 & . & . & . & . & . & . & . & 0 & . & . & 0 \\ 0 & 0 & 0 & N_{i,x} & 0 & . & . & . & . & . & . & . & 0 & . & . & 0 \\ 0 & 0 & 0 & 0 & N_{i,y} & . & . & . & . & . & . & . & 0 & . & . & 0 \\ 0 & 0 & 0 & N_{i,y} & N_{i,x} & . & . & . & . & . & . & . & 0 & . & . & 0 \\ . & . & . & . & . & . & . & . & . & . & . & . & . & . & . & . \\ . & . & . & . & . & . & . & . & . & . & . & . & . & . & . & . \\ . & . & . & . & . & . & . & N_{i,x} & 0 & 0 & 0 & 0 & 0 & . & . & 0 \\ . & . & . & . & . & . & . & 0 & N_{i,y} & 0 & 0 & 0 & 0 & . & . & 0 \\ . & . & . & . & . & . & . & N_{i,y} & N_{i,x} & 0 & 0 & 0 & 0 & . & . & 0 \\ . & . & . & . & . & . & . & 0 & 0 & 0 & N_{i,x} & 0 & 0 & . & . & 0 \\ . & . & . & . & . & . & . & 0 & 0 & 0 & 0 & N_{i,y} & 0 & . & . & 0 \\ . & . & . & . & . & . & . & 0 & 0 & 0 & N_{i,y} & N_{i,x} & 0 & . & . & 0 \end{bmatrix} \tag{224}$$

The matrix B_i^ν of dimension $(n-1)\times(6n-1)$ is defined as

$$B_i^\nu = \begin{bmatrix} 0 & 0 & -N_i & 0 & 0 & 0 & 0 & N_i & 0 & 0 & . & . & . & . & . & . & . & . & . & . & 0 & . & 0 \\ . & . & . & . & . & 0 & 0 & -N_i & 0 & 0 & . & . & . & . & . & . & . & . & . & . & 0 & . & 0 \\ . & . & . & . & . & . & . & . & . & . & . & . & . & . & . & . & . & . & . & . & 0 & . & 0 \\ . & . & . & . & . & . & . & . & . & . & . & . & . & . & . & . & . & . & . & . & 0 & . & 0 \\ . & . & . & . & . & . & . & . & . & . & . & . & . & -N_i & 0 & 0 & 0 & 0 & N_i & 0 & 0 & 0 & . & 0 \end{bmatrix} \tag{225}$$

The matrix B_i^Q of dimension $(4n-2)\times(6n-1)$ is defined as

$$
B_i^Q = \left[\begin{array}{cccccccccccccccc}
0 & 0 & N_{i,x} & N_i & 0 & 0 & 0 & 0 & 0 & 0 & . & . & . & . & . \\
0 & 0 & N_{i,y} & 0 & N_i & 0 & 0 & 0 & 0 & 0 & . & . & . & . & . \\
-N_i & 0 & 0 & -\frac{e^1}{2}N_i & 0 & N_i & 0 & 0 & -\frac{e^2}{2}N_i & 0 & . & . & . & . & . \\
0 & -N_i & 0 & 0 & -\frac{e^1}{2}N_i & 0 & N_i & 0 & 0 & -\frac{e^2}{2}N_i & . & . & . & . & . \\
. & . & . & . & . & . & . & . & . & . & . & . & . & . & . \\
. & . & . & . & . & . & . & . & . & . & . & . & . & . & . \\
. & . & . & . & . & . & . & . & . & . & . & . & -N_i & 0 & 0 \\
. & . & . & . & . & . & . & . & . & . & . & . & 0 & -N_i & 0 \\
. & . & . & . & . & . & . & . & . & . & . & . & 0 & 0 & 0 \\
. & . & . & . & . & . & . & . & . & . & . & . & 0 & 0 & 0
\end{array}\right.
$$

$$
\left.\begin{array}{ccccccccc}
. & . & . & . & . & . & 0 & . & 0 \\
. & . & . & . & . & . & 0 & . & 0 \\
. & . & . & . & . & . & N_{i,x} & . & 0 \\
. & . & . & . & . & . & N_{i,y} & . & 0 \\
. & . & . & . & . & . & . & . & . \\
. & . & . & . & . & . & . & . & . \\
-\frac{e^{n-1}}{2}N_i & 0 & N_i & 0 & 0 & -\frac{e^n}{2}N_i & 0 & 0 & . & N_{i,x} \\
0 & -\frac{e^{n-1}}{2}N_i & 0 & N_i & 0 & 0 & -\frac{e^n}{2}N_i & 0 & . & N_{i,y} \\
0 & 0 & 0 & 0 & N_{i,x} & N_i & 0 & 0 & . & 0 \\
0 & 0 & 0 & 0 & N_{i,y} & 0 & N_i & 0 & . & 0
\end{array}\right] \tag{226}
$$

The matrix B_i^λ of dimension $(n-1)\times(6n-1)$ is defined as

$$
B_i^\lambda = \left[\begin{array}{cccccccc}
0 & . & . & 0 & N_i & . & . & 0 \\
. & . & . & . & . & . & . & . \\
. & . & . & . & . & . & . & . \\
0 & . & . & 0 & 0 & . & . & N_i
\end{array}\right] \tag{227}
$$

A.2.1 Stress-strain relation

The *SCLS1* generalized strains and stresses relationship can be expressed in the matrix from as

$$
[E] = [S][\Sigma] + [E^o] \tag{228}
$$

The vector contains terms related to surface stresses $\underline{T}^-$ and $\underline{T}^+$. These are problem data. So we are dealing with a problem with initial deformation. Its resolution is the subject of the next section. where The compliance matrix S of dimension (12n-4)×(12n-4) are

$$
S = \left[\begin{array}{cccc}
S^K & S^{K\nu} & 0 & S^{K\pi} \\
S^{\nu K} & S^{\nu} & 0 & S^{\nu\pi} \\
0 & 0 & S^Q & 0 \\
S^{\pi K} & S^{\pi\nu} & 0 & S^{\pi}
\end{array}\right] \tag{229}
$$

Where the compliance matrices S^K, S^ν, S^Q, S^π, $S^{K\nu}$, $S^{K\pi}$, $S^{\nu K}$, $S^{\nu\pi}$, $S^{\pi K}$ and $S^{\pi\nu}$:
The matrix S^K of dimension $6n\times 6n$ is defined as

$$S^K = \begin{bmatrix} S_1^K & 0 & . & . & 0 \\ 0 & S_2^K & . & . & 0 \\ . & . & . & . & . \\ 0 & 0 & . & . & S_n^K \end{bmatrix} \tag{230}$$

where

$$S^K = \begin{bmatrix} \frac{S_{11}^1}{e^1} & \frac{S_{12}^1}{e^1} & \frac{S_{16}^1}{e^1} & 0 & 0 & 0 \\ \frac{S_{21}^1}{e^1} & \frac{S_{22}^1}{e^1} & \frac{S_{26}^1}{e^1} & 0 & 0 & 0 \\ \frac{S_{16}^1}{e^1} & \frac{S_{26}^1}{e^1} & \frac{S_{66}^1}{e^1} & 0 & 0 & 0 \\ 0 & 0 & 0 & \frac{12S_{11}^1}{(e^1)^3} & \frac{12S_{12}^1}{(e^1)^3} & \frac{12S_{16}^1}{(e^1)^3} \\ 0 & 0 & 0 & \frac{12S_{21}^1}{(e^1)^3} & \frac{12S_{22}^1}{(e^1)^3} & \frac{12S_{26}^1}{(e^1)^3} \\ 0 & 0 & 0 & \frac{12S_{16}^1}{(e^1)^3} & \frac{12S_{26}^1}{(e^1)^3} & \frac{12S_{66}^1}{(e^1)^3} \end{bmatrix} \tag{231}$$

The matrix S^ν of dimension $(n-1)\times(n-1)$ is defined as

$$S^\nu = \begin{bmatrix} \frac{13(e^1S_{33}^1+e^2S_{33}^2)}{35} & \frac{9e^2S_{33}^2}{70} & . & . & . \\ \frac{9e^2S_{33}^2}{70} & \frac{13(e^2S_{33}^2+e^3S_{33}^3)}{35} & \frac{9e^3S_{33}^3}{70} & . & . \\ . & . & . & . & . \\ . & . & \frac{9e^{n-2}S_{33}^{n-2}}{70} & \frac{13(e^{n-2}S_{33}^{n-2}+e^{n-1}S_{33}^{n-1})}{35} & \frac{9e^{n-1}S_{33}^{n-1}}{70} \\ . & . & . & \frac{9e^{n-1}S_{33}^{n-1}}{70} & \frac{13(e^{n-1}S_{33}^{n-1}+e^nS_{33}^n)}{35} \end{bmatrix} \tag{232}$$

where S_{33}^j is flexibility on the snatching forces of the layer j (r.f. section A.2.2.3).
The matrix S^Q of dimension $(4n-2)\times(4n-2)$ is defined as

$$S^Q = \begin{bmatrix} \frac{6S_Q^1}{5e^1} & \frac{-S_Q^1}{10} & 0 & 0 & . & . & . & . & . & . & . \\ \frac{-S_Q^1}{10} & \frac{2(e^1S_Q^1+e^2S_Q^2)}{15} & \frac{-S_Q^2}{10} & \frac{-e^2S_Q^2}{30} & . & . & . & . & . & . & . \\ 0 & \frac{-S_Q^2}{10} & \frac{6S_Q^2}{5e^2} & \frac{-S_Q^2}{10} & 0 & 0 & . & . & . & . & . \\ 0 & \frac{-e^2S_Q^2}{30} & \frac{-S_Q^2}{10} & \frac{2(e^2S_Q^2+e^3S_Q^3)}{15} & \frac{-S_Q^3}{10} & \frac{-e^3S_Q^3}{30} & . & . & . & . & . \\ . & . & 0 & \frac{-S_Q^3}{10} & \frac{6S_Q^3}{5e^3} & \frac{-S_Q^3}{10} & 0 & 0 & . & . & . \\ . & . & 0 & \frac{-e^3S_Q^3}{30} & \frac{-S_Q^3}{10} & \frac{2(e^3S_Q^3+e^4S_Q^4)}{15} & \frac{-S_Q^4}{10} & \frac{-e^4S_Q^4}{30} & . & . & . \\ . & . & . & . & . & . & . & . & . & \frac{-S_Q^n}{10} & \frac{6S_Q^n}{5e^n} \end{bmatrix} \tag{233}$$

where S_Q^j is the shear flexibility of the layer j (r.f. section A.2.2.2).
The matrix S^π of dimension $(n-1)\times(n-1)$ is defined as

$$S^{\pi} = \begin{bmatrix} \frac{1}{105}\left(e^{1^3} S_{\nu}^{1} + e^{2^3} S_{\nu}^{2}\right) & -\frac{e^{2^3}}{140} S_{\nu}^{2} & 0 & . & . & . \\ -\frac{e^{2^3}}{140} S_{\nu}^{2} & \frac{1}{105}\left(e^{2^3} S_{\nu}^{2} + e^{3^3} S_{\nu}^{3}\right) & -\frac{e^{3^3}}{140} S_{\nu}^{3} & . & . & . \\ . & . & . & . & . & . \\ . & . & . & . & . & . \\ . & . & . & . & . & -\frac{e^{n-1^3}}{140} S_{\nu}^{n-1} \\ & & & & & \\ & & & & & \\ & & & & & \\ & & & & & \\ & & & & & \\ & & & & & \frac{1}{105}\left(e^{n-1^3} S_{\nu}^{n-1} + e^{n^3} S_{\nu}^{n}\right) \end{bmatrix} \tag{234}$$

The matrix $S^{K\nu}$ of dimension $6n \times (n-1)$ is defined as

$$S^{K\nu} = \begin{bmatrix} \frac{S_3^1}{4} & 0 & 0 & . & . & . & . \\ \frac{3S_3^1}{5e^1} & 0 & 0 & . & . & . & . \\ \frac{S_3^2}{4} & \frac{S_3^2}{4} & 0 & . & . & . & . \\ \frac{-3S_3^2}{5e^2} & \frac{3S_3^2}{5e^2} & 0 & . & . & . & . \\ 0 & \frac{S_3^3}{4} & \frac{S_3^3}{4} & . & . & . & . \\ 0 & \frac{-3S_3^3}{5e^3} & \frac{3S_3^3}{5e^3} & . & . & . & . \\ . & . & . & . & . & . & . \\ . & . & . & . & . & . & . \\ . & . & . & . & . & \frac{S_3^{n-1}}{4} & \frac{S_3^{n-1}}{4} \\ . & . & . & . & . & \frac{-3S_3^{n-1}}{5e^{n-1}} & \frac{3S_3^{n-1}}{5e^{n-1}} \\ . & . & . & . & . & 0 & \frac{S_3^n}{4} \\ . & . & . & . & . & 0 & \frac{-3S_3^n}{5e^n} \end{bmatrix} \tag{235}$$

where S_3^j is the flexibility of coupling between the membrane and snatching stresses of the layer j (r.f. section A.2.2.4).

The matrix $S^{K\pi}$ of dimension $6n \times (n-1)$ is defined as

$$S^{K\pi} = \begin{bmatrix} \frac{S_3^1 e^1}{24} & 0 & . & . & . \\ \frac{S_3^1}{20} & 0 & . & . & . \\ \frac{-S_3^2 e^2}{24} & \frac{S_3^2 e^2}{24} & . & . & . \\ \frac{S_3^2}{20} & \frac{S_3^2}{20} & . & . & . \\ . & . & . & . & . \\ . & . & . & . & . \\ . & . & . & . & \frac{-S_3^n e^n}{24} \\ . & . & . & . & \frac{S_3^n}{20} \end{bmatrix} \tag{236}$$

The matrix $S^{\nu K}$ of dimension $(n-1) \times 6n$ is defined as

$$S^{\nu K} = \begin{bmatrix} \frac{S_3^1}{4} & \frac{3S_3^1}{5e^1} & \frac{S_3^2}{4} & -\frac{3S_3^2}{5e^2} & 0 & 0 & . & . & . & . & . & . \\ 0 & 0 & \frac{S_3^2}{4} & \frac{3S_3^2}{5e^2} & \frac{S_3^3}{4} & -\frac{3S_3^3}{5e^3} & . & . & . & . & . & . \\ . & . & . & . & . & . & . & . & . & . & . & . \\ . & . & . & . & . & . & . & . & . & . & . & . \\ . & . & . & . & . & . & . & \frac{S_3^{n-1}}{4} & \frac{3S_3^{n-1}}{5e^{n-1}} & \frac{S_3^n}{4} & -\frac{3S_3^n}{5e^n} \end{bmatrix} \tag{237}$$

The matrix $S^{\nu\pi}$ of dimension $(n-1)\times(n-1)$ is defined as

$$S^{\nu\pi} = \begin{bmatrix} \frac{11}{210}\left(e^{1^2}S_\nu^1 - e^{2^2}S_\nu^2\right) & \frac{13}{420}e^{2^2}S_\nu^2 & 0 & . & . \\ -\frac{13}{420}e^{2^2}S_\nu^2 & \frac{11}{210}\left(e^{2^2}S_\nu^2 - e^{3^2}S_\nu^3\right) & \frac{13}{420}e^{3^2}S_\nu^3 & . & . \\ . & . & . & . & . \\ . & . & . & . & . \\ . & . & . & . & . \\ . & . & & & \\ . & . & & & \\ . & . & & & \\ . & . & & & \\ -\frac{13}{420}e^{n-1^2}S_\nu^{n-1} & \frac{11}{210}\left(e^{n-1^2}S_\nu^{n-1} - e^{n^2}S_\nu^n\right) & & & \end{bmatrix} \tag{238}$$

The matrix $S^{\pi K}$ of dimension $(n-1)\times 6n$ is defined as

$$S^{\pi K} = \begin{bmatrix} \frac{e^1S_3^1}{24} & \frac{S_3^1}{20} & -\frac{e^2S_3^2}{24} & \frac{S_3^2}{20} & 0 & 0 & . & . & . & . & . & . \\ 0 & 0 & \frac{e^2S_3^2}{24} & \frac{S_3^2}{20} & -\frac{e^3S_3^3}{24} & \frac{S_3^3}{20} & . & . & . & . & . & . \\ . & . & . & . & . & . & . & . & . & . & . & . \\ . & . & . & . & . & . & . & . & . & . & . & . \\ . & . & . & . & . & . & . & \frac{e^{n-1}S_3^{n-1}}{24} & \frac{S_3^{n-1}}{20} & -\frac{e^nS_3^n}{24} & \frac{S_3^n}{20} \end{bmatrix} \tag{239}$$

The matrix $S^{\pi\nu}$ of dimension $(n-1)\times(n-1)$ is defined as

$$S^{\pi\nu} = \begin{bmatrix} \frac{11}{210}\left(e^{1^2}S_\nu^1 - e^{2^2}S_\nu^2\right) & -\frac{13}{420}e^{2^2}S_\nu^2 & 0 & . & . \\ \frac{13}{420}e^{2^2}S_\nu^2 & \frac{11}{210}\left(e^{2^2}S_\nu^2 - e^{3^2}S_\nu^3\right) & -\frac{13}{420}e^{3^2}S_\nu^3 & . & . \\ . & . & . & . & . \\ . & . & . & . & . \\ . & . & . & . & . \\ . & . & . & . & . \\ . & . & . & & \\ . & . & . & & \\ . & . & . & & \\ . & . & . & & \\ . & . & . & & \\ \frac{13}{420}e^{n-2^2}S_\nu^{n-2} & \frac{11}{210}\left(e^{n-2^2}S_\nu^{n-2} - e^{n-1^2}S_\nu^{n-1}\right) & -\frac{13}{420}e^{n-1^2}S_\nu^{n-1} & & \\ 0 & \frac{13}{420}e^{n-1^2}S_\nu^{n-1} & \frac{11}{210}\left(e^{n-1^2}S_\nu^{n-1} - e^{n^2}S_\nu^n\right) & & \end{bmatrix} \tag{240}$$

The vector of initial deformations E^0 due to surface stresses imposed, of dimension $12n$-4 is defined by

$$E^o = \left\{ \begin{array}{c} E^{K^0} \\ 0 \\ . \\ 0 \\ E^{K^{n+1}} \\ \frac{9}{70} e^1 S^1_{33} \nu^{0,1} - \frac{13 e^{1^2}}{420} S^1_{33} \pi^{0,1} \\ 0 \\ . \\ 0 \\ \frac{9}{70} e^n S^n_{33} \nu^{n,n+1} + \frac{13 e^{n^2}}{420} S^n_{33} \pi^{n,n+1} \\ E^{Q^0} \\ 0 \\ . \\ 0 \\ E^{Q^{n+1}} \\ \frac{13}{420} e^{1^2} S^1_{33} \nu^{0,1} - \frac{e^{1^3}}{140} S^1_{33} \pi^{0,1} \\ 0 \\ . \\ 0 \\ -\frac{13}{420} e^{n^2} S^n_{33} \nu^{n,n+1} - \frac{e^{n^3}}{140} S^n_{33} \pi^{n,n+1} \end{array} \right\} \begin{array}{c} 1 \to 6 \\ 7 \\ \downarrow \\ 6n-6 \\ 6n-5 \to 6n \\ 6n+1 \\ 6n+2 \\ \downarrow \\ 7n-2 \\ 7n-1 \\ 7n \to 7n+3 \\ 7n+4 \\ \downarrow \\ 11n-7 \\ 11n-6 \to 11n-3 \\ 11n-2 \\ 11n-1 \\ \downarrow \\ 12n-3 \\ 12n-4 \end{array} \tag{241}$$

where

$$E^{K^0} = \left\{ \begin{array}{c} \frac{S^1_{13}}{4} \nu^{0,1} - \frac{e^1}{24} S^1_{13} \pi^{0,1} \\ \frac{S^1_{23}}{4} \nu^{0,1} - \frac{e^1}{24} S^1_{23} \pi^{0,1} \\ \frac{S^1_{36}}{4} \nu^{0,1} - \frac{e^1}{24} S^1_{36} \pi^{0,1} \\ -\frac{3}{5e^1} S^1_{13} \nu^{0,1} + \frac{1}{20} S^1_{13} \pi^{0,1} \\ -\frac{3}{5e^1} S^1_{23} \nu^{0,1} + \frac{1}{20} S^1_{23} \pi^{0,1} \\ -\frac{3}{5e^1} S^1_{36} \nu^{0,1} + \frac{1}{20} S^1_{36} \pi^{0,1} \end{array} \right\}$$

$$E^{K^{n+1}} = \begin{Bmatrix} \frac{S^n_{13}}{4}\nu^{n,n+1} + \frac{e^n}{24}S^n_{13}\pi^{n,n+1} \\ \frac{S^n_{23}}{4}\nu^{n,n+1} + \frac{e^n}{24}S^n_{23}\pi^{n,n+1} \\ \frac{S^n_{36}}{4}\nu^{n,n+1} + \frac{e^n}{24}S^n_{36}\pi^{n,n+1} \\ \frac{3}{5e^n}S^n_{13}\nu^{n,n+1} + \frac{1}{20}S^n_{13}\pi^{n,n+1} \\ \frac{3}{5e^n}S^n_{23}\nu^{n,n+1} + \frac{1}{20}S^n_{23}\pi^{n,n+1} \\ \frac{3}{5e^n}S^n_{36}\nu^{n,n+1} + \frac{1}{20}S^n_{36}\pi^{n,n+1} \end{Bmatrix}$$

$$E^{Q^0} = \begin{Bmatrix} -\frac{1}{10}(S^1_{55}\tau^{0,1}_x + S^1_{54}\tau^{0,1}_y) \\ -\frac{1}{10}(S^1_{45}\tau^{0,1}_x + S^1_{44}\tau^{0,1}_y) \\ -\frac{e^1}{30}(S^1_{55}\tau^{0,1}_x + S^1_{54}\tau^{0,1}_y) \\ -\frac{e^1}{30}(S^1_{45}\tau^{0,1}_x + S^1_{44}\tau^{0,1}_y) \end{Bmatrix}$$

$$E^{Q^{n+1}} = \begin{Bmatrix} -\frac{e^n}{30}(S^n_{55}\tau^{n,n+1}_x + S^n_{54}\tau^{n,n+1}_y) \\ -\frac{e^n}{30}(S^n_{45}\tau^{n,n+1}_x + S^n_{44}\tau^{n,n+1}_y) \\ -\frac{1}{10}(S^n_{55}\tau^{n,n+1}_x + S^n_{54}\tau^{n,n+}_y) \\ -\frac{1}{10}(S^n_{45}\tau^{n,n+1}_x + S^n_{44}\tau^{n,n+}_y) \end{Bmatrix}$$

A.2.2 Behavior matrices

Terms definition:

c	=	$\cos\theta$
s	=	$\sin\theta$
E_L, E_T, E_N	=	Longitudinal, Transverse and Normal Young's moduli respectively
G	=	Shear modulus
ν	=	Poisson's ratio
L, T and N axes and angle θ	=	These axes and angle are detailed in Fig. A.1

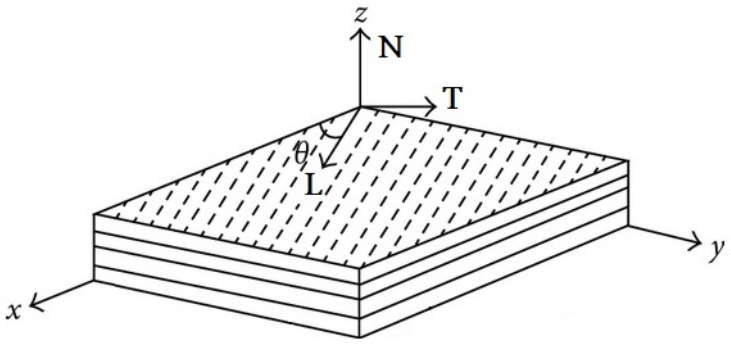


Fig. A.1. Description of fiber orientation axes and angle.

A.2.2.1 Membrane behavior

The plane part of S^i 3×3, consisting of $S_{\alpha\beta\delta\gamma}$ with $\alpha,\beta,\delta,\gamma = 1,2$ that characterize the behavior of the membrane plate.

$$S^i = \begin{bmatrix} S_{11} & S_{12} & S_{16} \\ S_{21} & S_{22} & S_{26} \\ S_{61} & S_{62} & S_{66} \end{bmatrix} \tag{242}$$

where

$$\begin{aligned}
S_{11} &= \frac{c^4}{E_L} - \frac{2c^2s^2\nu_{LT}}{E_L} + \frac{s^4}{E_T} + \frac{c^2s^2}{G_{LT}} \\
S_{12} = S_{21} &= \frac{c^2s^2}{E_L} - \frac{c^4\nu_{LT}}{E_L} - \frac{s^4\nu_{LT}}{E_L} + \frac{c^2s^2}{E_T} - \frac{c^2s^2}{G_{LT}} \\
S_{22} &= \frac{s^4}{E_L} - \frac{2c^2s^2\nu_{LT}}{E_L} + \frac{c^4}{E_T} + \frac{c^2s^2}{G_{LT}} \\
S_{16} = S_{61} &= \frac{2c^3s}{E_L} - \frac{2cs^3\nu_{LT}}{E_L} + \frac{2c^3s\nu_{LT}}{E_L} - \frac{2cs^3}{E_T} - \frac{c^3s}{G_{LT}} + \frac{cs^3}{G_{LT}} \\
S_{26} = S_{62} &= \frac{2cs^3}{E_L} - \frac{2c^3s\nu_{LT}}{E_L} + \frac{2cs^3\nu_{LT}}{E_L} - \frac{2c^3s}{E_T} + \frac{c^3s}{G_{LT}} - \frac{cs^3}{G_{LT}} \\
S_{66} &= \frac{4c^2s^2}{E_L} + \frac{8c^2s^2\nu_{LT}}{E_L} + \frac{4c^2s^2}{E_T} + \frac{c^4}{G_{LT}} + \frac{s^4}{G_{LT}} - \frac{2c^2s^2}{G_{LT}}
\end{aligned}$$

A.2.2.2 Transverse shear behavior

We identify the matrix S^i_Q 2×2 linking shear and transverse strain.

$$S^i_Q = \begin{bmatrix} S_{44} & S_{45} \\ S_{54} & S_{55} \end{bmatrix} \tag{243}$$

where

$$\begin{aligned}
S_{44} &= \frac{c^2}{G_{TN}} + \frac{s^2}{G_{LN}} \\
S_{45} = S_{54} &= \frac{cs}{G_{LN}} - \frac{cs}{G_{TN}} \\
S_{55} &= \frac{c^2}{G_{LN}} + \frac{s^2}{G_{TN}}
\end{aligned}$$

A.2.2.3 Snatching efforts behavior

We identify the matrix S_{ν}^{i} 1×1 of the three-dimensional snatching efforts.

$$S_{\nu}^{i} = \left[\begin{array}{c} S_{33} \end{array} \right] = \left[\begin{array}{c} \frac{1}{E_N} \end{array} \right] \tag{244}$$

A.2.2.4 Coupling behavior between membrane and snatching forces

We identify the matrix S_{3}^{i} 1×3 or 3×1 characteristic of the coupling between the membrane three-dimensional and snatching efforts.

$$S_{3}^{i} = \left[\begin{array}{ccc} S_{31} & S_{32} & S_{63} \end{array} \right] \tag{245}$$

or

$$S_{3}^{i} = \left[\begin{array}{c} S_{13} \\ S_{23} \\ S_{36} \end{array} \right] \tag{246}$$

where

$$\begin{aligned} S_{13} = S_{31} &= -\frac{c^2 \nu_{LN}}{E_L} - \frac{s^2 \nu_{TN}}{E_T} \\ S_{23} = S_{32} &= -\frac{s^2 \nu_{LN}}{E_L} - \frac{c^2 \nu_{TN}}{E_T} \\ S_{36} = S_{63} &= -\frac{2cs\nu_{LN}}{E_L} + \frac{2cs\nu_{TN}}{E_T} \end{aligned}$$

APPENDIX B

Appendix for the Bending-Gradient model

B.1 Other boundary conditions

The Bending-Gradient theory has been presented for laminated plates which are clamped at their lateral boundaries. Nevertheless, this theory can handle other situations where some components of the boundary conditions (166) can be relaxed on some part of $\partial\omega$.

In this section, $\underline{\boldsymbol{n}}$ and $\underline{\boldsymbol{t}}$ denote respectively the outer normal to the plate boundary $\partial\omega$ and the tangent vector to $\partial\omega$. It is thus convenient to express directly the component of plate tensor fields in this local basis. This allows the following shorter notation: $\underline{\boldsymbol{n}} \cdot \underset{\sim}{\boldsymbol{M}} \cdot \underline{\boldsymbol{t}} = M_{\alpha\beta} n_\alpha t_\beta = M_{nt}$ or $\underline{\boldsymbol{t}} \cdot (\underset{\approx}{\boldsymbol{\Phi}} \cdot \underline{\boldsymbol{n}}) \cdot \underline{\boldsymbol{t}} = \Phi_{\alpha\beta\gamma} t_\alpha t_\beta n_\gamma = \Phi_{ttn}$.

One can see from the weak formulation of the equilibrium equations that $\underset{\sim}{\boldsymbol{M}}$ and $(\underset{\approx}{\boldsymbol{i}} \vdots \underset{\sim}{\boldsymbol{R}}) \cdot \underline{\boldsymbol{n}} = \underline{\boldsymbol{Q}} \cdot \underline{\boldsymbol{n}}$ are respectively in duality with $\underset{\approx}{\boldsymbol{\Phi}} \cdot \underline{\boldsymbol{n}}$ and U_3 on the boundary $\partial\omega$. The out-of-plane work $(\underline{\boldsymbol{Q}} \cdot \underline{\boldsymbol{n}}) U_3$ is the same as in Reissner-Mindlin plate theory. However, the work $\underset{\sim}{\boldsymbol{M}} : (\underset{\approx}{\boldsymbol{\Phi}} \cdot \underline{\boldsymbol{n}})$ is related to the generalized rotation and needs interpretation.

Because $\underset{\approx}{\boldsymbol{\Phi}}$ is in $\underset{\approx}{\boldsymbol{\mathcal{S}}}$, the boundary condition may degenerate depending on the dimension of $\underset{\approx}{\boldsymbol{\mathcal{S}}}$. Hence $\underset{\approx}{\boldsymbol{\Phi}} \cdot \underline{\boldsymbol{n}}$ must be in the subspace $\underset{\sim}{\boldsymbol{\mathcal{S}}}(\underline{\boldsymbol{n}})$:

$$\underset{\sim}{\boldsymbol{\mathcal{S}}}\left(\underline{\boldsymbol{n}}\right) = \left\{ \underset{\sim}{\boldsymbol{X}} \in \mathbb{R}_{\underset{\sim}{s}} \mid \exists \underset{\sim}{\boldsymbol{X}} \in \underset{\approx}{\boldsymbol{\mathcal{S}}},\ \ \underset{\sim}{\boldsymbol{X}} = \underset{\sim}{\boldsymbol{X}} \cdot \underline{\boldsymbol{n}} \right\}. \tag{247}$$

Here, $\mathbb{R}_{\underset{\sim}{s}}$ is the usual vector space of symmetric second order tensors:

$$\mathbb{R}_{\underset{\sim}{s}} = \left\{ \underset{\sim}{\boldsymbol{X}} = \left(X_{\alpha\beta}\right) \in \mathbb{R}^4 \mid X_{\alpha\beta} = X_{\beta\alpha} \right\}. \tag{248}$$

Depending on the Bending-Gradient shear compliance tensor, the subspace $\underset{\sim}{\boldsymbol{\mathcal{S}}}(\underline{\boldsymbol{n}})$ has only dimension two or three. Indeed, it has been established in the first part that all $\underset{\approx}{\boldsymbol{\Phi}}$ of the form $\underset{\approx}{\boldsymbol{\Phi}} = \underset{\approx}{\boldsymbol{i}} \cdot \underline{\boldsymbol{\varphi}}$, where $\underline{\boldsymbol{\varphi}}$ is a two-component vector, are in $\underset{\approx}{\boldsymbol{\mathcal{S}}}$. This form corresponds to the case where the rank of $\underset{\approx}{\boldsymbol{h}}$ is only 2 and the Bending-Gradient is turned into a Reissner-Mindlin theory. We have: $\left(\underset{\approx}{\boldsymbol{i}} \cdot \underline{\boldsymbol{\varphi}}\right) \cdot \underline{\boldsymbol{n}} = \underline{\boldsymbol{\varphi}} \otimes \underline{\boldsymbol{n}}$. Hence, the subspace of $\underset{\sim}{\boldsymbol{\mathcal{S}}}(\underline{\boldsymbol{n}})$ generated by $\underset{\approx}{\boldsymbol{\Phi}} = \underset{\approx}{\boldsymbol{i}} \cdot \underline{\boldsymbol{\varphi}}$ has dimension two. So, if the dimension of $\underset{\sim}{\boldsymbol{\mathcal{S}}}(\underline{\boldsymbol{n}})$ is exactly two, then it is necessarily of the form $\underline{\boldsymbol{\varphi}} \otimes \underline{\boldsymbol{n}}$, or equivalently:

$$\underset{\sim}{\boldsymbol{\mathcal{S}}}\left(\underline{\boldsymbol{n}}\right) = \left\{ \underset{\sim}{\boldsymbol{X}} \in \mathbb{R}_{\underset{\sim}{s}} \mid X_{tt} = 0 \right\}. \tag{249}$$

In other words, this means that, if the dimension of $\underset{\sim}{\boldsymbol{\mathcal{S}}}(\underline{\boldsymbol{n}})$ is 2, then the component Φ_{ttn} is already set to 0. Note that when the Bending-Gradient theory is actually a Reissner-Mindlin's one, all the $\underset{\approx}{\boldsymbol{\Phi}}$ in $\underset{\approx}{\boldsymbol{\mathcal{S}}}$ are of the form $\underset{\approx}{\boldsymbol{i}} \cdot \underline{\boldsymbol{\varphi}}$. Hence, in this specific case, the dimension of $\underset{\sim}{\boldsymbol{\mathcal{S}}}(\underline{\boldsymbol{n}})$ is exactly two.

Free boundary conditions

Free boundary conditions are prescribed vanishing all static degrees of freedom working on the boundary.

Considering first the case $\dim \underset{\sim}{\boldsymbol{\mathcal{S}}}(\underline{\boldsymbol{n}}) = 3$ this leads to:

$$\underset{\sim}{\boldsymbol{M}} = \underset{\sim}{\boldsymbol{0}} \quad \text{and} \quad \underline{\boldsymbol{Q}} \cdot \underline{\boldsymbol{n}} = 0. \tag{250}$$

Contrary to the Reissner-Mindlin plate theory, there is an additional condition: $M_{tt} = 0$ on the boundary. Since $M_{tt} = \langle x_3 \sigma_{tt} \rangle$, it seems to involve a 3D stress component to which no 3D boundary condition should apply. Actually it does through the stress localization: $\sigma^{BG}_{nn} = s^M_{nntt} M_{tt}$ and $\sigma^{BG}_{tn} = s^M_{tntt} M_{tt}$. Indeed, s^M_{nntt} and s^M_{tntt} do not vanish in general and generate a local stress σ^{BG}_{nn} and σ^{BG}_{nt} related to M_{tt}. The requirement $M_{tt} = 0$ is thus related to a boundary layer ensuring $\sigma^{BG}_{nn} = \sigma^{BG}_{nt} = 0$.

Assuming now that dim $\underset{\sim}{\boldsymbol{\mathcal{S}}}(\underline{\boldsymbol{n}}) = 2$, it is possible to prove that M_{tt} is not required to vanish in order to ensure 3D free boundary condition. Then the free boundary condition becomes identical to Reissner-Mindlin theory:

$$\underset{\sim}{\boldsymbol{M}} \cdot \underline{\boldsymbol{n}} = \underset{\sim}{\boldsymbol{0}} \quad \text{and} \quad \underset{\sim}{\boldsymbol{Q}} \cdot \underline{\boldsymbol{n}} = 0. \tag{251}$$

Simple support boundary condition

With Reissner-Mindlin plate theory, there are two kinds of simple support conditions: soft or hard simple support. Whereas soft simple support may be interpreted as letting free both in-plane displacements (u_n and u_t, which also means that $\sigma_{nn} = \sigma_{nt} = 0$), hard simple support condition consists in enforcing $u_t = 0$ (and $\sigma_{nt} \neq 0$). With the Bending-Gradient plate theory this distinction does not always make sense because of the introduction of the generalized rotation $\underset{\sim}{\boldsymbol{\Phi}}$.

Without further assumption, it appears that each of the three components of $\underset{\sim}{\boldsymbol{\Phi}} \cdot \underline{\boldsymbol{n}}$ mixes projections of both in-plane displacements u_n and u_t. Consequently, it is not possible to choose which component of $\underset{\sim}{\boldsymbol{\Phi}} \cdot \underline{\boldsymbol{n}}$ to vanishes in order to selectively enforce $u_t = 0$. Hence, in the general case, only soft simple support may be applied and the corresponding boundary condition is similar to the free boundary condition where the transverse displacement is set to 0:

- if dim $\underset{\sim}{\boldsymbol{\mathcal{S}}}(\underline{\boldsymbol{n}}) = 3$, $\quad \underset{\sim}{\boldsymbol{M}} = \underset{\sim}{\boldsymbol{0}} \quad$ and $\quad U_3 = 0$.
- if dim $\underset{\sim}{\boldsymbol{\mathcal{S}}}(\underline{\boldsymbol{n}}) = 2$, $\quad \underset{\sim}{\boldsymbol{M}} \cdot \underline{\boldsymbol{n}} = \underline{\boldsymbol{0}} \quad$ and $\quad U_3 = 0$.

Let us assume now that the constitutive material is orthotropic with respect to $(\underline{\boldsymbol{n}}, \underline{\boldsymbol{t}})$ all through the thickness. The following hard simple support boundary condition is suggested when the constitutive material of the plate is orthotropic with respect to $(\underline{\boldsymbol{n}}, \underline{\boldsymbol{t}})$:

- if dim $\underset{\sim}{\boldsymbol{\mathcal{S}}}(\underline{\boldsymbol{n}}) = 3$, $\quad M_{nn} = 0, \quad M_{tt} = 0, \quad \Phi_{ntn} = 0 \quad$ and $\quad U_3 = 0$.
- if dim $\underset{\sim}{\boldsymbol{\mathcal{S}}}(\underline{\boldsymbol{n}}) = 2$, $\quad M_{nn} = 0, \quad \Phi_{ntn} = 0 \quad$ and $\quad U_3 = 0$.

Clamped boundary condition

When the plate is completely clamped on $\partial\omega_0 \subset \partial\omega$, all the kinematic variables $\underset{\sim}{\boldsymbol{\Phi}} \cdot \underline{\boldsymbol{n}}$ and U_3 are set to zero. Equivalently: $U_3 = 0$, $\Phi_{nnn} = 0$, $\Phi_{ntn} = 0$ and $\Phi_{ttn} = 0$.

B.2 Computation of the generalized shear compliance matrix

An orthotropic material is used, and characterized by $c, s, \theta, E_L, E_T, E_N, G, \nu$ and axis L, T and N already introduced in A.2.2

Membrane behavior

The plane part of $\underset{\approx}{\boldsymbol{S}}^{\sigma}$ 3×3, characterizes the behavior of the membrane plate.

$$\underset{\approx}{\boldsymbol{S}}^{\sigma} = \begin{bmatrix} S_{11} & S_{12} & S_{16} \\ S_{21} & S_{22} & S_{26} \\ S_{61} & S_{62} & S_{66} \end{bmatrix} \tag{252}$$

where

$$
\begin{aligned}
S_{11} &= \frac{c^4}{E_L} - \frac{2c^2s^2\nu_{LT}}{E_L} + \frac{s^4}{E_T} + \frac{c^2s^2}{2G_{LT}} \\
S_{12} = S_{21} &= \frac{c^2s^2}{E_L} - \frac{c^4\nu_{LT}}{E_L} - \frac{s^4\nu_{LT}}{E_L} + \frac{c^2s^2}{E_T} - \frac{c^2s^2}{2G_{LT}} \\
S_{22} &= \frac{s^4}{E_L} - \frac{2c^2s^2\nu_{LT}}{E_L} + \frac{c^4}{E_T} + \frac{c^2s^2}{2G_{LT}} \\
S_{16} = S_{61} &= \frac{2c^3s}{E_L} - \frac{2cs^3\nu_{LT}}{E_L} + \frac{2c^3s\nu_{LT}}{E_L} - \frac{2cs^3}{E_T} - \frac{c^3s}{2G_{LT}} + \frac{cs^3}{2G_{LT}} \\
S_{26} = S_{62} &= \frac{2cs^3}{E_L} - \frac{2c^3s\nu_{LT}}{E_L} + \frac{2cs^3\nu_{LT}}{E_L} - \frac{2c^3s}{E_T} + \frac{c^3s}{2G_{LT}} - \frac{cs^3}{2G_{LT}} \\
S_{66} &= \frac{4c^2s^2}{E_L} + \frac{8c^2s^2\nu_{LT}}{E_L} + \frac{4c^2s^2}{E_T} + \frac{c^4}{2G_{LT}} + \frac{s^4}{2G_{LT}} - \frac{c^2s^2}{G_{LT}}
\end{aligned}
$$

Transverse shear behavior

We identify the matrix $\underset{\sim}{S}^{\gamma}$ 2×2 linking shear and transverse deformation.

$$
\underset{\sim}{S}^{\gamma} = \begin{bmatrix} S_{44} & S_{45} \\ S_{54} & S_{55} \end{bmatrix} \tag{253}
$$

where

$$
\begin{aligned}
S_{44} &= \frac{c^2}{G_{TN}} + \frac{s^2}{G_{LN}} \\
S_{45} = S_{54} &= \frac{cs}{G_{LN}} - \frac{cs}{G_{TN}} \\
S_{55} &= \frac{c^2}{G_{LN}} + \frac{s^2}{G_{TN}}
\end{aligned}
$$

The Bending-Gradient shear compliance tensor may be derived as follows:

$$
\left[\underset{\approx}{\boldsymbol{h}}\right] = \left\langle \left(\int_{-\frac{h}{2}}^{x_3} {}^{T}[\![y_3 \underset{\approx}{\boldsymbol{C}}^{\sigma}(y_3) : \underset{\approx}{\boldsymbol{d}}]\!] dy_3 \right) . \underset{\sim}{\boldsymbol{S}}^{\gamma}(x_3) . \left(\int_{-\frac{h}{2}}^{x_3} [\![y_3 \underset{\approx}{\boldsymbol{C}}^{\sigma}(y_3) : \underset{\approx}{\boldsymbol{d}}]\!] dy_3 \right) \right\rangle \tag{254}
$$

By expanding the shear compliance tensor's equation and taking parts as piecewise constant functions, we obtain:

$$
\begin{aligned}
\left[\underset{\approx}{\boldsymbol{h}}\right] = \sum_{p=1}^{n} \Bigg[& \left(\sum_{q=1}^{p} S_q [\![\underset{\approx}{\boldsymbol{C}}^{\sigma,q} \underset{\approx}{\boldsymbol{d}}]\!] - \frac{e_p}{2} \left(l_p + \frac{e_p}{6} \right) [\![\underset{\approx}{\boldsymbol{C}}^{\sigma,q} \underset{\approx}{\boldsymbol{d}}]\!] \right)^{T} \underset{\sim}{\boldsymbol{S}}^{\gamma,p} e^p \left(\sum_{r=1}^{p} S_r [\![\underset{\approx}{\boldsymbol{C}}^{\sigma,q} \underset{\approx}{\boldsymbol{d}}]\!] - \frac{e_p}{2} \left(l_p + \frac{e_p}{6} \right) [\![\underset{\approx}{\boldsymbol{C}}^{\sigma,q} \underset{\approx}{\boldsymbol{d}}]\!] \right) \\
& + \frac{e_p^2}{12} \left(l_p^2 + \frac{e_p^2}{60} \right)^{T} \left([\![\underset{\approx}{\boldsymbol{C}}^{\sigma,q} \underset{\approx}{\boldsymbol{d}}]\!] \right) \underset{\sim}{\boldsymbol{S}}^{\gamma,p} e^p \left([\![\underset{\approx}{\boldsymbol{C}}^{\sigma,q} \underset{\approx}{\boldsymbol{d}}]\!] \right) \Bigg]
\end{aligned} \tag{255}
$$

where

$$
S_p = e_p l_p, \quad l_p = \frac{Z_p + Z_{p+1}}{2}
$$

The double stroked brackets $[\![\underset{\approx}{\bullet}]\!]$ denote here the following matrix representation of a fourth-order tensor:

$$[\![\underset{\approx}{\underset{\sim}{\boldsymbol{L}}}]\!] = \begin{pmatrix} L_{1111} & L_{1122} & \sqrt{2}L_{1121} & L_{1211} & L_{1222} & \sqrt{2}L_{1221} \\ L_{2111} & L_{2122} & \sqrt{2}L_{2121} & L_{2211} & L_{2222} & \sqrt{2}L_{2221} \end{pmatrix} \tag{256}$$

For instance, this notation enables to rewrite triple contraction products such as $\underset{\approx}{\underset{\sim}{\boldsymbol{i}}} \vdots \underset{\sim}{\boldsymbol{R}} = \underset{\sim}{\boldsymbol{Q}}$ as:

$$[\![\underset{\approx}{\underset{\sim}{\boldsymbol{i}}}]\!].\left[\underset{\sim}{\boldsymbol{R}}\right] = \underset{\sim}{\boldsymbol{Q}}, \tag{257}$$

where:

$$[\![\underset{\approx}{\underset{\sim}{\boldsymbol{i}}}]\!] = \begin{pmatrix} 1 & 0 & 0 & 0 & 0 & \dfrac{1}{\sqrt{2}} \\ 0 & 0 & \dfrac{1}{\sqrt{2}} & 0 & 1 & 0 \end{pmatrix} \tag{258}$$

Bibliography

Abisset, E., Daghia, F., Sun, X., Wisnom, M., Hallett, S., 2016. Interaction of inter- and intralaminar damage in scaled quasi-static indentation tests: Part 1 – experiments. Composite Structures 136, 712–726. URL: http://www.sciencedirect.com/science/article/pii/S0263822315009356, doi:doi:http://dx.doi.org/10.1016/j.compstruct.2015.09.061.

Alvarez-Lima, R., Diaz Diaz, A., Caron, J., Chataigner, S., 2012. Equations and theoretical validation. Composite Structures 94, 1694–1702.

Ambartsumian, S., 1960. On the theory of bending of anisotropic plates and shallow shells. Journal of Applied Mathematics and Mechanics 24, 500 – 514. URL: http://www.sciencedirect.com/science/article/pii/0021892860900526.

Ambartsumyan, S., 1969. Theory of anisotropic plate. Technomic Publishing Co.

Averill, R.C., 1994. Static and dynamic response of moderately thick laminated beams with damage. Composites Engineering 4, 381–395. URL: http://www.sciencedirect.com/science/article/pii/S0961952609800130, doi:doi:http://dx.doi.org/10.1016/S0961-9526(09)80013-0.

Barbero, E.J., Reddy, J.N., 1991. Modeling of delamination in composite laminates using a layerwise plate theory. International Journal of Solids and Structures 28, 373–388.

Baroud, R., Sab, K., Caron, J.F., Kaddah, F., 2016. A statically compatible layerwise stress model for the analysis of multilayered plates. International Journal of Solids and Structures 96, 11–24. URL: http://www.sciencedirect.com/science/article/pii/S0020768316301457, doi:doi:http://dx.doi.org/10.1016/j.ijsolstr.2016.06.030.

Botello, S., Onate, E., Canet, J.M., 1999. A layer-wise triangle for analysis of laminated composite plates and shells. Computer and Structures 70, 635–646.

Caillerie, D., Nedelec, J.C., 1984. Thin elastic and periodic plates. Mathematical Methods in the Applied Sciences 6, 159–191. URL: http://dx.doi.org/10.1002/mma.1670060112, doi:doi:10.1002/mma.1670060112.

Caron, J., Ehrlacher, A., 1997. Modelling the kinetics of transverse cracking in composite laminates. Composites Science and Technology 57, 1261–1270. URL: http://www.sciencedirect.com/science/article/pii/S0266353897000596, doi:doi:http://dx.doi.org/10.1016/S0266-3538(97)00059-6.

Caron, J.F., Diaz Diaz, A., Carreira, R.P., Chabot, A., Ehrlacher, A., 2006. Multi-particle modelling for the prediction of delamination in multi-layered materials. Composites Science and Technology 66, 755–765.

Carreira, R.P., Caron, J.F., Diaz Diaz, A., 2002. Model of multilayered materials for interface stresses estimation and validation by finite element calculations. Mechanics of Materials 34, 217–230.

Carrera, E., 1998. Mixed layer-wise models for multilayered plates analysis. Composite Structures 43, 57–70.

Carrera, E., 1999a. Multilayered shell theories that account for a layer-wise mixed description. part I. governing equations. American Institute of Aeronautics and Astronautics Journal 37, 1107–1116.

Carrera, E., 1999b. Multilayered shell theories that account for a layer-wise mixed description. part II. numerical evaluations. American Institute of Aeronautics and Astronautics Journal 37, 1117–1124.

Carrera, E., 2000. An assessment of mixed and classical theories on global and local response of multilayered orthotropic plates. Composite Structures 50, 183 – 198. URL: http://www.sciencedirect.com/science/article/pii/S0263822300000994, doi:doi:http://dx.doi.org/10.1016/S0263-8223(00)00099-4.

Carrera, E., 2002. Theories and finite elements for multilayered, anisotropic, composite plates and shells. Archives of Computational Methods in Engineering 9, 87–140. URL: http://dx.doi.org/10.1007/BF02736649, doi:doi:10.1007/BF02736649.

Carrera, E., 2003. Historical review of zig-zag theories for multilayered plates and shells. Applied Mechanics Reviews 56.

Carrera, E., 2004. On the use of the murakami's zig-zag function in the modeling of layered plates and shells. Computers and Structures 82, 541–554.

Cecchi, A., Sab, K., 2007. A homogenized reissner-mindlin model for orthotropic periodic plates: Application to brickwork panels. International Journal of Solids and Structures 44, 6055–6079.

Chabot, A., 1997. Interface Stress Analysis between Layers of composite Materials with the aid of Multi-particle Modellings of Multilayered Materials (M4). Theses. Ecole Nationale des Ponts et Chaussées. URL: https://pastel.archives-ouvertes.fr/tel-00197853. document scanné à partir de sa version papier originale de 1997.

Chataigner, S., Caron, J., Duong, V., Diaz Diaz, A., 2011. Experimental and numerical investigation of shear strain along an elasto-plastic bonded lap joint. Construction and Building Materials 25, 432–441.

Cho, M., Parmerter, R.R., 1993. Efficient higher order composite plate theory for general lamination configurations. American Institute of Aeronautics and Astronautics Journal 31, 1299–1305.

Chue, C.H., Liu, C.I., 2002. Disappearance of free-edge stress singularity in composite laminates. Composite Structures 56, 111–129.

CIMNE, GID, . The personal pre/postprocessor. Universitat Politechnica de Catalunya, Barcelone, Spain.

Daghia, F., de Miranda, S., Ubertini, F., Viola, E., 2008. A hybrid stress approach for laminated composite plates within the first-order shear deformation theory. International Journal of Solids and Structures 45, 1766–1787. URL: http://www.sciencedirect.com/science/article/pii/S0020768307004477, doi:doi:http://dx.doi.org/10.1016/j.ijsolstr.2007.10.020.

Dakshina Moorthya, C.M., Reddy, J.N., 1998. Modeling of delamination using a layerwise element with enhanced strains. International Journal for Numerical Methods in Engineering 43, 755–779.

Dallot, J., Sab, K., 2008. Limit analysis of multi-layered plates. part II: Shear effects. Journal of the Mechanics and Physics of Solids 56, 561–580.

Dhatt, G.., Touzot, G., 1984. Une présentation de la méthode des éléments finis. Maloine, Paris.

Di Sciuva, M., 1984. A refined transverse shear deformation theory for multilayered anisotropic plates. Atti. Accad. Sci. Torino 118, 279–295.

Diaz Diaz, A., 2001. Delaminage des materiaux multicouches : Phenomenes, modeles et criteres. Theses. Ecole Nationale des Ponts et Chaussées.

Diaz Diaz, A., Caron, J.F., 2006. Interface plasticity and delamination onset prediction. Mechanics of Materials 38, 648–663.

Diaz Diaz, A., Caron, J.F., Carreira, R.P., 2002. Software application for evaluating interfacial stresses in inelastic symmetrical laminates with free edges. Composite Structures 58, 195–208.

Duong, V.A., Diaz Diaz, A., Chataigner, S., Caron, J.F., 2011. A layerwise finite element for multilayers with imperfect interfaces. Composite Structures 93, 3262–3271.

Gaudenzi, P., Barboni, R., Mannini, A., 1995. A finite element evaluation of single-layer and multi-layer theories for the analysis of laminated plates. Computer and Structures 30, 427–440.

Giunta, G., Catapano, A., Belouettar, S., Vannucci, P., Carrera, E., 2012. Failure analysis of composite plates subjected to localized loadings via a unified formulation. Journal of Engineering Mechanics 138, 458–467. URL: http://dx.doi.org/10.1061/(ASCE)EM.1943-7889.0000358, doi:doi:10.1061/(ASCE)EM.1943-7889.0000358, arXiv:http://dx.doi.org/10.1061/(ASCE)EM.1943-7889.0000358.

Hadj-Ahmed, R., Foret, G., Ehrlacher, A., 2001. Stress analysis in adhesive joints with a multiparticle model of multilayered materials (m4). International Journal of Adhesion and Adhesives 21, 297–307. URL: http://www.sciencedirect.com/science/article/pii/S0143749600000348, doi:doi:http://dx.doi.org/10.1016/S0143-7496(00)00034-8.

He, L.H., 1994. A linear theory of laminated shells accounting for continuity of displacements and transverse shear stresses at layer interfaces. International Journal of Solids and Structures 31, 613–627. URL: http://www.sciencedirect.com/science/article/pii/0020768394901414, doi:doi:http://dx.doi.org/10.1016/0020-7683(94)90141-4.

Hildebrand, F.B., Reissner, E., Thomas, G.B., 1938. Notes on the foundations of the theory of small displacements of orthotropic shells. NACA TN-1833 .

Icardi, U., 2001. Higher-order zig-zag model for analysis of thick composite beams with inclusion of transverse normal stress and sublaminates approximations. Composites Part B: Engineering 32, 343–354. URL: http://www.sciencedirect.com/science/article/pii/S1359836801000166, doi:doi:http://dx.doi.org/10.1016/S1359-8368(01)00016-6.

Idlbi, A., Karama, M., Touratier, M., 1997. Comparison of various laminated plate theories. Composite Structures 37, 173–184. URL: http://www.sciencedirect.com/science/article/pii/S0263822397800104, doi:doi:http://dx.doi.org/10.1016/S0263-8223(97)80010-4.

Kant, T., Owen, D., Zienkiewicz, O., 1982. A refined higher order c0 plate bending element. Computers and Structures 15, 177–183. URL: http://www.sciencedirect.com/science/article/pii/0045794982900657, doi:doi:http://dx.doi.org/10.1016/0045-7949(82)90065-7.

Kant, T., Swaminathan, K., 2000. Estimation of transverse/interlaminar stresses in laminated composites – a selective review and survey of current developments. Composite Structures 49, 65 – 75. URL: http://www.sciencedirect.com/science/article/pii/S0263822399001269, doi:doi:http://dx.doi.org/10.1016/S0263-8223(99)00126-9.

Kant, T., Swaminathan, K., 2002. Analytical solutions for the static analysis of laminated composite and sandwich plates based on a higher order refined theory. Composite Structures 56, 329–344.

Karama, M., Harb, B.A., Mistou, S., Caperaa, S., 1998. Bending, buckling and free vibration of laminated composite with a transverse shear stress continuity model. Composites Part B: Engineering 29, 223–234. URL: http://www.sciencedirect.com/science/article/pii/S1359836897000243, doi:doi:http://dx.doi.org/10.1016/S1359-8368(97)00024-3.

Kassapoglou, C., 1986. An efficient method for the calculation of interlaminar stresses in composite materials. Journal of Applied Mechanics 53, 744–750.

Kassapoglou, C., Lagace, P., 1987. Closed form solutions for the interlaminar stress field in angle-ply and cross-ply laminates. Journal of Composite Materials 31, 292–308.

Lebée, A., Sab, K., 2011a. A bending-gradient model for thick plates. part I: Theory. International Journal of Solids and Structures 48, 2878–2888.

Lebée, A., Sab, K., 2011b. A bending-gradient model for thick plates. part II: Closed-form solutions for cylindrical bending of laminates. International Journal of Solids and Structures 48, 2889–2901.

Lebée, A., Sab, K., 2012. Homogenization of thick periodic plates: Application of the bending-gradient plate theory to a folded core sandwich panel. International Journal of Solids and Structures 49, 2778–2792.

Lebée, A., Sab, K., 2016a. On the generalization of reissner plate theory to laminated plates, part i: Theory. Journal of Elasticity , 1–28URL: http://dx.doi.org/10.1007/s10659-016-9581-6, doi:doi:10.1007/s10659-016-9581-6.

Lebée, A., Sab, K., 2016b. On the generalization of reissner plate theory to laminated plates, part ii: Comparison with the bending-gradient theory. Journal of Elasticity , 1–28URL: http://dx.doi.org/10.1007/s10659-016-9580-7, doi:doi:10.1007/s10659-016-9580-7.

Lebée, A., Sab, K., 2017. The Bending-Gradient Theory for Laminates and In-Plane Periodic Plates. Springer International Publishing, Cham. chapter The Bending-Gradient theory for laminates and in-plane periodic plates. pp. 113–148. URL: http://dx.doi.org/10.1007/978-3-319-42277-0_3, doi:doi:10.1007/978-3-319-42277-0_3.

Leguillon, D., 1999. A method based on singularity theory to predict edge delamination of laminates. International Journal of Fracture 100, 105–120.

Leguillon, D., Sanchez-Palencia, E., 1987. Computation of Singular Solutions in Elliptic Problems and Elasticity. volume 68. WILEY-VCH Verlag.

Lekhnitskii, S.G., 1981. Theory of elasticity of an anisotropic body. Mir Publishers, Moscow.

Lerpiniere, A., Caron, J., Diaz Diaz, A., Sab, K., 2014. The *LS* 1 model for delamination propagation in multilayered materials at $0^\circ/\theta^\circ$ interfaces: A comparison between experimental and finite elements strain energy release rates. International Journal of Solids and Structures 51, 3973–3986.

Levinson, M., 1980. An accurate, simple theory of the statics and dynamics of elastic plates. Mechanics Research Communications 7, 343–350. URL: http://www.sciencedirect.com/science/article/pii/009364138090049X, doi:doi:http://dx.doi.org/10.1016/0093-6413(80)90049-X.

Lewinski, T., 1991a. Effective models of composite periodic plates i. asymptotic solution. International Journal of Solids and Structures 27, 1155 – 1172.

Lewinski, T., 1991b. Effective models of composite periodic plates ii. simplifications due to symmetries. International Journal of Solids and Structures 27, 1173 – 1184.

Lewinski, T., 1991c. Effective models of composite periodic plates iii. two-dimensional approaches. International Journal of Solids and Structures 27, 1185 – 1203.

Librescu, L., 1975. Elastostatics and kinematics of anisotropic and heterogeneous shell type structures. Noordhoff.

Lo, K.H., Christensen, R.M., Wu, E.M., 1977a. A higher-order theory of plate deformation. part I: Homogeneous plates. Journal of Applied Mechanics 44, 663–668.

Lo, K.H., Christensen, R.M., Wu, E.M., 1977b. A higher-order theory of plate deformation. part II: Laminated plates. Journal of Applied Mechanics 44, 669–676.

Marco, D.S., Ugo, I., 1993. Discrete-layer models for multilayered shells accounting for interlayer continuity. Meccanica 28, 281–291.

Mittelstedta, C., Becker, W., 2005. Asymptotic analysis of stress singularities in composite laminates by the boundary finite element method. Composite Structures 71, 210–219.

Murakami, H., 1986. Laminated composite plate theory with improved in-plane responses. Journal of Applied Mechanics 53, 661–666.

Murthy, M., 1981. An improved transverse shear deformation theory for laminated anisotropic plate. Technical Report. NASA.

Naciri, T., Ehrlacher, A., Chabot, A., 1998. Interlaminar stress analysis with a new multiparticle modelization of multilayered materials (m4). Composites Science and Technology 58, 337–343.

Nelson, R.B., Lorch, D.R., 1974. A refined theory for laminated orthotropic plates. Journal of Applied Mechanics 41, 177–183.

Nguyen, T.K., Sab, K., Bonnet, G., 2008. First-order shear deformation plate models for functionally graded materials. Composite Structures 83, 25–36.

Nguyen, V.T., 2004. Finite elements for global and local modelling of multilayered plates. Theses. Ecole des Ponts ParisTech. URL: https://pastel.archives-ouvertes.fr/pastel-00001003.

Nguyen, V.T., Caron, J.F., 2006. A new finite element for free edge effect analysis in laminated composites. Computers and Structures 84, 1538–1546.

Nguyen, V.T., Caron, J.F., 2009. Finite element analysis of free-edge stresses in composite laminates under mechanical an thermal loading. Composites Science and Technology 69, 40–49.

Noor, A.K., Burton, W.S., 1989. Assessment of shear deformation theories for multilayered composite plates. Applied Mechanics Reviews 42, 1–13.

Ossadzow, C., Touratier, M., 2001. An improved shear-membrane theory for multilayered shells. Composite Structures 52, 85–95. URL: http://www.sciencedirect.com/science/article/pii/S026382230000194X, doi:doi:http://dx.doi.org/10.1016/S0263-8223(00)00194-X.

Pagano, N., 1969. Exact solutions for composite laminates in cylindrical bending. Journal of Composite Materials 3, 398–411.

Pagano, N., Pipes, R., 1970. Composite Laminates Under Uniform Axial Extension. Journal of Composite Materials , 538–548.

Pagano, N., Soni, S., 1983. Global-local laminate variational model. International Journal of Solids and Structures 19, 207–228. URL: http://www.sciencedirect.com/science/article/pii/0020768383900586",author="N.J.PaganoandS.R.Soni, doi:doi:http://dx.doi.org/10.1016/0020-7683(83)90058-6.

Pagano, N.J., 1970. Exact solutions for rectangular bidirectional composites and sandwich plates. Journal of Composite Materials 4, 20–34.

Pagano, N.J., 1978. Stress fields in composite laminates. International Journal of Solids and Structures 14, 385–400.

PAGANO, N.J., HATFIELD, H.J., 1972. Elastic behavior of multilayered bidirectional composites. AIAA Journal 10, 931–933. URL: http://dx.doi.org/10.2514/3.50249, doi:doi:10.2514/3.50249.

Panc, V., 1975. Theories of elastic plates. Noordhoff.

Polit, O., Touratier, M., 1997. A new laminated triangular finite element assuring interface continuity for displacements and stresses. Composite Structures 38, 37–44. URL: http://www.sciencedirect.com/science/article/pii/S0263822397000391, doi:doi:http://dx.doi.org/10.1016/S0263-8223(97)00039-1.

Polit, O., Touratier, M., 2002. A multilayered/sandwich triangular finite element applied to linear and non-linear analyses. Composite Structures 58, 121–128. URL: http://www.sciencedirect.com/science/article/pii/S0263822302000338, doi:doi:http://dx.doi.org/10.1016/S0263-8223(02)00033-8.

R.D., M., 1951. Influence of rotary inertia and shear on flexural motions of isotropic, elastic plates. Journal of Applied Mechanics 18, 31–38.

Reddy, J.N., 1984. A simple higher-order theory for laminated composite plates. Journal of Applied Mechanics 51, 745–752.

Reddy, J.N., 1987. A generalization of two-dimensional theories of laminated composite plates. Communications in Applied Numerical Methods 3, 173–180. URL: http://dx.doi.org/10.1002/cnm.1630030303, doi:doi:10.1002/cnm.1630030303.

Reddy, J.N., 1989. On refined computational models of composite laminates. International Journal for Numerical Methods in Engineering 27, 361–382. URL: http://dx.doi.org/10.1002/nme.1620270210, doi:doi:10.1002/nme.1620270210.

Reissner, E., 1944. On the theory of bending of elastic plates. Journal of Mathematics and Physics 23, 184–191. URL: http://dx.doi.org/10.1002/sapm1944231184, doi:doi:10.1002/sapm1944231184.

Reissner, E., 1945. The effects of transverse shear deformation on the bending of elastic plates. Journal of Applied Mechanics 12, 69–76.

Reissner, E., 1950. On a variational theorem in elasticity. Journal of Mathematics and Physics 29, 90–95. URL: http://dx.doi.org/10.1002/sapm195029190, doi:doi:10.1002/sapm195029190.

REISSNER, E., 1972. A consistent treatment of transverse shear deformations in laminated anisotropic plates. AIAA Journal 10, 716–718.

Reissner, E., 1984. On a certain mixed variational theorem and a proposed application. International Journal for Numerical Methods in Engineering 20, 1366–1368. URL: http://dx.doi.org/10.1002/nme.1620200714, doi:doi:10.1002/nme.1620200714.

Reissner, E., Stavsky, Y., 1961. Bending and stretching of certain types of heterogeneous aeolotropic elastic plates. Journal of Applied Mechanics 28, 402–408. URL: http://dx.doi.org/10.1115/1.3641719.

Ren, J., 1986. A new theory of laminated plate. Composites Science and Technology 26, 225–239. URL: http://www.sciencedirect.com/science/article/pii/0266353886900874, doi:doi:http://dx.doi.org/10.1016/0266-3538(86)90087-4.

Robbins, D.H., Reddy, J.N., 1993. Modeling of thick composites using a layerwise laminate theory. International Journal for Numerical Methods in Engineering 36, 655–677.

Sab, K., Lebée, A., 2015. Homogenization of Heterogeneous Thin and Thick Plates. Wiley-ISTE. URL: https://hal-enpc.archives-ouvertes.fr/hal-01266702, doi:doi:10.1002/9781119005247.

Saeedi, N., Sab, K., Caron, J.F., 2012a. Delaminated multilayered plates under uniaxial extension. part I: Analytical analysis using a layerwise stress approach. International Journal of Solids and Structures 49, 3711–3726.

Saeedi, N., Sab, K., Caron, J.F., 2012b. Delaminated multilayered plates under uniaxial extension. part II: Very efficient layerwise mesh strategy for the prediction of delamination onset. International Journal of Solids and Structures 49, 3727–3740.

Saeedi, N., Sab, K., Caron, J.F., 2013a. Cylindrical bending of multilayered plates with multi-delamination via a layerwise stress approach. Composite Structures 95, 728–739.

Saeedi, N., Sab, K., Caron, J.F., 2013b. Stress analysis of long multilayered plates subjected to invariant loading: Analytical solutions by a layerwise stress model. Composite Structures 100, 307–322.

di Sciuva, M., 1986. Bending, vibration and buckling of simply supported thick multilayered orthotropic plates: An evaluation of a new displacement model. Journal of Sound and Vibration 105, 425–442. URL: http://www.sciencedirect.com/science/article/pii/0022460X86901690, doi:doi:http://dx.doi.org/10.1016/0022-460X(86)90169-0.

Seide, P., 1980. An improved approximate theory for the bending of laminated plates. Mechanics Today 5, 451–466.

Senthilnathan, N.R., Lim, S.P., Lee, K.H., Chow, S.T., 1987. Buckling of shear deformable plates. AIAA Journal 25, 1268–1271.

Srinivas, S., 1973. A refined analysis of composite laminates. Journal of Sound and Vibration 30, 495–507. URL: http://www.sciencedirect.com/science/article/pii/S0022460X73801701, doi:doi:http://dx.doi.org/10.1016/S0022-460X(73)80170-1.

Srinivas, S., Rao, A.K., 1970. Bending, vibration and buckling of simply supported thick orthotropic rectangular plates and laminates. International Journal of Solids and Structures 6, 1463–1481.

Srinivas, S., Rao, A.K., 1973. Flexure of thick rectangular plates. Journal of Applied Mechanics 40, 298–299.

Sun, X., Wisnom, M., Hallett, S., 2016. Interaction of inter- and intralaminar damage in scaled quasi-static indentation tests: Part 2 – numerical simulation. Composite Structures 136, 727–742. URL: http://www.sciencedirect.com/science/article/pii/S0263822315009368, doi:doi:http://dx.doi.org/10.1016/j.compstruct.2015.09.062.

Swaminathan, K., Ragounadin, D., 2004. Analytical solutions using a higher-order refined theory for the static analysis of antisymmetric angle-ply composite and sandwich plates. Composite Structures 64, 405–417.

Tahani, M., Nosier, A., 2003. Edge effects of uniformly loaded cross-ply composite laminates. Materials and Design 24, 647—-658.

Tarun, K., D.R.J., O., O.C., Z., 1982. A refined higher-order c0 plate bending element. Computers and Structures 15, 177–183. URL: http://www.sciencedirect.com/science/article/pii/0045794982900657, doi:doi:http://dx.doi.org/10.1016/0045-7949(82)90065-7.

Techniwood, . système constructif industriel composite bois/isolant écologique, panobloc. Brevet n2220 305 B. .

Thai, N.D., D'Ottavio, M., Caron, J.F., 2013. Bending analysis of laminated and sandwich plates using a layerwise stress model. Composite Structures 96, 135 – 142. URL: http://www.sciencedirect.com/science/article/pii/S0263822312003984, doi:doi:http://dx.doi.org/10.1016/j.compstruct.2012.08.032.

Ting, T.C.T., Chou, S.C., 1981. Edge singularities in anisotropic composites. International Journal of Solids and Structures 17, 1057–1068.

Touratier, M., 1991. An efficient standard plate theory. International Journal of Engineering Science 29, 901–916. URL: http://www.sciencedirect.com/science/article/pii/002072259190165Y, doi:doi:http://dx.doi.org/10.1016/0020-7225(91)90165-Y.

Vannucci, P., 2013. The design of laminates as a global optimization problem. Journal of Optimization Theory and Applications 157, 299–323. URL: http://dx.doi.org/10.1007/s10957-012-0175-6, doi:doi:10.1007/s10957-012-0175-6.

Wang, A., Crossman, F.W., 1977a. Some New Results on Edge Effect in Symmetric Composite Laminates. doi:doi:10.1177/002199837701100110.

Wang, A.S.D., Crossman, F.W., 1977b. Some new results on edge effect in symmetric composite laminates. Journal of Composite Materials 11, 92–106.

Wang, S.S., Choi, I., 1982. Boundary-layer effects in composite laminates. part I: Free-edge stress singularities. Journal of Applied Mechanics 49, 541–548.

Whitney, J.M., 1969. The effects of transverse shear deformation on the bending of laminated plates. Journal of Composite Materials 3, 534–547.

Whitney, J.M., 1973. Shear correction factors for orthotropic laminates under static load. Journal of Applied Mechanics 40, 302–304.

Whitney, J.M., Pagano, N.J., 1970. Shear deformation in heterogeneous anisotropic plates. Journal of Applied Mechanics 37, 1031–1036.

Whitney, J.M., Sun, C.T., 1973. A higher-order theory for extensional motion of laminated composites. Journal of Sound and Vibration 30, 85–97.

Yang, P., Norris, C.H., Stavsky, Y., 1966. Elastic wave propagation in heterogeneous plates. International Journal of Solids and Structures 2, 665–684. URL: http://www.sciencedirect.com/science/article/pii/002076836690045X, doi:doi:http://dx.doi.org/10.1016/0020-7683(66)90045-X.

Yin, W.L., 1994. Free-edge effects in anisotropic laminates under extension, bending and twisting, part i: A stress-function-based variational approach. Journal of Applied Mechanics 61, 410–415.